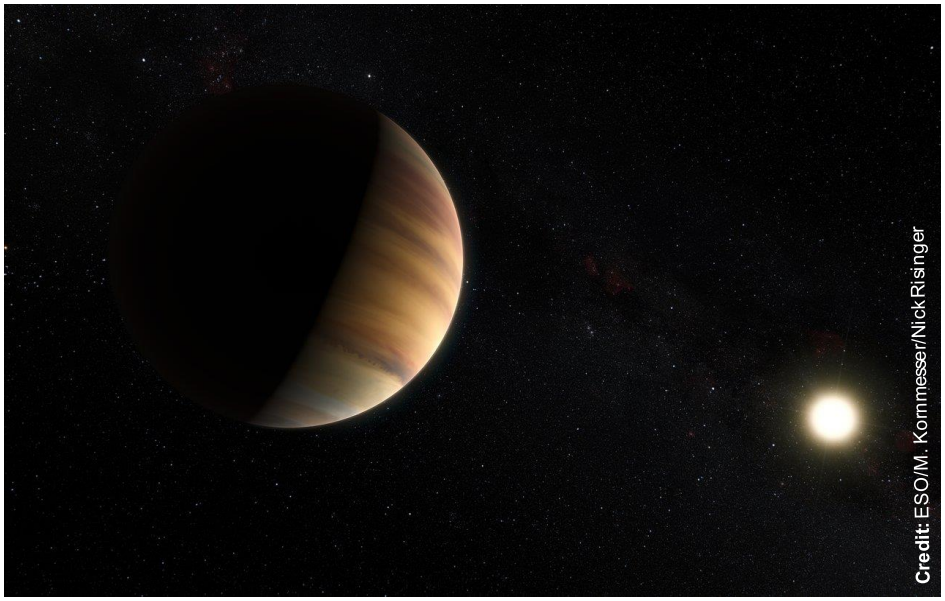

Characterizing the atmosphere of exoplanets using high-resolution spectroscopy

Jorge Humberto Costa Martins
Programa Doutoral em Astronomia
Departamento de Física e Astronomia
2017

Orientador
Pedro Ricardo Lourenço Figueira
Investigador Auxiliar
Instituto de Astrofísica e Ciências do Espaço

Coorientador
Nuno Miguel Cardoso Santos
Professor Associado Convidado
Faculdade de Ciências

Characterizing the atmosphere of exoplanets using high-resolution spectroscopy

PhD in Astronomy Dissertation

Author:

Jorge Humberto Costa Martins[1,2]

Supervisors:

Pedro Ricardo Lourenço Figueira[1] and Nuno Miguel Cardoso Santos[1,2]

Affiliations:

[1]Instituto de Astrofísica e Ciências do Espaço, Universidade do Porto, CAUP, Rua das Estrelas, 4150-762 Porto, Portugal

[2]Departamento de Física e Astronomia, Faculdade de Ciências, Universidade do Porto, Rua do Campo Alegre, 4169-007 Porto, Portugal

Acknowledgements

I must admit that when I began this endeavor I had no idea of the amount of work and sacrifice required to complete a PhD. And regardless of the amount of work, patience and dedication oneself puts into it, no one goes through it alone. As such, I would like to express my most sincere gratitude to all whom helped me complete this project, without you it would have been an impossible task.

Foremost, I would like to acknowledge the financial support from CAUP/IA during this PhD project, from funds from the European Research Council (ERC), under the European Community's FP7, through grant agreement nº ERC-2009-StG-239953 (EXOEarths) and from the Fundação para a Ciência e a Tecnologia (FCT) through national funds and by FEDER through COMPETE2020 by these grants UID/FIS/04434/2013 & POCI-01-0145-FEDER-007672 and PTDC/FIS-AST/1526/2014 & POCI-01-0145-FEDER-016886. I would also like to acknowledge the financial support of the European Southern Observatory (ESO), in the form a studentship at ESO/Chile.

I would like to thank my research supervisors, Dr. Pedro Figueira and Prof. Nuno Santos, for giving me the opportunity to perform my PhD thesis on such an interesting subject. I extend this gratitude to Dr. Claudio Melo, that mentored me during my ESO studentship in Chile. To all of them I thank deeply their patient supervision and enthusiastic encouragement all through this PhD project, both on the professional and personal levels. Not only I consider them excellent mentors and leaders, but also good friends.

I would also like to thank my colleagues at both CAUP/IA and ESO – including other researchers/students but also outreach and administrative people – for their help and support. In particular to the stars and planets group, many thanks for all the help, friendship and the many interesting discussions, work and non-work related, either at the workplace or around drink/food (sometimes both).

Last but not least, I would like express my gratitude for my family and friends. To my wife, a huge and heartfelt thank you for her constant support and patience, the substantial sacrifices she made so I could complete this herculean endeavor successfully, for believing in me and always being by my side. To my son, *g'acias* for being adorable and patient when daddy was too busy writing his thesis to play with him. To my parents and siblings, a big thank you for always supporting my "adventures", regardless where they take me. To my friends – in particular those I consider family, regardless on where in the world you are – thank you not only for putting up with me but also the help provided during this undertaking.

Resumo

A descoberta de planetas em torno de outras estrelas é uma das significantes descobertas científicas do Século XX. Hoje em dia, a *Exoplanetologia* é um dos ramos da Astronomia que mais interesse suscita, não só da comunidade cientifica, mas também dos media e público em geral. Isso garante-lhe um grande apoio de ambos, que lhe reconhecem o mérito cientifico e o apoiam no desenvolvimento de vários projectos (em missões espaciais como Kepler, PLATO ou em observatórios terrestres como o espectrógrafo ESPRESSO instalado no VLT ou o telescópio ELT do ESO).

Este trabalho foca-se na oportunidade criada pela espectroscopia de alta-resolução no ótico para caracterizar as atmosferas de outros planetas, em particular o seu albedo. A forma como um exoplaneta interage com a luz proveniente da sua estrela é essencial para entender algumas propriedades extremamente interessantes do planeta, como por exemplo, o seu clima, cobertura de nuvens, equilíbrio químico, habitabilidade, etc. Em particular, a luz de uma estrela refletida pela atmosfera de um planeta vai ser modulada pela refletividade (ou albedo) do planeta, uma quantidade extremamente dependente das suas propriedades químicas e físicas. Na banda do ótico, a assinatura de um planeta é maioritariamente luz refletida da sua estrela, mas várias ordens de grandeza mais ténue. Esta luz refletida aparece sobreposta ao espectro da estrela hospedeira, e escondida por entre o ruído estelar. Isso torna a sua deteção um difícil desafio observacional, no limite da geração atual de instalações astronómicas.

Ao longo deste projeto doutoral, estudamos a possibilidade de recuperar a dininuta assinatura ótica de planetas em torno de outras estrelas e estimar o albedo desses mesmo planetas para inferir a sua composição atmosférica. O resultado mais importante deste projeto foi a primeira deteção do espectro refletido de um exoplaneta (51 Pegasi b) na banda do ótico a partir de observações do sistema com o espectrógrafo de alta-resolução HARPS. Com base nessa deteção, conseguimos inferir que este planeta é provavelmente um planeta "inchado" com um albedo alto. Para chegar a este resultado, desenvolvemos uma técnica que faz uma correlação cruzada dos espectros de alta-resolução com uma máscara binária, o que permite amplificar o sinal do planeta e pô-lo em evidência face ao ruído estelar. Também implementámos uma variante desta tecnica não só permite recuperar o sinal de banda larga do planeta, mas também a sua dependência no comprimento de onda da radiação detetada. Testamos essa nova versão da técnica em observações simuladas com os espectrógrafos ESPRESSO e HIRES de vários planetas conhecidos. Em todos os casos conseguimos recuperar com sucesso as funções de albedo simuladas e distinguir entre possíveis modelos atmosféricos com composições diferentes.

A deteção do espectro ótico refletido de 51 Pegasi b é um grande passo para a compreensão das atmosferas de exoplanetas. No entanto, os verdadeiros desafios virão com a próxima geração de instrumentos como o ESPRESSO e os telescópios de 30 m como o ELT. Estes irão colocar-nos numa posição privilegiada para a deteção de luz refletida de exoplanetas e sonda as suas atmosferas com um nível de detalhe nunca antes atingido e talvez mesmo encontrar provas de vida noutros planetas.

Palavras chave: espectroscopia de alta-resolução, exoplanetas, luz refletida, função de correlação cruzada, albedo

Abstract

The discovery of planets around other stars is one of the greatest scientific discoveries of the 20^{th} century. Nowadays, exoplanetology is one of the fields in Astronomy that generates most interest, not only from the scientific community but also from the media and public in general. This grants it a large support from both, which recognize this field's scientific value and support the development of several projects (space missions like Kepler, PLATO or ground based like ESPRESSO, ESO's ELT) with exoplanet science as one of their main drivers.

This work focuses on the opportunity that arises from optical high-resolution spectroscopy to characterize exoplanetary atmospheres, in particular their albedo. How an exoplanet atmosphere interacts with the radiation coming from its host star is paramount to understand some highly interesting planet's characteristics such as its climate, cloud coverage, chemical balance, habitability, etc. In particular, when the light from a star is reflected on a planet's atmosphere, it will be modulated by the planet's reflectance – or albedo – which is highly dependent on the atmospheric chemical and physical characteristics. At visible wavelengths, an exoplanet's signature is essentially reflected light from the host star, only several orders of magnitude fainter. However, it is superimposed on the stellar host spectrum and hidden amidst the stellar noise. This makes its detection a difficult observational challenge, pushing the limits of current generation of observing facilities.

In this doctoral project, we studied the possibility to recover the minute optical signature from exoplanets and infer the planetary albedo to hint at its atmospheric composition. The major result from this project was the recovery of the reflected optical spectral signal from 51 Pegasi b from HARPS observations of the system, and infer that this planet is most likely a highly-inflated planet with a high albedo. To do so, we cross-correlated these observations with a spectral mask to amplify the planetary signal and make it surface above the stellar noise. We extended the cross-correlation technique to make it capable to not only recover the broadband albedo from the planet, but also its color dependency. We tested the technique to simulated ESPRESSO and HIRES observations of known planets. In all cases, we were able to successfully recover the simulated albedo function and distinguish between possible atmospheric models with different compositions.

The detection of the reflected optical spectrum from 51 Pegasi b is a major step towards the understanding of exoplanet atmospheres. However, the real challenges will come with the next generation of instruments such as ESPRESSO and 30-m class telescopes like the ELT. These will put us in a privileged position to detect reflected light from exoplanets, probe their atmospheres in unsurpassed detail and maybe even find proof of life.

Keywords:high-resolution spectroscopy,exoplanets,reflected light,cross-correlation function,albedo

Contents

List of Tables

Figures

Page

Acronyms

ADI Angular Differential Imaging. 32

ALMA Atacama Large Millimeter Array. 156

AO Adaptive Optics. 32, 127

ARIEL Atmospheric Remote-sensing Infrared Exoplanet Large-survey. 127

CCF Cross Correlation Function. 62–65, 67–70, 73, 74, 76–91, 93, 94, 96, 98, 99, 101, 102, 113–116, 119, 121, 122, 126, 127, 159, 181, 192, 193

CHEOPS CHaracterising ExOPlanet Satellite. 127

CRIRES CRyogenic high-resolution InfraRed Echelle Spectrograph. 39, 40, 88

ELT Extremely Large Telescope. 7, 9, 16, 58, 93, 100, 121, 122, 124, 126, 127, 148, 149

ESO European Southern Observatory. 5, 7, 9, 31, 33, 54, 56–59, 72, 86, 87, 89, 93, 98, 121, 127, 149, 156

ESPRESSO Echelle SPectrograph for Rocky Exoplanet and Stable Spectroscopic Observations. 7, 9, 26, 40, 55, 57–59, 93–96, 98–101, 113–116, 125–127, 148, 185, 186

ETC Exposure Time Calculator. 15, 16, 72, 95, 99, 116, 117, 121, 124

FLAMES Fibre Large Array Multi Element Spectrograph. 55

FWHM Full Width at Half Maximum. 54, 67, 73, 77, 79, 81, 84–87, 159

G-CLEF GMT – CfA Large Earth Finder. 125

GAIA Global Astrometric Interferometer for Astrophysics. 28

GMT Giant Magellan Telescope. 125, 149, 153

GPI Gemini Planet Imager. 32

HARPS High Accuracy Radial Velocity Planet Searcher. 7, 9, 15, 26, 53–59, 63, 68, 71, 72, 74–76, 82, 86, 87, 93, 95, 96, 99, 101, 113, 116, 117, 125, 159, 181, 182

HARPS DRS HARPS Data Reduction Software. 67, 72, 73, 90, 181

HARPS-N HARPS-N. 72, 181, 182

HDS+HCI High-Dispersion Spectroscopy and High-Contrast Imaging. 39

HIRES HIgh RESolution spectrograph for the E-ELT. 7, 9, 58, 59, 93–101, 113, 116, 125–127, 148, 185–187

HST Hubble Space Telescope. 36, 46

JWST James Webb Space Telescope. 127

MACAO Multi-Application Curvature Adaptive Optics. 40

MNRAS Montly Notices of the Royal Astronomy Society. 103

PDI Polarized Differential Imaging. 32

PHASES Palomar High-precision Astrometric Search for Exoplanet Systems. 27

PSF Point Spread Function. 32, 54, 55, 72

RV radial velocity. 23–26, 28, 30, 31, 33, 34, 38, 45, 53–57, 62, 64–70, 72–79, 81, 83, 84, 119, 127, 159, 181

S/N signal-to-noise ratio. 19, 100, 115–117, 121, 122, 192, 193

SPHERE Spectro-Polarimetric High-contrast Exoplanet REsearch. 33, 40, 127

TNG Telescopio Nazionale Galileo. 55

TTV transit timing variations. 23, 30, 31

UVES Ultraviolet and Visual Echelle Spectrograph. 18, 43, 55–57, 71, 72, 88–91, 126, 159

VLT Very Large Telescope. 7, 40, 55–57, 93, 96, 100, 122, 125–127, 148

Chapter 1.

Introduction

The detection of 51 Pegasi b (Mayor et al., 1995) – the first exoplanet discovered around a solar-type star other than the Sun – is one of the greatest scientific discoveries of the 20th century. This breakthrough had huge implications in Astronomy, in particular by confirming that our Solar System was not alone. At the moment of writing, more than 3600 planets in over 2700 systems have been announced (Schneider et al., 2011), with more than 2600 additional candidates from the Kepler and K2 missions still awaiting confirmation (Borucki et al., 2010; Howell et al., 2014). Figure 1.1 shows the number of confirmed planets by year and method since the discovery of 51 Pegasi b as per the *exoplanet.eu* database (Schneider et al., 2011). It can be seen that the transit technique (e.g with the Kepler Mission, Lissauer et al., 2014; Rowe et al., 2014) has been the most prolific, shortly followed by the radial velocities method (e.g. with the HARPS spectrograph – Mayor et al., 2003; Bonfils et al., 2013).

Initially, researchers were only able to detect large and massive planets in short period circular orbits (51 Pegasi b – Mayor et al., 1995; ups And b & τ Boo b - Butler et al., 1997, among others). These so called hot Jupiter-type planets were completely unlike any planet known in the Solar System where giant planets orbit our Sun with periods of several years. These discoveries challenged the accepted canons regarding planetary systems

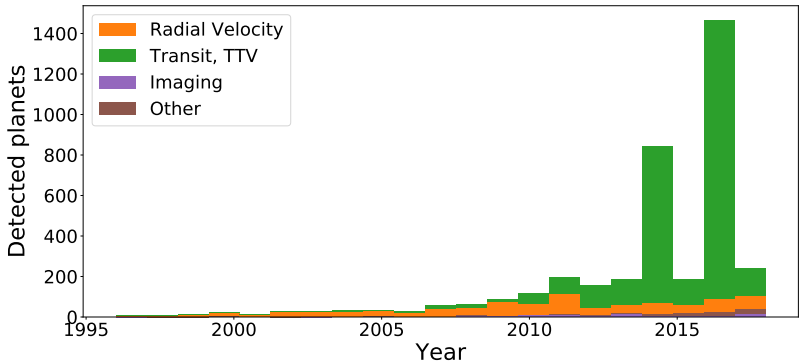

Figure 1.1: Exoplanet detection by year and method (data taken from the *exoplanet.eu* database as of December 2017).

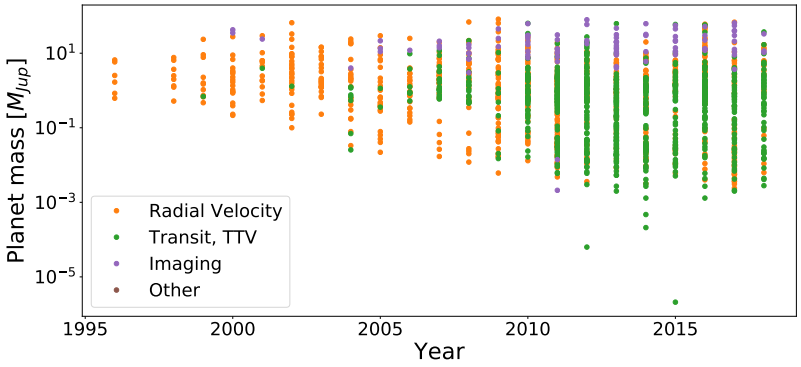

Figure 1.2: Confirmed exoplanets by year and mass (data taken from the *exoplanet.eu* database as of December 2017).

architecture and formation models (e.g. Pollack et al., 1996). At that time, the main current of thought dictated that our own Solar System should be a typical planetary system: small rocky planets close to the star, giant gaseous planets away from the star. 51 Pegasi b did not fit any of those categories: while being a Jupiter mass planet, it was orbiting its host star at an orbital separation of 0.052 A.U., much closer to the star than Mercury is from the Sun. Subsequent discoveries (e.g., Butler et al., 1997; Charbonneau et al., 2000) confirmed that 51 Pegasi b was not alone and the so called hot Jupiter-class planets were indeed real. With time, the development of more sensitive instruments and advanced data analysis techniques have allowed to steadily detect increasingly smaller and lighter planets (see Figure 1.2) at incrementing distances from their hosts.

Currently, astronomers are already able to probe into the Earth mass domain (e.g. Dumusque et al., 2012) and Earth-like periods (e.g. Santos et al., 2004b; Fischer et al., 2008; Mayor et al., 2011). Some planets have already been found on the so called Habitable Zone (e.g. Pepe et al., 2011; Borucki et al., 2012) of their stars, the torus sharped region around a star where where water on a planet can be stably maintain a liquid state for extended periods of time. Of those, the most notable case – due to its proximity to the Sun – is arguably Proxima Centauri b (Anglada-Escudé et al., 2016), making it an ideal target for the search for life.

Figure 1.3 presents the current census of exoplanets in terms of distance to the host and masses, by detection

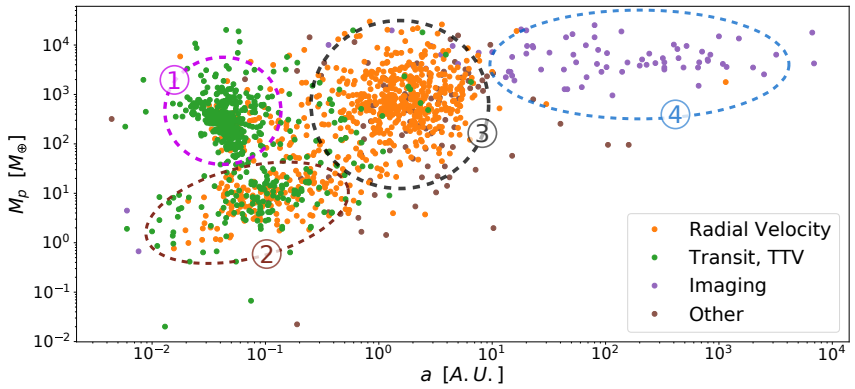

Figure 1.3: Confirmed exoplanets by orbital period and mass per detection method (data taken from the *exoplanet.eu* database as of December 2017). Different planet populations are identified: ①: hot Jupiters; ②: low-mass planets in close-in orbits; ③: warm gas giants; ④: cold gas giants.

method. Note that this plot only shows planets with known masses and as such does not include a large fraction of the Kepler candidates that were validated statistically and for which only only the radius is known. In this figure, several planets populations can be easily identified – with clear gaps separating them – which we highlighted with colored ellipses and numbers. Population 1 corresponds to hot Jupiter type planets, gas giants ($\mathrm{M_p} > 0.3\mathrm{M_{Jup}}$ – Hatzes et al., 2015) with orbital periods typically under 10 days, of which 51 Pegasi b is the prototype. These planets are highly irradiated by their hosts and have equilibrium temperatures of about 1500-2500 K (Komacek et al., 2016), which caused them to have typically have anomalously large radii (e.g Guillot et al., 2002). Currently, it is believed that these planets did not form *in-situ*, but far from their hosts and then migrated inwards (e.g. Kley et al., 2012). Population 2 corresponds to low-mass planets also with close-in orbits. This population is mainly composed of hot or warm Neptunes and super-earths, planets with $\mathrm{M}\sin(\mathrm{i}) < 30\mathrm{M}_\oplus$ and orbital periods inferior to 50 days. It is worth noting that while hot or warm Neptunes and super-earths might cover similar mass ranges, their compositions will be quite different (e.g., hot or warm Neptunes will have a much larger amount of H_2/He, which lead to quite different bulk densities for each planet type. As such, mass and radii measurements will permit to estimate the planet bulk density and composition and distinguish between hot or warm Neptunes and super-earths (see Section 2.1 for more details). Population 3 corresponds to warm gas giant planets, large gaseous with orbital periods between 10 and 200 days and equilibrium temperatures under 1000 K. Although similar to their hot Jupiter counterparts, warm Jupiters are thought to have formed *in-situ* (e.g Boley et al., 2016). Population 4 corresponds to cold gas giants, similar to to Jupiter and Saturn, which have been found and characterized in much lower numbers, most of them through microlensing.

The large number of known exoplanets has led to some interesting statistical studies on planet populations. it is now accepted that the planetary populations are dominated by hot or warm Neptunes, super-earths, and potentially lower mass planets, which we are only now starting to discover. Currently accepted values suggest an occurrence rate of such low-mass planets at about 30% around FGK stars (Howard et al., 2010; Mayor et al., 2011) and about 40% around M dwarfs (Bonfils et al., 2013). In spite of being the first to be discovered due to the large amplitude they induce on their host, hot Jupiter-type planets are thought to orbit only 1.2% of FGK planet-hosts (Mayor et al., 2011; Wright et al., 2012).

DETECTION METHODS 1.1

As mentioned before, Figure 1.3 shows the current outlook of the detected planets in terms of distance to the host and masses. In the plot, different colors denote different detection methods. It is clear from the plot that each detection technique is sensitive to a different parameter space. In brief, the radial velocity (RV), transit and transit timing variations (TTV) techniques are more sensitive to giant planets in close orbits as they measure the impact of the presence of the planet on the stellar spectroscopic and photometric signals, which is proportional to the planetary mass/radius and inversely proportional to the distance to the host. Imaging techniques will be more sensitive to hot young giant planets far from their hosts as they are highly dependent on the angular separation

between the planet and host, as well as the planetary flux (higher in the infrared for young planets).

Note that all planet detection method have their limitations, for example the subset of physical parameters they measure (e.g. the RV method does not allow to recover the planetary radius) or that the effect they detect can be mimicked by phenomena other than planets (e.g., grazing eclipses of a binary star might mimic a transit - Winn, 2011; or radial velocity variations induced by stellar activity Queloz et al., 2001). As such, it is commonplace for researchers to combine multiple detection methods to confirm the detection of a planet. When not possible, the statistical validation of the planet candidates is normally performed (e.g with the BLENDER – Morton et al., 2011; – and PASTIS – Díaz et al., 2014, –data analysis algorithms). A more extensive discussion can be found in Seager (2011), as well as a complete derivation of the equations used in this chapter.

RADIAL VELOCITY 1.1.1

The principle behind this technique – depicted in the left panel of Figure 1.4 – is to measure the variations on a star radial velocity (RV) induced by the gravitational pull of a companion. This is the method that led to the detection of 51 Pegasi b. The right panel of Figure 1.4 shows the RV variation of 51 Pegasi measured by Mayor et al. (1995) to detect its orbiting planet.

At any given moment, a star's RV can be obtained by comparing the wavelength shift of its spectral lines relative to their rest wavelength. Let's consider a single spectral line i of a given spectrum, with rest wavelength λ_i. As a result of the non-relativist Doppler effect, when an object is moving with a radial velocity RV, spectral line i will have its wavelength shifted to λ_i', as per

$$\lambda_i' = \lambda_i(1 + \frac{RV}{c}) \tag{1.1}$$

where c the speed of light in vacuum.

If a star has no companions (planetary or otherwise), Equation 1.1 will yield the RV of the star relatively to the Sun resulting from its proper motion around the galactic center. When a companion is present, the star will

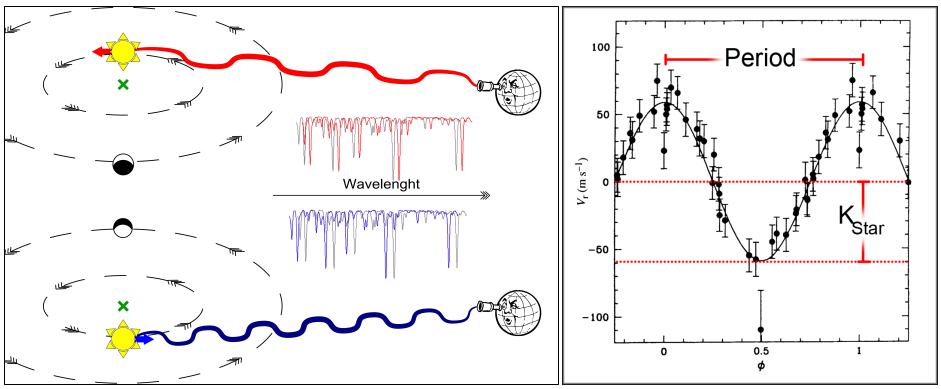

Figure 1.4: ***Left***: Diagram depicting the Radial Velocity method. Star spectra get Doppler shifted towards longer wavelengths if moving away from the observer (red-shifted), and towards shorter wavelengths when it moves towards the observer (blue-shifted). ***Right***: Phase folded observations from the first detection of 51 Peg b (from Mayor et al., 1995).

oscillate around the system's barycenter, which will produce a periodic variation in its RV (Left panel of Figure 1.4). The amplitude of this RV variation is proportional to the companion/star mass ratio. Such stellar RV oscillations can be modeled by the RV equation (Paddock et al., 1913)

$$RV_* = RV_0 - k_* \left(cos(\omega + f) + e\, cos(\omega)\right) \tag{1.2}$$

where RV_0 is the radial velocity of the center of mass of the system relatively to the Sun, ω is the argument of periapsis from the orbit and f is the true anomaly[1]. K_* is the RV semi-amplitude, defined as

$$K_* = \frac{RV_{max} - RV_{min}}{2}, \tag{1.3}$$

where RV_{max} and RV_{min} are respectively the highest and lowest measured radial velocities of the star. Assuming that $m_* >> m_p$ – where m_* and m_p are respectively the mass of the star and the planet – this quantity can be related to the orbital parameters by

$$K_* = \left(\frac{2\,\pi\,G}{P}\right)^{1/3} \frac{m_p\, sin(i)}{m_*^{2/3}} \frac{1}{\sqrt{1-e^2}} \tag{1.4}$$

where e is the orbital eccentricity, i is the inclination of the orbit relatively to the plane of the sky, P is the orbital period and G is the gravitational constant.

As seen in Equation 1.4, the amplitude of the observed signal will depend on both the orbital inclination (i) and the planetary mass. However, the planetary mass and orbital inclination are degenerate, and the RV method can only recover the minimum mass of the planet, defined as $m_p\ sin(i)$. Nonetheless, if we assume that the average value of $\sin(i)$ for a random distribution of angles is ~ 0.79, the average factor of overestimation on the planetary masses is only ~ 1.27. Therefore, it is statistically more likely for planets detected with the RV method to have close to edge-on orbits and thus the minimum mass of detected systems is, on average, quite close to the real planet's mass.

Table 1.1 presents the RV semi-amplitude induced for selected archetypal planets with different masses and periods on a solar mass star. As noted before, a direct consequence of the previous equations is that the RV

		K_*			
m_p	p =	3 days	1 year	5 years	
m_{Jup}		140.8	28.4	16.6	$[m/s]$
m_{Nep}		7.60	1.53	0.90	$[m/s]$
m_{Earth}		44.3	8.9	5.2	$[cm/s]$

Table 1.1: Orbital semi-amplitude of the star for different planetary masses and orbital periods (from Figueira, 2010).

[1]The angle between the periastron direction and the star or planet position on its orbit. For circular orbits the $\omega = 0$ and f is replaced by the orbital phase ϕ, defined from the point of maximum radial velocity.

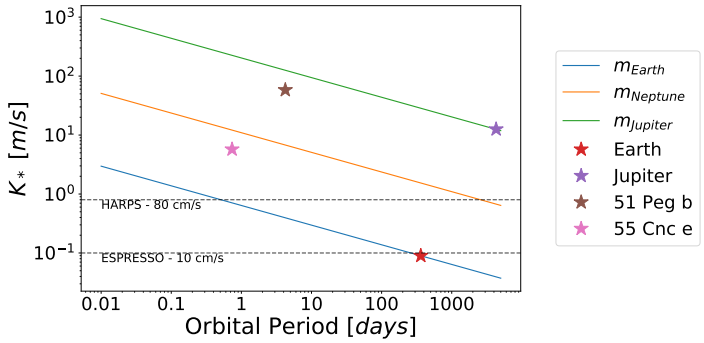

Figure 1.5: RV semi-amplitude induced a one solar mass star, as a function of orbital period for different planet masses (colored lines). The colored stars shows the position of selected known planets. The horizontal dashed lines correspond to the proposed RV detection limits for HARPS and ESPRESSO as per the literature (Pepe et al., 2000; Pepe et al., 2010).

method is more sensitive to giant planets in close orbits, as the combination of larger masses with shorter orbital semi-axis causes larger amplitude "wobbles" to the RV of the star (see Equation 1.4). As such, the first exoplanets to be detected were, as expected, giant planets in close orbits (e.g. hot Jupiters like 51 Pegasi b – Mayor et al., 1995; – υ And b & τ Boo b – Butler et al., 1997, – among many others). The subsequent increase in instrumental precision (e.g. with HARPS) allowed the detection and mass measurement of increasingly lower mass planets (e.g. hot Neptunes such as Gliese 436 b – Butler et al., 2004; and super-earths such as CoRoT-7b – Léger et al., 2009) at increasing distances from their hosts (e.g. HD 134987 b – Jones et al., 2010). More recently, the development of new data analysis methods (e.g. gaussian processes – Rajpaul et al., 2015) are enabling researchers to move into the Earth-type planets domain (e.g. Kepler-78b – Grunblatt et al., 2015). In terms of instrumentation, the next generation of observing facilities (e.g. ESPRESSO – Pepe et al., 2010) will permit to detect variation of the order of 10 cm/s, a requirement to detect Earth like planets. Figure 1.5 shows the variation on the RV semi-amplitude induced over a one solar mass star, as a function of orbital period for different planet masses (colored lines). The horizontal dashed lines correspond to the proposed RV detection limits for HARPS and ESPRESSO as per the literature (Pepe et al., 2000; Pepe et al., 2010). The colored stars shows the position of some archetypal planets: i) the Earth, ii) Jupiter, iii) 51 Pegasi b (hot Jupiter with about half the mass of Jupiter and a 4.23 day orbital period) and iv) 55 Cancri e (super-earth with about 8 times the mass of the Earth and a 17.5h orbital period).

ASTROMETRY 1.1.2

The physical principle behind this method is the same as with the RV method – both are based on the gravitational pull a companion exerts over its host star – but measure different quantities. While the RV method measures variations on the star's RV, with astrometry what is measured are tiny periodic variations in the star's position, i.e., its movement on the plane of the sky. These variations result from dynamical perturbations induced on the star proper motion due to the presence of a companion.

After subtracting Earth's orbital motion, as it orbits the galactic center a star with no companions will follow an apparent straight path on the sky. However, the gravitational influence of a companion will make it wobble

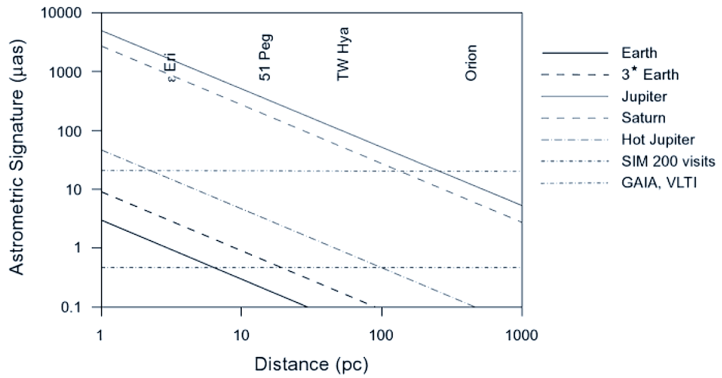

Figure 1.6: Astrometric signal for different planet types, as well as the detection limits of several facilities (from Quirrenbach, 2010).

around the straight path followed by the barycenter of the system. The amplitude of this wobble is proportional to the companion/star mass ratio[2] and the orbital parameters of the system can be extracted by using Kepler's Laws. The amplitude of the astrometric signature (θ) of a planet on a circular orbit (assuming $M_p << M_*$) is given by

$$\begin{aligned} \theta = \frac{M_p}{M_* + M_p}\frac{a}{D} &\approx \frac{M_p}{M_*}\left(\frac{G}{2\pi^2}\right)^{1/3}\frac{M_p}{M_*^{2/3}}\frac{P^{2/3}}{D} \\ &\approx \frac{M_p}{M_*}\frac{a}{1\ A.U.}\frac{D}{1\ pc}^{-1} arcsec \end{aligned} \tag{1.5}$$

where M_p and M_* are respectively the mass of the planet and the star, a the semi-major axis of the orbit and D the distance from the observer to the system (Perryman, 2011). This quantity corresponds to the semi-major axis of the apparent ellipse the star describes in the sky in angular units. Figure 1.6 shows the astrometric signal for different planet types, as well as the detection limits of several facilities, where M_p and M_* are respectively the mass of the planet and the star, P is their orbital period, a the semi-major axis of the orbit and D the distance from the observer to the system. This quantity corresponds to the semi-major axis of the apparent ellipse the star describes in the sky in angular units. Figure 1.6 shows the astrometric signal for different planet types, as well as the detection limits of several facilities.

Figure 1.7 shows the modeled path of a star at 50 pc perturbed by a $15\ M_{Jup}$ planet on an orbit with $a = 0.6\ a.u$ and $e = 0.2$ (Perryman, 2000).The straight dashed line represents the path of the system's barycenter, as seen from the Solar system barycenter. The dotted line shows the same path but as seen from Earth. The solid line shows the perturbation to the movement of the star due to the presence of the planet, but magnified 30 times for visibility. At the moment of writing there is only one confirmed planet discovered with this technique: HD 176051 b with the Palomar High-precision Astrometric Search for Exoplanet Systems (PHASES) survey (Muterspaugh et al., 2010). This planet has a mass of about $1\ M_{Jup}$ and orbits its host in a circular orbit with a period of about

[2]Since we are observing a 2-dimensional projection of a 3-dimensional orbit, some degree of degeneracy is expected on the detected companion/star mass ratio.

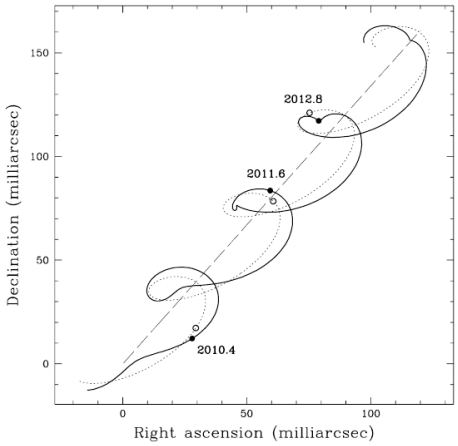

Figure 1.7: Modeled path of a star at 50 pc perturbed by a $15\,M_{Jup}$ planet on an orbit with $a = 0.6a.u$ and $e = 0.2$ (Perryman, 2000). The straight dashed line represents the path of the system's barycenter, as seen from the Solar system barycenter. The dotted line shows the same path but as seen from Earth. The solid line shows the perturbation to the movement of the star due to the presence of the planet, but magnified 30 times for visibility.

one thousand days.

The major strength of the astrometry technique is that, when combined with the RV technique, it has the ability to reconstruct a 3-dimensional model of the planetary orbit and as such to recover all orbital parameters, including the inclination of the orbit, as well as the mass for the planet. However, the major obstacle for the technique is that it requires very precise measurements of the astrometric angles of the host stars – typically $\leq$ 1 mas – over long periods of time. Although challenging, this is within the capabilities of the Global Astrometric Interferometer for Astrophysics (GAIA) mission. Albeit not primarily designed as a planet hunting mission, it is estimated that its high astrometric precision should permit to detect about 21 000 large mass planets over its 5 year mission (Perryman et al., 2014).

TRANSITS 1.1.3

This method is to date the most prolific planet detection method. At the moment of writing, it has detected over 70% of all confirmed planets, most of them detected with the Kepler mission (Borucki et al., 2010). It relies on the quantification of the periodic dimming in the flux from a star as an orbiting planets crosses the observer's line-of-sight, effectively causing a mini-eclipse. As such, this method is restricted to the detection of planets in edge-on orbits, i.e., orbits aligned (within a few degrees) with the observer's line-of-sight. Figure 1.8 shows the light curve for Kepler-15 and its orbiting planet (Endl et al., 2011) and a diagram of a transiting system.

The main deliverable of this method is the planet/star radius ratio, as

$$\frac{\Delta L}{L} \sim \left(\frac{R_p}{R_*}\right)^2 \tag{1.6}$$

where L and ΔL are respectively the luminosity and its maximum variation, and R_p and R_* the radii of both the planet and the star. Note that planets can only be detected through this method if the inclination of their orbit is

close to $90°$. As such, the geometric probability P for a planet to transit its host star decreases with the distance to the host and can be estimated from

$$P \approx \frac{R_*}{a\,(1-e^2)} \tag{1.7}$$

where R_* is the stellar radius, a is the semi-major axis of the planetary orbit and e is its eccentricity (Barnes et al., 2007).

The main limitation of the transit method is its inability to directly recover the mass of the detected planet or its orbital eccentricity. Therefore, it needs to be combined with other methods – e.g. RVs – to fully characterize a system in terms of orbital parameters. The ambiguity on the planet mass makes also this method extremely susceptible to false-positive detections. Several astrophysical phenomena can mimic transiting planets (see Figure 1.9 for a few of the most common) and as such independent confirmation from other methods is required. Most of these confirmations come from RV follow-ups (e.g. Santerne et al., 2011) and when confirmation is not possible (e.g., the reflex motion of the star is too small to be measured with existing instrumentation), planetary candidates need to be statistically validated (e.g with the BLENDER – Morton et al., 2011; – and PASTIS – Díaz et al., 2014, – data analysis algorithms). From the analysis of K2 data, Fressin et al. (2013) finds a false positive rate of 9.4% (17.7% for giant planets, 6.7% for small Neptunes and 12.3% for Earth size planets), while for short period giant planets Santerne et al. (2012) reported a false-positive rate as high as 35%. The 6-year RV followup with the SOPHIE spectrograph (OHP, France) of 129 giant planets with orbital periods under 400 days yields even higher values, a 54.6% false positive rate (Santerne et al., 2016). Note that these estimated false-positive rates cannot be compared directly. First of all, Santerne et al. (2016) had access to a candidate sample (Kepler quarters Q1-Q17 – Coughlin et al., 2016) with twice as many planet candidates as the other authors (Kepler quarters Q1-Q6 – Batalha et al., 2013). Furthermore, the selection criteria differed for each author. For example, Fressin et al. (2013) defined their giant-planet candidates based on their radii, while Santerne et al. (2016) made their

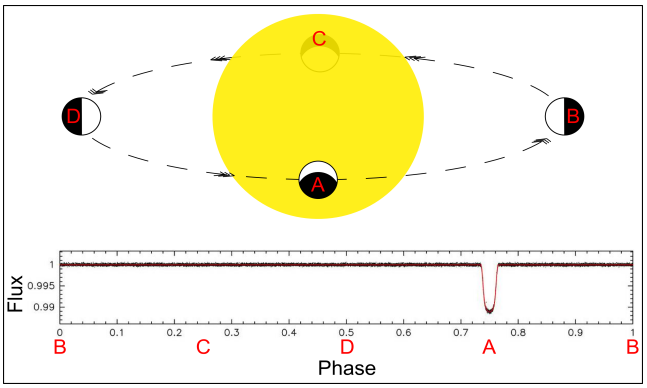

Figure 1.8: ***Top***: Diagram of the orbit of a transiting planet. *(A)* corresponds to the primary transit point and *(B)* to opposition. ***Bottom***: Light curve for Kepler-15 b (Endl et al., 2011) with each of the orbit points in the top diagram identified. A large depression can be seen that corresponds to the transit epoch.

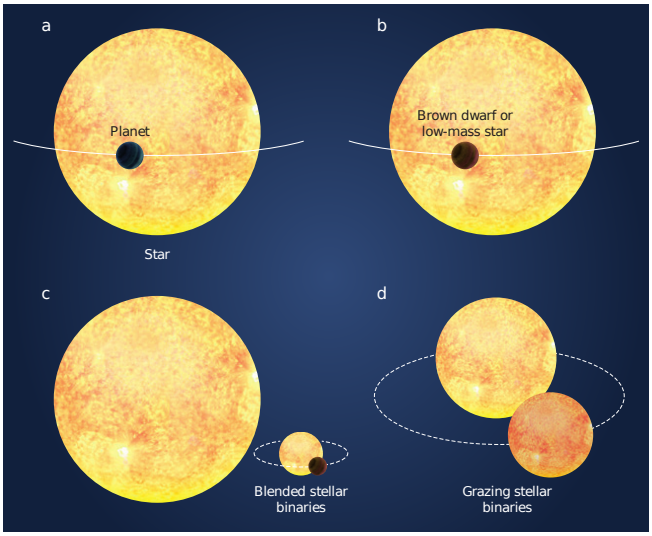

Figure 1.9: Some examples of astrophysical effects can mimic the signature of a transiting planet: *a)* real transiting planet; *b)* an orbiting white dwarf or low mass star; *c)* blended stellar binaries in a triple star system ; *d)* grazing binary stars (from Cameron, 2012).

selection based on the transit depth. Finally, Fressin et al. (2013) did not consider eclipsing binaries as a source for false-positives, overestimating the rate of giant planets in Kepler data. The confirmation of transiting planets – or at least their statistical validation – will remove any bias on the their parameters – in particular radius and periods – leading to better understanding planet formation and migration processes. Note that the statistical validation of multiple transiting planet systems is more straightforward as the probability of having multiple false positives on the same star is much lower than the probability of having multiple planets in the system (e.g. Lissauer et al., 2012).

Note that in some particular cases it is possible to determine the masses of transiting planets. For systems with a single planet and star, transits are extremely predictable periodic events. However, if additional planets exist, they induce dynamical perturbations to the transiting planet orbit that will periodically delay or anticipate the transit event. This method – known as the transit timing variations (TTV) method – is particularly useful to detect planets in multi-planetary systems (e.g Steffen et al., 2007; Steffen et al., 2010; Holman et al., 2010)

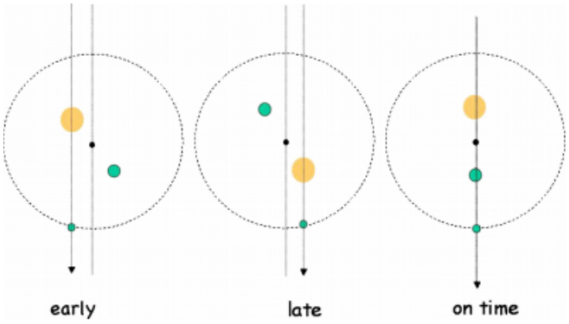

Figure 1.10: Diagram showing changes in the timing of a transiting planet induced by a perturbing planet interior to its orbit (from Agol et al., 2005).

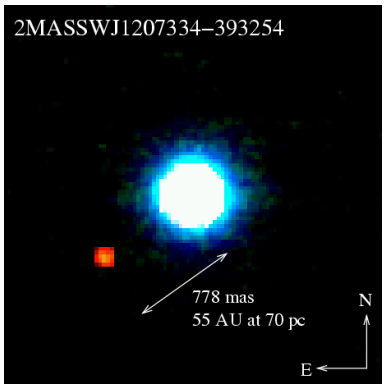

Figure 1.11: Composite image of brown dwarf 2M1207 and its orbiting planet in H (blue), K_s (green) and L' (red) bands. The planetary companion 2M1207 b is clearly distinguishable from its host brown dwarf (Chauvin et al., 2004).

and sensitive enough to the masses of the perturbing planets to be able to detect planets with RV signals too small for detection via the RV method (e.g Agol et al., 2005; Holman et al., 2004). This enables also the TTV method to recover the mass of the transiting planet, and fully characterize its orbit. Note that the amplitude of the TTV perturbation is highly dependent on the mass ratio between the perturbing planet and the transiting planet, limiting in mass the planets that can be detected with this method. However, it was found that when the planets are in close to mean-motion resonances, the TTV perturbation is amplified, allowing the detection of perturbing planets with masses down to the Earth's (e.g Agol et al., 2005). Figure 1.10 depicts a TTV event (from Agol et al., 2005).

Similarly to the RV method, the transit detection method is particularly sensitive to large planets in short orbits. The potential of this method for planet characterization will be discussed in detail in Section 1.2.1.

DIRECT IMAGING 1.1.4

As implied by the name, this method focuses on imaging directly the planet and spatially resolving it from the host star. The first direct image of an exoplanet corresponds to 2MASSWJ 1207334-393254 with ESO's VLT/NACO instrument (See Figure 1.11 – Chauvin et al., 2004) and has only been possible for under a hundred sub-stellar objects (Schneider et al., 2011). Note that only 46 of these objects have masses under $15M_{Jup}$ and the lightest – Fomalhaut b – has a mass of $3M_{Jup}$ (Kalas et al., 2008), putting them in the transition region between giant planets and brown dwarfs.

Direct imaging techniques face two main challenges: i) the minute planet-to-star flux ratio and ii) the small angular separation between the planet and its hosts star.

The minute angular separation – $\theta \approxeq \frac{a}{D}$ (in arcseconds), where a is the semi-major axis of the orbit in astronomical unit (A.U.) and D is the distance to the system in parsecs[3] – is the main obstacle to the direct imaging of exoplanets. Figure 1.12 shows the angular separation as a function of the distance to the system for 3 different semi-major axis (colored lines). The horizontal dashed lines correspond to the detection limits for the

[3]Note that we are using the small angle approximation $\theta \approxeq \tan(\theta)$

NICMOS and SPHERE/ZIMPOL instruments (Schneider et al., 1999; Kervella et al., 2016).

Even with instruments such as SPHERE (Beuzit et al., 2008) and GPI (Macintosh et al., 2008), that represent the current frontline in direct imaging, it is very hard to resolve spatially the planets, even for planets around the closest stars. Observing in the infrared (e.g. with SPHERE/IRDIS Langlois et al., 2010) partially mitigates the effect of the small planet-to-star flux ratio, in particular when observing extremely young large planets. At those wavelengths, thermal emission from the planets is dominant and they will appear much brighter than for other wavelengths. Extremely young giant planets are highly favorable candidates for this method as i) they have formed very recently and thus are still cooling down; ii) they have a larger surface area, dictated by their inflated radius.

Nowadays, diverse methods are enabling imaging techniques to overcome these issues and observe targets increasingly closer to the star and with smaller contrasts. Adaptive Optics (AO) systems are becoming more common and enabling telescopes to minimize the stellar contamination at the planet's location, greatly increasing the planet–star contrast in that region (e.g. with ESO's SPHERE@VLT Chauvin et al., 2017). With Angular Differential Imaging (ADI) (Marois et al., 2005), researchers use the field rotation of the telescope to distinguish the planetary signal from spurious speckles of light created by static noise of the stellar Point Spread Function (PSF). In summary, multiple observations with the telescope's field rotation disabled are taken sequentially, and then stacked after correction of their relative individual field rotation. This will dilute the speckles of light into background noise, while enhancing the planet's Signal-to-noise ratio (S/N) (e.g Marois et al., 2010). Polarized Differential Imaging (PDI) (e.g. Schmid et al., 2005) combines polarized and non-polarized images of planetary systems to remove the (not polarized) stellar light from the polarized images and extract the (polarized) planetary signal. By physically blocking the light from the star – either externally via a starshade (e.g. Sirbu et al., 2017) or internally to the telescope using coronographs (e.g. Mawet et al., 2005; Wang et al., 2017) – should permit to achieve the level of contrast required for the detection of Earth twins around other stars (e.g Trauger et al., 2007; N'Diaye et al., 2016).

Currently, direct imaging exoplanets allow to reconstruct low-resolution exoplanet spectra by imaging the planet in different bands (e.g. Kuzuhara et al., 2013). Figure 1.13 shows multiband images of the HR 8799 system taken

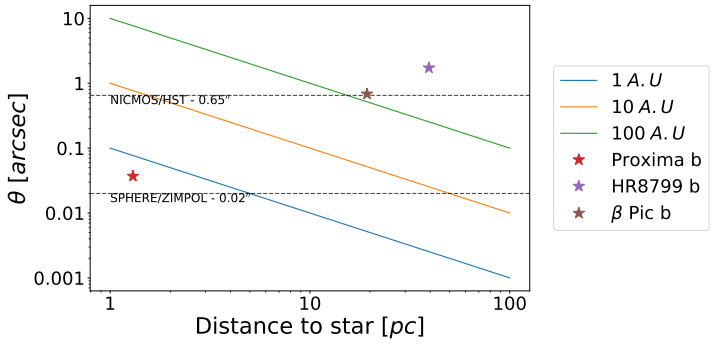

Figure 1.12: Angular separation as a function of the distance to the system for 3 different semi-major axis (colored lines). The horizontal dashed lines correspond to the detection limits for the NICMOS and SPHERE instruments (Schneider et al., 1999; Kervella et al., 2016)

with ESO's SPHERE-IRDIS instrument (from Zurlo et al., 2015).

Imaging techniques are particularly sensitive to large planets with long-period orbits, allowing to probe the outer regions of planetary systems and thus filling a parameter space currently unavailable to other techniques such as RV and transit. In the infrared, these techniques have permitted to image forming planets (e.g. Kraus et al., 2012; Sallum et al., 2015) and place constrains on planetary formation models (e.g Spiegel et al., 2011).

MICROLENSING 1.1.5

As predicted by General Relativity, when a star passes in front of another star, it will act as a gravitational lense and bend the light reaching us from the background star. This effect was first measured during the solar eclipse of May 29th 1919 when Sir Arthur Eddington and his team took photographs of the Hyades cluster which the Sun was crossing. Comparing these photographs with the ones taken before the eclipse – when the Sun is not crossing their path – they got the first observational confirmation of Einstein's General Theory of Relativity.

This effect can also be used for planet detection. The left panel of figure 1.14 shows a diagram of the microlensing event created by a star+planet system . When a foreground star crosses the line-of-sight between the observer and a background star, its gravity will bend the rays from the background star and magnify the light we receive from it. If the lens star has any planets, they will induce caustics on the detected signal. These caustics will show as peaks in the light curve from the background star. The right panel of figure 1.14 shows the light curve of micro-lensing event OGLE2005-BLG-390 (Beaulieu et al., 2006). The main lensing event – centered around JD-2453583 – corresponds to the increase in the flux of the background star when the foreground star crosses the line-of-sight of the observer. This event has a small caustic – the smaller peak at around JD-2453592 and amplified on the smaller axis – on it that corresponds to the micro-lensing event caused by the planet orbiting the lensing star.

The major limitation of this method is that in most cases it is impossible to replicate as it is very unlikely that the lens star will cross the line-of-sight of another background star. Nonetheless, once detected, these planets can, in principle, be confirmed via other means, such as the RV or transit methods. However such cases are still low-probability events, and as such scarce, with only a handful of candidates confirmed (Kubas et al., 2012; Bennett

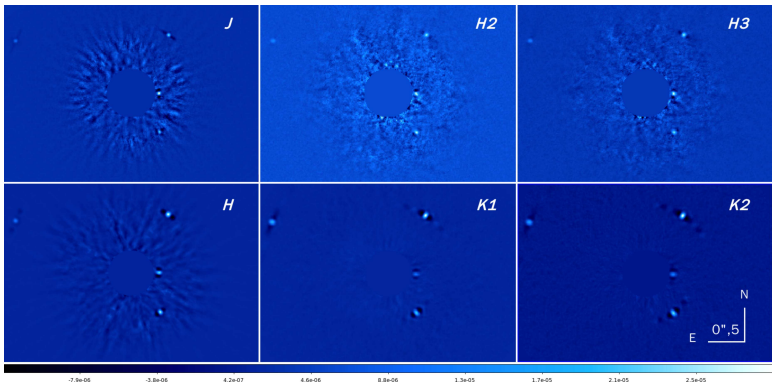

Figure 1.13: Multiband images of the HR 8799 system taken with ESO's SPHERE-IRDIS instrument (from Zurlo et al., 2015).

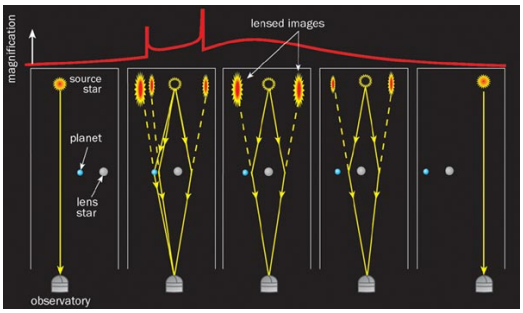

(a) Credit: David Bennett, Notre Dame University.

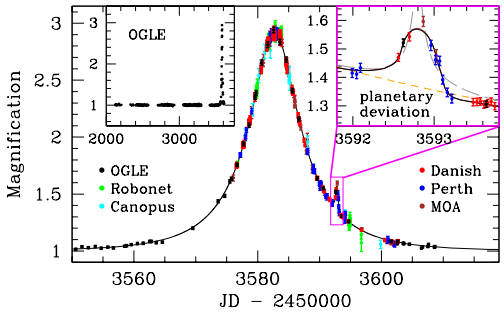

(b) The magnification of the micro-lensing effect caused by the planet can be seen on the *Top Right* panel (Beaulieu et al., 2006).

Figure 1.14: *Left Panel:* Microlensing event diagram. *Right Panel:* Fitted light curve of micro-lensing event OGLE2005-BLG-390.

et al., 2015; Batista et al., 2015; Fukui et al., 2015; Santerne et al., 2016).This explains the low amount of planets discovered using this technique (59 as per the exoplanet.eu database at the end of 2017 – Schneider et al., 2011). An interesting case is the OGLE-2006-109L b, c system, where two planets similar to Jupiter and Saturn have been found (Bennett et al., 2010). Note that the fitting of a caustic by a function of planetary and stellar parameters is strongly degenerate. Different combinations of stellar and planetary parameters can represent/originate the same caustic, and requires confirmation by other means to characterize the system (e.g. Gould et al., 2000).

This method is particularly useful as it probes a planet parameter space inaccessible to current RV and transit surveys, as the micro-lensing technique is more sensitive to low mass planets behind the so called "snow-line", i.e., the point in the proto-planetary disk where water will be frozen. This is of great interest as, combined with other methods, it gives a picture of planet demographics in our galaxy (e.g. Gould et al., 2010; Shvartzvald et al., 2015). One of the most important results of this technique is being the only one to date to demonstrate the ubiquity of cold Neptunes that are likely to be the most widespread class of planets beyond the "snow-line" (e.g. Sumi et al., 2010; Suzuki et al., 2016). Furthermore, this technique also enables to discover free-floating planets and recover their parameters (i.e., not gravitationally linked to any star,e .g. Sumi et al., 2011), something not possible with other indirect methods.

PULSATIONS TIMING VARIATION 1.1.6

This method is responsible for the first discovery of a planet mass object orbiting a star other than the Sun (Wolszczan et al., 1992). Pulsars are beacon-like neutron stars with extremely high rotating velocities. This type of star has a strong radio emission in narrow beams coming from the star's magnetic poles. Since the magnetic and rotation poles are misaligned, we observe periodic pulses when the radio beams point towards the Earth. The presence of a companion will periodically delay or anticipate these pulses. This method can in principle be used to any kind of pulsating star with stable oscillations (e.g. white dwarfs – Hermes et al., 2017).

Of particular interest for the detection of exoplanets are millisecond pulsars, which, as the name suggests, have rotation periods in the order of milliseconds. These pulsars have extremely stable rotation periods, making then useful as extremely precise clocks. When in the presence of a companion, the period between two consecutive pulses will have a periodic variation as the pulsar orbits the center of mass: the period increases as the pulsar

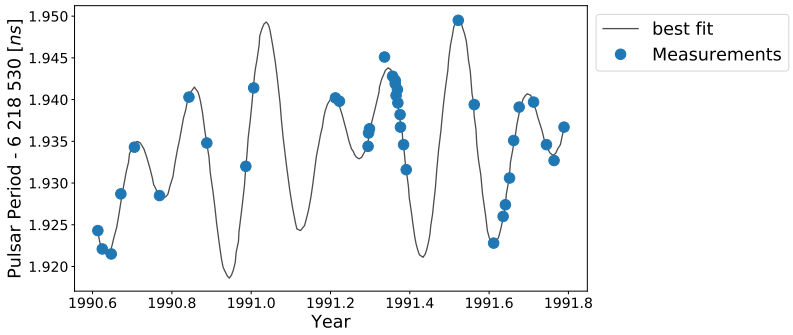

Figure 1.15: Timing variations of pulsar PSR1257 + 12. The solid line represents the modeled fit of the best fitting timing variations due to the presence of two super-earths with respectively $m_p\, sin(i) = 3.4 m_\oplus, P = 66.6\, days$ and $m_p\, sin(i) = 2.8 m_\oplus, P = 98.2\, days$(adapted from Wolszczan et al., 1992).

moves away from us and decreases as it gets closer (Figure 1.15). The precision at which the variation of the period of a pulsar can be currently measured is such that a radial velocity precision of a few centimeters per second can be achieved (Phillips et al., 1994), making it sensitive to small planets in long period orbits (e.g. Earth twins). An important result from this technique is that is has shown that second-generation planets exist, formed from the remnants of dead systems, even after a catastrophic ending.

EXOPLANET ATMOSPHERES CHARACTERIZATION TECHNIQUES 1.2

In parallel to the detection of exoplanets through any the methods described in the previous section, researchers are pursuing their detailed characterization. One of the most interesting aspects of exoplanet characterization is their spectral characterization. The techniques we will briefly describe in this section represent the current front line of exoplanet spectral characterization, limited only by the precision required for detection, due to the low planet-to-star flux ratio. For example, in the visible wavelength domain, a Jupiter sized planet in 3 days orbit has a planet-to-star flux ratio of $\sim 10^{-4}$, with the planetary flux being mostly due to the light from the host star that the plane reflects. At infrared wavelengths, thermal emission from the planet dominates and this flux ratio raises to up to $\sim 10^{-3}$. That means reaching a S/N level above 10^4 in the visible and above 10^3 in the infrared just in order to have the planetary signal at the same level as the noise. These thresholds only recently have been breached with current observing facilities and are still a challenge for researchers. We sorted current available techniques in 3 categories: i) Photometric, ii) High-dispersion spectroscopic and iii) hybrid techniques.

PHOTOMETRIC TECHNIQUES 1.2.1

TRANSMISSION AND OCCULTATION SPECTROSCOPY

When a transiting planets crosses the stellar disk of its host star (primary transit – position A in Figure 1.8), its atmosphere will filter the light from the host. Different/elements molecules leave distinct spectral fingerprints on the spectrum from the background star, i.e., absorb the light from the host star at different wavelengths and depths in the atmosphere, depending on composition and structure of the planetary atmosphere. As such, the cross-section of the transiting planet will be wavelength dependent and the measured planetary radius will vary with wavelength. Measuring the drop in the photometric flux due to the transit event over several wavelength bins enables the construction of the absorption spectra of a planetary atmosphere[4] (e.g. Charbonneau et al., 2002). Photometric transmission spectroscopy is mainly performed from space observatories, due to the atmospheric contamination from Earth's atmosphere.

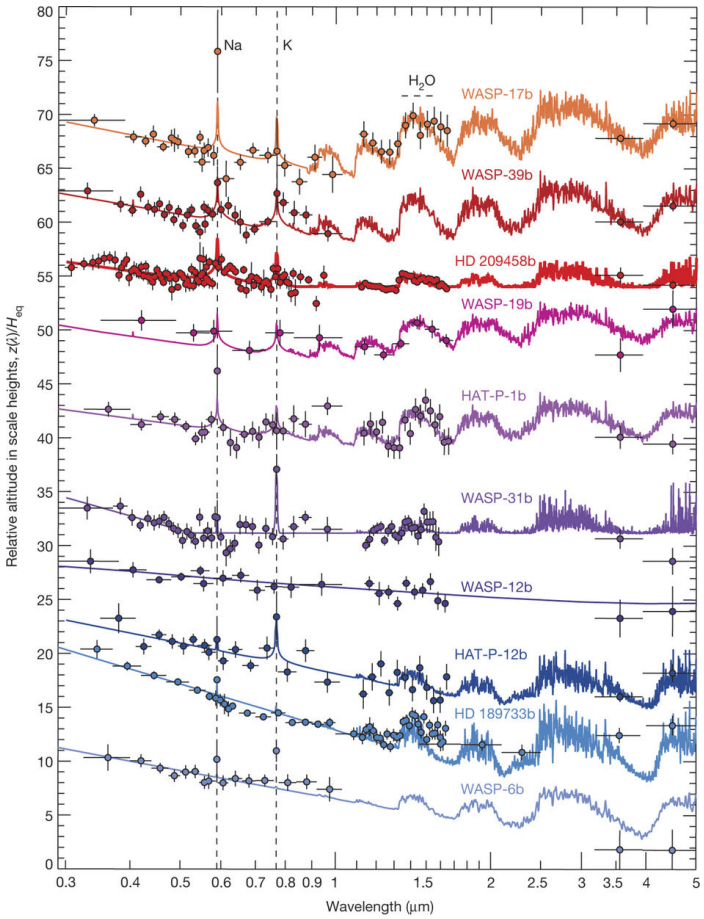

Figure 1.16: Transmission spectra for several Hot-Jupiter type planets (colored dots) with their respective best-fit atmospheric models (colored solid lines) (from Sing et al., 2016).

Figure 1.16 shows the transmission spectra for several Hot-Jupiter type planets (from Sing et al., 2016) from Hubble Space Telescope (HST) observations where the data (colored markers) is compared against fitted

[4]Note that this can also be done with high-resolution spectrographs – see Section 1.2.2.

atmospheric models. The *y-axis* shows the scale height at which the light from the star being covered by the planet is absorbed. Scale heights are a typical measure of depth in planetary atmospheres, and are defined as the vertical distance in an atmosphere over which the density and pressure drop by a factor of e, assuming an isothermal atmosphere of uniform composition. Mathematically speaking it is defined as $H = \frac{kT}{mg}$ (e.g. Iribarne et al., 1981, Chapter 8.85), where k is the Boltzman constant, T the temperature, m the mean molecular mass of the gas and g the gravitational acceleration. Assuming an isothermal profile for the atmosphere, it relates to the pressure and density by

$$\frac{P(z)}{P_0} = e^{-\frac{z}{H}} \qquad\qquad \frac{\rho(z)}{\rho_0} = e^{-\frac{z}{H}} \tag{1.8}$$

where *z* is the altitude, and P_0 and ρ_0 are respectively the pressure and density at the surface. In summary, extended atmospheres – e.g. inflated hot Jupiters – have large scale heights (i.e. small pressure and density gradients) and compact atmospheres have small scale heights (i.e. large pressure and density gradients). It is interesting to note that if we integrate the density function over all the atmosphere, we get that H corresponds to the height of the atmosphere if all the gas was compressed into an atmosphere of constant density ρ_0.

When a transiting planet passes behind its host star (also known as secondary eclipse or occultation – position C in Figure 1.8), a drop in flux will occur as we stop receiving light from the planet. At this point of the orbit, the recovered signal will only have the stellar component, allowing to measure the baseline stellar flux. However, on both sides of the opposition (i.e., right before or after it), the recovered signal will consist in the sum of the stellar and planetary signals. Since the planet is colder than the star, in a first order approximation the thermal component will follow a Planck curve and be dominant at infrared wavelengths; the reflected component dominates in the optical and mimic the spectrum of the star (modulated by a few absorption lines). Therefore, measuring the variation in flux during the secondary transit allows to infer the planet's brightness temperature and recover the planet's thermal (e.g. Deming et al., 2005) and reflected (Alonso et al., 2009) signatures. Doing so at at different wavelengths, will allow to recover the planet's emission and reflection spectra, which will be indicative of the planet's atmospheric composition (e.g. Stevenson et al., 2014).

PHASE VARIATIONS

This method relies on measuring the planetary flux variation as it moves over its orbital path and present us its day/night hemispheres alternately. Similarly to occultation spectroscopy, variations in both the thermal and reflected signatures can be measured.

Multiband phase curves of an exoplanet will permit to estimate the planet's energy budget (e.g. Knutson et al., 2009; Esteves et al., 2013; Schwartz et al., 2017), i.e., the net balance between the absorbed, reflected and emitted fluxes. Optical phase curves will be mainly modeled by the albedo (the fraction of incident light the planet reflects to the observer at full phase and highly dependent on the chemical properties of the atmosphere) and phase function (a measure of the fraction of the planet being illuminated by the host star and quantity highly dependent

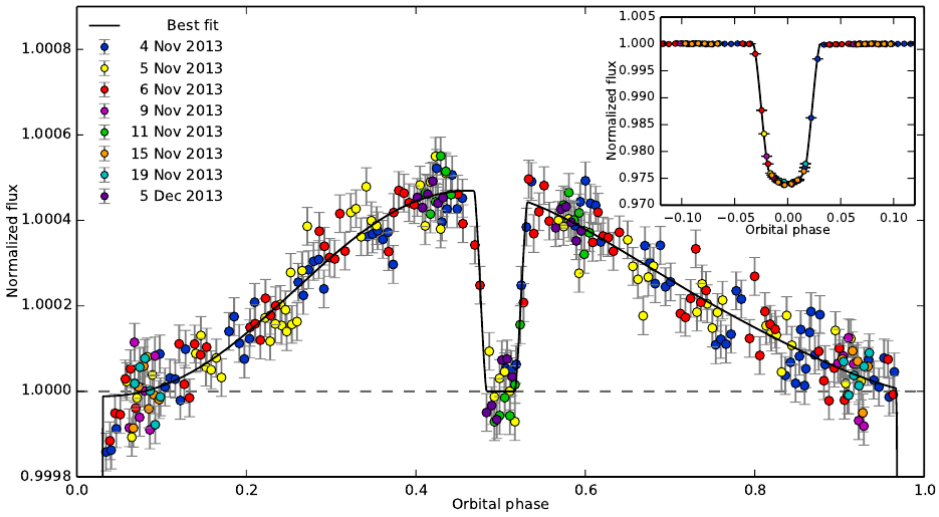

Figure 1.17: Band integrated phase curve of WASP-43b (from HST infrared data - Stevenson et al., 2014).

on the scattering properties and aerosol content of the atmosphere, e.g. Madhusudhan et al., 2012; Oreshenko et al., 2016). Infrared phase curves are largely modulated by the thermal emission from the planet and can provide insights on its thermal structure and heat circulation (e.g. Goodman, 2009; Cowan et al., 2011; Knutson et al., 2012; Koll et al., 2016). Figure 1.17 show the band integrated phase curve of WASP-43b (from HST infrared data - Stevenson et al., 2014), where a obvious phase offset on the star+planet emitted flux can be observed. This offset suggests that the planet hottest point does not correspond to the sub-stellar point, i.e., the point in the planet's surface closest to the star. Simulations show that this comes as a result of the existence of a broad superrotating jet that moves the hotest point in the planetary atmosphere from the sub-stellar point (Showman et al., 2002). A much cooler night side – an indication of a inefficient day/night heat distribution mechanism – can be inferred from the large phase curve amplitude in Figure 1.17. Should the planetary atmosphere have efficient day/night heat distribution mechanism, it would quickly average out the temperature over the whole atmosphere and show a low variation in the amplitude of the infrared phase curve.

HIGH-DISPERSION SPECTROSCOPIC TECHNIQUES 1.2.2

High-dispersion spectroscopic techniques rely on high-resolution spectrographs installed on ground based facilities such as HARPS@ESO-3.6m or HIRES@Keck observatory. In most cases, the planet and the star cannot be spatially resolved, and their spectral signatures are stacked on the same spectrum. However, when the planet and the star have different RVs, astronomers can attempt to separate them spectroscopically when their signals are not spectroscopically blended.

Typically, researchers cross-correlate high S/N high-resolution observations with model planetary templates to recover it signal. First attempts at recovering the reflected spectrum from exoplanets used this class of methods, allowing to put upper limits on the reflectivity of their targets in the optical (e.g. Cameron et al., 1999; Charbonneau et al., 1999). In the infrared, this technique has been much more successful – mainly due to the larger planet-to-

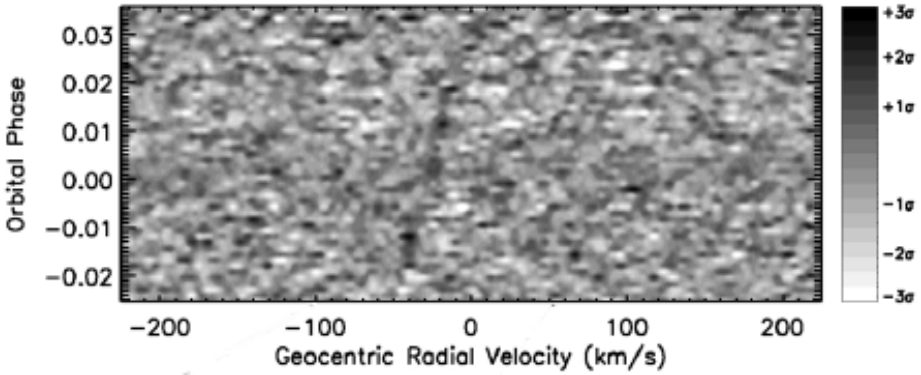

Figure 1.18: The detected cross-correlation signal with a carbon monoxide template of CRIRES observations of HD 209458 b (from Snellen et al., 2010)

star flux ratio – and permitted to recover the planetary signal for several targets (e.g. Snellen et al., 2010; Kok et al., 2013; Birkby et al., 2017).

High-dispersion spectroscopy has also provided invaluable data for ground based observatories to catch-up with space observatories and recover the transmission spectrum of transiting exoplanets (e.g. Redfield et al., 2008; Wyttenbach et al., 2015; Khalafinejad et al., 2017). The main advantage of high-dispersion spectroscopic techniques over space-based transmission spectroscopy (e.g. with the HST) is the access to the large collecting areas of current and future ground based facilities and the ability to observe at high resolution. Furthermore, the main advantage high-dispersion spectroscopy has over ground-based photometric transmission spectroscopy is the ability to resolve spectroscopically Earth's atmospheric absorption lines – in particular water – and the equivalent spectral lines in the planet's atmosphere which allows to recover the spectral profile of several elements with minimum telluric contamination.

When possible to spatially resolve the signal from the planet, researchers are able to recover directly its spectrum with little or no stellar contamination (e.g. Brogi et al., 2012; Konopacky et al., 2013; Snellen et al., 2014). Unfortunately, this is extremely difficult to perform due to small angular separation between the planet and its host, which is inversely proportional to the distance from our Sun to the star. This limits this type of analysis to either planetary systems close to ours and/or planets far from their hosts stars.

HYBRID TECHNIQUES 1.2.3

One of the most promising techniques for the future is the High-Dispersion Spectroscopy and High-Contrast Imaging (HDS+HCI) technique (Snellen et al., 2015), which combines high-dispersion spectroscopy and high contrast imaging to recover the spectrum from exoplanets. In brief, the authors propose to use adaptive optics to minimize stellar contamination and enhance the image contrast, and as such the planet-to-star flux ratio, at the expected location of the planet. At the location in the sky corresponding to the expected planet position at time of observations, a fiber will be placed and connected to a high-resolution spectrograph to recover the planetary spectrum. Although no current instruments exist with this configuration, the main principle behind this technique had been previously tested successfully by combining the CRyogenic high-resolution InfraRed Echelle

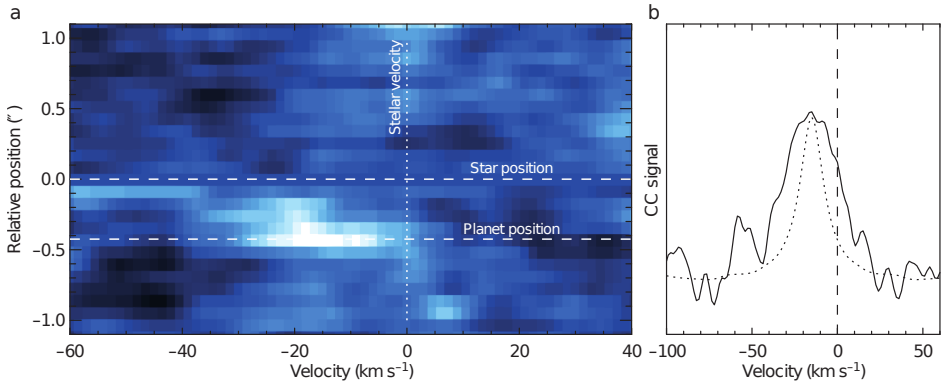

Figure 1.19: *Left panel:* $CO + H_2O$ cross-correlation signal from β Pictoris b as a function of angular separation from the star and radial velocity. The signal's maximum corresponds to the planet's location. *Right panel:* Recovered $CO + H_2O$ signature of β Pictoris b at the planet's location. (from Snellen et al., 2014).

Spectrograph (CRIRES) with the Multi-Application Curvature Adaptive Optics (MACAO) system on the VLT. Instead of using fibers, (Snellen et al., 2014) aligned both β Pictoris and its orbiting planet on the slit of CRIRES spectrograph and were able to recover the carbon monoxide (CO)+water (H_2O) cross-correlation signal of β Pictoris b atmosphere and infer the planet's rotation period (See Figure 1.19 Snellen et al., 2014). An interesting future application of this technique has been proposed by Lovis et al. (2017). The authors propose to combine the high-contrast imaging capabilities of SPHERE@ VLT with the high-resolution and stability of ESPRESSO@ VLT by building an interface that would physically link both instruments by means of an optical fiber bundle. With this setup in place, their simulations predict that it should be possible to detect the reflected spectrum of Proxima b at a 5-σ significance with 20-40 nights worth of observing time, spread over 3 years. Furthermore, with 60 nights of observations, they expect to be able to retrieve with a 3.6-σ significance the signature of molecular oxygen, assuming the planet has an Earth-like atmospheric composition.

MOTIVATION 1.3

Before space missions that permitted to visit them, the characterization of the planets in the Solar System was very similar to what is now being done with exoplanets. The analysis of the solar light reflected on Solar System planets was an important tool for their characterization, in particular of their atmospheres. Exoplanet researchers are performing similar analyses – on a much lower S/N domain – to attempt to recover the composition and dynamics of exoplanetary atmospheres (Chapter 2).

The main motivation behind this dissertation is to study how the light from a star at optical wavelengths reflected on an orbiting planet can be used to characterize the said planet, in particular its atmosphere. Specifically, we focus on using a technique that cross-correlates high-resolution spectral observations with binary masks to unveil and recover the minute planetary spectral signature from exoplanets. The main challenge we face is to detect the planetary signal, as it is a minute signal next to the much brighter stellar host, even in the best scenarios. The best targets for detection and characterization are typically hot and large planets with short period orbits (i.e

hot Jupiters). In the infrared, their planet-to-star flux ratio can reach 10^{-3}, mainly due to their thermal emission peaking at these wavelengths, while in the optical, the planet-to-star flux ratio can reach up to only 10^{-4}.

Notwithstanding that the planetary flux is higher at infrared than at optical wavelengths, attempting the recovery of the planetary reflected signal in the optical has several advantages to study its reflectivity/albedo (See Chapter 4), leading us to choose optical wavelengths for the recovery of the reflected spectra from exoplanets. To do so, we developed a new technique that computes the cross-correlation function of high-resolution optical spectra with a spectral line mask to amplify the planetary reflected signal above the stellar noise (Chapter 4). With this method, we were able to detect the optical reflected signature of 51 Pegasi b from HARPS observations and infer that this prototypical hot Jupiter is most likely a highly-inflated hot Jupiter type planet with a high albedo. Going further, we attempted to perform the same analysis to UVES@VLT data and recover the planetary albedo and its color dependency. The detailed analysis of this data and results are presented in Chapter 5.

Yet the true challenges for the detection of the reflected signal from exoplanets come with the advent of next-generation observing facilities. These will permit to move our observations into much higher S/N domains with unsurpassed precision. From simulated observations with ESPRESSO@VLT and HIRES@ELT, we can conclude that not only we should be able to recover the planetary albedo, but also its color dependency, a key factor to hint a planetary atmosphere composition (see Chapter 6).

Chapter 2.
The structure, composition and atmospheres of exoplanets

STRUCTURE AND COMPOSITION 2.1

How can we gain insight on the planet's composition? In the case of our Earth, seismic data makes it possible to directly probe the interior of our planet and infer its structure in much detail. For many years, researchers have been able to perform high-resolution spectroscopy (e.g. Titan with UVES – Civeit et al., 2005) of most planets in the Solar System, as well as image them from the ground (e.g., Jupiter with the Gemini, Keck and HST observatories – Pater et al., 2010). In addition, most planets were visited by space missions which allowed high-definition imaging (e.g., of Saturn with the Cassini spacecraft – Del Genio et al., 2017) of the planets, as well as probing their atmospheres (e.g., microwave sounding, near-infrared mapping and gravity field measurements of Jupiter from the Juno spacecraft – Bolton et al., 2017) and even made surface measurements (e.g., of Mars with the Mars Exploration Rover – Squyres et al., 2004). It is obvious that due to their proximity and visiting space missions the level of detail of the acquired data exceeds by orders of magnitude the one from exoplanets. Still, even in the Solar System, most internal structure data still comes from detailed models based and constrained by the above mentioned observational evidence and the equations of state from the observed elements at either the surface or the outer atmosphere (e.g, for Jupiter – Wahl et al., 2017; and Saturn – Vazan et al., 2016).

The properties of planet atmospheres, both on our Solar System and outside it, are deeply linked to the planet structure and composition. From observations it is evident that structurally different types of planets exist in our Solar System. The composition of the planets in our Solar System can be broken down into 3 main components (see Stern et al., 2002): i) rock (silicates, metals, etc), ii) ices (any ice-forming materials – e.g. water, methane, etc – in either solid and fluid forms) and iii) gases (Hydrogen and Helium).

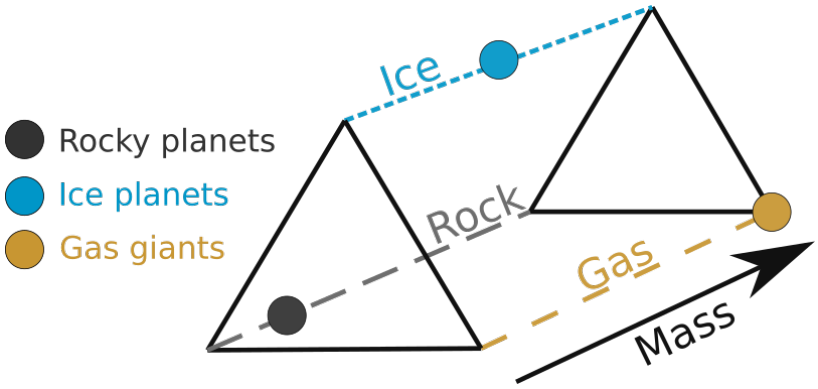

Figure 2.1: Schematic diagram showing the prototypical exoplanet types (adapted from Figure 1 of Chapter "Terrestrial Planet Formation" by John Chambers of the "Exoplanets" book - Seager et al., 2010).

Although the combinations are endless, the relative proportions of each component make it possible to define an ad-hoc catalog for planets – both in the Solar System and outside – based on their most abundant component: i) Rocky (including Earth-like and Super-Earths, e.g. Earth, Kepler-10 b, 55 Cnc e), ii) Icy (e.g. Neptune, HD 76700 b) and iii) Gaseous (e.g. Jupiter, 51 Pegasi b, HD 209548 b) planets. This classification system is summarized in Figure 2.1, which shows a schematic diagram showing the prototypical planet types (adapted from Figure 1 of Chapter "Terrestrial Planet Formation" by John Chambers of the "Exoplanets" book - Seager et al., 2010).

The vast majority of the chemical elements that compose a planet – and its host star – will likely originate from the proto-planetary cloud of which it originated (e.g. Santos et al., 2001). If we consider that on a first order approach, the relative elemental abundances in the galactic disk are similar and as such exoplanetary disks will have similar compositions as well (e.g. Lodders, 2010), it is intuitive to attempt to extrapolate this to exoplanets (e.g. Guillot et al., 2006; Delgado-Mena et al., 2010; Santos et al., 2017). Note that this extrapolation is only valid in terms of bulk compositions, i.e., does not apply to the fine-structure of the planet or its detailed composition.

Note that when looking in more detail, different stars will have different chemical abundances. This difference translates itself into a different composition of the planet-forming protoplanetary disk. Therefore, the precise determination of stellar abundance is of huge relevance towards the characterization of exoplanets and the refinement of formation models. A correlation between stellar metallicity and the presence of giant planets exists as stars hosting giant planets are systematically more metallic than a normal sample of stars (e.g. Santos et al., 2004a). In terms of planet formation models, this favours core accretion over disk-instability mechanisms as the main responsible for the formation of giant planets (e.g. Mordasini et al., 2012). The core accretion model states that planets from by the coalescence of debris from the proto-planetary disk which grow into small rocky cores or planetesimals. Once these planetesimals are massive enough, they start accreting a gas envelope and form giant planets. For low-mass rocky planets, which are now believed to be abundant and outnumber the higher-mass population characterized up to now (Mayor et al., 2011), researchers have that this correlation either does dot exist or is much weaker (e.g. Wang et al., 2015; Zhu et al., 2016). This result is still compatible with the core accretion model.

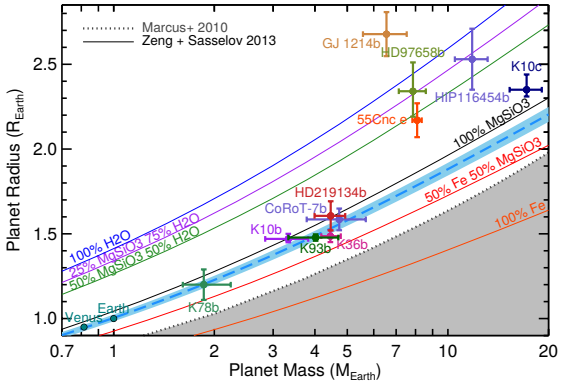

Figure 2.2: Mass-radius relationships for low-mass rocky planets assuming different possible compositions (from Motalebi et al., 2015).

The mean density of a planet (also referred to as "bulk density") has been used for many years as a proxy for planet composition. This quantity can be computed directly from its mass and radius. However it is not always possible to recover both these parameters. The radii of exoplanets can be obtained for transiting planets, with most radius measurements having been obtained by the Kepler and K2 missions which yield extremely precise radii. Following RV surveys permitted the recovery of masses of these planets, but for many of them the error bars are quite large with the RV only allowing to place upper limits on the mass of the planet (e.g. K2-33 b – David et al., 2016). To be able to recover the mass with high precision for these planets is a challenge beyond current facilities as the RV amplitudes to be detected are close to instrumental precision and the photon noise is frequently an order of magnitude larger (e.g. Lovis et al., 2010).

Additionally, the radius is impossible to recover for non-transiting planets detected only by the RV method, limiting further the sample of planets for which the density can be estimated. However, the combination of empirical data from observations and the derivation of the equations of state for each of the interior components (e.g. Seager et al., 2007; Swift et al., 2012) led to the development of mass-radius relations for exoplanets. Figure 2.2 shows the mass-radius relationships for low-mass rocky planets assuming different possible compositions superimposed on observational data for several planets (from Motalebi et al., 2015).

Low-mass planets tend to be mostly rocky with small or no atmospheres. In a first order approximation of its equation of state, rock can be seen as in-compressible – a result confirmed from empirical data (e.g. Weiss et al., 2014) – and is practically insensitive to the incident flux. This means that mass-radius relations hold for the low mass regime, and the bulk composition of the planet can be inferred. However, in terms of inner structure, for the same mass, infinite combinations of iron cores, silicate mantles, and water outer layers can yield the same radius (e.g. Seager et al., 2007). Note that the radius of solid exoplanets is quite sensitive to the gas content of the atmosphere, and a small increase in H/He in the planet atmosphere can yield a large increase in the radius (e.g. Adams et al., 2007).

As the mass increases, ice and gas layers become more predominant and the mean bulk density of the planet lowers. When the H/He layer becomes dominant, planets will start to have radii that are independent of their masses (e.g. Lopez et al., 2014). Also, for planets with a high H/He content (e.g., gas giants), the irradiation of

the planet – depending on the planet's distance to its host – is a major factor in the equation of state for their gaseous component (e.g. Fortney et al., 2009). In consequence, these planets present a vast range of different radii for similar masses (e.g. 51 Pegasi b – Martins et al., 2015a; WASP-113 b – Barros et al., 2016; CoRoT-28 b – Pätzold et al., 2012, among many others).

EXOPLANET ATMOSPHERES 2.2

Currently, the frontier of exoplanet characterization has been pushed toward the study of exoplanet atmospheres, both from a composition and dynamics point of view. The ultimate goal behind this is the detection of life around another planet, for which a clear path passes through the detection of bio-signature gases (e.g. Des Marais et al., 2002; Seager et al., 2013).

In terms of dynamics, exoplanetary atmospheres have been found to be as complex as their Solar System counterparts. Doppler shifts in the spectral lines of some elements permitted to detect high speed winds in strongly irradiated planets like Hot Jupiters (e.g. Snellen et al., 2010), a feature previously predicted from simulations (e.g. Showman et al., 2002). As proposed by Kawahara, 2012, spectral line broadening has been used to successfully recover the rotation of the planetary atmospheres (e.g. Snellen et al., 2014; Brogi et al., 2015; Louden et al., 2015).

The techniques presented in Section 1.2 have been paramount to the characterization of exoplanetary atmospheres. The first measurement of an exoplanetary atmosphere was performed with HST around HD 209458 b (Charbonneau et al., 2002), one of the better studied exoplanets to date. By using transit spectroscopy they detected the strong sodium absorption line at 589.3-nm predicted by Seager et al., 1998 (See Figure 2.3). This discovery laid the groundwork for the detection of many more elements and molecules from transmission spectra of exoplanets, with both space observatories (for example, water – Tinetti et al., 2007; – and methane in HD 189733 b – Swain et al., 2008) and high-resolution spectrographs on the ground (e.g. sodium in – HD 189733 b Redfield et al., 2008; Wyttenbach et al., 2015; and CO and water in HD 179949 b – Brogi et al., 2014). Clouds have also been detected in exoplanetary atmospheres, as they create grey absorption/reflection spectra (i.e. with constant and as such wavelength-independent fluxes), masking the constituents of the atmosphere (e.g. Barman et al., 2011; Line et al., 2016; Sing et al., 2016). Note that recently, to bypass this problem, MacDonald et al. (2017) have proposed an atmospheric retrieval algorithm that models in-homogeneous clouds to unmask the atmospheres from their cloud/hazes and recover the principal molecular components from transmission spectra of cloudy exoplanetary atmospheres.

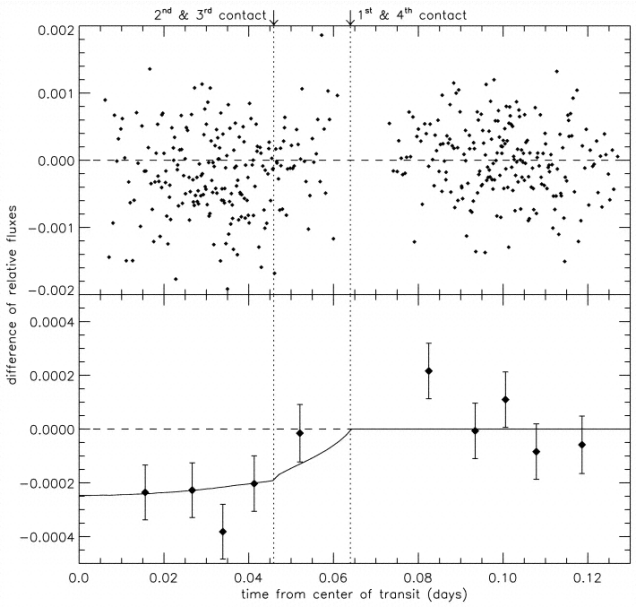

Figure 2.3: Atmosphere detection around HD 209458 b (from Charbonneau et al., 2002).

REFLECTED LIGHT AND THE ALBEDO FUNCTION 2.3

As done in the past with the planets in our Solar System, the direct detection of reflected light from exoplanets can be used as a tool towards the comprehension of their atmospheres. When reflected on the atmosphere of a planet, the spectrum of the host star will be modulated by its atmosphere composition and dynamics.

At optical wavelengths, the wavelength dependent planet-to star flux ratio is given by :

$$\frac{F_{planet}\left(\lambda,\phi\right)}{F_{star}\left(\lambda\right)} = A_g\left(\lambda\right)\ g\left(\lambda,\alpha\right)\left(\frac{R_{planet}}{a}\right)^2 \tag{2.1}$$

where:

- ϕ is the orbital phase;
- $A_g\left(\lambda\right)$ is the planetary albedo function;
- $g\left(\alpha\lambda\right)$ is the phase function;
- α is the orbital phase;
- R_{planet} is the radius of the planet and
- a is the semi-major axis of the orbit (Leigh et al., 2003).

The phase function of an exoplanet is a combination of both the percentage of the planet illuminated by the star (i.e., the "day portion" of the planet) and the scattering properties of the planet's surface/atmosphere. Figure 2.4 shows the phase function for different single scattering models as a function of orbital phase where $\alpha = 0$

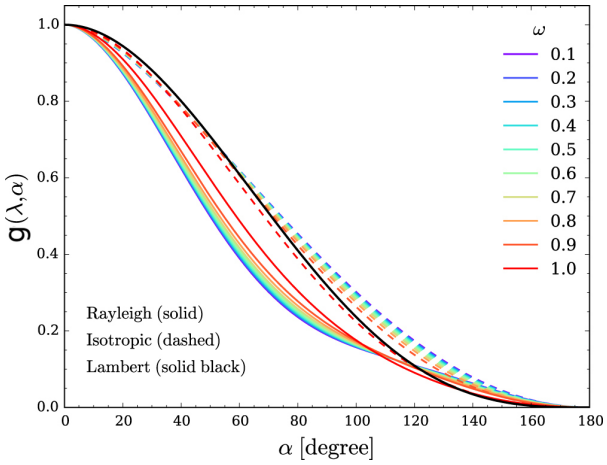

Figure 2.4: Phase function for different scattering models as a function of orbital phase where $\alpha = 0$ corresponds to opposition/full phase (from Greco et al., 2015). Note that the Lambert phase function is independent of the scattering albedo ω.

corresponds to opposition/full phase (from Greco et al., 2015) and ω represents 3 different scattering albedos functions: i) Rayleigh ii) Isotropic and iii) Lambert scattering. In most works (e.g Esteves et al., 2013), Lambert scattering phase-functions are assumed for simplicity, as this scattering has an analytically solution and thus is easy to model. Lambert scattering assumes that the scattering surface reflects light isotropically and the scattering does not depend upon the angle of incidence (Sobolev et al., 1975). Similarly for the sake of simplicity – but with no loss of generality – we will adopt Lambert scattering phase functions all through this work (see Langford et al., 2010), which are defined as

$$g(\alpha) = \frac{[sin(\alpha) + (\pi - \alpha)\, cos(\alpha)]}{\pi} \tag{2.2}$$

where α is the phase angle, given by

$$cos(\alpha) = sin(I)\, cos(2\pi\phi) \tag{2.3}$$

where I is the inclination of the orbit and ϕ is the orbital phase.

The albedo function measures the reflectivity of a planetary atmosphere as a function of wavelength. Different elements and molecules will reflect/absorb/scatter light with different intensities and at different wavelengths. As such, this function can be used as a probe to constraint and improve our knowledge of the physics of current atmospheric models (e.g. Marley et al., 1999; Cowan et al., 2011; Madhusudhan et al., 2012). Figure 2.5 shows possible theoretical albedo functions at optical wavelengths for different temperatures and metallicities of the atmosphere (from Greco et al., 2015).

Indirect methods – such as the energy budget from the secondary eclipse (e.g. Christiansen et al., 2010) or

	p $[days]$	a $[A.U.]$	R_p $[R_{Jup}]$	$\left(\frac{R_p}{a}\right)^2$	A_g	Reference for the albedo
51 Peg b	4.23	0.052	**1.90**[a)]	292	**0.50**[a)]	Martins et al., 2015a
HD 189733 b	2.22	0.0314	1.14	286	0.40±0.12	Evans et al., 2013
HD 209458 b	3.52	0.0475	1.38	185	0.04±0.045	Rowe et al., 2008
Kepler-5 b	3.55	0.0506	1.43	174	0.16±0.03	Angerhausen et al., 2015
Kepler-6 b	3.23	0.0457	1.32	183	0.07±0.03	Angerhausen et al., 2015
Kepler-7 b	4.89	0.0625	1.61	146	0.32±0.03	Demory et al., 2011
Kepler-8 b	3.52	0.0483	1.42	188	0.11±0.03	Angerhausen et al., 2015
Kepler-10 b	0.84	0.0169	0.13	13	0.55±0.11	Hu et al., 2015
Kepler-12 b	4.44	0.0556	1.70	203	0.09±0.02	Angerhausen et al., 2015

Table 2.1: Recovered geometric albedos for an arbitrary sample of exoplanets. *a)* Note that for 51 Pegasi b the recovered albedo and radius are degenerate as Martins et al., 2015a recovered $A_g R_p^2$ (See Chapter 5).

from the phase the planet presents us as it orbits its host (e.g. Snellen et al., 2009) – have proved invaluable to recover the albedo of exoplanets. Even nowadays, the sample of planets with known albedos is quite small (see e.g. Demory, 2014, for Super-Earths; and Angerhausen et al., 2015; Schwartz et al., 2015; Esteves et al., 2015, for larger planets), all of them obtained through indirect methods. For most Hot-Jupiters in this sample, low albedos have been detected (e.g. 0.04 for HD209458b Rowe et al., 2008), which is in agreement with early theoretical models which predict heavy absorption in the optical from TiO and VO and/or alkali metals (e.g Marley et al., 1999). However, several exoplanets have been detected with high albedo values (e.g $A_g < 0.4$ for τ Boo – Rodler et al., 2010; 0.32 for Kepler-7b – Demory et al., 2011; 0.44 for Kepler-91b – Esteves et al., 2015; 0.5 for 51 Pegasi b – Martins et al., 2015a). Table 2.1 presents the geometric albedos for a sample of exoplanets selected from the exoplanet.eu database.

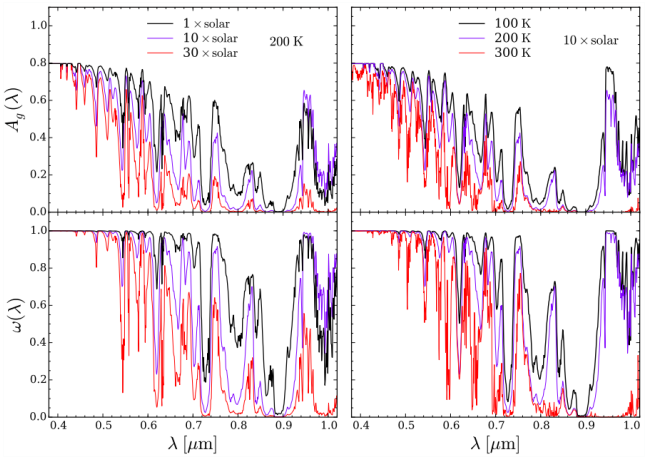

Figure 2.5: Examples of possible geometric (*top panel*) and scattering (*bottom panel*) albedo functions for different temperatures and metallicities of the atmosphere (from Greco et al., 2015).

Despite the increasing number of planets with measured albedos, no unifying picture on the properties of exoplanet atmospheres has emerged so far. An important step in that direction was given by the recent work of Sing et al. (2016), which shows that the detection of absorption features in an atmosphere depends on the presence of clouds and hazes for a variety of planets.

The main purpose of this work is the recovery of the reflected spectrum from exoplanets and the albedo function from their atmosphere as a proxy for exoplanet characterization. To do so, we developed a technique that cross-correlates high-resolution spectra with stellar masks. With this technique we were able to perform a direct detection of the reflected spectrum from the prototypical hot Jupiter 51 Pegasi b and conclude that 51 Pegasi b is most likely a highly-inflated planet with a high albedo (i.e., we inferred an albedo of 0.5 for a radius of $1.9\ R_{Jup}$ Martins et al., 2015a). In the following chapter we proceed to describe the technique in detail.

Chapter 3.
High-resolution spectroscopy concepts

Ubiquitous in all fields of Astronomy, a spectrograph is an instrument capable of measuring the flux of a target as a function of wavelength by dispersing the light from the target, similarly to water droplets that create rainbows. Figure 3.1 presents a simple schematic showing the major components of a spectrograph. The component responsible for dispersing the light is the *disperser*, of which the most common types are prisms and gratings.

The diffraction of light by prisms is due to the refraction of the beam inside the prism (see Figure 3.2). As per Snell's law

$$n_i \, sin\,(\theta_i) = n_r \, sin\,(\theta_r) \tag{3.1}$$

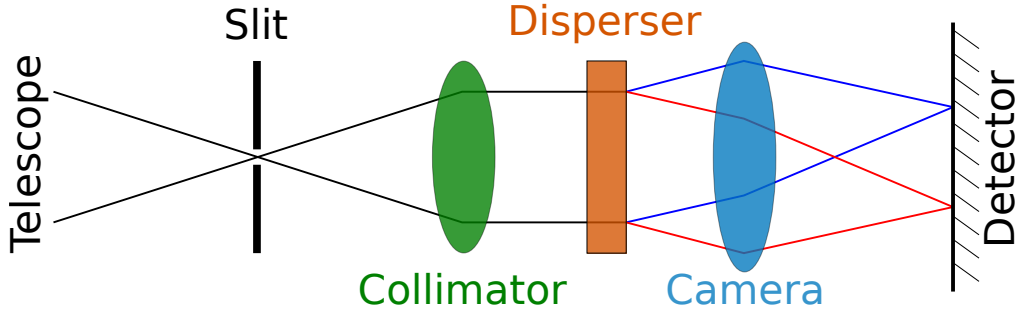

Figure 3.1: Spectroscopy: simple spectrograph diagram.

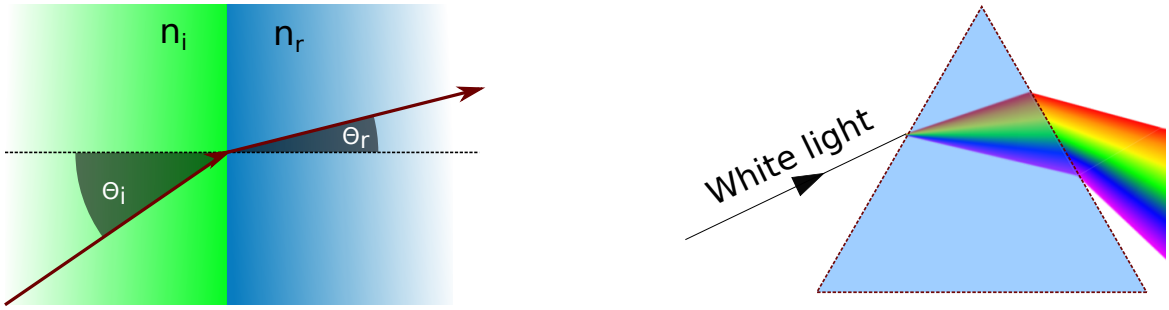

(a) Snell's Law **(b)** Dispersion of light

Figure 3.2: Dispersion of light by a prism.

where n_i and n_r are respectively the refraction index outside and inside the prism[1] and θ_i and θ_r are respectively the angle of the incident (outside the prism) and refracted beam (inside the prism) relatively to the normal to the prism-outside medium interface. Since the refraction index of a material is wavelength dependent, the refraction angle θ_r of an incident beam will vary with wavelength and thus white light will be dispersed. Note that the dispersion obtained by refraction is quite small and thus the resolution achievable by this method is quite limited. In order to achieve high-resolutions, dispersers capable of dispersing the light more efficiently are required. The most commonly used of these alternative dispersers is the dispersion grating.

Dispersion gratings are optical elements that consist in narrow slits (transmission grating, left panel of Figure 3.3) or grooves (reflection grating, right panel of Figure 3.3) parallel to each other and very close together. Incident light will be diffracted by the slits/grooves and interfere to create spectral orders that obey the grating equation:

$$m\,\lambda = d\;\left[sin\left(\theta_i\right) \pm \left(sin\left(\theta_r\right)\right)\right] \tag{3.2}$$

where m is the spectral order, λ is the wavelength, d is the distance between the grating slits/grooves, θ_i is the incident angle of light relative to the normal to the grating, and θ_r is the reflected angle relative to the normal to the grating for order m.

Echelle spectrographs (Figure 3.4) are a special genre of spectrographs that get their name from the type of grating they use: an echelle grating. This genre of spectrograph permits to record high-resolution spectra,

(a) Transmission grating **(b)** Reflected grating

Figure 3.3: Dispersion of light by gratings.

[1] The refraction index of vacuum is $n = 1$.

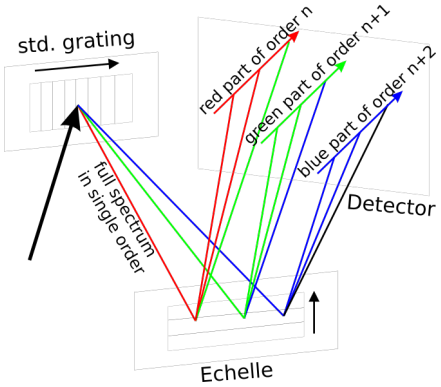

Figure 3.4: Simple echelle spectrograph diagram (from *Wikipedia*).

while covering a wide wavelength range (e.g. HARPS – Pepe et al., 2000). This is possible by combining two perpendicular dispersion elements, one that will provide the high-resolution – typically a high-dispersion grating – and another that will disperse the orders (also known as a cross-disperser).

We will now present briefly a few useful concepts from high-resolution spectroscopy used throughout this work, as well as the instruments that were used.

CONCEPTS 3.1

SPECTRAL RESOLUTION

The spectral resolution of a spectrograph represents its capacity to measure an as small as possible wavelength difference $\Delta\lambda$. Mathematically, for a given wavelength λ it is defined as

$$R = \frac{\lambda}{\Delta\lambda} \tag{3.3}$$

The higher the resolution, the smaller the $\Delta\lambda$ it can measure and the better it can sample a spectral line (and the more precise will RV measurements be). Typically, spectrographs can be classified as i) low-resolution ($R < 1000$), ii) medium-resolution ($1000 < R < 20\,000$) and iii) high-resolution ($R > 20\,000$).

Note that all spectrographs used all through this work – and in typical RV planet detection studies as well – permit spectral resolutions that are considered high even for the "high-resolution" standard (e.g., the HARPS spectrograph with $R \sim 115\,000$ Pepe et al., 2000).

SPECTRAL COVERAGE

The spectral coverage of a spectrograph is the range of wavelengths covered by the spectrograph.

SPECTRAL BLENDING

Two spectral lines are said to be blended when they cannot be spectrally resolved, i.e., cannot be measured individually. This occurs when the distance between their centers is smaller than $\Delta\lambda$.

SPECTRAL SAMPLING

The spectral sampling of the spectrograph corresponds to the number of pixels of the sensor used to sample the Full Width at Half Maximum (FWHM) of the PSF.

HIGH-RESOLUTION SPECTROGRAPHS USED IN THIS WORK 3.2

HARPS 3.2.1

The HARPS spectrograph (Pepe et al., 2000) is a fiber-fed and cross-dispersed high-resolution echelle spectrograph installed on ESO's 3.6-m telescope at the LaSilla-Paranal observatory. The main scientific goal that led to its development was the detection of exoplanets from extremely precise RV measurements.

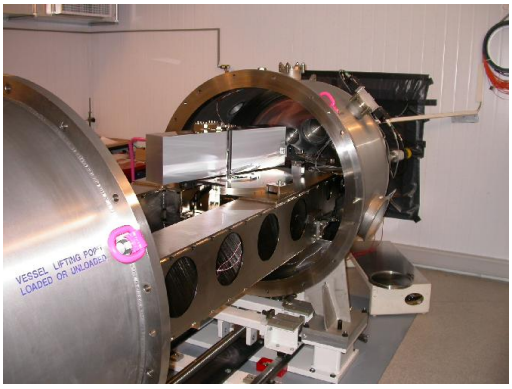

Figure 3.5: The echelle grating of the HARPS spectrograph inside its vacuum sealed container (©ESO).

HARPS has several key features that turned it into the workhorse of RV surveys. The combination of its high-resolution ($R \sim 115000$) with precise wavelength calibrations and extreme stability allows it to achieve a RV precision of about 80 cm/s (Lo Curto et al., 2012). The wavelength calibration is usually performed by using a Th-Ar lamp or a laser-frequency comb being fed trough a second fiber, allowing to simultaneously obtain the science and calibration observations[2]. Note that the installation of a Laser Frequency Comb (Lo Curto et al., 2012) – currently undergoing testing – allowed to increase the RV precision down to a few cm/s.

[2]Note that the simultaneous mode is only used to track instrumental drift during an observing night, with the wavelength calibrations being performed at the beginning of the night.

The HARPS spectrograph is also extremely stable thermally, as it is sealed in a pressure and temperature controlled vacuum container (See Figure 3.6), which guarantees an invariable refraction index for the whole optical path inside the spectrograph. Furthermore, its fiber scrambling setup ensures an evenly illuminated fiber exit, regardless of variations in the illumination at the entrance of the fiber. These factors makes it so that HARPS has an extremely stable PSF over large periods of time, guaranteeing an unsurpassed long term stability for RV measurements.

In terms of wavelength coverage, HARPS covers most of the visible spectrum (378-691 nm), where thousands of precisely known spectral lines can be used for precise RV calculations and stellar characterization. Note that in a typical 2-dimensional echelle spectrographs (e.g. HARPS), there is usually an overlap in wavelength between adjacent orders.

Besides the default High Accuracy Mode (HAM), HARPS also has a high efficiency mode (EGGS) with projected aperture on the sky of 1.4 arcsec against 1 arcsec for the default mode. This leads to an increase in flux of about 75 per cent for a seeing of 0.8. This increase comes at the expense of a higher diffuse light contamination on the resulting spectra (See Table 9.1 of the HARPS user manual[3] for more details). Table 3.1 presents some of the technical specification of the spectrograph[4].

Some scientific highlights on the exoplanetary field are:

* the detection of a trio of Neptune-like planets around HD 69830 (Lovis et al., 2006)

* the detection of Proxima b, the first Earth-like planet in its host Habitable Zone (Anglada-Escudé et al., 2016);

More recently, HARPS-North (Cosentino et al., 2012) – a clone of HARPS – was commissioned for the Telescopio Nazionale Galileo (TNG) telescope in the Canary Islands, Spain. Details on the facility can be found at `http://www.tng.iac.es/instruments/harps/`.

UVES 3.2.2

The UVES spectrograph is a high-resolution fiber spectrograph installed in UT2 of the VLT, at the La Silla-Paranal observatory (Dekker et al., 2000).

UVES has two arms – that can either be used separately or together – and a resolution of up to 80 000 for the *blue arm*: (300-500 nm) and up to $110\ 000$ with the *red arm* (420-1100 nm). It can also be coupled with Fibre Large Array Multi Element Spectrograph (FLAMES) – the VLT multifiber instrument – to obtain the spectra of multiple objects simultaneously. The spectrum of each individual object will have a spectral resolution of $R \sim 47\ 000$.

The technical specifications of UVES can be found in Table 3.2.

Although not developed primarily with this goal in mind, some attempts have been made at the detection and characterization of exoplanets. However, UVES lacks the stability of either HARPS or ESPRESSO, which

[3] `http://www.eso.org/sci/facilities/lasilla/instruments/harps/doc/manual/userman2_1.pdf`

[4] A detailed description of HARPS can be found at `http://www.eso.org/sci/facilities/lasilla/instruments/harps/inst/description.html`

System	2 fibres (1" dia.) spectral range 378-691nm, collimated beam 208mm
Echelle grating	R4, 31.6 gr/mm blaze angle 75 degrees, mosaic 2x1 on Zerodur monolith 840x214x125mm, efficiency > 65% in the visible
Cross disperser grism	FK5 grism, 257.17 gr/mm blazed at 480nm, 240x230x50mm, T=73% (av)
Collimator mirror	Zerodur with protected silver coating, f=1560mm, used diameter 730mm, triple pass
Camera	all dioptric, 6 elements in 6 groups, f=728mm, f/3.3, T>85%
Spectral format	upper" CCD (Jasmin): 89-114, 533-691nm lower" CCD (Linda): 116-161, 378-530nm
Spectral resolution	RS=120,000 (measured)
Sampling per spectral element	4.1 px per FWHM
Separation of spectra from fibres A and B	17.3 px
Order separation	Jasmin: order 89: 1.510mm = 100.7px, order 114: 0.940mm = 62.7px Linda: order 116: 0.910mm = 60.7px, order 161: 0.513mm = 34.2px

Table 3.1: Technical specifications of HARPS (from `http://www.eso.org/sci/facilities/lasilla/instruments/harps/inst/description.html`)

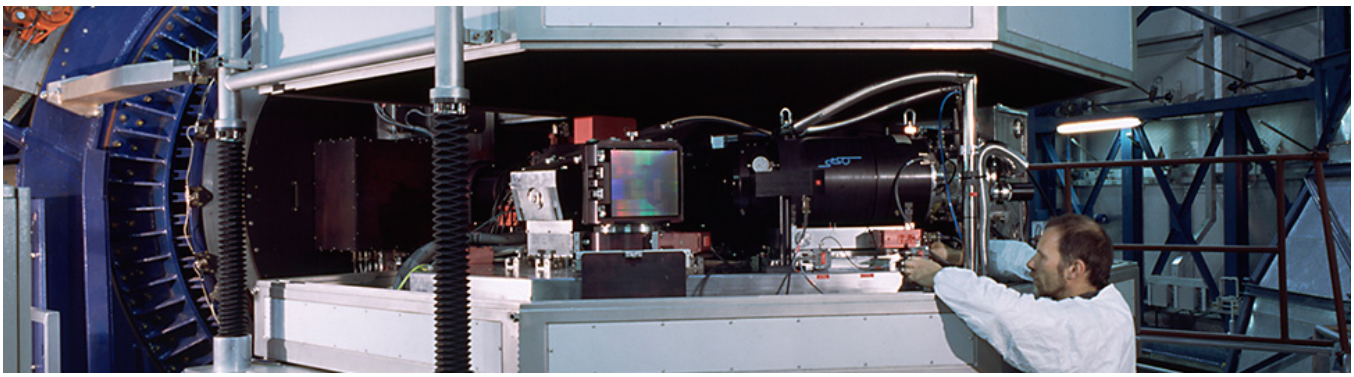

Figure 3.6: The UVES spectrograph at the VLT (©ESO/H.Zodet).

translates into not being able to perform long term precise RV measurements at a level of 1 m/s. Furthermore, calibration errors have been detected (Whitmore et al., 2010), which significantly increase the error bars on RV measurements. Some scientific highlights on the exoplanetary field are:

* the detection of atmospheric sodium in the atmosphere of HD 189733b (Khalafinejad et al., 2017);

* observing the Earth as an extrasolar transiting planet (Arnold et al., 2014).

ESPRESSO 3.2.3

ESPRESSO (Pepe et al., 2010) is a new high-resolution fiber-fed optical spectrograph (380-686 nm) currently being commissioned for the VLT at ESO's La Silla-Paranal Observatory. The main science drivers behind its development are

- the search and characterization of rocky planets around solar-type stars with precise RVs;
- the detailed determination of the chemical composition of stars in nearby galaxies and
- the measurement of the variability of the physical constants.

ESPRESSO will ally a HARPS-like high-resolution and stability to the collecting power of up to all four VLT 8.4-m telescopes. It will have 3 available observing modes: i) Multi UT Mode (MR) with a resolution of 60 000; ii) High-Resolution (HR) with a resolution of 135 000; and iii) Ultra High-Resolution (UHR) with a resolution of 200 000.

In MR mode, ESPRESSO will be able to combine incoherently the light from up to all 4 VLT Unit Telescopes (UT), effectively increasing the collecting area up to the equivalent of a 16m telescope. In both HR and UHR modes, it will only be able to receive the light for one of the telescope UT. For both MR and HR modes, ESPRESSO will be fed by a 1″ fiber, while on UHR mode, the fiber diameter drops to 0.5″. While allowing for a large increase in the resolution for the UHR mode, it comes at the cost of a lower photon collecting power.

Figure 3.7 shows the efficiency curve of all 3 resolution modes of ESPRESSO (Pepe, Lovis and Sosnowska - private communication), as well as the efficiency curve of HARPS (from HARPS ETC). Both HARPS and ESPRESSO (all 3 modes) efficiency curves were computed for a seeing of 0.65″and air mass of 1.0 (i.e. pointing towards the zenith). For all of them, the efficiency includes the transmission factors of the atmosphere, telescope, and spectrograph, as well as slit losses.

The technical specifications of ESPRESSO can be found in Table 3.3 and the optical setup of ESPRESSO is shown in Figure 3.8.

	Blue	**Red**
Wavelength range	300-500 nm	420-1100 nm
Max. resolution	∼80,000 (0.4" slit)	∼110,000 (0.3" slit)
Limiting magnitude	18.0 at R=58 000 in U	19.5 at R=62 000 in V
(1.5 hr integration, S/N=10, 0.7" slit)		
Overall detective quantum efficiency	12% at 400 nm	14% at 600 nm
(DQE)(from the top of the telescope, wide slit)		
Min. order separation	10 arcsec or 40 pixels	12 arcsec or 70 pixels

Table 3.2: Technical specifications of UVES (adapted from `http://www.eso.org/sci/facilities/paranal/instruments/uves/inst.html`)

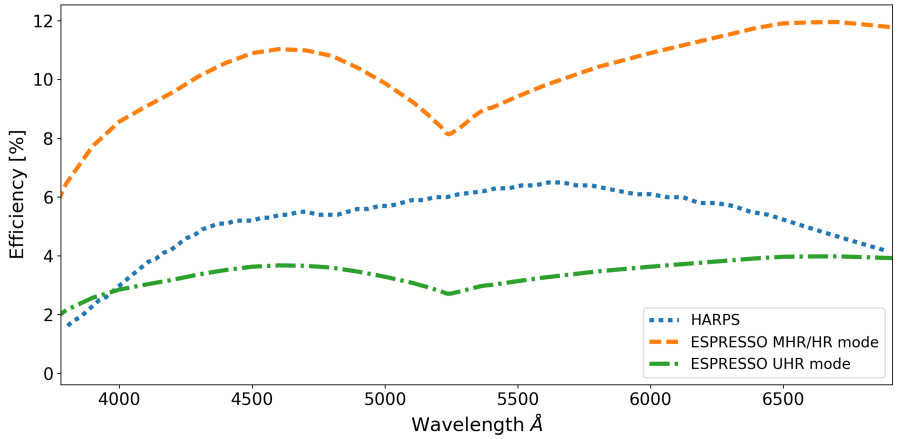

Figure 3.7: Total efficiency of ESPRESSO (in all resolution modes) and HARPS as a function of wavelength. The efficiency of the atmosphere, telescope, optical components and detector are included in the total efficiency of the instrument. Note that these are the theoretical efficiencies for all 3 modes. The first results from the instrument's commissioning shows a global efficiency 20-30 per cent lower than predicted.

HIRES 3.2.4

HIRES (Maiolino et al., 2013) is a high-resolution spectrograph proposed for ESO's ELT that will operate simultaneously at visible and infrared wavelengths (0.4–1.8 μm) with a spectral resolution of $R \sim 100000$. The primary science drivers behind HIRES are

- the characterization of low-mass exoplanet atmospheres and to search for bio-signatures;
- to study the evolution of stars and galaxies;
- to study the first generation of stars in the young Universe;
- the determination ot the time variability of some of the fundamental constants of physics and

	HR mode	**MHR mode (4UT)**	**UHR mode**
Wavelength Range	380-686 nm	380-686 nm	380-686 nm
Resolving Power	135 000	60 000	200 000
Aperture on Sky	1.0 arcsec	4x1.0 arcsec	0.5 arcsec
Sampling (average)	3.3 pixels	4.0 pixels (binned x2)	2.1 pixels
Spatial Sampling	6.9 pixels	4.0 pixels (binned x2)	3.5 pixels
Simultaneous reference	Yes (no sky)	Yes (no sky)	Yes (no sky)
Sky subtraction	Yes (no sim. ref.)	Yes (no sim. ref.)	Yes (no sim. ref.)
Total Efficiency	>10% at peak	>10% at peak	>7% at peak
Instrumental RV precision (requirement)	<10 cm/sec	<=5 m/sec	<=5 m/sec

Table 3.3: Technical specifications of ESPRESSO (adapted from `https://www.eso.org/sci/facilities/develop/instruments/espresso.html`)

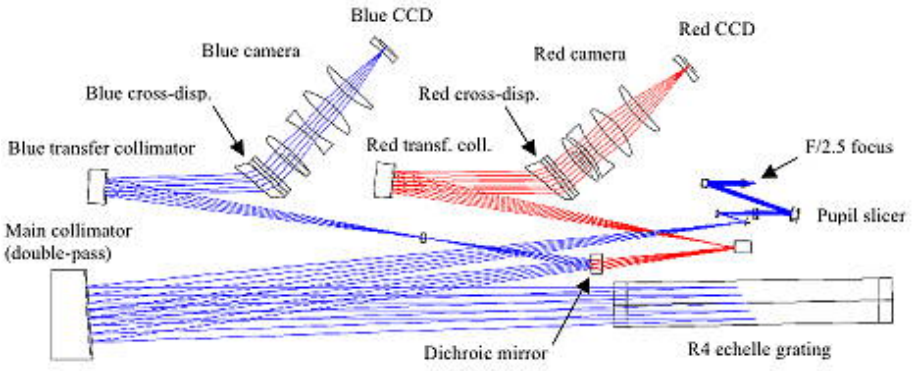

Figure 3.8: Optical configuration of the ESPRESSO spectrograph (©ESO).

- the direct measurement of the acceleration of the expansion of the Universe.

A detailed description for the spectrograph can be found at `https://www.eso.org/public/portugal/teles-instr/elt/elt-instr/hires/?lang`.

Since the instrument is still in the planning phase, very little information from it is available. As such, throughout this work we will assume and a HARPS-like profile for HIRES in terms of efficiency and spectral format, using HARPS calibration files as a spectral template.

Chapter 4.
Recovering the reflected spectrum from exoplanets

Planets are comparatively small and far from their hosts, and as such have very small effective cross-sections. Adding to that, for most of the orbit, only a fraction of the day-side of the planet will be visible from the observer's vantage point. Finally, they will not reflect the totally of the incident light, it will partially be absorbed and scattered by its surface/atmosphere (see Figure 4.1). As such, the main issue with detecting optical light reflected on an exoplanet is the extremely low planet-to-star flux ratio, which can be computed from Equation 2.1.

The best targets for detection and characterization are typically hot and large planets with short period orbits (i.e hot Jupiters). In the infrared, their planet-to-star flux ratio can reach 10^{-3}, mainly due to their thermal emission peaking at these wavelengths. At optical wavelengths, the planet-to-star flux ratio can reach up to only 10^{-4} [1] (see Cameron et al., 1999). As such, to recover this signal with a 3-σ_{noise} confidence, it would require

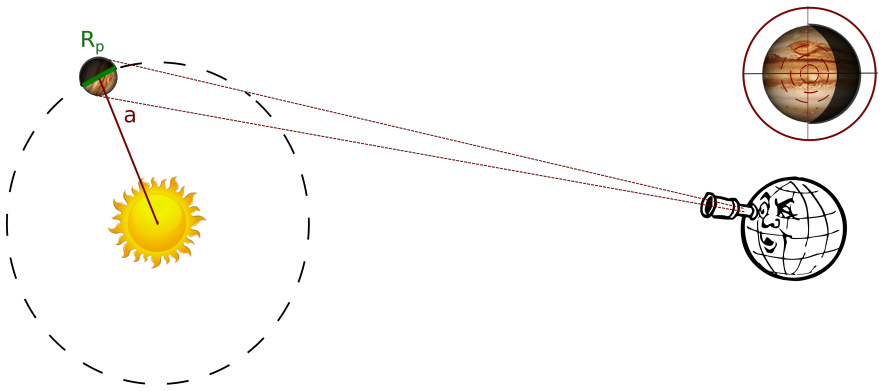

Figure 4.1: Diagram illustrating the minute amount of light from a star reflected by an orbiting planet assuming a circular orbit.

[1] Note that in the case of an Earth-Sun analog system, the planet-to-star flux ratio will be around 10^{-9}.

observations with S/Ns well above 10^4. Notwithstanding that the planetary flux is higher at infrared than at optical wavelengths, attempting the recovery of the planetary reflected signal in the optical has several advantages to study its reflectivity/albedo. First of all, in the optical it will be mainly a reflected and scaled-down copy of the stellar spectrum[2], modulated by the planetary albedo function, while in the infrared thermal emission dominates, which creates a far more complex spectra, difficult to model with the current knowledge. Furthermore, in the infrared the Earth's atmospheric transmission and emission features – in particular water vapor absorption – severely imprints themselves on the recovered spectra (e.g. Smette et al., 2015) contrary to what happens at optical wavelengths. These reasons led us to choose optical wavelengths for the recovery of the reflected spectra from exoplanets. To so so, we employ a technique that mathematically increases the S/N of observations by cross-correlating them with a mask of spectral lines present the host star spectrum.

THE CROSS CORRELATION FUNCTION TECHNIQUE 4.1

The Cross Correlation Function (CCF) of high-resolution spectra with binary masks has been used very successfully for many years to determine with high-precision the radial velocity of astronomical objects (e.g. Zinn et al., 1984; Baranne et al., 1996; Mayor et al., 2003). In particular for exoplanets, astronomers cross-correlate high-resolution spectra of stellar systems with numerical masks over a range around the host's radial velocity. These masks are fundamentally lists of spectral lines identified on the particular spectral type of the host. Each spectral line on the mask is represented by a theoretical initial and final wavelengths, as well as the weight for each line. These parameters are computed assuming that the line can be represented by a rectangle with the same area as the real spectral line, with the continuum normalized to one and the weight corresponding the relative depth of the line, centered at the rest wavelength of the spectral line. Using this technique, researchers are able to recover the periodic variations in the star RV due to the dynamical pull of an orbiting planet with high-precision (see Chapter 1.1.1).

Let's consider a spectral line i from an hypothetical high-resolution spectrum of a star. If the star is moving with radial velocity v relative to the observer, its measured wavelength will be λ_i'. The same spectral line will have rest wavelength λ_i on the spectral mask template. The relation between the two is given by Equation 1.1 (See Section 1.1.1)

The Cross Correlation Function (CCF) computes the degree of similarity between the spectral mask and each spectrum over a given radial velocity range, with the maximum similarity obtained for the correct radial velocity of the star. Mathematically speaking, the particular CCF implementation we use can be found in Baranne et al.,

[2] **Lopez-Morales2007** have shown that this is not necessarily true for all cases, e.g. super close-in hot Jupiters might have a non-negligible contribution in red bands.

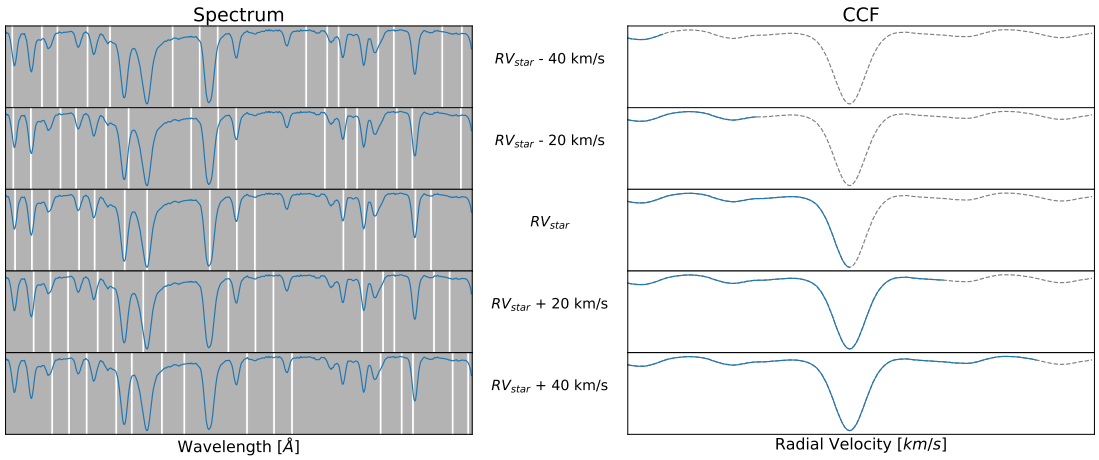

Figure 4.2: Diagram depicting the construction of a CCF. *Left Panel:* order 6 of an arbitrary UVES spectrum (blue line) of 51Pegasi b with the spectral mask superimposed for different radial velocities. The white bands correspond to the spectral lines selected for the CCF computation, with their wavelength corrected for the radial velocity presented in the center panel. It can be seen that for the radial velocity of the star (RV_{star}), the spectral lines of the mask are aligned with the respective lines in the spectrum. *Central Panel:* different radial velocities for which the CCF is computed relative to RV_{star}. *Right Panel:* CCF for order 6 of the spectrum of the left for different radial velocities. The black dotted line corresponds to the complete CCF over the whole wavelength range for which it was computed. The blue line corresponds to the CCF computed up to the radial velocity on the central panel. The lowest value of the CCF corresponds to the highest degree of similarity between the spectrum and the stellar mask.

1996. For a given velocity v, the CCF is defined by

$$C(v) = \sum_{x,l} w_l \, p_{l,x}(v) \, f_x \tag{4.1}$$

where l is the spectral line, x the pixel number. The fraction of line l that falls on pixel (x) is given by $p_{l,x}$, f_x is the flux for the same pixel and w_l is the relative weight for each spectral line and a function of the relative line depths for each line.

Figure 4.2 depicts the construction of a CCF. The CCF stacks together the spectral information from all spectral lines included in the mask, creating what can be seen as an average spectral line[3]. In brief, the CCF measures the degree of similarity between the spectrum and the mask as a function of the radial velocity of the object. The velocity that corresponds to the object's radial velocity will be the one with the highest degree of similarity between both spectra, which corresponds to the minimum of the CCF. Assuming that the spectral mask matches the spectral type of the star (i.e., that the lines contained in the mask match the lines in the spectrum) and that all lines have equal weight (i.e., $w_l = 1$ for each line) or the weight is taken into account optimally (w.g., see Pepe et al., 2002), the S/N of the CCF will be

$$S/N_{CCF} \approx \sqrt{n} \, S/N_{spectrum} \tag{4.2}$$

where S/N_{CCF} and $S/N_{spectrum}$ are respectively the S/N of the CCF and of the spectrum, and n is the number of spectral lines in the mask used in the calculus of the CCF. Typical masks for solar-type stars have thousands of spectral lines, yielding a significant increase in the S/N of the observations. For example, the HARPS mask for a

[3]In a common abuse of notation, this average line is also known as CCF.

G2 type star has about 4100 lines, increasing the S/N of the observations by ~ 64.

Note that when computing the CCF with a non-weighted spectral mask, broad weak lines would contribute to the CCF as much as deep narrow lines. However, deep lines contain more spectral information than weak lines (Gray et al., 1992). As such, when using a non-weighted spectral mask all this information is averaged out. By weighting the spectral lines in the mask against their depth ensures that no spectral information is lost (e.g., Pepe et al., 2002).

4.1.0

Albeit not spectra in the strict sense, the CCFs from high-resolution spectra contain the spectral information of the spectrum that originated them and inherit some of the properties of the original spectrum. For example, the CCF of stacked spectra is equivalent to the sum of the CCFs from the individual spectra. Let's consider a star with an orbiting planet being observed with an high-resolution echelles spectrograph. For any given order o and pixel x, the flux measured in the spectrograph is $f_{x,total}$. As per Equation 4.1, the CCF of the generated spectrum for an arbitrary velocity v is given by

$$\begin{aligned} CCF_{total}(v) &= \sum_{l,x} p_{l,x}(v) f_{x,total} \\ &= \sum_{l,x} p_{l,x}(v) \left(f_{x,star} + f_{x,planet}\right) \\ &= \sum_{l,x} p_{l,x}(v) f_{x,star} + \sum_{l,x} p_{l,x}(v) f_{x,planet} \end{aligned} \tag{4.3}$$

By definition:

$$\begin{aligned} CCF_{star}(v) &= \sum_{l,x} p_{l,x}(v) f_{x,star} \\ CCF_{planet}(v) &= \sum_{l,x} p_{l,x}(v) f_{x,planet} \end{aligned} \tag{4.4}$$

where $CCF_{star}(v)$ and $CCF_{planet}(v)$ are respectively the CCFs of the star and planet. Therefore

$$CCF_{total}(v) = CCF_{star}(v) + CCF_{planet}(v) \tag{4.5}$$

Another particularly useful property of the CCF is that similarly to their spectral analogues, its noise follows a Poisson distribution (see Appendix C for details on spectral noise statistics). Since the sum of CCFs is still a CCF, its noise will also follow a Poisson distribution. Therefore, when stacking multiple CCFs on the same rest frame – i.e. corrected for the radial velocity of the object being observed, effectively aligning its signal on the RV domain – the S/N of the CCF increases with the square root of the number of stacked CCFs.

We now proceed to describe the method we developed to recover the optical signature from exoplanets.

THE RECOVERY METHOD 4.1.1

For simplicity – but with no loss of generality – let's consider we intend to recover the optical reflected signature from a planet in a single star+planet system, from high-resolution spectra covering a wavelength range between λ_{ini} and λ_{fin}. The method we propose can be summarized by 4 major steps:

- Phase coverage constraints,
- Computation of the CCFs,
- Removal of the stellar signature and
- Recovery of the reflected signal from the planet.

We now proceed to describe each step of the technique in detail as applied to an arbitrary wavelength range.

PHASE COVERAGE CONSTRAINTS

When planning the observations, the main factor to consider is the selection of the orbital phases at which the planet will be observed. Since we are attempting to recover the reflected signal from the planet in the optical, as the planet orbits the star, it will present alternately its day and night sides to the observer. Figure 4.3 illustrates the variations in planet-to-star flux ratio (top panel, from Eq. 2.1) and radial velocity (bottom panel, from Eq. 1.4) for 51 Pegasi b as it orbits its host. The orbital parameters were obtained from Martins et al. (2015a). The corresponding orbital position is shown on the right panel from the figure. Orbital phase $\phi = 0$ has been defined as the orbital phase when the planet is closest to the observer. At this point of their orbit – also known as inferior conjunction – the movement of both the planet and the star will be tangential to the plane of the sky and they will present no radial velocity[4]. Note that 51 Pegasi b has an almost circular and edge-on orbit, but the conclusions of this analysis are valid for any type of orbit with no loss of generality.

It is clear that in terms of flux, the most privileged orbital phases are the ones close to opposition/superior conjunction (phase $\phi = 0.5$), and for which the planet is not occulted by the star (relevant only for occulting planets). At those points in the orbit, the fraction of flux reflected by the planet towards the observer is at its maximum. On the other hand, the worst choice of orbital phase is close to transit/inferior conjunction, when the planet reflection towards the observer is at is minimum – or null for edge-on orbits.

However, to be able to recover the planetary signal, it is necessary to be able to separate the planet and host signals. This will be easiest to perform the further apart the signals are in the RV domain. Looking at the bottom panel from Figure 4.3, it is easy to perceive that this will happen close to maximum elongation, i.e., phase 0.25 and 0.75. Note that for those phases the planet-to-star flux ratio will have dropped to under 50% of its maximum value, making it less than ideal to recover the planetary signal. On the other hand, close to superior conjunction – when the planet is at its brightest – the difference in RV between to the planet and the star is negligible and both signals are spectroscopically blended. Since the stellar lines a a few orders of magnitude deeper than the planetary

[4]Note that the same will happen at superior conjunction, i.e., $\phi = 0.5$.

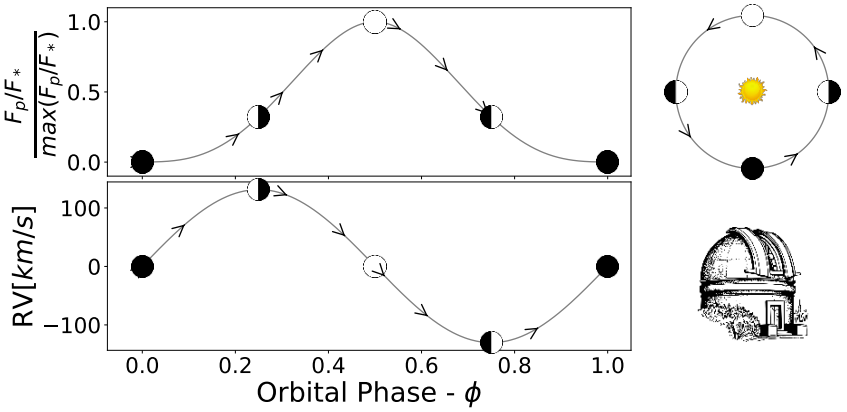

Figure 4.3: *Top panel*: Variation of the planet-to-star flux ratio as a function of orbital phase. *Bottom panel*: Variation of the planet radial velocity as a function of orbital phase.

signal, the residuals of the removal of the stellar signal are much stronger than the planetary signal itself, making it impossible to recover the planetary signal. Therefore, we have defined that the minimum distance between the planet and the star in the RV domain to be able to recover the planetary signal to be about 3 times the FWHM of the stellar CCF. For example, in the case of the star 51 Pegasi, this corresponds to about 18 km/s on each side of superior conjunction. Outside this region, the noise structures left after the removal of the stellar signal are negligible comparing to the planetary signal.

We have defined as *optimal windows*, the orbital phases that balance the need to retrieve as much flux as possible from the planet and the ability to spectroscopically resolve the stellar and planetary signals.

Figure 4.4 shows the variation in the planet-to-star flux ratio across the orbit as a function the difference in radial velocity between the star and the planet for the 51 Pegasi system. The green regions correspond to the radial velocities where the planet-to-star is within 75% and 95% of its maximum at superior conjunction (in this case, the *optimal windows* correspond to the orbital phases within 15 and 45 degrees on each side of opposition/superior

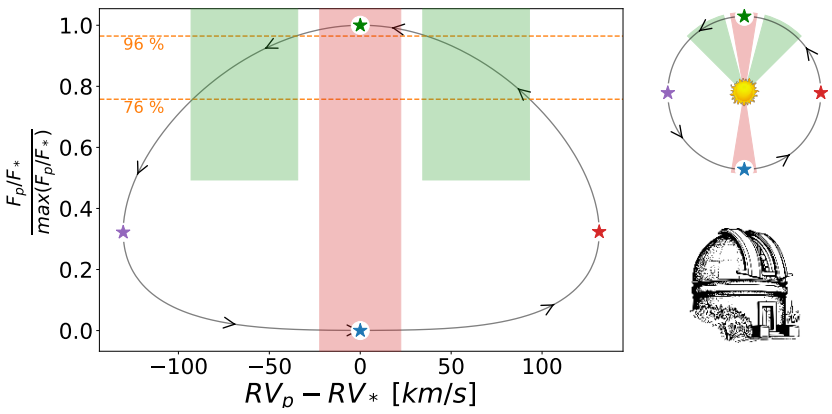

Figure 4.4: Normalized planet-to-star flux ratio as a function of the planet-star distance in the RV domain. The red region corresponds to radial velocities for which we assume that the planetary and stellar signals cannot be separated. The green regions correspond to the optimal observing windows.

conjunction). The red region corresponds to radial velocities for which we estimate that the planetary and stellar signals cannot be separated (phases around the blue and green stars).

COMPUTATION OF THE CCF

Equation 4.1 shows a mathematical implementation of the Cross Correlation Function (CCF). To recover the planetary signal, the CCF will need to be computed for several radial velocities over a large RV range that encompasses the whole orbit of the planet.

To define this range, we need to take into account that planets have much larger radial velocity amplitudes than their host stars, and as such the computation of the CCF will need to be performed over large radial velocity ranges. Equation 1.4 allows to compute the radial velocity semi-amplitude of the stellar orbit (K_*) from its orbital elements. The radial velocity semi-amplitude of the planetary orbit (K_p) can be obtained from K_* given that

$$K_p \, m_p \, \sin i = -K_* \, m_* \, \sin i \tag{4.6}$$

$K = |K_p - K_*|$ will be the largest RV separation between the planet and its host star. This will be the maximum distance between the center of their CCFs over one full orbit. We also assume that all the relevant information from the planetary CCF to be encompassed within a radial velocity range

$$W = 3 \times \ FWHM_* \tag{4.7}$$

on each side of the center of the planetary CCF, where $FWHM_*$ corresponds to the FWHM of the stellar CCF. Such a large range will allow for the detection of the CCFs from the planet, even after being affected by broadening effects such as rotation (e.g. Kawahara, 2012), or atmospheric thermodynamics (e.g. Hedges et al., 2016). Furthermore, a fraction $C = 3 \times \ FWHM_*$ of the wings of the planetary CCF needs to be added to act as a continuum (C) of the planetary CCF and allow to characterize the noise level of the CCF.

In the end, the CCF will be computed for radial velocities in the range

$$RV_* - (K + W + C) < RV < RV_* + (K + W + C) \tag{4.8}$$

Figure 4.5 exemplifies the factors in the definition of the radial velocity range for the computation of the CCF.

Another parameter that needs pondering is the CCF computation step, i.e., the distance between two consecutive points in the above interval for which the CCF is computed. In several points of the recovery process, it is necessary to shift the CCFs in RV. This will implicate an interpolation between consecutive pixels. Therefore, the selection of a step as small as possible is favored, as it will minimize the interpolation errors during the shift. However, the computation of the CCF is computationally intensive, and too small CCF step might make the computing time unacceptably lengthy. The default step CCF for the HARPS Data Reduction Software (HARPS DRS) CCF computation routine is 250 m/s. Bellow 50 m/s we do not expect to see any appreciable difference in

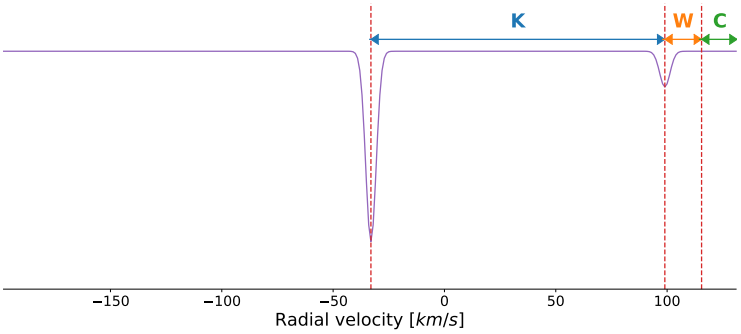

Figure 4.5: Definition of the radial velocity range for the computation of the CCF. The amplitude of the signal for the planet has been amplified to be noticeable.

the CCF. Note that a single pixel from a HARPS spectrum corresponds to about 800 m/s.

Finally, the correct spectral mask need to be selected for the computation of the CCF. The spectral masks used in computing the CCFs of high-resolution spectra for planet detection via the RV method consist in spectral line lists tailored to the spectral type of the star being observed[5]. As stated before, since we are searching for the spectrum of the star reflected on the planet, the same spectral mask can be used to detect both the stellar and planetary signals.

REMOVING THE STAR

A critical step in the method we developed is the separation of the planetary signal from the stellar one. After the computation of the CCFs of the observations, the spectral signature of both the planet and star are still stacked together. To remove the stellar signal, we construct a extremely high S/N stellar template by stacking together the CCFs from multiple observations, after correcting them individually from stellar radial velocity drift. This way, the S/N will be enhanced by a factor proportional to the square root of the number of stacked CCFs (See Equation 4.2). The stellar signal will then be removed by normalizing each individual CCF by the stellar template.

Some caution is required when constructing the stellar template CCF. First of all, its S/N needs to be significantly higher than the one of the individual CCFs. Using a template with a S/N comparable to that of the individual CCFs will introduce non-negligible noise to the planetary CCF. As a rule of thumb, we normally consider that the S/N of the template should be at least 10 times larger than the one of the individual CCFs. This implies that at least 100 observations should be used in its construction. A detailed statistical analysis of the problem is discussed in Appendix C.

Note that extremely high-resolution and S/N stellar models are currently available (e.g. Kurucz, 2006) which could be used to construct a noiseless stellar template, with no planetary contamination. However, constructing it from real observations will allow it to be model independent and enable the template to mimic effects affecting the observations and/or the stellar flux (e.g. atmospheric Cunha et al., 2014; or instrumental effects Lovis et al., 2011).

[5]Note that the same mask might be suited for several sub-types.

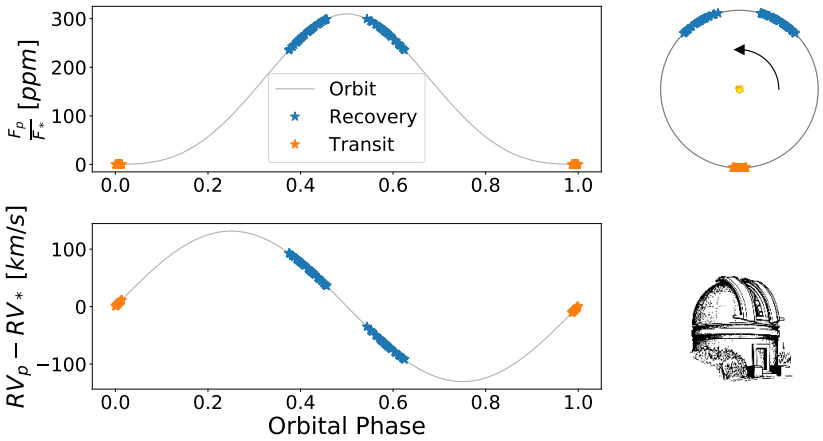

Figure 4.6: Randomly distributed observations across two optimal observing windows as defined in Section 4.1.1 (blue stars) and close to inferior conjunction (orange stars).

The most intuitive strategy is to construct the stellar template from observations at orbital phases where the planetary signal is null or negligible. Such is the case from observations performed when the planet is at inferior conjunction (or transit for transiting planets – orange stars in Figure 4.6). This strategy allows for the construction of the purest stellar template and has two main advantages. The first one is that the signal from the optical signature of the planet will be, in principle, null, as its night side will be facing the observer[6]. The second one is that the stellar and planetary signals will have matching radial velocities and be spectroscopically blended. As such, the planetary contamination in the template will be negligible in the RV ranges/orbital phases where we will be searching for the planet (see Section 4.1.1). The main disadvantage is that it requires additional observing time just for the template creation. While this might not be a problem for bright targets (e.g. 51 Pegasi) where short exposure times will yield easily 100+ observations. However, the required time to obtain enough observations to construct a template for fainter targets (e.g. HD 209458 b) will increase greatly due to the large number of additional observations required.

When observations close to inferior conjunction are not available or are insufficient to provide a high-S/N template, an alternative strategy is to construct the template by stacking all available observations. This strategy has the advantages of maximizing the exposure time to recover the planetary signal, with no "lost" time to construct the stellar template and maximizing the S/N of the template. However, it is critical to minimize planetary contamination as the observations include both the planetary and stellar signals. If the orbital phases of the planet for each observation are randomly spread across a large orbital phase range, the planetary signal on each CCF will appear at different radial velocities. Co-adding them all together – after correction of the stellar RV motion – will dilute the planetary signal amidst the stellar noise, making it negligible and creating a high-quality template. However, if the RV of the planet – a function of the orbital phase of the planet – does not vary significantly and is similar to the one of the CCF being normalized, the template might also remove the planetary signal.

[6]Albeit not true for planets not on edge-on – or close to – orbits, it was demonstrated that most planets detected via the RV method have high-inclination orbits (e.g. Jorissen et al., 2001).

RECOVERING THE ALBEDO

Once the CCFs of the observations have been normalized by the stellar template, we are left with planetary CCF and noise. To further increase the S/N of the planetary signal, we stack the normalized CCFs after correction of the planetary RV. The final result is the CCF of the planet over the selected radial velocity range.

Since the CCF can be seen as an average spectral line, it can be approximated by an inverted Gaussian profile G, given by

$$G = B - Ae^{-4\,\ln 2\,\left(\frac{x-\mu}{FWHM}\right)^2} \tag{4.9}$$

where B is the level of the continuum of the CCF, μ is the mean or center of the CCF, A is the amplitude of the CCF and $FWHM$ is the full width at half maximum of the CCF (a measure of the width of the CCF). The area of the Gaussian profile defined by Equation 4.9 is given by

$$Area = \int_{-\infty}^{\infty} G\,dx = C \times A \times FWHM \tag{4.10}$$

where C is a constant. This equation can then be used to compute the areas of both the recovered planetary and stellar template CCFs.

The ratio of the areas of the recovered planetary CCF and of the stellar template CCF will be the planet-to-star flux ratio $\frac{F_{planet}}{F_{star}}$. Hence, the planetary albedo can be recovered inverting Equation 2.1:

$$A_g = \frac{1}{< g\,(\alpha) >} \times \left(\frac{a}{R_{planet}}\right)^2 \times \left(\frac{F_{planet}}{F_{star}}\right) \tag{4.11}$$

where $< g\,(\alpha) >$ is the mean of the phase function over the CCFs used in the recovery of the planetary signal. Note that we are considering the ideal case where the planetary radius R_{planet} is known. When that does not occur, it is only possible to recover $A_g\,R_{planet}^2$. Despite the degeneracy of the problem, this value can still be used to characterize the planetary atmosphere properties.

Chapter 5.
Reflected optical light from 51 Pegasi b

To apply our method to real data, we chose to observe the 51 Pegasi system with both the HARPS and UVES spectrographs installed at the LaSilla-Paranal observatory.

As per Equation 2.1, the amount of incident light that gets reflected by a planet towards the observer is proportional to i) the orbital phase at the moment fo the observations, ii) its albedo, iii) radius and iv) distance from the host. The orbital phase can be carefully selected to maximize the fraction of day-side it presents the observer (see Section 4.1.1 for details). The ratio of the radius by the distances suggest that giant planets in close orbits such as hot Jupiters are the best candidates for such a detection. Considering a conservative value of $A_g = 0.1$ for the albedo, the planet-to-star flux ratio will be at most 10^{-4}, requiring a S/N of the order of $10^4 - 10^5$. To choose a target, it is also important to take into account the visual magnitude of the host as it will impact the required exposure time for a detection. In summary, our ideal target needs to be a giant planet orbiting a bright star on a short orbit. 51 Pegasi b is the ideal candidate, as it is a hot Jupiter type planet, on 4.23 days orbit around a $mag_V = 5.49$ G2 star. It also has the added attraction of having historical importance as it was the first exoplanet to be detected.

In terms of instrument, the detection of the reflected light from an exoplanet requires large collecting areas or high exposure times to achieve the required S/N level. Furthermore, long term stability of the instrument is essential, as we require to stack a high number of observations taken over long periods of time. Finally, a high-resolution spectrographs is indispensable to be able to resolve a high number of spectral lines. The HARPS spectrograph[1] was at the time the only instrument with the necessary high-resolution and proven long term stability to detect the broadband integrated geometric albedo of the planet. With it, we were able to recover the reflected signal from 51 Pegasi b with a 3-σ significance from 12.5 h of data and infer that it is most likely a highly-inflated planet ($R_p = 1.9 R_{Jup}$) with a large geometric albedo ($A_g = 0.5$). These results were published as *Evidence for a spectroscopic direct detection of reflected light from 51 Pegasi b* in Astronomy & Astrophysics, 2015, Volume

[1] Details on the HARPS spectrograph can be found in Chapter 3.2.1.

576, id.A134 (Martins et al., 2015a).

As for UVES[2] it combines its high-resolution with the collecting power of a 8.2-m telescope, allowing to achieve the required S/N with short exposure times. With it, we expected that instead of detecting a single broadband albedo for the planet, we could – in principle – recover the wavelength dependence of the albedo. However, the extra collecting power comes at the expense of a lower intrumental PSF stability over long periods of time. This aspect turned out to preclude our ability to detect the reflected signal for the planet (See Section 5.2 for details). These results are presented in Section 5.2.

In parallel, we acquired archival observations for the 55 Cnc system obtained with HARPS and HARPS-N. A brief description of the analysis performed on this data can be found in Appendix C.

RECOVERING THE ALBEDO FROM 51 PEGASI B 5.1

For this project, we acquired a total of 12.5h of HARPS observations of the 51 Pegasi system under ESO's programme *091.C-0271* (PI: Santos, N. C.). As discussed in Section 4.1.1, to maximize the detectability of the planet, the observations need to be performed as close to superior conjunction as possible, while keeping the spectroscopic signals of both the planet and the star separated on the RV domain. Therefore, the observations were performed in several carefully selected time windows that were computed from the ephemeris provided by Butler et al. (2006). These observations span over seven different nights and consist in 91 spectra with a S/N on the $50^{\rm th}$ order ($\sim$556-nm) that varies between 122 and 388. As per HARPS ETC, the predicted S/N on the $50^{\rm th}$ for a 600s exposure, an airmass of 1.5 and a seeing of 1.0 is around 420. Note that although the 51 Pegasi system is a bright target, the S/N of most of the gathered observations for the same order is much lower, due to the presence of clouds for some of the nights (e.g., an exposure of 600s on 2013-08-02 yields a S/N of $\sim$150, while on 2013-09-30 it reaches $\sim$390 after 450s).

A summary of the observational parameters of the acquired data are presented in Table 5.1. Individual exposure times range from 300s to 600s. Table B.1 presents the detailed description of the observational parameters for each independent observation.

The reduction of the data was performed with HARPS DRS (Mayor et al., 2003) version 3.6 using the default settings.

[2]Details on the UVES spectrograph can be found in Section 3.2.2.

Night	Number of Spectra	Total exposure [seconds]	S/N range
2013-06-08	3	1360	243 - 296
2013-06-25	10	5260	273 - 351
2013-08-02	2	1092	145 - 151
2013-08-04	20	10000	215 - 311
2013-09-05	4	2400	191 - 248
2013-09-09	13	7810	122 - 265
2013-09-30	39	17100	179 - 388

Table 5.1: Summary of the observational parameters of the acquired data on a per night basis (from Martins et al., 2015a). Individual exposure times range from 300s to 600s.

COMPUTATION OF THE CCF 5.1.1

The computation of the CCF was also executed with HARPS DRS with the following parameters:

SPECTRAL MASK

51 Pegasi is a G2 spectral type star, for which HARPS DRS has a weighted spectral mask available with 4165 spectral lines (Pepe et al., 2002). This will lead to a S/N increase by a factor of 64 when measured on the CCF relative to that measured on the original spectra.

INITIAL RV

For the initial estimate of the RV location of the center of the CCF we provided $-33.02\ km/s$ as presented in the *SIMBAD* astronomical database for the systematic RV of the 51 Pegasi system (Nidever et al., 2002).

CCF WIDTH

In terms of CCF width, the expected planet semi-amplitude is around 130 km/s (e.g. Brogi et al., 2013) and the FWHM of the star is about 7.5 km/s. This means that $K + W + C$ – the minimum value for the CCF width as defined in Section 4.1.1 – is about 175 km/s. This allowed to cover the full orbit of the planet en terms of RV, while allowing for a continuum section large enough on both sides of the planetary CCF to account for broadening effects of the planetary signal and estimate its noise level.

Instrument	Number of measurements	Dates	$RV_{\rm System}$ [km/s]	Reference
ELODIE@OHP	153		-33.252	Naef et al. (2004)
KECK, AAT, Lick	256		-0.002	Butler et al. (2006)
HARPS	91	Jun-Sep 2013	-33.152	Martins et al. (2015a)

Table 5.2: 51 Pegasi radial velocity data used to derive the orbital parameters. $RV_{\rm system}$ corresponds to the radial velocity of the system as measured by the corresponding instrument (from Martins et al., 2015a).

CCF STEP

After testing the construction of the CCF with different values for the CCF step, we selected a value of 50 m/s, which adequately balances the required precision for the CCF and the extensive computational time required to compute it.

The computation of the CCF of each observation allowed to derive precise radial velocities (See Table B.1) for our observations. To do so, a Gaussian profile defined by Equation 4.9 is fitted to each CCF. For each individual observation, the radial velocity of the star corresponds to the center of the Gaussian fitted to the computed CCF. The measured radial velocity of the star for all observations is listed in Table B.1.

These measurements were combined with measurements from other facilities available in the literature, which permitted to derive a new set of precise orbital parameters for the star and its planetary companion. The combined set of measurements spans over almost 20 years and is summarized in Table 5.2.

To compute the new orbital solution, we used the $YORBIT$ (Ségransan et al., 2011) code. The eccentricity – and thus the longitude of the ascending node ω – was set to zero as the initially fitted value was not statistically different from zero. The new orbital parameters are presented in Table 5.3, and were used through the remainder of this work. Note that the recovered parameters do not fully characterize the orbit as the fitted mass is the minimum mass, as the inclination of the orbit is degenerate. We note that this degeneracy does not have an impact on the orbital phase, of importance to us here. However, the direct detection of the planetary signal will enable to lift this degeneracy (see Section 5.1.3).

Figure 5.1 shows the measured radial velocity (RV_*) of each HARPS observation as a function of orbital phase (blue dots), with the best-fitting orbital solution (red line) in the top panel. The horizontal blue line corresponds to the barycentric radial velocity of the system. In the bottom panel, Figure 5.1 shows the residuals on the measured radial velocity (RV_*) of the star versus the fitted one (RV'_*). The error bars correspond to the 1-σ errors on the measurements as delivered by the pipeline. Note that a large dispersion in the stellar RV residual can be observed for phases $0.5 < \phi < 0.6$, which we attribute to bad weather that deteriorated the seeing for the corresponding night.

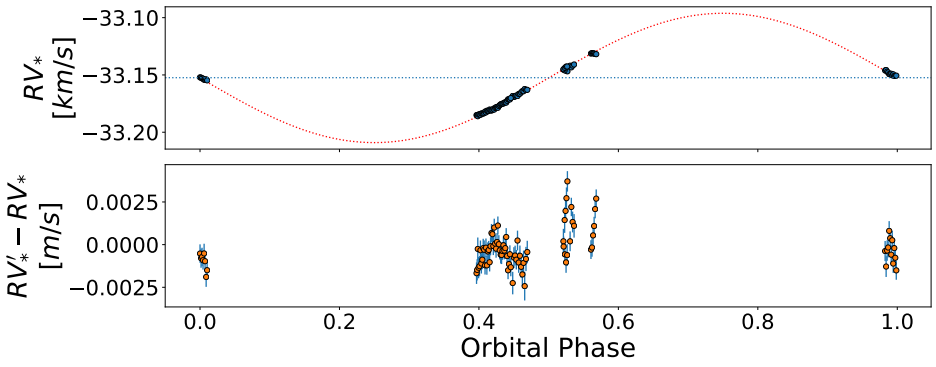

Figure 5.1: *[Top panel]*: Measured radial velocity of each HARPS observation as a function of orbital phase (blue dots), with the best-fitting orbital solution (red line). The horizontal blue line corresponds to the barycentric radial velocity of the system. *[Bottom panel]*: Residuals on the measured radial velocity (RV_*) of the star versus the fitted one (RV'_*) . The error bars correspond to the 1-σ errors on the measurements.

REMOVAL OF THE STELLAR SIGNAL 5.1.2

A stellar template that replicates as closely as possible the stellar signal is of paramount importance to remove the stellar signal from the observations. For our work, we constructed the stellar template by stacking together real observations, after correction of the RV drift of the star for each observations (see Table B.1).

As highlighted in Section 4.1.1, ideally it should be constructed from observations where there is little or no planetary contamination. Yet, it requires a S/N much higher than that of the observations to makes sure the removal of the stellar signal will not introduce additional noise of significance. With those parameters in mind, we decided to construct two different stellar templates and test their performance.

Parameter	Unit	Value
$RV_{\rm system}$	[km/s]	-33.152
Period	[days]	4.231
e		$0.0(fixed)$
a	[AU]	0.052
k_*	[m/s]	55.2
$m_p\ sin(i)$	[$M_{\rm Jup}$]	0.450
m_*	[$M_\odot$]	1.04
ω	[degrees]	$0.0(fixed)$
t_0	[BJD-2400000]	56021.256

Table 5.3: Orbital parameters for the 51 Pegasi system recovered by $YORBIT$ (from Martins et al., 2015a).

TEMPLATE #1 (hereafter **T1**)

We created this template with the objective of maximizing its S/N while sacrificing the purity of the template. As such, we constructed it by stacking all available HARPS observations. It is expected that each observation will contaminate slightly the stellar template with some reflected planetary flux. However, the RV of the planet varies very rapidly and the observations are spread more or less randomly across the orbit. Therefore, the planetary signal is diluted amidst the stellar jitter and should be negligible.

TEMPLATE #2 (hereafter **T2**)

In this case we chose to favour the purity of the template in expense of S/N. Therefore, to construct this template, we selected only observations close to inferior conjuntion ($0.9 < \phi < 0.1$, where ϕ is the orbital phase). At this point of the orbit, not only the observer is facing the planetary night side, but also the planetary and stellar signals have matching RVs. Therefore, the planetary contamination in the wings of the stellar CCF – where we expect the planetary signal to be located on the observations from which it will be recovered – is negligible. However, the number of observations at that point of the orbit is limited, and the template was constructed from only 20 of the 93 available observations. As such, the S/N of Template #2 is expected to be around ∼40% of the S/N of **T1**.

Finally to remove the stellar signal, we normalized independently all our observations by both stellar templates. Doing so will permit to choose the most adequate stellar template for this study.

RECOVERY OF THE PLANETARY REFLECTED SIGNAL 5.1.3

For both stellar templates, after removal of the stellar signal we selected the observations from which the planetary signal would be recovered. As discussed in detail in Section 4.1.1, it is necessary that both the stellar and planetary signals do not overlap on the RV domain. However, observations as close to superior conjuntion as possible will maximize the effective cross-section for the planet and the reflected flux collected from the planet. To balance these two factors, we only considered observations for which the RV difference between the planet and the star is over 60 km/s (see Section 4.1.1).

For each observation, the RV of the planet can be computed from the previously measured stellar radial velocity if we consider that the planet-to-star mass ratio (q) is given by

$$q \equiv \frac{M_p}{M_*} = \frac{K_*}{K_p} \tag{5.1}$$

where K_* and K_p are respectively the RV semi-amplitudes for the stellar and planetary orbits. However, although K_* can be inferred from the orbital fit of the RV measurements and Equation 1.3, K_p is degenerate as the RV technique only yields the minimum mass of the planet. Figure 5.2 shows in orange the observations that meet the above criteria, assuming that the planetary mass is equal to the minimum mass from Table 5.3. On the left panel,

it presents the normalized planet-to-star flux ratio ($F_p/F_* = 1$ for $\phi = 0.5$) as a function of the distance between the planet and the star in the RV domain. On the right panel, it shows the distribution of all observations along the orbit.

To recover the real semi-amplitude of the orbit, we computed the RV of the planet for each observation assuming different values for the planetary orbital semi-amplitude[3] K_p, in the range $75\ km/s \leq K_p \leq 275\ km/s$. Then, for each of these possible orbital solutions, we aligned the CCF on the expected RV of the planet and stacked them together. As done with the stellar signal, the parameters of the recovered planetary signal for each orbital solution are obtained by fitting the Gaussian profile defined by Equation 4.9 to the stacked CCFs (and not to the individual CCFs). Note that some physical restrictions had to be put in place on the fitted parameters:

- $FWHM_p > 0.9\ FWHM_*$ - Noise on the CCF might affect the fitting of the Gaussian profile of the planetary CCF and as such make it appear narrower that the stellar CCF. However, this effect is expected to be minimal and as such allowing for a 10% decrease on the FWHM of the planetary CCF should suffice. Note that it is possible for the convective envelope of the host to be tidally locked to the planet. In that case, an observer on the planet would "see" the stellar unaffected by rotation and as such the reflected planetary CCF would present a narrower FWHM that the star's (for further details see Charbonneau et al., 1999). In the case of the 51 Pegasi system, the stellar rotation period is much longer than the planetary orbital period ($\sim$ 21 days against $\sim$ 4 days, see Simpson et al., 2010), hence this effect should be negligible;

- $FWHM_p < 4\ FWHM_*$ - This value was selected to allow for enough continuum on each side of the planetary CCF to permit to estimate the noise on the CCF ($1 \times FWHM_*$) while allowing for Doppler broadening due to the rotation of the planet (Kawahara, 2012). It corresponds to the extreme case of a hot Jupiter class planet with the same rotation period as Jupiter ($\sim$ 10h) but twice its radius being observed edge on. However, it is expected that hot Jupiter class planets such as 51 Pegasi b to be tidally locked to

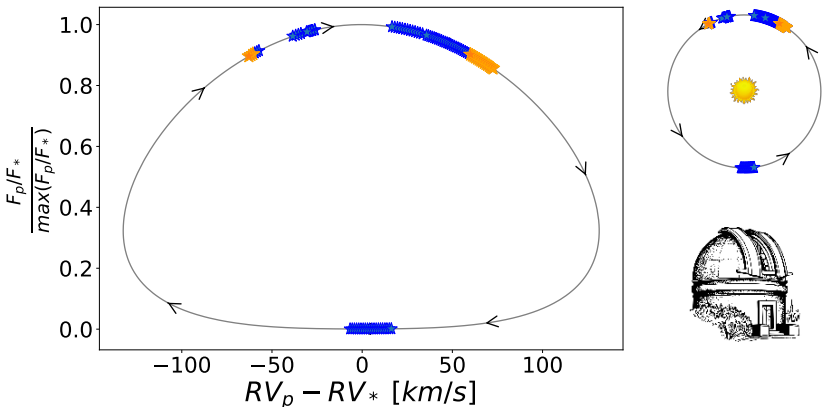

Figure 5.2: *Left panel*: Normalized planet-to-star flux ratio ($F_p/F_*\,(\phi = 0.5) = 1$) as a function of the distance between the planet and the star in the RV domain; *Right panel*: Distribution of our observations along the orbit. The orange stars correspond to the observations used for the recovery of the planetary signal.

[3]Note that each different K_p will correspond to a different inclination of the orbit.

their hosts (Goldreich et al., 1966) and thus Doppler broadening should be much lower.

To quantify which orbital solution corresponds better fits the data, we have defined the significance of the detection – or detectability – of the planetary signal as:

$$D = \left| \frac{A_p}{\sigma_{\rm noise}} \right| \tag{5.2}$$

where A_p is the amplitude of a Gaussian fit to the planetary signal and σ_{noise} is the continuum noise of the CCF on both sides of the recovered signal. The continuum region of the CCF was defined the regions whose distance to the center of the fitted Gaussian profile on the RV domain is $> 2 \times FWHM_p$. The continuum noise is defined as the standard deviation of the pixel intensity of the stacked CCFs on the continuum regions.

It is expected that at the correct K_p, when stacking the CCFs together, the signal of the planet will be aligned and increasing the significance of the detected planetary signal. As we move away from the correct orbital solution, the signal of the planet on each CCF will not be aligned and thus the final signal will be diluted amidst the noise and the detectability D will be of the order of unity (or smaller). Thus, the correct radial velocity semi-amplitude for the planetary orbit should occur at for the maximum value of the detectability of the planetary signal. At the end we expect the recovery signal of the planet to be centerd at $RV = 0$ and with a $FWHM \sim 7.5$ km/s.

Assuming the derived value for the stellar mass presented in Table 5.3 and using Equation 5.1, the real mass of the planet can be inferred, and consequently the inclination of the planetary orbit. Note that, given the planetary orbital parameters presented in Table 5.3, the maximum possible planetary semi-amplitude (i.e., for an edge-on orbit) is $Kp = 133.6$ km/s (assuming $M_* = 1.04\ M_\odot$ and $M_p\ \sin(i) = 0.460\ M_{Jup}$).

THE ALBEDO FROM 51 PEGASI B 5.1.4

As discussed in detail in the previous Section, we computed the radial velocity of the planet for each normalized CCF for uniformly distributed orbital semi-amplitudes in the $[75 - 275]$ km/s range, with a step of 50 m/s. Then, for each K_p, after correction of the RV of the planet all CCF for which the planet-star RV difference is over 60 km/s were aligned on the RV of the planet and stacked. Note that the number of CCFs that can be stacked will decrease as K_p decreases, leading to a decrease in the S/N of the stacked CCF as K_p decreases as well.

Then, for each K_p, the detection significance of the recovered planetary CCFs was computed from Equation 5.2. The detection significance for all Gaussian fits that did not meet the physical restriction criteria presented previously was set to zero. This procedure was repeated for both templates.

Figure 5.3 shows the detectability of the recovered planetary CCFs as a function of K_p/orbital inclination for both **T1** (*left panel*) and **T2** (*right panel*). On each plot, the red vertical line corresponds to K_p with the maximum detectability for each template.

Template **T1**, yields a maximum detection significance of 3.7-σ_{noise} for $K_p = 132\ km/s$. In terms of error bars, a visual inspection of the detectability as a function of K_p shows clearly that the detectability curve is almost flat for values of K_p in the $[120 - 150]$ km/s range, while always above 3-σ_{noise}. As such, we defined the error

bars on K_p as the range of RV semi-amplitude where the detection significance is above 3.0-$\sigma_{\rm noise}$. This yields a final detection significance of 3-σ_{noise} for the best fitting planetary orbital semi-amplitude of $K_p = 132^{+19}_{-15}$ km/s for **T1**.

In the case of **T2**, a maximum detection significance of 5.6-σ_{noise} for $K_p = 133\ km/s$ is attained. To be conservative, the error bars on K_p were defined as the range of RV semi-amplitude where the fitted amplitude to the recovered signal is within a 2-σ uncertainty in the best-fitting amplitude at maximum detectability. This yields a best fitting planetary orbital semi-amplitude of $K_p = 133^{+19}_{-20}$ km/s for **T2**. This choice of error bars results from the fact that for maximum detectability, **T2** was constructed from only 25 observations ($\sim$ 27% of the available 91). Albeit the higher detectability for **T2**, **T1** represents much more accurately the stellar signal as it has a much higher S/N and much less liable to introduce additional noise into the CCF (see discussion in Section 4.1.1). Using the same reasoning, we chose to proceed with template **T1** for the reminder of this work.

Figure 5.4 shows the recovered planetary CCF for maximum detection significance, using Template **T1**. The red line corresponds to the best fitting Gaussian profile computed using a Levenberg-Marquardt algorithm. For both signals, the CCF continuum has been set to 1 by normalizing the continuum regions of both CCFs by the median pixel value of the continuum. The continuum regions were defined as the RVs of the CCF outside a region within $2 \times FWHM_*$ of the central position of both the stellar and planetary signals. The fitted parameters for the best-fitting Gaussian profile are presented in Table 5.4, against the parameters of the stellar CCF (computed from fitting a Gaussian profile to **T1**). To estimate the errors bars on the parameters from the best fitting Gaussian profile to the recovered planetary CCF, we:

(a) subtracted the best-fitting Gaussian to the recovered planetary CCF;

(b) injected in the residuals from step **(a)** a Gaussian profile defined by Equation 4.9 with the same amplitude and FWHM of the best-fitting Gaussian, but a different mean RV;

(c) recovered the injected Gaussian profile;

(d) repeated steps **(a)** to **(c)** 10 000 times.

Figure 5.3: Detection significance as a function of K_p. The red line correspond to the K_p value for maximum detection. It can be seen that the maximum detection occurs for similar K_p value for both templates. The amplitude values set to zero corresponds to K_p values for which no Gaussian fit with the aforementioned restrictions could be achieved. *Left Panel:* Using template #1; *Right Panel:* Using template #2. (from Martins et al., 2015a)

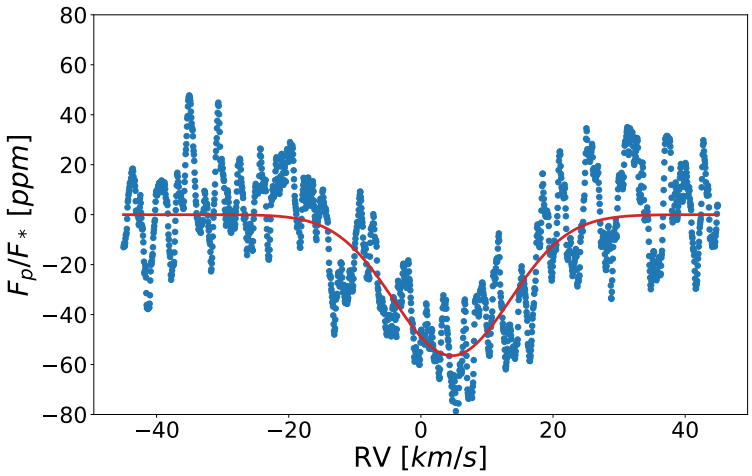

Figure 5.4: Recovered planetary signal for maximum detection (in blue), using Template **T1**. The red line corresponds to the best fitting Gaussian profile computed using a Levenberg-Marquardt algorithm.

		Star	Planet	
Amplitude		0.48	6.0±0.4	$\times 10^{-5}$
Significance	$[\sigma_{noise}]$	–	3.7±0.2	
FWHM	$[km/s]$	7.43	22.6±3.6	

Table 5.4: Comparison of fitted parameters of both the stellar and planetary CCFs, after setting the continuum region to one.

The 1-σ errors listed in Table 5.4 correspond to the standard deviation for each parameter of the recovered Gaussian profiles.

Figure 5.5 displays the recovered planetary CCFs for different values of K_p over the $[75 - 175]$ km/s range, centered on the expected radial velocity of the planet. It is clear that for the planetary orbital semi-amplitude that corresponds to maximum detectability – $K_p = 132km/s$ – the recovered signal is well defined and its wings less noisy, closer to the distribution of the expected Gaussian profile of a CCF. As the value of K_p gets further from 132 km/s, when stacking the individual CCF for each observation, the planetary signals for each individual CCF will not be aligned with each other but spread out across the continuum. As such, the recovered signal will be of lower significance as the signal from multiple CCFs will be spread across the wings which will seem more noisy in consequence due to the presence of the non-superimposed signal from the different CCFs. Note that close to $K_p = 132km/s$, a signal can still be seen clearly above the noise level (for example, for $K_p = 115km/s$ and $K_p = 120km/s$ in Figure 5.5). While for those values of K_p, the recovered signal might appear of similar amplitude than the one at maximum detectability, the detection significance will be lower due to the dilution of the signal from the planet across the CCF continuum.

TESTING THE DETECTED SIGNAL 5.1.5

SPURIOUS COMBINATION OF RANDOM NOISE?

It is possible that the detected signal is not of physical origin but an artifact resulting from a spurious combination of random noise. To test for this scenario, we devised the following test. As before, after removal of the planetary signal, we computed the orbit for uniformly distributed orbital semi-amplitudes in the $[75 - 275]$ km/s range, with a step of 50 m/s. However, after computing the RV of each observations, the RV-spectrum pairs were shuffled, resulting in the signal being stacked with an RV that does not correspond to its observation. Finally, the CCF were centered on the assigned RV of the planet, stacked and a Gaussian profile was fit to the resulting CCF.

In none of the cases was a significant signal detected which gave us confidence that the detected CCF of the planet is not a mere artifact resulting from the combination of random noise. Figure 5.6 displays the resulting stacked CCFs with randomly assigned RVs for selected values of K_p. Note that in some of the panels in Figure 5.6, some structures can be identified (e.g., the center structure in the 115 km/s panel of the figure) which could be identified as the planetary signal. However, all of them have FWHMs much smaller ($\sim 2 - 3$ km/s) than the stellar one (7.43 km/s). As mentioned in Section 5.1.3, it would be possible that the planet would "see" the star unaffected by rotation (See Charbonneau et al., 1999, for details) and thus the planet CCF could in theory present a smaller FWHM. However, in the case of the 51 Pegasi system this effect should be negligible and thus the structures that can be seen in Figure 5.6 can all be discarded as nonphysical.

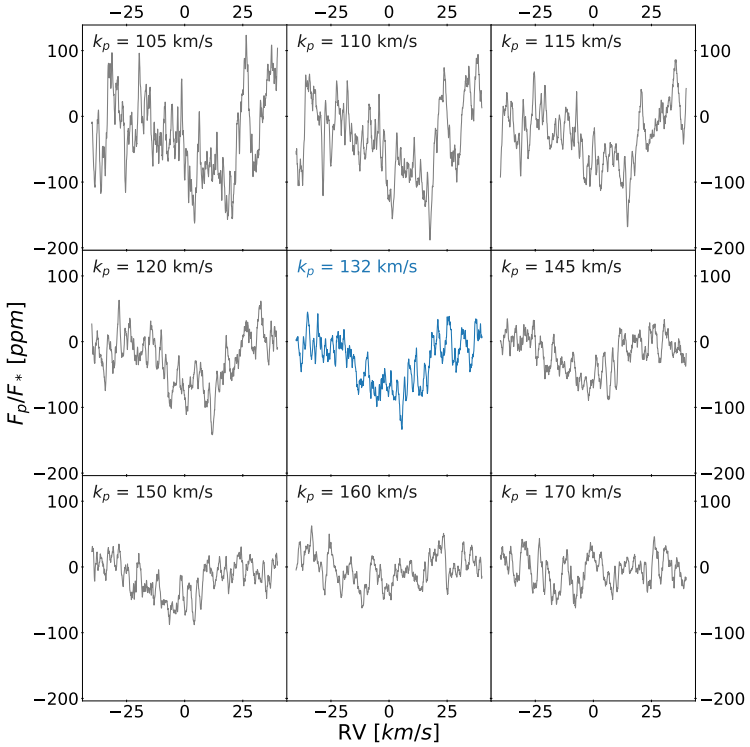

Figure 5.5: Recovered planetary signal for different selected values of K_p over the $[75 - 175]$ km/s range. It is clear that as the value of K_p gets closer to the value corresponding to maximum detectability, the signal becomes better defined and the continuum noise lowers.

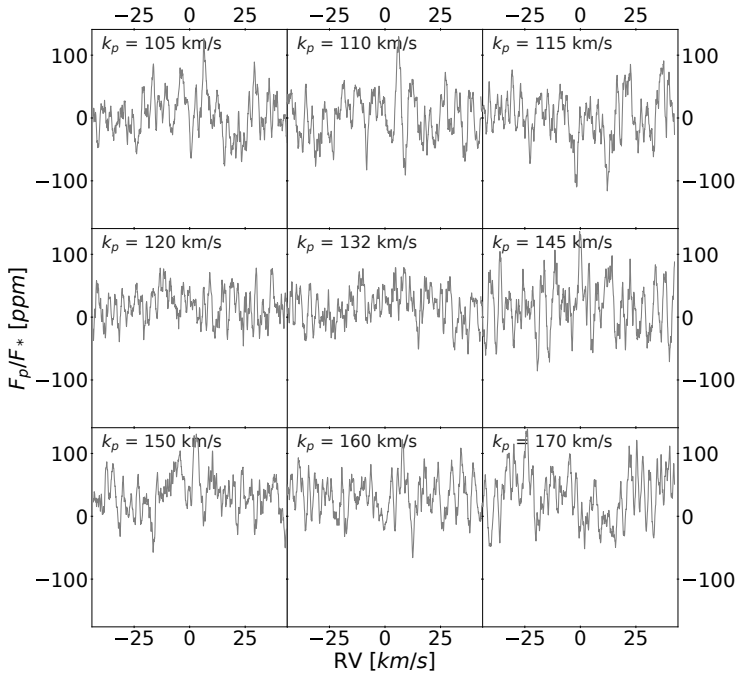

Figure 5.6: Detected signals as a function of k_{Planet} but for random sections of the normalised CCF where the planetary signal is not expected to be found.

STELLAR CONTAMINATION

We explored the possibility that the detected signal could be contamination of stellar origin (This is highly unlikely, it would mean that the contaminating signal had to have the correct radial velocity and be in phase for most – if not all – observations). The option of a visual stellar companion has been discarded by adaptive optics search for stellar companions on stars with planets with the Keck telescope (Luhman et al., 2002). The other possibility was the presence of a background star that could contaminate our observations with a signal with the magnitude of our detection's. To inject a signal as strong as the one we detected, and considering the magnitude of 51 Pegasi ($mag_v = 5.49$), would required a background star with $mag_v < 16$, assuming the worst case scenario where all of the background's star flux would be collected by the HARPS fiber. To estimate the probability of such an alignment, we used the Besançon galactic model (Robin et al., 2003). According to this model, there are only 760 FGK and M stars per square degree at the coordinates of 51 Pegasi with $mag_v < 16$. Note that we can safely discard all other spectral types as the CCF mask would not be compatible with them. Assuming that the recovered signal could be produced by any star within 2.6″of 51 Pegasi, the probability of this signal to be the result of a background star is below 0.1% (for details see Cunha et al., 2013), making contamination by a background star highly unlikely.

RECOVERY ALGORITHM ERROR

We also tested the planet CCF recovery algorithm to make sure it was recovering the signal correctly. To do so, we created 100 sets of noiseless CCFs simulating the observations of the 51 Pegasi system. The goal of this exercise was to test if the planetary signal could be recovered from each simulated set of observations. Each set of simulations consists in 91 observations of the star and planet – mimicking our observations – and was attributed a random RV semi-amplitude for the planet in the $[100, 180]$ km/s range. Each observation was built by adding one Gaussian profile for the planet to a Gaussian profile for the star at their corresponding radial velocities. Both Gaussian profiles were computed from the stellar parameters presented in Table 5.4, except for the amplitude of the planetary signal which was set to 5×10^{-5} (a similar value to the one recovered for 51 Pegasi b).

For all simulated sets, the injected signal was successfully recovered. Furthermore, the recovered values of K_p were always close to the injected ones with a standard deviation of only 0.11%. A similar result was obtained for the amplitude, which was always recovered with a standard deviation under 0.01%. This test shows that the recovery algorithm is working correctly and can be used safely to retrieve the planetary signal.

CHARACTERIZING THE PLANET 5.1.6

BREAKING THE MASS-INCLINATION DEGENERACY

The direct detection of the reflected spectrum from the planet enabled to lift the mass-inclination degeneracy that results from the RV method which only yields the minimum mass. Note that the orbital inclination is limited to 90 degrees, and as such the planet's mass cannot be inferior to the minimum mass. Assuming a stellar mass of is $1.04\ M_{\odot}$ (Santos et al., 2013), and the 90 degrees limit on the inclination, Equation 5.1 yields a real mass of $0.46^{+0.06}_{-0.01}\ M_{Jup}$ for 51 Pegasi b. Combining this value with the minimum mass presented in Table 5.3 ($m_p\ sin\,(i) = 0.45\ M_{Jup}$), we derived an orbital inclination of 80^{+10}_{-19} degrees. This result is compatible with results from the literature: $79.6^{\circ} < i < 82.2^{\circ}$ for Brogi et al. (2013); $70^{\circ} < i < 82.2^{\circ}$ for Birkby et al. (2017). Note that the upper limit on the inclination found by these authors corresponds to the limit for which the planet would transit, which has been discarded from photometric surveys of the system (e.g. Henry et al., 1997).

THE ALBEDO

In principle, the recovery of the reflected planetary signal should enable us to estimate the planetary albedo from Equation 4.11. However, 51 Pegasi b does not transit its host, and thus we have no information on the planetary radius of the planet[4]. Yet, it is still an interesting exercise to attempt to infer what possible albedo/radius combinations can plausibly create the signal we have detected.

First of all, we need to estimate the planet-to-star flux ratio. In Section 4.1.1, we mentioned that this value would be given by the ratio of the areas of the planetary and stellar CCF. However, a visual inspection of Figure

[4]As discussed in Chapter 2, no mass-radius relations for hot-Jupiters exits due to the degeneracy in the measured radii for planets with similar masses.

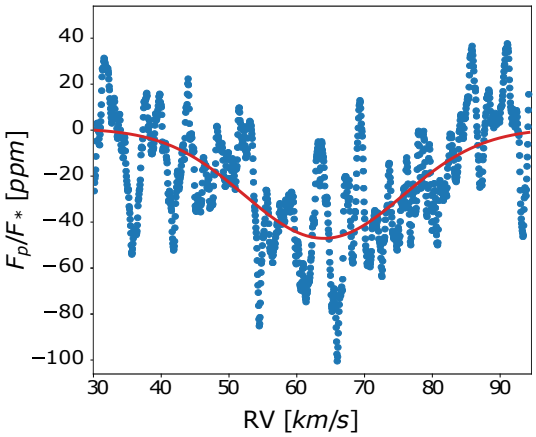

Figure 5.7: Simulated signal injected at +60 km s^{-1} in relation to the position of the center of the planetary CCF.

5.4 shows that the planetary CCF is dominated by noise and the planetary CCF appears extremely broadened relatively to the stellar one. The most obvious physical explanation for the broadening of the planetary CCF is rotational broadening. However, such close-in planets are expected to be tidally locked to their hosts, which for a radius of $1.2R_{Jup}$ would imply a rotational velocity of $\sim 2\ km/s$. For the same radius, to explain the detected broadening requires a much higher rotational velocity of $\sim 18\ km/s$. Additionally, the error on the stellar RV measurements is of the order of the m/s, which transposed into the planetary RV domain correspond to errors inferior to 2-3 km/s, clearly insufficient to explain this level of broadening.

A simple test has suggested that this broadening could be noise-related. On each observed CCF (before the removal of the stellar signal) we injected an artificial signal (a pure Gaussian) with an amplitude of 5×10^{-5} and a FWHM equal to the star's at +60 km/s relatively to the position of the planet (where only noise is expected). Then, we ran anew our recovery pipeline to attempt to recover the injected signal.

Figure 5.7 shows the recovered signal which was recovered with a similar amplitude (4.6×10^{-5}). However, what is most intriguing is that the FWHM of the recovered signal is much larger that the injected one ($\sim$ 27.6 km/s against 7.43 km/s). Note that this level of broadening is similar to the broadening detected on the recovered planetary signal of 51 Pegasi b ($FWHM = 22.6 \pm 3.6$ km/s) . We repeated this test for several injected signals with different amplitudes (but same FWHM as the star). When the injected signal amplitude is much larger than the noise, the recovered parameters are close to the injected ones. However, if the injected signal has an amplitude close to the noise level, the recovered CCF appears extremely broadened. Since we are working close to the noise level, this result indicates that the FWHM of the CCF is strongly affected by noise. Note that this effect was not identified when recovering artificial signals from noiseless CCFs (i.e., pure Gaussian functions) to test the recovery algorithm (see previous Section), which supports the assumption that the broadening is noise-related.

The tests we have performed make us confident on the validity of the detection. However, the amount of structured noise that can be seen on the recovered planetary CCF (Figure 5.4) suggest that the parameters of the recovered planetary CCF might not all be reliable to derive physical parameters for the planet. In summary, the results presented in the previous paragraph suggest that:

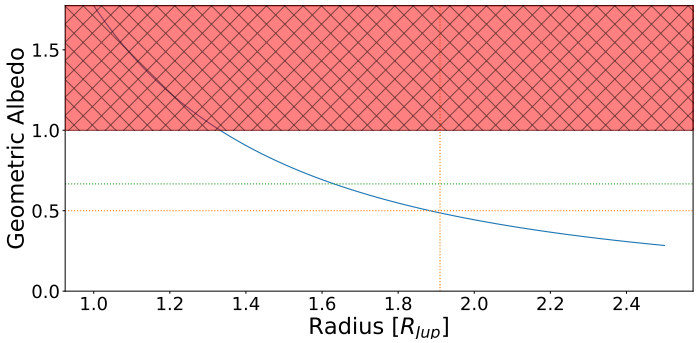

Figure 5.8: Possible albedo values for the detected signal for a range of planetary radii between 1 and 2.5 Jupiter radius. The red region corresponds to albedo values above unity and thus nonphysical. The green line corresponds to an albedo of 2/3, corresponding to a Lambert sphere. The orange lines correspond to the albedo ($A_g = 0.5$) and radii ($R_p = 1.9$) we chose.

- the amplitude of the injected signals was always recovered correctly, suggesting that the impact the structured noise on the recovered amplitude of the planetary CCF for 51 Pegasi b is negligible;
- the recovered simulated signals would always appear significantly broadened, meaning that the structured noise on the recovered planetary CCF impacts severely the FWHM of the planetary signal. Therefore, we believe that the FWHM of the recovered signal is not reliable to derive physical parameters of the planet (e.g. the rotation of the planet Kawahara, 2012; or atmospheric winds Snellen et al., 2010).

Therefore, when computing the planet-to-star flux ratio, we chose to ignore the broadening of the CCF and compute it from the ratio of the amplitudes of the planetary ($6.0 \pm 0.4 \times 10^{-5}$) and stellar signals ($0.48$), yielding $\frac{F_p}{F_*} = 1.25 \times 10^{-4}$ (see Table 5.4). Figure 5.8 shows the possible albedo values as a function of the planetary radius in the $[1 - 2.5]\ R_{Jup}$ range. These were computed for a phase function $g(\alpha) = 0.87$, the average value for the phase functions corresponding to the observations used in recovering the signal. The red region corresponds to nonphysical albedo values, i.e., above unity. Note that for a Lambertian sphere (i.e., the planetary surface reflects isotropically in all directions), it has been shown that the the planetary albedo will not be larger than $2/3$ (Tiatco, 2016). For that value of the albedo, 51 Pegasi b would have a radius of $1.6 \pm 0.2\ R_{Jup}$ (the error bars on the radius were estimated from the error in the CCF amplitude). In the Solar System, cloud covered planets have been shown to behave as Lambertian surfaces (e.g., Venus - see Knutson, 2013), making this assumption plausible should 51 Pegasi b be covered with clouds. To have a higher value of the albedo would imply for the planet to be strongly back-scattering which although physically plausible (Buratti et al., 1990, e.g. the saturnian satellites Mimas, Enceladus and Thetys) is highly unlikely due to the low ice content of hot Jupiters. Planets with no or thin atmospheres tend to reflect more uniformly (e.g., the Earth and the Moon - see Knutson, 2013) than Lambertian surfaces. If we assume a geometric albedo of 0.5, the radius of the planet will increase to $1.9 \pm 0.3\ R_{Jup}$. Such a large radius is not uncommon and has been observed in other highly inflated hot Jupiters with similar masses (e.g. WASP-17 b with $\sim 2R_{Jup}$ Anderson et al., 2011; HAT-P-67 b with $\sim 2.1R_{Jup}$ Zhou et al., 2017; Kepler-12 b with $\sim 1.7R_{Jup}$ Fortney et al., 2011), making this notion plausible.

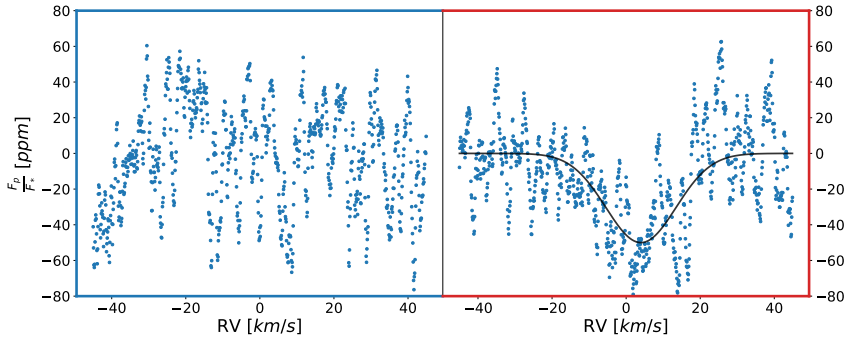

Figure 5.9: Recovered signal for $K_p = 132$ km/s with the *blue mask* (left panel) and the *red mask* (right panel). The grey line on the right panel corresponds to the best-fitting Gaussian profile.

A COLOR-DEPENDENT ALBEDO?

As mentioned previously, the albedo function from an exoplanet is a quantity highly dependent on a the composition of its atmosphere and its wavelength dependence can be used to hint at possible compositions. As such, we decided to probe further at the HARPS observations of 51 Pegasi b and check if it was possible to find some color dependency on the recovered albedo.

To do so, we divided the $G2$ spectral mask into two sub-masks: the *red mask* covering a spectral range from 462-nm to 680-nm and the *blue mask* covering a spectral range from 378-nm to 462-nm. Each sub-masks is composed of about 2000 spectral lines.

The recovery procedure for the signal was the same as the one used previously to recover the broadband reflected signal of 51 Pegasi b, assuming a semi-amplitude for the planet of $K_p = 132 km/s$. Figure 5.9 shows the recovered signal with both masks. No signal was detected on the CCF computed with the *blue mask* (left panel). With the *red mask*, a signal is detected with a $2.4 \pm 0.1\sigma$ significance. The best fitting Gaussian profile to this signal (in grey) has an amplitude of $5.0 \pm 0.2 \times 10^{-5}$ and a FWHM of 22.3 ± 1.2 km/s, similar to the signal recovered with the standard $G2$ mask.

A few interesting considerations can be made from these results. Firstly, it appears that the majority of the planetary reflected flux originates in the redder regions of the spectrum. It is known that spectrographs are more sensible towards redder wavelengths than in the bluer regions. As such, it is possible that the signal is still present on the bluer regions – with a similar amplitude as the signal in redder wavelengths – but below the detection threshold and hidden amidst the noise. It can be seen clearly that the noise amplitude on the right panel is significantly larger than for the left panel. Also, the reduction in detection significance from using the *red mask* (∼2000 lines) instead of the standard *G2* mask (∼4000 lines) is close to the expected from halving the number of lines of the CCF computation (1.54 against $\sqrt{2}$). However, the significance of these results is not high enough to be conclusive.

To study this result in more detail, we have submitted a proposal additional observation of the 51 Pegasi system with HARPS (ESO Program ID: *0101.C-0106*). The additional time totals 27.5h, that combine with the

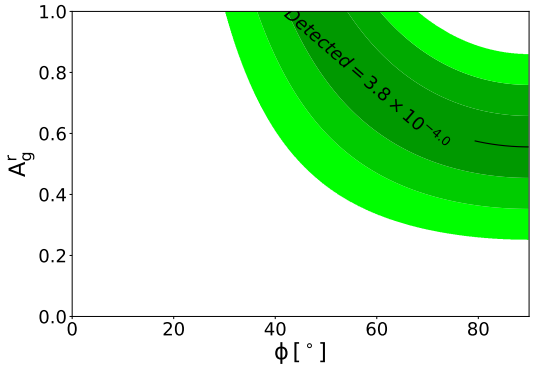

Figure 5.10: Possible ϕ-albedo configurations for a planet with $R_p = 1R_{Jup}$ and rings within $1-3\ R_{Jup}$. ϕ represents the rings/orbit misalignment. The green gradient corresponds respectively to the 1,2 and 3-σ confidence levels on the recovered flux.

data from ESO's programme *091.C-0271* should enable to reach a S/N on the CCF around 5300. After the albedo recovery process we should be able to reach a final S/N of around 150 000. This data should permit to recover (or at least put an upper limit) down to a geometric albedo of ~ 0.09 with a 3σ confidence over 3 wavelength subsets of the HARPS spectral coverage. Although not enough for a detailed characterization of the planet's atmosphere, these 3 albedo measurements should permit to probe the impact of the sodium doublet at 589-nm and the cloud coverage of the planetary atmosphere. At the moment of writing, ESO still hasn't released the results regarding observing call P101.

EXOPLANETARY RINGS?

It is possible that the recovered broadened FWHM of the CCF is of physical origin, and not the result of noise as proposed in Section 5.1.6. In this case, computing the planet-to-star flux ratio from the ratio of the areas of the planetary and stellar CCFs yields $\frac{F_p}{F_*} \approx 3.8 \times 10^{-4}$. To explain such a high flux, Santos et al. (2015) proposed that a large system of misaligned rings would orbit 51 Pegasi b. Figure 5.10 shows possible ϕ-albedo configurations for a planet with $R_p = 1R_{Jup}$ and rings within $1-3\ R_{Jup}$. ϕ represents the rings/orbit misalignment. The green gradient corresponds respectively to the 1, 2 and 3-σ confidence levels on the recovered flux.

However, dynamical analysis of the system suggest that for tidally locked hot Jupiter planets (such as 51 Pegasi b), it is highly unlikely that the rings will be misaligned with the orbital plane. A rings system co-planar with the planetary orbit is insufficient to explain the measured flux. No alternative physical mechanism has been proposed to explain such a high flux.

PLANETARY CCF OFFSET

A visual analysis of Figure 5.4 suggests that the planetary signal could be red-shifted $\sim 5km/s$ from the expected location for the real orbital semi-amplitude ($RV = 0$). It is enthralling to search for plausible physical origins for this offset: (i) high-speed winds from the day-side to the night-side due to the temperature gradient (e.g. Miller-Ricci Kempton et al., 2012); (ii) observational bias from stacking observations all on the same side of the superior conjunction (see Figure 5.2); (iii) a higher contribution of noise in the redder parts of the CCF.

A similar offset was found in HD 189733 b, where Wyttenbach et al. (2015) used to identify a $\sim 8km/s$ blue-shift of the sodium doublet (590-nm) in the planetary atmosphere. This value was later revised by Brogi et al. (2016), who found a blue-shift of $\sim 1.7km/s$ on the planetary signal from CRIRES observations of the planetary transit. Snellen et al. (2010) have also detected $\sim 2km/s$ blue-shift of the carbon monoxide signal from transit observations of HD 209458 b with CRIRES. In the case of transmission spectra – which observe the terminator region of the atmosphere – this genre of offset on transmission spectra has been predicted by theoreticians (e.g. Kempton et al., 2014, propose net blue-shifts of up to $3km/s$). When looking at reflected light, we are observing the other side of the orbit and thus the signal appear red-shifted, in concordance to what we apparently detected in 51 Pegasi b. However, the observed red-shift is larger than the expected $\sim 3km/s$, which could be attributed the large amount of noise seen on the planetary CCF.

UVES OBSERVATIONS OF 51 PEGASI B 5.2

To test if a color-dependency could be found in the reflected signal of 51 Pegasi on its orbiting planet, we acquired UVES observations of the the system. Being mounted on a larger telescope, UVES should be able to recover the reflected light from 51 Pegasi b on a much larger S/N domain, and thus allow for the recovery of the wavelength dependency of the albedo.

Our data was collected with the red arm of UVES spectrograph at ESO's Very Large Telescope at La Silla-Paranal Observatory, as part of ESO programme 093.C-0929. It consists of 575 spectra (resolution: 110 000) observed in five different nights adding up to slightly over 8 h of observing time. These observations were split into several carefully selected time windows in which the planet could be observed close to superior conjunction (i.e. when the day side of the planet is facing us) in order to maximise the planet's flux (maximum phase). These time windows were computed from the ephemeris provided by Butler et al. (2006). The obtained individual spectra have a S/N that varies between 130 and 363. The spectra cover the wavelengths range from roughly 450-nm to 750-nm. Table 5.5 summarizes the parameters of the collected observations. More detailed information can be found in Table B.2.

DATA REDUCTION 5.2.1

To be able to recover the reflected light spectrum of the exoplanet, we require 2-dimensional wavelength-calibrated spectra of our target. Our first reduction was performed with ESO Reflex Environment (Freudling et al., 2013), which by default returns 1-dimensional wavelength and flux calibrated spectra of point-like objects (see `http://www.eso.org/sci/observing/phase3/data_releases.html#idps`). Using the default 1-dimensional spectra would cause i) loss of spectral information and ii) possible errors in the computation of the CCF in the "stitching" regions of the spectra. Note that it is possible to force this software to produce the 2-dimensional spectra by hacking some of the data reduction recipes and actors in the graphical reduction pipeline of ESO Reflex Environment.

We also tested reducing the data with Gasgano and ESORex (ESO Recipe Execution Tool), two alternative data reduction packages provided by ESO that work as wrappers for ESO's data reduction recipes. Both these packages permit great control over the data reduction procedure by permitting to fine-tune every parameter in the process. However, they do not permit an easy automation of the data reduction process, which is essential for the number of spectra we acquired. Ultimately we chose to create our own data reduction pipeline in python that uses the *python-cpl* libraries to interface directly with ESO's CPL (Common Pipeline Library) recipes. This strategy combines the possibility to automate the data reduction process for a large number of observations with the high-degree of customization resulting from interfacing directly with ESO's CPL recipes to reduce the UVES data. This method permits two different approaches: i) run the *red chain* recipe that would perform the whole reduction; ii) perform a step-by-step data reduction using the individual data reduction recipes. We chose the latter approach as it permits complete control over the whole data reduction process. Table 5.6 shows the reduction steps, as well as the ESO CLP recipes in the order they were used and the settings we found more adequate for our study.

When performing the flat-fielding of the science raw spectra, the UVES reduction recipes will remove the instrumental profile (blaze function) information from the spectra. This means that the reduced spectra will have an apparent flux variability that is not physical as we get closer to the edges of each order. Furthermore, the correction of the blaze function will give incorrect weights to the spectral lines closer to the edges when computing

Night	Number of spectra	Total exposure [seconds]	S/N range L-side	S/N range R-Side
2014-07-31	49	1127	126-181	138-181
2014-08-17	107	7875	129-223	148-253
2014-08-25	177	8058	113-223	130-255
2014-09-28	198	7242	126-214	147-247
2014-10-28	44	4779	199-312	229-363

Table 5.5: Description of the available data on a per night basis. The S/N columns correspond to the S/N at the central wavelength of order 104 ($\lambda = 587.22$-nm) for the L-side of the spectrograph and order 128 ($\lambda = 477.14$-nm) for the R-side.

Step	CLP recipes	Description
1. Master Bias	$uves\_cal\_mbias$	default settings
2. Order definition	$uves\_cal\_predict$ $uves\_cal\_orderpos$	default settings
3. Wavelength Solution	$uves\_cal\_wavecal$	default settings
4. Science Data Reduction	$uves\_obs\_scired$	Flatfield removal was performed in pixel-space instead of spectral space, as the later introduced additional noise. All other setting were kept at their default values.

Table 5.6: Reduction steps with used CLP recipes and adopted settings.

the CCF. To mend this issue, we used the extracted reduced master flat functions for each order to reconstruct the blaze function, i.e., the instrumental profile of the instrument on each order. These were constructed by performing a moving average over the extracted flat function for each order with a window of 100 pixels in the spectral space. This permits to recover the blaze function of the instrument for each order, by smoothing the flat function over a 100 pixels region in the spectrum space to discard local defects (e.g., due to bad pixels). Each 2-dimensional spectrum was then multiplied by the reconstructed blaze function.

THE CROSS CORRELATION FUNCTION 5.2.2

As done for many years to compute precise radial velocities, we require to cross correlate our spectra with a binary mask that contains the rest wavelengths of thousands of spectral lines across the spectrographs wavelength coverage. Initially we attempted to use the cross correlation recipe from the HARPS DRS on our UVES data. Unfortunately,this approach required that the headers of the FITS files would have to be heavily modified. Thus we decided to implement our own cross-correlation recipe, which is similar to the one implemented for HARPS (see Baranne et al., 1996). We defined our cross-correlation function for a given order $order$ as follows:

$$CCF_{order} = \sum_{lines,order} \left(d_{line} \times \sum_{pixels} \left(f_{line,pix}\, F_{line,pix} \right) \right) \tag{5.3}$$

where d_{line} is the depth of the selected line (from the mask), $pixels$ represents the list of spectral pixels covered by the selected line, $f_{line,pix}$ the fraction of the pixel that falls on the line, $F_{line,pix}$ the flux of the line for each pixel (from the spectrum).

For the spectral binary mask, we used the *new_G2* mask from the HARPS DRS (Mayor et al., 2003) version 3.6. Although originally built to be used with HARPS data, the wavelength coverage of both instruments is similar

enough ([450-750]nm for UVES, against [378-691]nm for HARPS) that the same masks can be used (albeit at the expense of loosing some spectral information). Figure 5.11 shows the CCF applied to two different orders from the red chip of one of the observations.

RESULTS AND DISCUSSION 5.2.3

After applying the recovery procedure presented in Chapter 4, the noise level attained on the UVES data was found to be much higher than the one achieved with the HARPS data, regardless of the larger collecting area of the VLT relatively to ESO's 3.6m telescope. The main reason appears to come from unexpected noise structures that appear on the CCF from the individual observations. This can be seen in Figure 5.11b, were some dips with amplitude comparable to the stellar CCF can be seen.

At the moment we do not know the origin of these structures – which will require additional attention – although in continuation of this work we intend to test for

1. the impact of telluric lines in the spectrum;
2. inner reflections in the instrument that might cause ghosts on the CCD;
3. the possibility for an erroneous wavelength calibration solution of the UVES spectrograph as proposed by Whitmore et al. (2010):
4. the impact of an imperfect flat-filed correction and
5. the impact of instrumental drift on our observations.

Understanding possible sources of noise is of great importance for future reflected light studies as we are looking for signals close to the noise limit of current observing facilities.

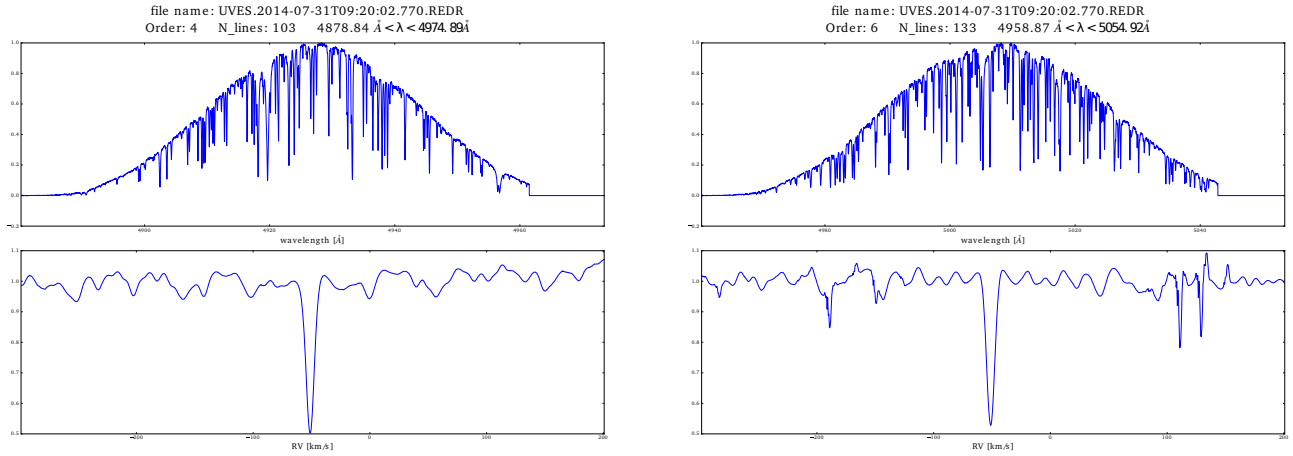

(a) Order 4 of one of the UVES observations **(b)** Order 6 of one of the UVES observations

Figure 5.11: Orders 4 and 6 of the UVES spectra. On both figures the top panel shows the 1D extracted spectrum and the bottom panel shows the resulting CCF.

Chapter 6.
Prospects for next-generation observing facilities

The next generation of high-resolution extremely stable spectrographs to be installed at 10-m and 40-m class telescopes presents a unique opportunity for exoplanet atmospheric characterization. The combination of a HARPS-like stability with the increased collecting power of larger telescopes should enable to probe exoplanets and their atmospheres in great detail.

With this in mind, we studied the potential of both ESPRESSO@VLT and HIRES@ELT in the recovery of the color-dependent reflected spectrum from exoplanets using the CCF technique and distinguish between possible atmospheric models. Additionally, we explored the possibility of recovering the reflected signal from exoplanets currently known to be inside their hosts Habitable Zone.

EXOPLANETARY ALBEDOS WITH ESPRESSO AND HIRES 6.1

The goal of this project was the recovery of the wavelength dependence of the albedo from high-resolution observations of prototypical single planet systems with both ESPRESSO@ESO's VLT and HIRES@ESO's ELT (see Section 3.2 for a description of the instruments). In terms of targets, we chose to simulate known single planet systems that would represent the following planet classes: i) hot Jupiters, ii) hot Neptunes and iii) short-period super-earths.

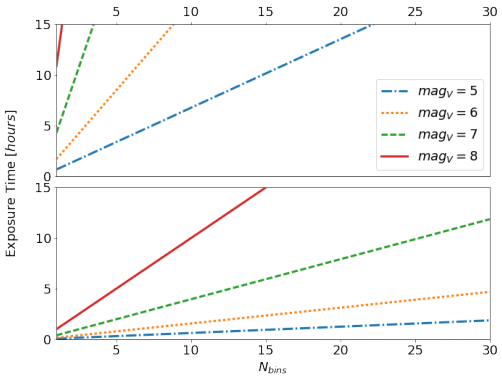

Figure 6.1: *Top Panel:* Estimated exposure times for the recovery of the grey albedo function ($A_g = 0.2$) for a 3-day period hot Jupiter with a radius of 1.2 $\mathrm{R_{Jupiter}}$ from ESPRESSO observation (HR mode) as a function of N_{bins} and of the host's magnitude. *Bottom Panel:* Same as top panel, but for HIRES observations (from Martins et al., 2017).

SAMPLING OF THE RECOVERED ALBEDO FUNCTION 6.1.1

For each planet class, we defined a fixed number N_{bins} of wavelength bins (i.e.,the number of wavelength subsets of the full coverage of the chosen spectrograph) for which the albedo will be recovered using the CCF technique. The number of wavelength bins selected for each planet type needs to balance the required exposure time and sampling of the recovered albedo function. Figure 6.1 shows on the top panel the estimated required times to recover the albedo function of a prototypical hot Jupiter ($p = 3\ days$; $R_P = 1.2 R_{Jupiter}$; grey albedo with $A_g = 0.2$) with ESPRESSO (HR mode), as a function of N_{bins} and different visual magnitudes of the host star. The bottom panel shows the same, but from HIRES observations.

Too high a value for N_{bins} and the exposure time cost will be prohibitively high (e.g., for $N_{bins} = 25$ the required S/N to recover the reflected light spectrum from the above target is close to 800 000). For a $mag_V = 8$ star this requires over 100 hours of ESPRESSO time. Too low a value for N_{bins} and the level of detail of the recovered albedo function will be too low to distinguish between possible albedo models. Note that $N_{bins} = 1$ corresponds to the work presented in Martins et al. (2015a).

As such, for simulated observations of hot Jupiters with ESPRESSO we settled on 15 wavelength bins for the recovered albedo function. For simulated observations with HIRES we selected i) 70 wavelength bins for hot Jupiters; ii) 6 wavelength bins for hot Neptunes and iii) 5 wavelength bins for Super-Earths. We believe these values to yield a good balance between exposure time and the level of detail in the recovered albedo function. Note that the proposed values of N_{bins} are just for this exploratory work, for real observations we would attempt different values for N_{bins} and try to maximize the level of detail on the recovered albedo function. Once the signal of an exoplanet is detected at 3-σ, we passed the detection threshold, and the significance for a detection on a different N_{bins} value or integration time can be calculated by scaling from the presented values.

ESTIMATING THE EXPOSURE TIME 6.1.2

The computation of the exposure time required to recover the albedo from an exoplanet involves the estimation of the planet-to-star flux ratio ($F_\star/F_p$, see Equation 2.1) of the planet over the selected phase range of the observations. To do so, we assumed for each selected planet: i) an average Lambertian phase function $g(\alpha) \approxeq 0.87$; ii) a grey albedo with $A_g = 0.2$; iii) the planetary radius R_p, and semi-major axis a from the exoplanet.eu database[1].

Under the above assumptions, the signal-to-noise ratio required ($SN_{required}$) to recover the planetary signal at a 3-σ_{noise} significance is given by

$$SN_{required} = \frac{3}{\frac{F_p}{F_\star}} \tag{6.1}$$

The S/N that can be achieved with both our simulated instruments was extrapolated from the S/N that can be accomplished with HARPS ($SN_{HARPS}(\lambda)$) given the same parameters. $SN_{HARPS}(\lambda)$ was estimated with HARPS ETC[2] version P100.2.

Note that all simulated targets are bright ($V_{mag} < 8$). As such, to avoid saturation and ensure linearity of the instrument, we fixed the individual exposure time in the ETC to 300s. For reference, for our brightest star – 51 Pegasi with $V_{mag} = 5.49$ – in 300s we only reach about 65% of the detector's saturation limit per pixel, a regime where the detector is still linear. The stellar parameters for each target were obtained from the exoplanet.eu database. The values for the other customized parameters of the ETC are shown in Table 6.1. The parameters not in the Table were left to their default values.

The S/N that can be obtained with either ESPRESSO or HIRES can be extrapolated from $SN_{HARPS}(\lambda, t)$

Parameter	Value
Target Input Flux Distribution	
Template spectrum	G2V (Kurucz)
Sky Conditions	
Moon phase	3 days
Airmass	1.2
Seeing	0.8
Instrument Setup	
Exposure Time	300 s

Table 6.1: HARPS ETC settings. The settings not in this table were left to their default values.

[1] Note that we intend to simulate known prototypical planets from the exoplanet.eu database.

[2] `https://www.eso.org/observing/etc/bin/gen/form?INS.NAME=\gls{harps}+INS.MODE=spectro` with HARPS User Manual, Issue 2.1, October 1st 2011 - `https://www.eso.org/sci/facilities/lasilla/instruments/harps/doc.html`

with

$$SN_{instrument}\left(\lambda,t\right)=\sqrt{A\times E\left(\lambda\right)}\,SN_{HARPS}\left(\lambda,t\right) \tag{6.2}$$

where $SN_{instrument}\left(\lambda\right)$ is the expected wavelength dependent S/N for the simulated instrument . A is the ratio of the collecting areas for the selected facility and HARPS 3.6m telescope ($A\approx 5.4$ for ESPRESSO@VLT (HR mode) and $A\approx 117.4$ for HIRES@ELT). $E\left(\lambda\right)$ is a scaling factor to account for the different wavelength dependent efficiencies between the ESPRESSO/HIRES and HARPS.

For ESPRESSO, this scaling factor is defined as

$$E\left(\lambda\right)=\frac{Eff_{ESPRESSO,mode}\left(\lambda\right)}{Eff_{HARPS}\left(\lambda\right)} \tag{6.3}$$

where $Eff_{ESPRESSO,mode}\left(\lambda\right)$ and $Eff_{HARPS}\left(\lambda\right)$ are respectively the efficiency of ESPRESSO for each mode (see Figure 3.7) and of the HARPS spectrograph. Note that for all 3 resolution modes of ESPRESSO, when estimating the required exposure time we assumed the same efficiency profile as HR mode. This will allow to compare the impact of the resolution on the error bars from the recovered albedos. However, when constructing the simulations (see Section 6.1.5), each mode will have the efficiency profile presented in Figure 3.7. In the case of HIRES, no efficiency profile is yet available and thus we assumed a HARPS-like efficiency (i.e., $E=1$). This assumption is reasonable as HARPS is the spectrograph that has its efficiency measured with the highest precision.

By using the CCF technique, the S/N of the observations will be increased by a factor proportional to the square root of the number of spectra lines used in the correlation. Since we intend a 3-σ detection per bin, we assume that the increase in SN per bin is proportional to the average number of spectral lines per bin and as such

$$\left\langle SN_{instrument,bin}\left(300s\right)\right\rangle=\left\langle SN_{instrument}\left(300s\right)\right\rangle\sqrt{\frac{N_{lines}}{N_{bins}}} \tag{6.4}$$

where $\left\langle SN_{instrument,bin}\left(300s\right)\right\rangle$ is the average SN per wavelength bin that can be achieved with the selected instrument after a 300s exposure with the cross correlation technique.

Therefore, the total exposure time t_{total} required to achieve $SN_{required}$ is given by:

$$t_{total}=300s\times\left(\frac{SN_{required}}{\left\langle SN_{instrument,bin}\left(300s\right)\right\rangle}\right)^{2} \tag{6.5}$$

	M_p $[M_{Jup}]$	R_p $[R_{Jup}]$	P $[days]$	a $[A.U.]$	k_p $[km/s]$	I $[degrees]$	$\left(\frac{R_p}{a}\right)^2$ $[ppm]$
51 Peg b	0.47	1.90	4.2	0.051	130.8	80.0	315
HD 209458 b	0.69	1.38	3.5	0.045	137.2	86.6	212
HD 109749 b	0.28	0.99	5.2	0.059	109.7	90.0	64
HD 76700 b	0.23	0.99	4.0	0.049	120.4	90.0	93
55 Cnc e	0.03	0.18	0.7	0.016	128.8	85.4	28

Table 6.2: Orbital parameters for simulated planets (from Martins et al., 2017).

TARGET SELECTION 6.1.3

Our initial pre-selection consisted in all the planet from the exoplanet.eu database orbiting FGK dwarfs with $V_{mag} \leq 10$ in under 10 days and have measured radii that are observable from ESO's La Silla-Paranal Observatory (i.e., whose host has a declination $-50^\circ < \delta < 20^\circ$). For all targets that met these criteria, we estimated the required exposure time to recover the albedo function from the planet (see Section 6.1.2 for a detailed description on how the required time was computed) assuming a grey albedo – i.e. wavelength independent – with $A_g = 0.2$. We also limited our list to target which could be detected within reasonable times ($t < 30h$ or $\sim$ 3 nights). The complete target lists can be found on Appendix A.

Of the resulting planet sample we selected a few targets which we consider representative of the different exoplanet types:i) two hot Jupiters – 51 Pegasi b, HD 209458 b – to be observed with both instruments[3]; ii) two hot Neptunes – HD 109749 b, HD 76700 b – to be observed with HIRES and iii) one super-earth – 55 Cnc e – to be observed with HIRES. Table 6.2 presents the orbital parameters for the selected planetary systems and Table 6.3 shows the parameters for their hosts.

The observational parameters for the simulated observations of our sample are presented in Table 6.4. For each target, we define one observing run as a of set of simulated observations whose cumulative exposure times

	$M_\star$ $[M_\odot]$	$k_\star$ $[m/s]$	T_{eff} $[K]$	Spectral Type	V_{mag}
51 Peg	1.11	52.9	5793	G2 IV	5.5
HD 209458	1.15	78.7	6092	G0 V	7.7
HD 109749	1.20	24.4	5610	G3 IV	8.1
HD 76700	1.00	26.4	5726	G6 V	8.1
55 Cnc	0.91	3.6	5196	K0IV-V	6.0

Table 6.3: Parameters for simulated hosts (from Martins et al., 2017).

[3]Selecting the same targets for instruments allows to compare the effect of an increased telescope size on sampling of the recovered albedo function.

	$\left(\frac{R_p}{a}\right)^2$	t_{exp}	$\langle S/N \rangle$	t_{total}	$\mathrm{N_{bins}}$
	$[ppm]$	$[seconds]$		$[hours]$	
ESPRESSO (all modes)					
51 Peg b	315	36	330	1.0	15
HD 209458 b	212	432	430	12.0	15
HIRES					
51 Peg b	315	36	1100	1.0	70
HD 209458 b	212	188	930	5.2	70
HD 109749 b	64	263	890	7.3	6
HD 76700 b	93	130	610	3.6	6
55 Cnc e	28	153	1850	4.25	5

Table 6.4: Parameters for simulated observing runs (from Martins et al., 2017).

is given by t_{total}. We fixed a minimum observing time of 1h, which corresponds to the maximum time length of one observing block with ESO instruments.

The simulation of observations and the computation of the CCF is computationally expensive and as such it is advisable to keep the number of simulation to a minimum to minimize the computational effort. However, as discussed on Section 4.1.1, the stellar template used in the removal of the stellar signal from the observations requires a S/N at least 10 times higher that of the individual observations. This corresponds to a minimum of 100 individual exposures just to construct the template, a value adopted for the number of observations for each simulated observing run. Note that if we were dealing with real observations, the proposed individual exposure times might saturate the simulated instrument. However, we can safely assume that each individual simulated observation can be constructed by stacking individual observations with lower exposure times until the equivalent S/N is attained. To construct the template, we will not be simulating dedicated in-transit observations, but construct it by stacking the simulated observations as done in Chapter 5 (i.e., template T1 from Section 5.1.2).

CONSTRUCTING THE SIMULATED SPECTRA 6.1.4

Our simulations were constructed from the extremely high-resolution ($R = 500000$) solar spectrum available at `http://kurucz.harvard.edu/sun.html` (hereafter Kurucz spectrum – Kurucz, 2006). The Kurucz spectrum was degraded[4] to the resolutions of both ESPRESSO (all modes) and HIRES (see Section 3.2). For each individual observation, with a given orbital phase ϕ, the simulated spectra will have three main components: i) the stellar signal $S_\star(\lambda, RV_\star(\phi))$, ii) the planetary signal $S_p(\lambda, \phi)$ and iii) noise.

These three components were co-added to create the final spectra. We defined the spectral template in

[4]Our convolution code was adapted from `https://github.com/jason-neal/equanimous-octo-tribble/blob/master/IP_Convolution.py`.

terms of spectral order, coverage and in-order characteristic efficiency (i.e., the blaze function) for each simulated instrument to be the same as HARPS instrumental profile. On other words, the computed spectra are projected on a wavelength grid defined by the HARPS spectrograph instrumental profile. Additionally, each order is multiplied by HARPS blaze function $B(\lambda)$) to account for in-order sensitivity variations. The resulting spectra were saved in the standard fits format used for HARPS observations, which allowed to use *HARPS DRS vs 3.6* to compute the CCF for each observation.

THE STELLAR COMPONENT

The stellar spectrum has a continuum flux defined as $F_\star(\lambda)$. Since the Kurucz spectrum used to construct the observations is normalized in flux, its continuum $S(\lambda, RV = 0)$ need to be scaled in flux to match the expected continuum flux of the host star. For each observation

$$F_\star(\lambda) = A \times E(\lambda) \times F_{HARPS}(\lambda) \tag{6.6}$$

where $F_{HARPS}(\lambda)$ corresponds to the collected flux from the star collected by HARPS (estimated from HARPS ETC). Both A (ratio between the collecting areas of the simulated telescopes and ESO's 3.6m) and $E(\lambda)$ (ratio of the efficiencies of ESPRESSO/HIRES and HARPS) are the same scaling factors defined in Section 6.1.2.

For each planet+instrument configuration, HARPS ETC was used to estimate the stellar flux ($F_\star(\lambda)$) for each observation (column *Obj* for the central column of each order) assuming the parameters from i) Table 6.2 for the star; ii) Table 6.4 for the exposure time and iii) Table 6.1 for the remaining settings.

THE PLANETARY SPECTRUM

Since we are working at optical wavelengths, the planetary spectrum will basically be a scaled down copy of the stellar spectrum given by

$$S_p(\lambda, \phi) = \frac{F_p(\lambda, \phi)}{F_\star(\lambda)} \times S(\lambda, RV_p(\phi)) \tag{6.7}$$

where $RV_p(\phi)$ is the radial velocity of the planet for phase ϕ, $F_p(\lambda)$ is the flux reflected by the planet, and $\frac{F_p(\lambda,\phi)}{F_\star(\lambda)}$ is computed from Equation 2.1.

Each individual observation was assigned a random orbital phase between 15 and 45 degrees on each side of opposition/superior conjunction. This choice of phase balances the need to collect as much flux as possible from the planet and the ability to spectroscopically resolve the stellar and planetary signals (see Section 4.1.1). The phase function $g(\alpha)$ was assumed for our observations a Lambertian (see Equation 2.2)

The main goal of this project is to test the CCF method to recover the color dependence of the reflected optical spectrum from an exoplanet. In particular, we are interested in the ability of the CCF technique to distinguish between possible atmospheric models and hint at the composition of the simulated planetary atmospheres. This

led us to use albedo function models with real physical meaning to construct our simulated observations. These models were computed by our collaborator Antonio Garcia-Muñoz, which simulated two different configurations in terms of atmospheric composition (*Model A* and *Model B*). Additionally, each configuration was simulated for two different scattering scenarios ($\times 1, \times 100$). These models are described in detail in Appendix B. For each planet+instrument configuration, we simulated independent observing runs assuming a grey albedo $A_g = 0.2$ and two different albedo models from the ones presented in Appendix B.

THE NOISE COMPONENT

For this study, we assumed the noise to be Gaussian with a mean of zero and a standard deviation of $\sigma = \sqrt{F_\star(\lambda_c)}$ as we are simulating extremely high signal-to-noise spectra and thus working in a photon noise limited domain (see e.g. Howell et al., 2000).

SIMULATIONS OVERVIEW 6.1.5

In total, we simulated ESPRESSO@VLT (in all 3 modes – MHR mode $R = 60000$, HR mode $R = 130000$ and UHR mode $R = 220000$) observations of 24 planet+star+instrument+albedo configurations, with an average S/N around $300 - 400$. For HIRES@ELT, we created 13 planet+star+instrument+albedo configurations, with an average S/N varying between 600 and 1800. The observational parameters for each observing run of each star+planet system are presented in Table 6.4. Note that although each ESPRESSO mode will have different efficiencies, the total exposure time for each star+planet system with ESPRESSO was set as the same for all modes.

For each planet+star+instrument+albedo configuration, we simulated 100 observing runs – each with the total exposure time presented in Table 6.2 – of 100 observations each. Table 6.5 summarizes the planet+star+instrument+albedo configurations that were simulated for this project.

RESOLUTION DEPENDENCE

Note that to test the impact of different resolutions/modes on the recovered albedos, we constructed additional simulated observations of the HD 209458 b system as observed with ESPRESSO in all 3 modes. Note that the MHR mode of ESPRESSO allows to combine incoherently the light from up to 4 of the UTs of VLT, and thus we simulated observations in this mode with 1, 2 and 4 UTs. For each star+planet+mode configuration we simulated 100 observing runs of 100 spectra with a total exposure time per run of 10h, independent of the simulated resolution mode. This ensures that the achievable S/N is much higher than the one required for a 3-σ per bin recovery of the reflected planetary signal, over 10 wavelength bins. For simplification purposes but no loss of generality, we assumed for all observations a grey albedo model with $A_g = 0.2$. The results of the recovery of the albedo function for these simulations will be discussed in Section 6.1.7.

Planet	Instrument	Mode	Albedo models
51 Pegasi b	ESPRESSO	HR mode	$A_g = 0.2$, Model A (x1,x100)
		MHR mode	$A_g = 0.2$, Model A (x1,x100)
		UHR mode	$A_g = 0.2$, Model A (x1,x100)
	HIRES		$A_g = 0.2$, Model A (x1,x100)
HD 209458 b	ESPRESSO	HR mode	$A_g = 0.2$, Model B (x1,x100)
		MHR mode	$A_g = 0.2$, Model B (x1,x100)
		UHR mode	$A_g = 0.2$, Model B (x1,x100)
	HIRES		$A_g = 0.2$, Model B (x1,x100)
HD 109749 b	HIRES		$A_g = 0.2$, Model A (x100), Model B (x100)
HD 76700 b	HIRES		$A_g = 0.2$, Model A (x1), Model B (x1)
55 Cnc e	HIRES		$A_g = 0.2$

Table 6.5: Summary of the simulated planet+star+instrument+albedo configurations.

RESULTS 6.1.6

For each configuration (see Table 6.5), we attempted the recovery of the reflected signal from the planet applying the methodology presented in Chapter 4 to each wavelength bin of each simulated observing runs independently. The wavelength bins were defined by dividing the wavelength coverage of HARPS into N_{bins} subsets with equal wavelength coverage (see Table 6.4, Section 6.1.3). Figure 6.2 shows the recovered planetary signal and albedo for simulated observations of the HD 209458 system over 15 contiguous wavelength ranges in the optical. The left panel shows the recovery planetary CCFs for each wavelength range. The right panel shows the recovered albedos for each range (orange dots) overlapped on the simulated albedo function (grey line). It is clear that the recovered albedo for each wavelength bin follows the simulated albedo curve.

The distribution of the recovered albedo values for each configuration permitted to estimate the 1-σ error inherent to the method. The recovered albedo distributions are presented in Figures 6.3 to 6.8 (from Martins et al., 2017). The green diamonds correspond do the mean of the recovered albedos for each wavelength bin, over all simulated observing runs for the selected configuration. The error bar corresponds to the 1-σ error bar of the distribution of the recovered albedos for each wavelength bin, over all simulated observing runs for the selected configuration. The blue horizontal lines represent the mean albedo for the simulated model over each wavelength bin. The horizontal orange lines correspond tot the upper limit for non-detection – or minimum detectable albedo – on each wavelength bin as 3 times the average noise across all 100 observing runs simulated per selected configuration. For the bins where the mean albedo from the model is lower than the minimum detectable albedo, we set the value for the recovered albedo as the upper detection limit (orange arrows).

For all configurations, we tested our recovered albedo function against all atmospheric models presented in

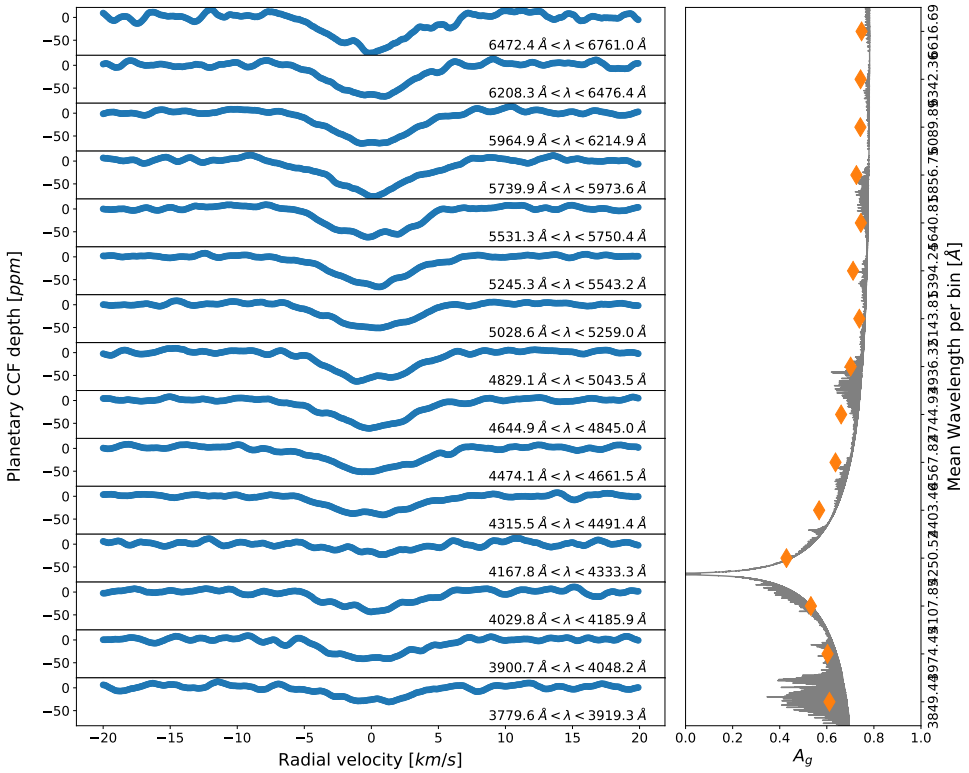

Figure 6.2: Example of a recovered albedo function from simulated observations of 51 Pegasi b with ESPRESSO*Left panel*: recovered planet CCFs for each wavelength bin. *Right panel*: Recovered albedo for each wavelength bin (in orange) versus the injected albedo model (grey line).

Appendix B plus a grey albedo with $A_g = 0.2$, with a simple reduced chi-squared (χ^2_ν) comparison. χ^2_ν was computed from:

$$\chi^2_\nu = \sum_{i=1}^{N_{bins}} \frac{1}{N} \frac{(< A_{measured,i} > - < A_{model,i} >)^2}{\sigma_i^2} \tag{6.8}$$

where $< A_{model,i} >$ is the mean of the simulated albedo function over the wavelength range covered by bin i; $< A_{measured,i} >$ is the mean of the measured albedo for wavelength bin i over all independent runs and σ_i is the standard deviation of the recovered albedos for all runs. The χ^2_ν results are presented in Tables 6.6 to 6.10. For each simulated configuration, the lowest reduced χ^2_ν value is highlighted with a red box.

Note that a different analysis using Akaike Information Criterion (AIC) or Bayesian Inference Criterion (BIC) could have been used to attempt to identify the correct simulated albedo model. However, the assumption of non-correlated noise makes it that the distribution of the recovered values for the albedo follows a normal distribution and consequently so does the likelihood. Furthermore, each model has the same number of parameters (in this case zero as we are comparing against a fixed albedo function). As a result the AIC/BIC values are only proportional

to the likelihood and therefore to the χ^2_ν value, being the analysis equivalent.

A visual inspection of Figures 6.3 to 6.8 shows that for each wavelength bin, the mean simulated albedo (horizontal blue lines) is within the 1-σ error bars of the recovered albedo functions and that in all cases the recovered albedo function is close to the simulated one. Furthermore, Tables 6.6 to 6.11 show that for each planet+star+instrument+albedo configuration – regardless of the simulated instrument or atmosphere – the lowest reduced χ^2 value (highlighted with a red box) occurs when the recovered albedo matches the simulated albedo function.

These results were accepted for publication in Montly Notices of the Royal Astronomy Society (MNRAS) as .

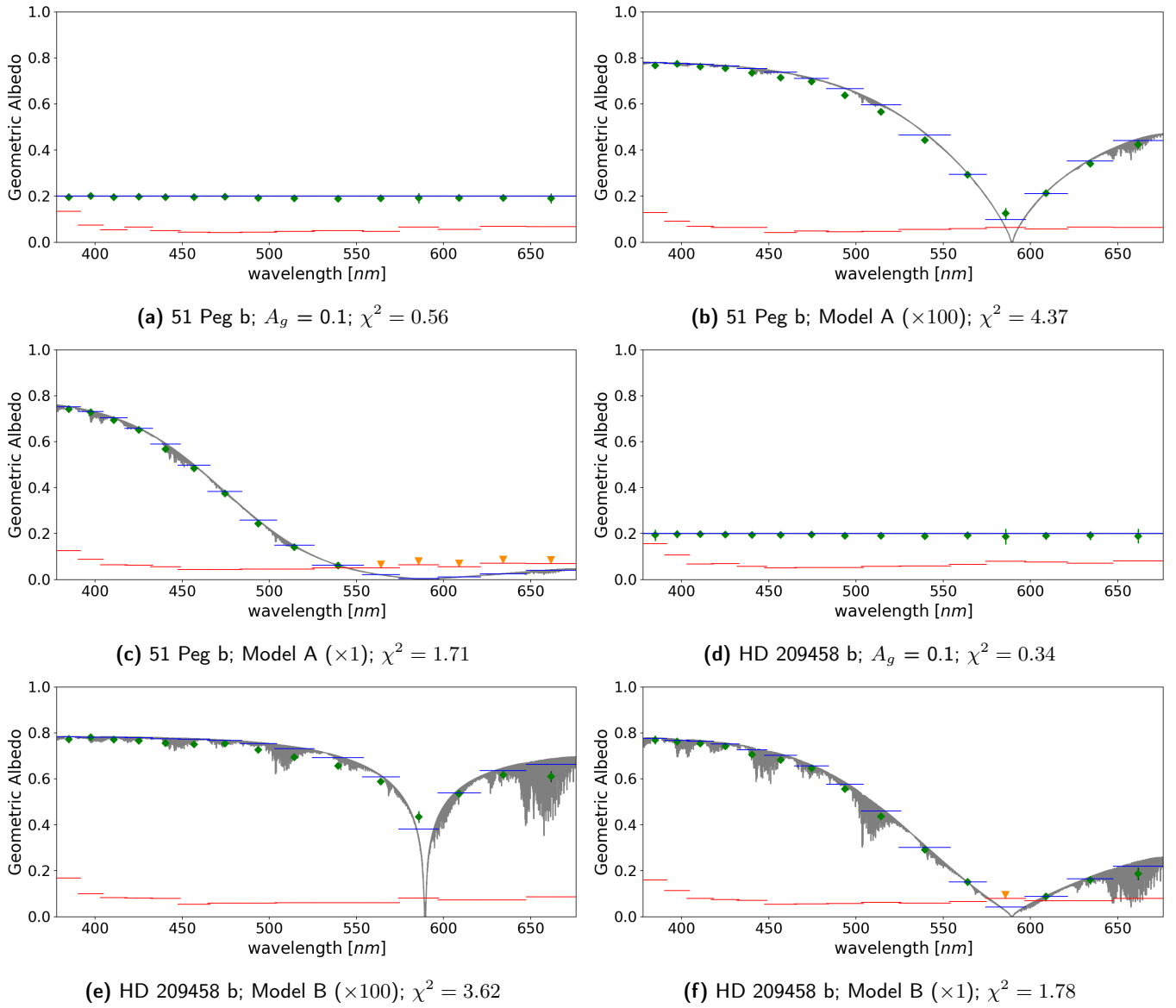

(a) 51 Peg b; $A_g = 0.1$; $\chi^2 = 0.56$

(b) 51 Peg b; Model A ($\times 100$); $\chi^2 = 4.37$

(c) 51 Peg b; Model A ($\times 1$); $\chi^2 = 1.71$

(d) HD 209458 b; $A_g = 0.1$; $\chi^2 = 0.34$

(e) HD 209458 b; Model B ($\times 100$); $\chi^2 = 3.62$

(f) HD 209458 b; Model B ($\times 1$); $\chi^2 = 1.78$

Figure 6.3: Distribution of the recovered albedo functions from the simulated ESPRESSO (HR mode) observations. For each wavelength bin: *i)* the green dots represent the mean recovered albedo over the 100 simulated runs with error bars given by their standard deviation; *ii)* the blue horizontal lines represent the mean albedo of the simulated model over the bin; *iii)* the orange horizontal bar represents the 3σ detection limit of the albedo.

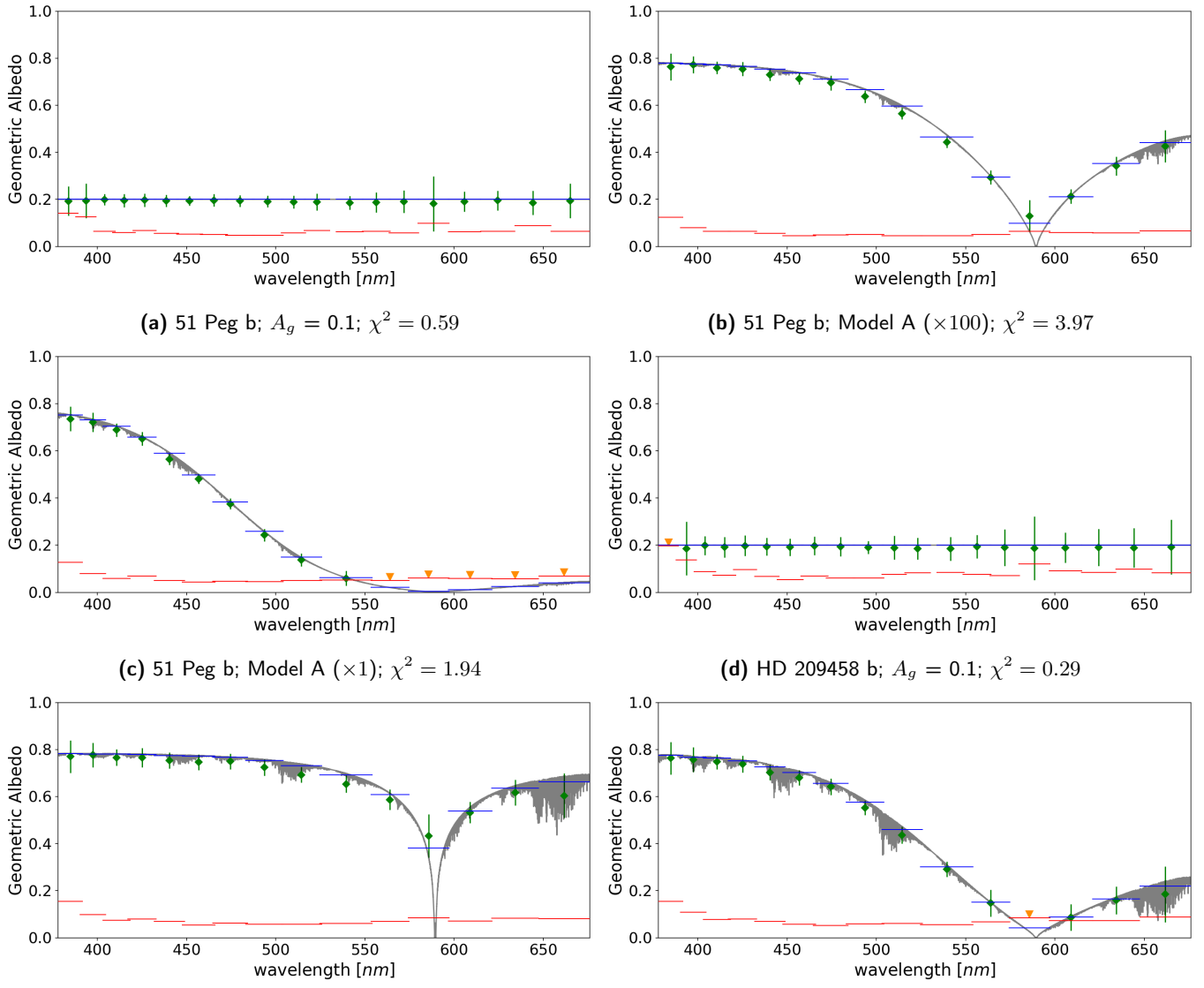

(a) 51 Peg b; $A_g = 0.1$; $\chi^2 = 0.59$

(b) 51 Peg b; Model A ($\times 100$); $\chi^2 = 3.97$

(c) 51 Peg b; Model A ($\times 1$); $\chi^2 = 1.94$

(d) HD 209458 b; $A_g = 0.1$; $\chi^2 = 0.29$

(e) HD 209458 b; Model B ($\times 100$); $\chi^2 = 3.51$

(f) HD 209458 b; Model B ($\times 1$); $\chi^2 = 1.72$

Figure 6.4: Distribution of the recovered albedo functions from the simulated ESPRESSO (MHR mode - 1UT) observations. For each wavelength bin: *i)* the green dots represent the mean recovered albedo over the 100 simulated runs with error bars given by their standard deviation; *ii)* the blue horizontal lines represent the mean albedo of the simulated model over the bin; *iii)* the red horizontal bar represents the 3σ detection limit of the albedo.

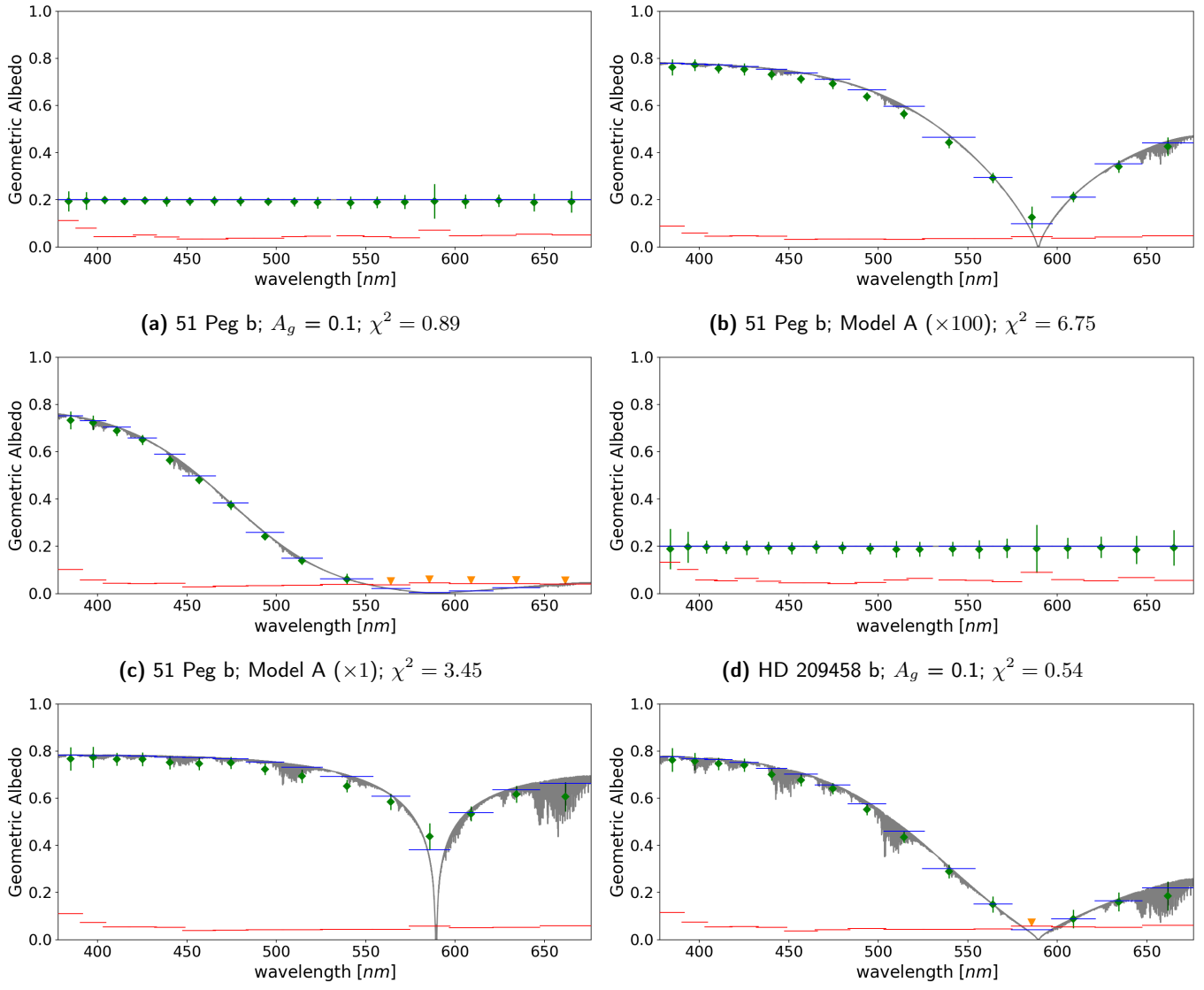

(a) 51 Peg b; $A_g = 0.1$; $\chi^2 = 0.89$

(b) 51 Peg b; Model A ($\times 100$); $\chi^2 = 6.75$

(c) 51 Peg b; Model A ($\times 1$); $\chi^2 = 3.45$

(d) HD 209458 b; $A_g = 0.1$; $\chi^2 = 0.54$

(e) HD 209458 b; Model B ($\times 100$); $\chi^2 = 6.68$

(f) HD 209458 b; Model B ($\times 1$); $\chi^2 = 3.44$

Figure 6.5: Distribution of the recovered albedo functions from the simulated ESPRESSO (MHR mode - 2UT) observations. For each wavelength bin: *i)* the green dots represent the mean recovered albedo over the 100 simulated runs with error bars given by their standard deviation; *ii)* the blue horizontal lines represent the mean albedo of the simulated model over the bin; *iii)* the red horizontal bar represents the 3σ detection limit of the albedo.

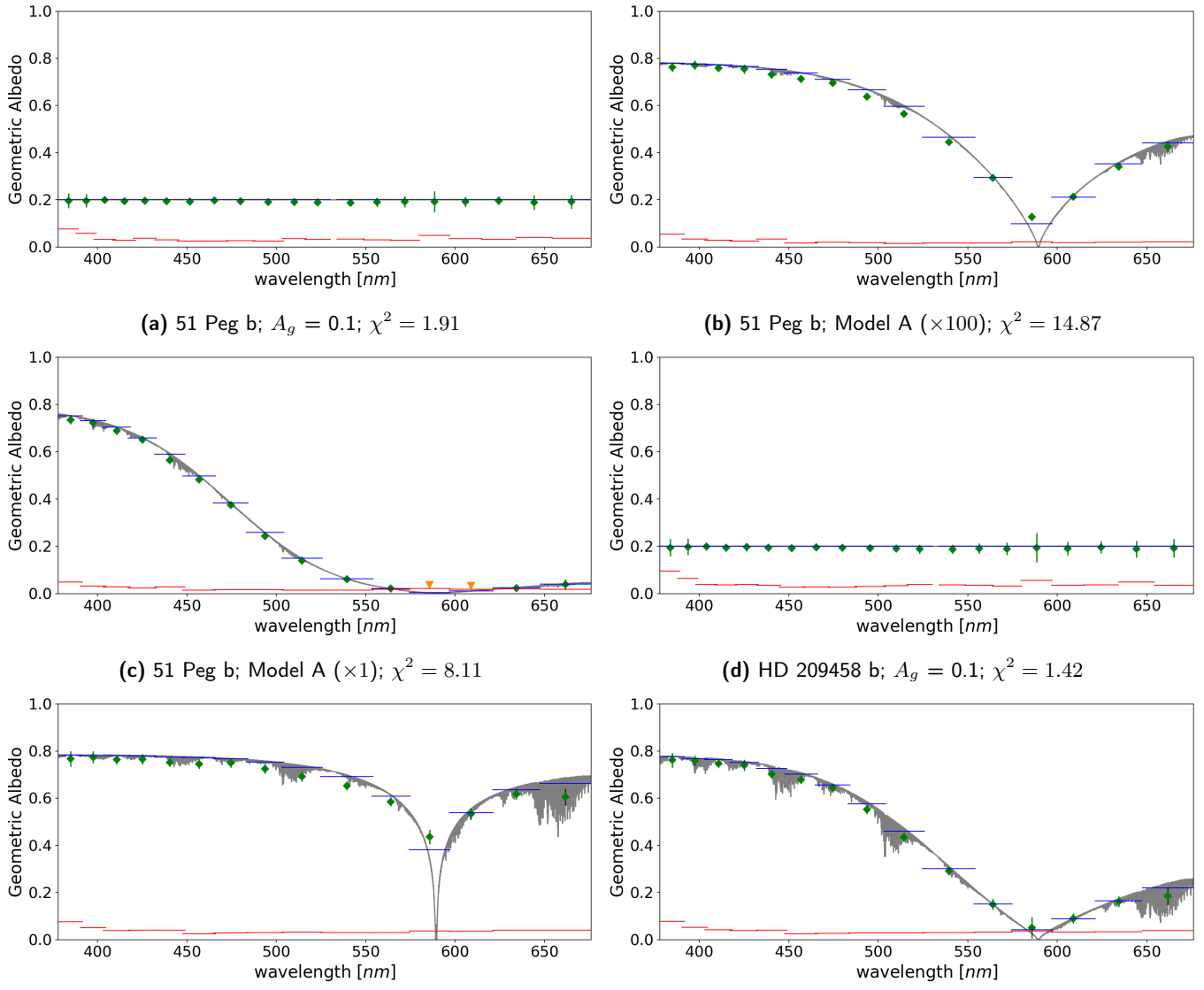

(a) 51 Peg b; $A_g = 0.1$; $\chi^2 = 1.91$

(b) 51 Peg b; Model A ($\times 100$); $\chi^2 = 14.87$

(c) 51 Peg b; Model A ($\times 1$); $\chi^2 = 8.11$

(d) HD 209458 b; $A_g = 0.1$; $\chi^2 = 1.42$

(e) HD 209458 b; Model B ($\times 100$); $\chi^2 = 13.79$

(f) HD 209458 b; Model B ($\times 1$); $\chi^2 = 5.98$

Figure 6.6: Distribution of the recovered albedo functions from the simulated ESPRESSO (MHR mode - 4UT) observations. For each wavelength bin: *i)* the green dots represent the mean recovered albedo over the 100 simulated runs with error bars given by their standard deviation; *ii)* the blue horizontal lines represent the mean albedo of the simulated model over the bin; *iii)* the red horizontal bar represents the 3σ detection limit of the albedo.

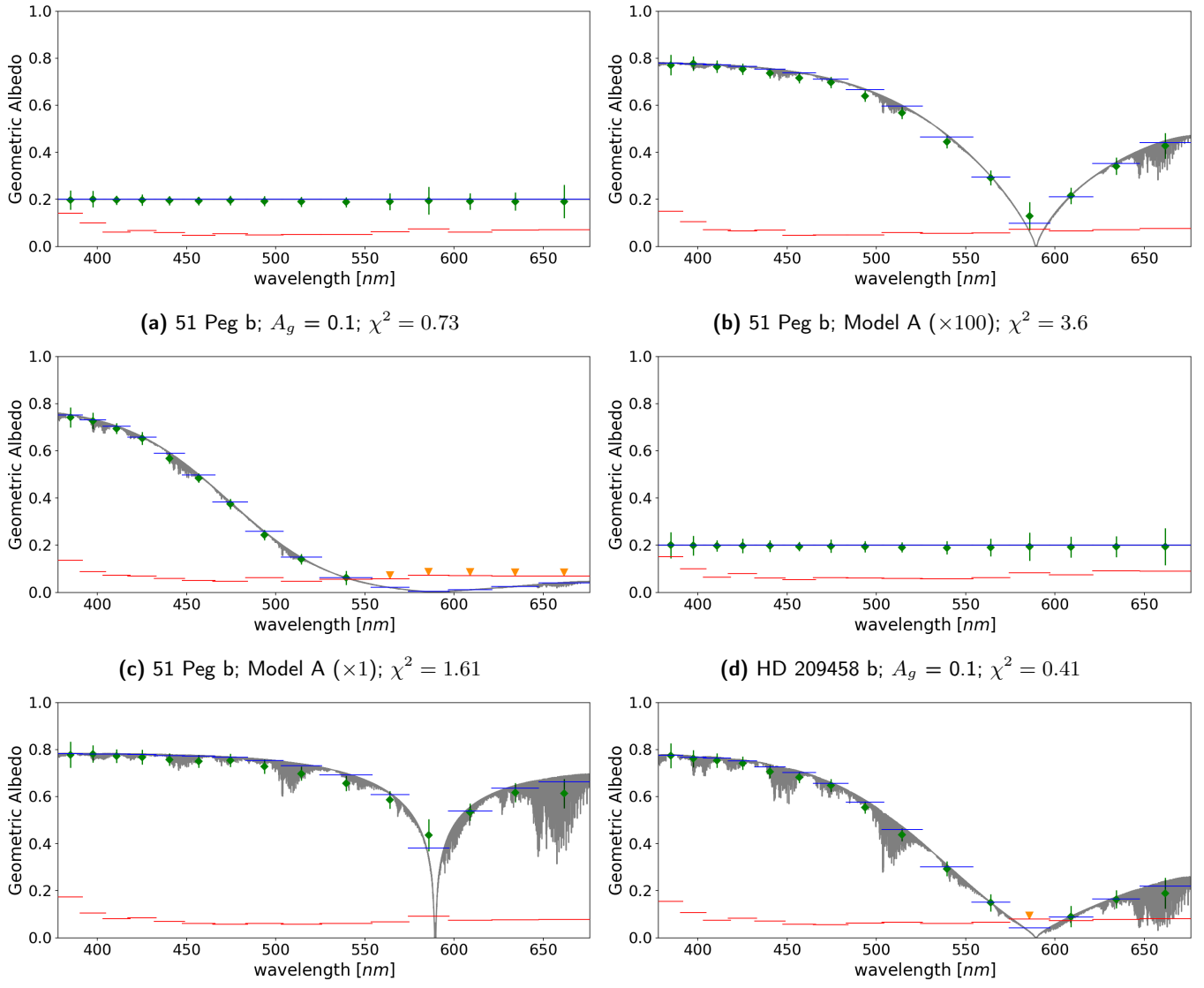

(a) 51 Peg b; $A_g = 0.1$; $\chi^2 = 0.73$

(b) 51 Peg b; Model A ($\times 100$); $\chi^2 = 3.6$

(c) 51 Peg b; Model A ($\times 1$); $\chi^2 = 1.61$

(d) HD 209458 b; $A_g = 0.1$; $\chi^2 = 0.41$

(e) HD 209458 b; Model B ($\times 100$); $\chi^2 = 3.96$

(f) HD 209458 b; Model B ($\times 1$); $\chi^2 = 1.99$

Figure 6.7: Distribution of the recovered albedo functions from the simulated ESPRESSO (UHR mode) observations. For each wavelength bin: *i)* the green dots represent the mean recovered albedo over the 100 simulated runs with error bars given by their standard deviation; *ii)* the blue horizontal lines represent the mean albedo of the simulated model over the bin; *iii)* the red horizontal bar represents the 3σ detection limit of the albedo.

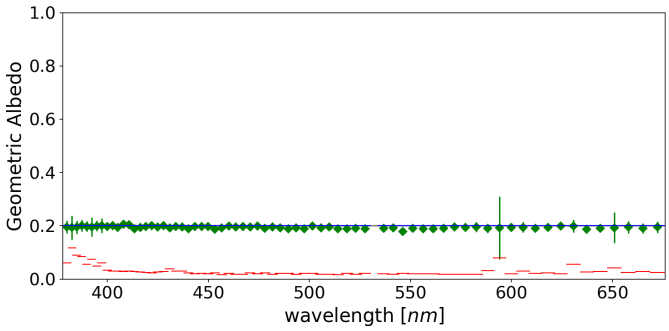

(a) 51 Peg b; $A_g = 0.1$; $\chi^2 = 5.38$

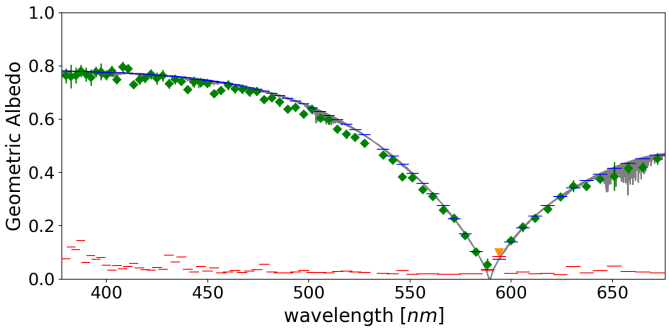

(b) 51 Peg b; Model A ($\times 100$); $\chi^2 = 19.77$

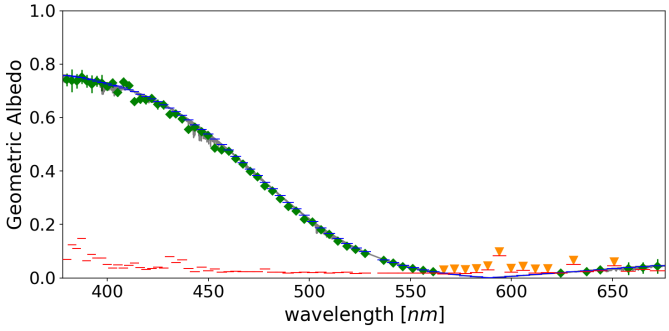

(c) 51 Peg b; Model A ($\times 1$); $\chi^2 = 7.84$

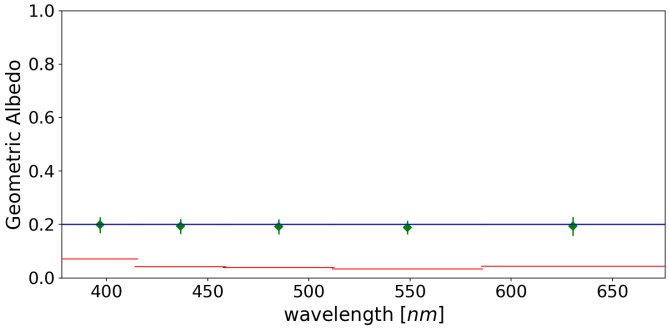

(d) 55 Cnc e; $A_g = 0.1$; $\chi^2 = 0.67$

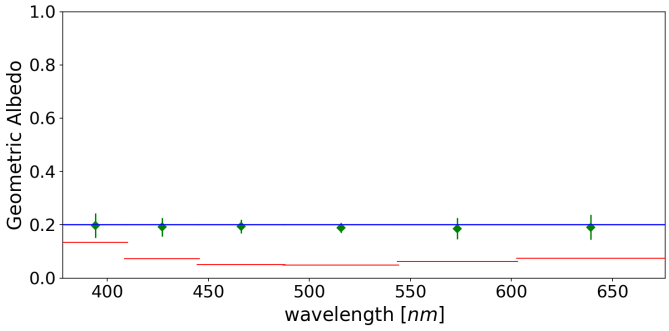

(e) HD 109749 b; $A_g = 0.1$; $\chi^2 = 1.05$

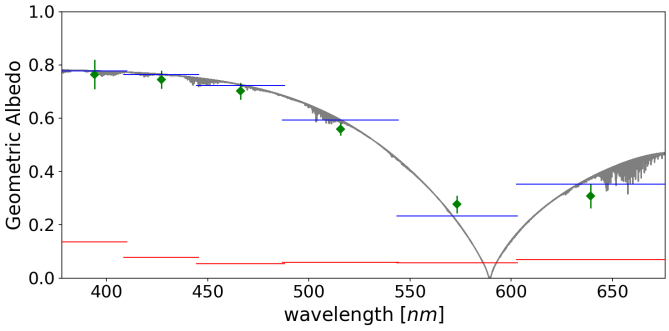

(f) HD 109749 b; Model A ($\times 100$); $\chi^2 = 8.24$

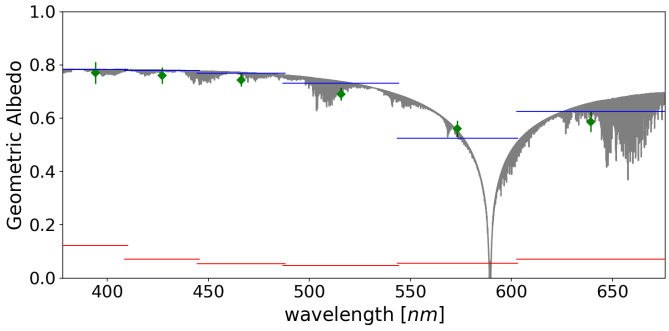

(g) HD 109749 b; Model B ($\times 100$); $\chi^2 = 10.29$

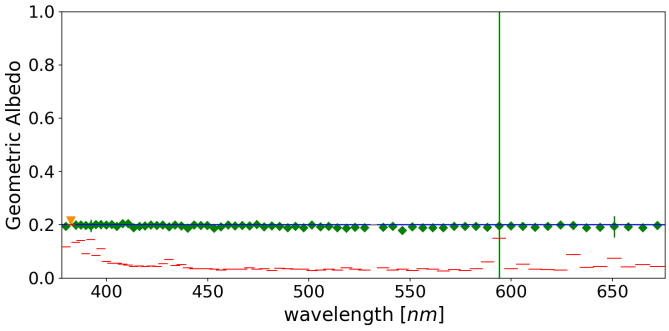

(h) HD 209458 b; $A_g = 0.1$; $\chi^2 = 2.04$

Distribution of the recovered albedo functions from the simulated HIRES observations. For each wavelength bin: *i)* the green dots represent the mean recovered albedo over the 100 simulated runs with error bars given by their standard deviation; *ii)* the blue horizontal lines represent the mean albedo of the simulated model over the bin; *iii)* the red horizontal bar represents the 3σ detection limit of the albedo. (continued . . .))

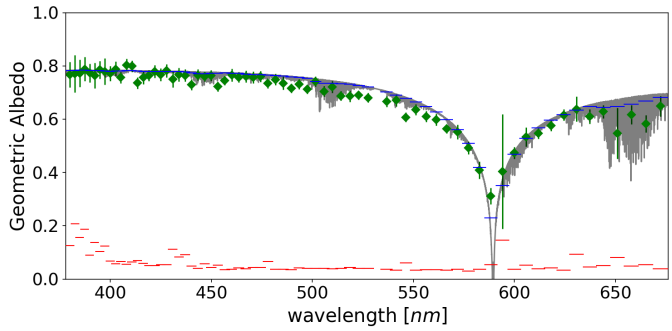

(i) HD 209458 b; Model B ($\times 100$); $\chi^2 = 15.94$

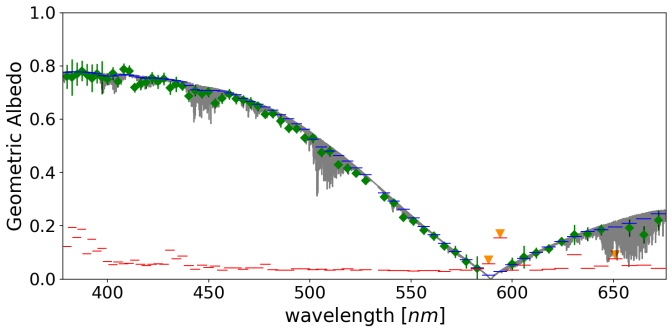

(j) HD 209458 b; Model B ($\times 1$); $\chi^2 = 8.17$

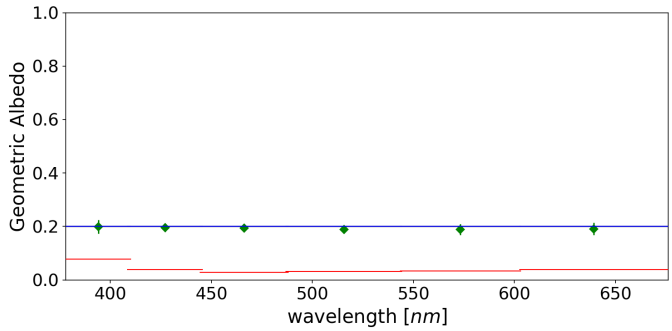

(k) HD 76700 b; $A_g = 0.1$; $\chi^2 = 2.13$

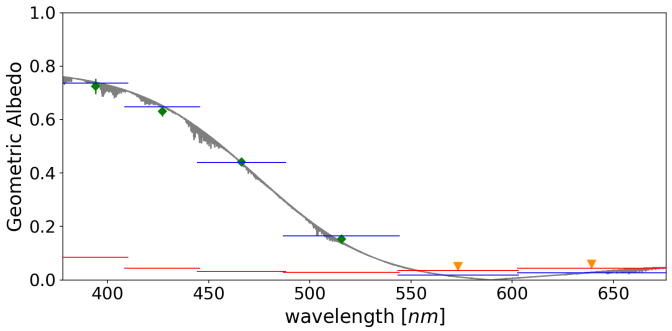

(l) HD 76700 b; Model A ($\times 1$); $\chi^2 = 3.0$

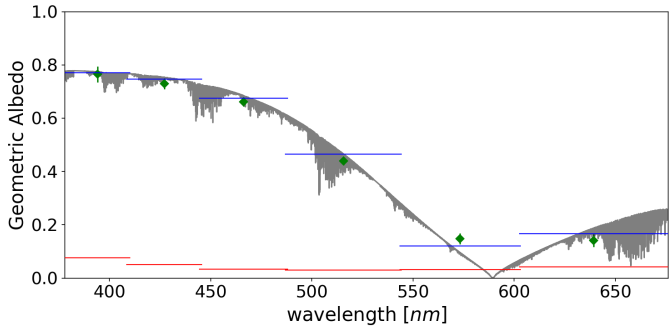

(m) HD 76700 b; Model B ($\times 1$); $\chi^2 = 10.91$

Figure 6.8: Distribution of the recovered albedo functions from the simulated HIRES observations. For each wavelength bin: *i)* the green dots represent the mean recovered albedo over the 100 simulated runs with error bars given by their standard deviation; *ii)* the blue horizontal lines represent the mean albedo of the simulated model over the bin; *iii)* the red horizontal bar represents the 3σ detection limit of the albedo.

ESPRESSO (HR mode)

		χ^2 value				
		$A_g = 0.1$	Model A ($\times 1$)	Model A ($\times 100$)	Model B ($\times 1$)	Model B ($\times 100$)
51 Peg b	$A_g = 0.1$	0.56	1252.09	2883.25	2380.86	3750.83
	Model A ($\times 100$)	3166.72	850.43	4.37	84.88	307.53
	Model A ($\times 1$)	1497.32	1.71	833.82	487.17	1324.44
HD 209458 b	$A_g = 0.1$	0.34	630.85	1415.97	1165.54	1855.49
	Model B ($\times 100$)	2362.25	937.77	111.94	308.75	3.62
	Model B ($\times 1$)	1672.73	244.56	74.97	1.78	383.86

Table 6.6: Results of the recovery of the albedo function for each batch of simulated ESPRESSO (HR mode) observations. The first column shows the simulated instrument+planet configurations, the second one the simulated albedo for each configuration, and the remaining columns the reduced χ^2 comparison between the simulated model and the models from Table B.1. For each configuration, the lowest χ^2 value is highlighted with a red box. Note that in all cases it occurs when the simulated model matches the comparison model, indicating that the correct albedo function has been recovered.

ESPRESSO (MHR mode - 1UT

		χ^2 value				
		$A_g = 0.1$	Model A ($\times 1$)	Model A ($\times 100$)	Model B ($\times 1$)	Model B ($\times 100$)
51 Peg b	$A_g = 0.1$	0.59	862.38	1992.87	1633.98	2618.26
	Model A ($\times 100$)	2511.01	688.48	3.97	74.61	285.29
	Model A ($\times 1$)	1240.68	1.94	707.1	413.69	1143.95
HD 209458 b	$A_g = 0.1$	0.29	342.57	846.75	682.27	1129.48
	Model B ($\times 100$)	1933.61	831.58	103.41	279.58	3.51
	Model B ($\times 1$)	1338.98	193.76	60.34	1.72	303.29

Table 6.7: Results of the recovery of the albedo function for each batch of simulated ESPRESSO (MHR mode - 1UT) observations. The first column shows the simulated instrument+planet configurations, the second one the simulated albedo for each configuration, and the remaining columns the reduced χ^2 comparison between the simulated model and the models from Table B.1. For each configuration, the lowest χ^2 value is highlighted with a red box. Note that in all cases it occurs when the simulated model matches the comparison model, indicating that the correct albedo function has been recovered.

ESPRESSO (MHR mode - 2UT)

		χ^2 value				
		$A_g = 0.1$	Model A ($\times 1$)	Model A ($\times 100$)	Model B ($\times 1$)	Model B ($\times 100$)
51 Peg b	$A_g = 0.1$	0.89	1819.82	3823.3	3176.37	5028.64
	Model A ($\times 100$)	4268.15	1154.99	6.75	133.3	508.01
	Model A ($\times 1$)	2101.37	3.45	1424.64	817.0	2315.4
HD 209458 b	$A_g = 0.1$	0.54	758.16	1742.24	1425.48	2325.58
	Model B ($\times 100$)	3312.67	1511.6	205.49	540.77	6.68
	Model B ($\times 1$)	2268.51	349.04	115.93	3.44	589.1

Table 6.8: Results of the recovery of the albedo function for each batch of simulated ESPRESSO (MHR mode - 2UT) observations. The first column shows the simulated instrument+planet configurations, the second one the simulated albedo for each configuration, and the remaining columns the reduced χ^2 comparison between the simulated model and the models from Table B.1. For each configuration, the lowest χ^2 value is highlighted with a red box. Note that in all cases it occurs when the simulated model matches the comparison model, indicating that the correct albedo function has been recovered.

ESPRESSO (MHR mode - 4UT)

		χ^2 value				
		$A_g = 0.1$	Model A ($\times 1$)	Model A ($\times 100$)	Model B ($\times 1$)	Model B ($\times 100$)
51 Peg b	$A_g = 0.1$	1.91	3074.13	6962.03	5675.48	9370.81
	Model A ($\times 100$)	8253.72	3034.02	14.87	453.84	1874.56
	Model A ($\times 1$)	4951.37	8.11	6415.28	3127.65	12758.4
HD 209458 b	$A_g = 0.1$	1.42	2213.95	5323.42	4298.97	7102.65
	Model B ($\times 100$)	6442.4	3093.26	493.54	1244.16	13.79
	Model B ($\times 1$)	4455.57	665.3	259.87	5.98	1476.43

Table 6.9: Results of the recovery of the albedo function for each batch of simulated ESPRESSO (MHR mode - 4UT) observations. The first column shows the simulated instrument+planet configurations, the second one the simulated albedo for each configuration, and the remaining columns the reduced χ^2 comparison between the simulated model and the models from Table B.1. For each configuration, the lowest χ^2 value is highlighted with a red box. Note that in all cases it occurs when the simulated model matches the comparison model, indicating that the correct albedo function has been recovered.

ESPRESSO (UHR mode)

		χ^2 value				
		$A_g = 0.1$	Model A ($\times 1$)	Model A ($\times 100$)	Model B ($\times 1$)	Model B ($\times 100$)
51 Peg b	$A_g = 0.1$	0.73	1422.0	3200.04	2636.73	4198.8
	Model A ($\times 100$)	3247.76	765.05	3.6	77.2	271.94
	Model A ($\times 1$)	1558.19	1.61	866.93	502.27	1394.81
HD 209458 b	$A_g = 0.1$	0.41	927.23	2207.22	1789.34	2935.23
	Model B ($\times 100$)	2919.3	1195.16	158.4	422.0	3.96
	Model B ($\times 1$)	2060.49	303.4	95.82	1.99	501.21

Table 6.10: Results of the recovery of the albedo function for each batch of simulated ESPRESSO (UHR mode) observations. The first column shows the simulated instrument+planet configurations, the second one the simulated albedo for each configuration, and the remaining columns the reduced χ^2 comparison between the simulated model and the models from Table B.1. For each configuration, the lowest χ^2 value is highlighted with a red box. Note that in all cases it occurs when the simulated model matches the comparison model, indicating that the correct albedo function has been recovered.

HIRES

		χ^2 value				
		$A_g = 0.1$	Model A ($\times 1$)	Model A ($\times 100$)	Model B ($\times 1$)	Model B ($\times 100$)
51 Peg b	$A_g = 0.1$	5.38	7150.26	17168.62	13772.93	23739.76
	Model A ($\times 100$)	7725.97	2878.74	19.77	391.53	1771.47
	Model A ($\times 1$)	4881.94	7.84	6924.96	3480.13	13008.05
HD 109749 b	$A_g = 0.1$	1.05	645.38	2006.96	1478.67	2928.78
	Model A ($\times 100$)	1897.37	662.68	8.24	70.7	241.85
	Model B ($\times 100$)	3610.79	1798.4	258.4	647.7	10.29
HD 209458 b	$A_g = 0.1$	2.04	2440.33	6088.13	4835.52	8452.54
	Model B ($\times 100$)	6073.89	2987.44	393.93	1055.57	15.94
	Model B ($\times 1$)	3911.57	801.72	317.0	8.17	1730.91
HD 76700 b	$A_g = 0.1$	2.13	2623.96	6485.17	5179.69	8967.27
	Model A ($\times 1$)	3007.09	3.0	2699.31	1508.58	4400.09
	Model B ($\times 1$)	4379.23	834.28	318.99	10.91	1777.48
55 Cnc e	$A_g = 0.1$	0.67	1081.99	2078.01	1732.81	2942.96

Table 6.11: Results of the recovery of the albedo function for each batch of simulated HIRES observations. The first column shows the simulated instrument+planet configurations, the second one the simulated albedo for each configuration, and the remaining columns the reduced χ^2 comparison between the simulated model and the models from Table B.1. For each configuration, the lowest χ^2 value is highlighted with a red box. Note that in all cases it occurs when the simulated model matches the comparison model, indicating that the correct albedo function has been recovered.

DISCUSSION 6.1.7

The results presented in the previous section confirm that the CCF technique can be used to recover the wavelength dependence of the reflected optical signal of exoplanets – and albedo – from spectra obtained with the next generation of high-resolution spectrographs.

Note that for this project we initially fixed the number of wavelength bins over the albedo function would be recovered for each simulated planet. An alternative approach could have been to fix the total exposure time for all targets (e.g. one night, $\sim$ 11h) and estimate the number of bins for which the albedo function could be recovered at a 3-σ significance per bin. Table 6.12 presents the number of wavelength bins for which the albedo could recovered at a 3-σ significance for a total observing time of 11 hours (about one observing night) for the selected targets, assuming different grey albedo functions. We limited N_{bins} at 70, which is the number of orders of the HARPS spectrograph. It is clear that as soon as 2018, ESPRESSO will make it possible to probe in detail the atmospheres of hot Jupiter planets such as 51 Pegasi b with a few hours worth of observing time. By increasing the exposure time or decreasing the level of detail will also enable ESPRESSO to probe smaller and/or longer period planets. The sheer increase of collecting power from moving to a 30-m class telescope will permit to facilities such as HIRES to probe those smaller and/or longer period planets with increased detail.

	N_{bins} for $\langle A_g \rangle$				
$\langle A_g \rangle$=	0.1	0.2	0.3	0.4	0.5
ESPRESSO					
51 Peg b	55	70	70	70	70
HD 209458 b	3	13	31	55	70
HIRES					
51 Peg b	70	70	70	70	70
HD 209458 b	37	70	70	70	70
HD 109749 b	2	9	20	36	56
HD 76700 b	4	18	41	70	70
55 Cnc e	3	12	29	51	70

Table 6.12: Estimated number of wavelength bins for which the albedo could recovered at an average 3-σ significance for a total observing time of 11 hours (about one observing night) for different grey albedos models. We limited N_{bins} at 70, which is the number of orders of the HARPS spectrograph (from Martins et al., 2017).

IDENTIFICATION OF SPECTRAL FEATURES

The spectral feature that dominates the selected albedo models (see Appendix B) is the optical sodium doublet at 589.59-nm and 588.99-nm. In an ideal case, where it is possible to recover the CCF of the planet for each order of the spectrograph (i.e., N_{bins} is equal number of orders of the spectrograph) each wavelength bin will be over 4-nm wide, clearly insufficient to resolve both lines of the doublet. However, this feature is extremely wide – typically over 10-nm – and it should be possible to sample it with two or more wavelength bins and resolve it. Note that the amount of aerosols impacts the width of the sodium doublet: the lower the fraction of aerosols, the wider the sodium doublet will appear and most likely to be sampled and resolved, even with a lower value for N_{bins}. More aerosols mean a decrease in the width of sodium doublet absorption line and a higher global geometric albedo. This can be easily understood if we consider that high-altitude aerosols prevent the access of the starlight to the deepest regions of the atmosphere (e.g. Sing et al., 2016), where the sodium absorption dominates and is responsible for the line broadening. On the other hand, less aerosols also mean a lower global albedo, making it more difficult to detect the reflected planetary signature. However, this decrease in albedo is not color-independent. Although the albedo towards bluer wavelengths will remain almost unchanged, towards redder bands the albedo might drop significantly (e.g., the albedo for the $\times 1$ configuration of the *Model A* family of atmospheric models – see Appendix B – is close to zero). Therefore, even in cases where the albedo can only be recovered for a small number of wavelength bins, the ratio of the recovered albedo for redder and bluer bands should permit to retrieve important information such as the aerosol fraction on the atmosphere.

Narrower spectral features – with widths smaller than the spectral range covered by 2-3 wavelength bins (e.g. water absorption lines) – will not be possible to resolve. However, for wavelength ranges where a significant number of absorption lines are present, the local average albedo will be lower than the expected continuum for the albedo function. This can be clearly seen on the simulations where albedo function from the *Model B* family were created. Since the ratio of water to alkali metals is lower, the albedo function is much more structured, i.e., a large amount of water absorption lines can be found. In those "water bands", the albedo will be lower than the albedo function continuum (e.g., panels e and f of Figures 6.3 to 6.7, panel g, i, j and m of Figure 6.8).

ESPRESSO RESOLUTION DEPENDENCE

As discussed in Section 3.2, the ESPRESSO spectrograph has 3 different resolution modes available: MHR mode with $R = 60000$, HR mode with $R = 130000$ and UHR mode with $R = 220000$. To test if the resolution of the spectrograph impacted the recovery of the albedo function from the planet, we attempted to recover the albedo from the simulations described in Section 6.1.5.

Figure 6.9 shows the relative error $X\left(A_{g,i}\right)$ on the geometric albedo $A_{g,i}$ recovered for each wavelength bin i, defined as

$$X\left(A_{g,i}\right) = \frac{\left\langle \sigma_{A_{g,i}} \right\rangle}{A_{g,i}} \tag{6.9}$$

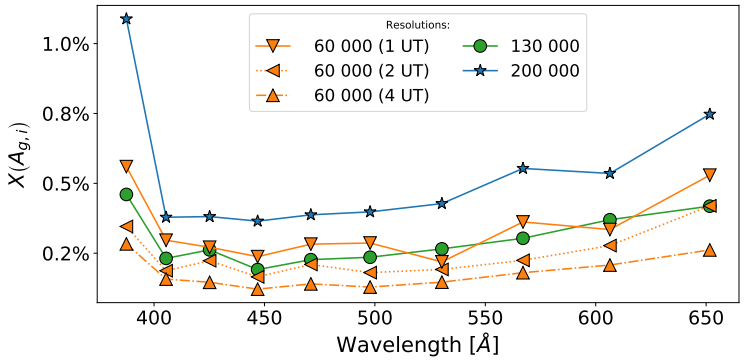

Figure 6.9: Relative errors for the recovered albedo function from simulated observations of HD209458 b with ESPRESSO in all 3 resolution modes. $X\left(A_{g,i}\right)$ represents the relative error on the geometric albedo $A_{g,i}$ recovered for each wavelength bin i, as defined in Equation 6.9. For the MHR mode, we simulated observations with 1, 2 and 4 UT telescopes.

where $A_{g,i}$ is the mean measured geometric albedo for bin i and $\sigma\left(A_{g,i}\right)$ is the dispersion over all simulated runs of $A_{g,i}$.

In UHR mode ($R = 220000$), the error on the recovered albedo is significantly larger than with the two other modes. In UHR mode the spectrograph is fed by a fiber with a diameter of 0.5" – half the diameter of the fiber feeding the spectrograph for HR and UHR mode – and thus a much lower number of photons reaches the detector, leading to observations on a much lower S/N domain. This can be seen clearly in Figure 6.7, panel d. When we computed the total exposure times for each observing run, we assume ESPRESSO to be in the HR configuration. Since the fiber diameter for the UHR mode is half of the fiber for the other modes, the planetary CCFs will be significantly noisier. Therefore, in most wavelength bins, the S/N of the recovered planetary CCF is lower than the upper limit for the albedo with a 3-σ confidence.

For both HR ($R = 135000$) and MHR ($R = 60000$) modes, no evidence can be found of the impact of the resolution on the recovered albedo errors. However, a clear decrease in the error on the recovered albedo can be seen as the collecting area increases, i.e., going from 1 UT to 4UT in MHR mode. Note that an increased resolution is paramount to be able to retrieve precise orbital parameters for both host and planet.

In summary, if only 1 UT is available, HR mode is the best choice, as it combines the highest resolution for the same collecting area. However, if 2 or more UT are available, the increase in collecting area will make MHR mode the ideal choice. Regardless of the number of UTs available, UHR mode does not present any advantage for the CCF technique over the other available modes as a result in the significantly smaller fiber.

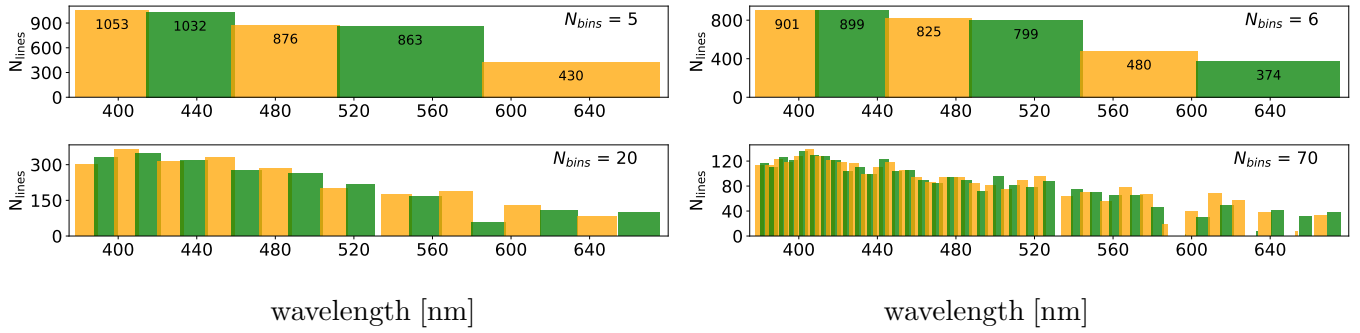

Figure 6.10: Number of spectral lines from the CCF mask per wavelength bin for 5, 6, 20 and 70 bins.

WAVELENGTH DEPENDENCE OF THE NOISE 6.1.8

From Figures 6.3 to 6.8 it can be seen that the noise per bin on the planetary CCF is wavelength dependent. This dependence results from the combination of i) the efficiency of the instrument, ii) the distribution of the mask lines along the spectral coverage and iii) the spectral type of the star. The measured efficiency curves for ESPRESSO (in all 3 resolution modes) and HARPS (used as a template for HIRES) are shown in Figure 3.7.

Figure 6.10 shows the distribution of spectral lines for the different number of wavelength bins simulated in this document (5, 6, 20 and 70 wavelength bins). The number of spectral lines of the mask per bin is inscribed on the individual histogram bars.It is clear that the number of spectral lines in the mask is not uniform and decreases towards larger wavelengths, yielding to a lower increase in S/N from CCF construction for redder wavelength bins.

For $N_{bins} = 70$, the wavelength range covered by each wavelength bin corresponds to a spectral order of the HARPS spectrograph and several gaps can be seen. The lack of mask lines around 530-nm corresponds to a gap between the two chips of the HARPS spectrograph. The other 3 gap in the number of mask lines (590-nm, 630-nm and 645-nm) correspond to orders where the number of spectral lines is inferior to 5. Those orders are known for significant telluric contamination and have larges wavelength ranges that are not considered for the CCF calculation. Note that these gaps do not show for lower values of N_{bins} as their orders will be merged with adjacent ones.

Different spectral types will have different spectral energy distributions. Figure 6.11 presents the expected S/N from a 300-s exposure with HARPS of $V_{mag} = 6.0$ F0, G2 K2 and M2 spectral type stars as computed with HARPS ETC. It can be seen that M stars will attain higher S/N towards redder wavelengths, while F stars will attain higher S/N than G to M stars towards bluer wavelengths, with G stars somewhere in the middle of both.

Note that for all simulations we have used a high-resolution G2 spectral template, independently of the spectral type of the stellar host. It is interesting to discuss how the spectral type of the star would affect the recovery of the planetary albedo function. It is clear from Equation 2.1 that the planet-to-star flux ratio is independent on the stellar type of the star.

However, the detectability limit of the albedo function (per bin) will depend on the stellar type. Assuming the same magnitude and exposure times:

- for redder wavelengths, the detection limit for the albedo function will decrease from F to M stars;
- for bluer wavelengths, the detection limit for the albedo function will increase from F to M stars;

It is interesting to compare this result with the albedo models presented in Appendix B (see Figure B.1). These models show higher albedos for shorter wavelengths, with most of the absorption (depending on the alkali metal concentration) occurring at larger wavelengths. As such, it is realistic to assume that cooler spectral type stars will be better targets than warmer stars as lower albedo detection limits can be attained for the same exposure time. Note that this assumption is only valid for the models we present here (or similar) and is not universal. It is not unusual in the solar system planets that some absorber affects the ultraviolet wavelengths and diminishes the planet reflectivity towards bluer wavelengths (e.g. the case Venus – Lee et al., 2017).

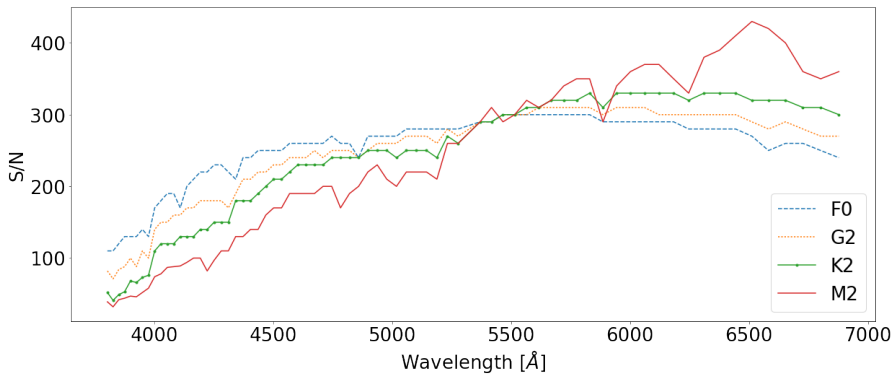

Figure 6.11: Comparison of the expected S/N from a 300s exposure with HARPS of $V_{mag} = 6.0$ F0, G2 K2 and M2 spectral type stars as per HARPS ETC (from Martins et al., 2017).

REFLECTED LIGHT FROM GIANT PLANETS IN HABITABLE ZONES

6.2

It is interesting to explore the possibility provided by future high-resolution spectrographs installed on 30-m class telescopes to recover the reflected signal of exoplanets in the habitable zones of their host stars. The results of this work were published in Martins et al. (2016)

WHAT IS THE HABITABLE ZONE? 6.2.1

Since liquid water is a requirement for life as we know it, the Habitable Zone of a star has been defined as the orbital region around a star in which an Earth-like planet can possess liquid water on its surface and possibly support life as we know it (e.g. Huang, 1959; Kasting et al., 1993).

For this work, we adopted the Habitable Zone criteria from the Habitable Exoplanet Catalog (`http://phl.upr.edu/hec`). However, we chose not to limit the planets by mass, to encompass possible giant planets in their star's Habitable Zone that might have habitable satellites. Mathematically speaking, the chosen Habitable Zone model is based on the model proposed by Kasting et al. (1993) defines the inner and outer limits (r_i and r_o, in $[A.U.]$) of the Habitable Zone by

$$\begin{aligned} r_i = & \left[r_{is} - a_i\left(T_{eff} - T_S\right) - b_i\left(T_{eff} - T_S\right)^2\right]\sqrt{\frac{L_*}{L_\odot}} \\ r_o = & \left[r_{os} - a_o\left(T_{eff} - T_S\right) - b_o\left(T_{eff} - T_S\right)^2\right]\sqrt{\frac{L_*}{L_\odot}} \end{aligned} \tag{6.10}$$

where r_i and r_o are the inner and outer limits of the Habitable Zone, L_* is the luminosity of the star and T_{eff} is the effective temperature of the star. The remaining factors are constants defined by the models of Selsis et al. (2007) and Underwood et al. (2003):

$$\begin{aligned} r_{is} &= 0.72 & a_i &= 2.7619 \times 10^{-5} & b_i &= 3.8095 \times 10^{-9} \\ r_{os} &= 1.77 & a_o &= 1.3796 \times 10^{-4} & b_o &= 1.4286 \times 10^{-9} \end{aligned} \tag{6.11}$$

$$T_S = 5700K$$

Using this model, we computed for all planets in the exoplanet.eu database (as of October 2017) the inner and outer limit of the Habitable Zone. Figure 6.12 shows the semi-major axis of their orbit and the effective temperature of their host between 2000K and 8000K. Currently, 54 planets orbiting stars with $V_{mag} < 12$ can be found in the Habitable Zone of their host (red dots).

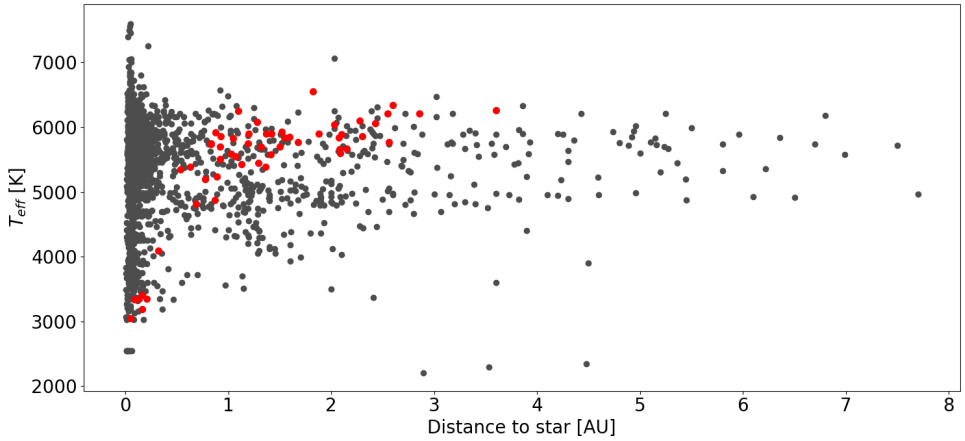

Figure 6.12: Effective temperature of all planets in the exoplanet.eu data bases as a function of the distance to their host star. The red dots correspond to the planets in the Habitable Zone of their host (from Martins et al., 2016).

REFLECTED LIGHT FROM HABITABLE ZONE PLANETS WITH ESO'S ELT 6.2.2

To estimate for which planets in their host's Habitable Zone it would be possible to detect the reflected signal using the CCF technique, we used Equation 2.1 (assuming $A_g = 0.5$) to estimate the planet-to-star flux ratio for all planets orbiting FGKM stars. In the cases where no radius is known (e.g., planets detected by the RV method), we used the empirical mass-radius relation proposed in Weiss et al. (2013):

$$\begin{aligned} M_p < 150 M_\oplus \quad &\longrightarrow \quad \frac{R_p}{R_\oplus} = 1.78 \left(\frac{M_p}{M_\oplus}\right)^{0.53} F_i^{-0.03} \\ M_p \geqslant 150 M_\oplus \quad &\longrightarrow \quad \frac{R_p}{R_\oplus} = 2.45 \left(\frac{M_p}{M_\oplus}\right)^{-0.039} F_i^{0.094} \end{aligned} \tag{6.12}$$

where M_p and R_p are respectively the mass and radius of the planet, and F_i (in $[c.g.s]$) is the stellar flux incident on the planet. This factor is given by

$$F_i = \sigma \, T_{eff}^4 \left(\frac{R_*}{a}\right)^2 \sqrt{\frac{1}{1-e^2}} \tag{6.13}$$

where σ is the Stephan-Boltzmann constant.

	Period $[days]$	a $[AU]$	T_{eff} $[K]$	r_i $[AU]$	r_o $[AU]$	M_p $[M_{Jup}]$	R_p $[R_{Jup}]$	$\frac{F_p}{F_*}$
16CygB b	800	1.68	5766	0.70	1.72	1.7	0.6	1.4×10^{-8}
47Uma b	1078	2.10	5892	0.92	2.25	2.5	0.6	8.3×10^{-9}
55Cnc f	261	0.78	5196	0.56	1.40	0.1	0.8	1.1×10^{-7}
GJ687 b	38	0.16	3413	0.11	0.30	0.1	0.5	9.8×10^{-7}
GJ876 b	61	0.21	3350	0.09	0.25	1.9	0.6	8.5×10^{-7}

Planets in the exoplanet.eu database within their host star HZ. (continued ...)

	Period $[days]$	a $[AU]$	T_{eff} $[K]$	r_i $[AU]$	r_o $[AU]$	M_p $[M_{Jup}]$	R_p $[R_{Jup}]$	$\frac{F_p}{F_*}$
GJ876 c	30	0.13	3350	0.09	0.25	0.9	0.7	2.8×10^{-6}
HD10647 b	1003	2.03	6039	0.85	2.07	0.9	0.6	9.5×10^{-9}
HD114729 b	1135	2.08	5662	1.01	2.49	0.8	0.6	9.7×10^{-9}
HD11506 b	1270	2.43	6058	1.08	2.61	3.4	0.6	6.1×10^{-9}
HD117618 c	318	0.93	5861	0.88	2.14	0.2	0.9	1.1×10^{-7}
HD125612 b	502	1.37	5897	0.78	1.91	3.0	0.6	2.2×10^{-8}
HD12661 b	264	0.83	5742	0.80	1.95	2.3	0.7	7.3×10^{-8}
HD128356 b	298	0.87	4875	0.45	1.14	0.9	0.6	5.7×10^{-8}
HD137388 b	330	0.89	5240	0.49	1.24	0.2	1.0	1.4×10^{-7}
HD141399 d	1070	2.09	5600	0.99	2.45	1.2	0.6	9.2×10^{-9}
HD141937 b	653	1.52	5925	0.80	1.94	9.7	0.6	1.6×10^{-8}
HD142415 b	386	1.05	5834	0.75	1.84	1.6	0.7	4.3×10^{-8}
HD147513 b	528	1.32	5701	0.70	1.72	1.2	0.6	2.4×10^{-8}
HD153950 b	499	1.28	6076	1.05	2.55	2.7	0.7	2.9×10^{-8}
HD154857 b	409	1.29	5445	1.14	2.82	2.2	0.7	2.9×10^{-8}
HD156411 b	842	1.88	5900	1.61	3.93	0.7	0.7	1.5×10^{-8}
HD164509 b	282	0.88	5922	0.79	1.94	0.5	0.7	7.2×10^{-8}
HD165155 b	434	1.13	5426	0.61	1.51	2.9	0.6	3.1×10^{-8}
HD169830 c	2102	3.60	6266	1.52	3.66	4.0	0.6	2.7×10^{-9}
HD196885A b	1326	2.60	6340	1.51	3.62	3.0	0.6	6.2×10^{-9}
HD202206 b	256	0.83	5750	0.73	1.78	17.4	0.6	6.1×10^{-8}
HD216435 b	1311	2.56	5767	1.43	3.51	1.3	0.6	6.5×10^{-9}
HD218566 b	226	0.69	4820	0.44	1.13	0.2	1.0	2.2×10^{-7}
HD224538 b	1189	2.28	6097	1.06	2.56	6.0	0.6	6.9×10^{-9}
HD23079 b	731	1.60	5848	0.83	2.03	2.5	0.6	1.5×10^{-8}
HD28254 b	1116	2.15	5664	1.03	2.53	1.2	0.6	9.6×10^{-9}
HD30562 b	1157	2.30	5861	1.21	2.94	1.3	0.6	8.5×10^{-9}
HD33564 b	388	1.10	6250	0.91	2.18	9.1	0.6	3.5×10^{-8}
HD43197 b	328	0.92	5508	0.66	1.63	0.6	0.7	6.5×10^{-8}
HD44219 b	472	1.19	5752	0.94	2.31	0.6	0.7	3.8×10^{-8}
HD564 b	492	1.20	5902	0.75	1.84	0.3	1.2	1.2×10^{-7}

Planets in the exoplanet.eu database within their host star HZ. (continued ...)

	Period $[days]$	a $[AU]$	T_{eff} $[K]$	r_i $[AU]$	r_o $[AU]$	M_p $[M_{Jup}]$	R_p $[R_{Jup}]$	$\frac{F_p}{F_*}$
HD69830 d	197	0.63	5385	0.57	1.41	0.3	1.1	3.1×10^{-7}
HD7199 b	615	1.36	5386	0.61	1.51	0.3	1.2	8.2×10^{-8}
HD73526 c	379	1.03	5590	1.01	2.49	2.2	0.7	4.7×10^{-8}
HD86264 b	1475	2.86	6210	1.53	3.69	7.0	0.6	4.8×10^{-9}
HIP57050 b	41	0.16	3190	0.09	0.26	0.3	1.2	5.7×10^{-6}
WASP-41 c	421	1.07	5546	0.67	1.67	3.2	0.6	3.6×10^{-8}
WASP-47 c	572	1.36	5576	0.77	1.91	1.2	0.6	2.3×10^{-8}
muAra b	643	1.50	5700	0.87	2.15	1.7	0.6	1.9×10^{-8}
muAra d	311	0.92	5700	0.87	2.15	0.5	0.7	6.5×10^{-8}
upsAn d d	1281	2.55	6212	1.33	3.20	23.6	0.6	5.1×10^{-9}

Table 6.13: Planets in the exoplanet.eu database within their host star HZ.

Table 6.13 presents all planets in their host star's Habitable Zone that orbit FGKM stars.The last column shows the maximum planet-to-star flux ratio as computed from Equation 2.1. This permitted us to estimate the total exposure time required for a 3-σ detection of the reflected optical light from their orbiting planets with ESO's ELT. This was done extrapolating the S/N computed for a 30s exposure of a $mag_V = 6$ star as estimated by ESO's online spectroscopic ETC for the ELT. Note that this ETC assumes a generic high-resolution spectrograph with a theoretical efficiency of 25% for telescope+instrument+detector. As such, the computed exposure times should be taken as indicative only as different instruments will have different efficiencies which are currently impossible to estimate. For more details, we refer you to the online documentation for the ELT's ETC, which can be found at `https://www.eso.org/observing/etc/doc/elt/etc_spec_model.pdf`.

Table 6.14 shows the parameters we used on the ELT's ETC. Then, we extrapolated from the S/N estimated for by the ETC to the S/N required for the detection of the reflected signal of each planet with

$$mag_{host} - mag_{ref} = -5log\left(\frac{SN_{host}}{SN_{ref}}\right) \tag{6.14}$$

where mag_{host} and SN_{host} are respectively the visual magnitudes and expected S/N of the host star, mag_{ref} is the reference value used in the ETC for the visual magnitude and SN_{host} is the predicted S/N.

The required total exposure time required for a 3-σ detection ($t_{3\sigma}$) of the target will be given by

$$t_{3\sigma} = \frac{t_{ref}}{N_{lines}}\left(\frac{SN_p}{SN_{host}}\right)^2 \tag{6.15}$$

where t_{ref} is the reference time used in the ETC, N_lines the number of spectral lines in the CCF masks and SN_p

Parameter		Value
Target Input Flux Distribution		
	Spectral Type	$G2V$
	Vega mag	$V = 6.0$
	Spatial distribution	Point source
Telescope Setup		
	Observatory site	Paranal (2635-m)
	Spatial distribution	39-m
Sky Conditions		
	Seeing	$0.8''$
	Airmass	1.5
Instrument Setup		
	AO mode	Seeing limited
	Observing wavelength	Band V (550-nm)
	Radius of circular S/N area	1000.0 mas
	Number of spectra on the detector	1
	Spectral resolution	100 000
Results		
	Exposure time	NDIT = 1
		DIT = 30s

Table 6.14: Observing parameters used for the ELT's ETC.

	Host Spectral type	SN_p	mag_V	$SN(30s)$	$t_{3\sigma}$
55Cnc f	K0IV-V	2.68×10^7	6.0	4031.8	89.5
GJ687 b	M3.5V	3.05×10^6	9.2	923.6	22.1
GJ876 b	M4V	3.54×10^6	10.2	577.4	76.1
GJ876 c	M4V	1.08×10^6	10.2	577.4	7.0
HD69830 d	K0V	9.60×10^6	6.0	4031.8	11.5
HIP57050 b	M4V	5.28×10^5	11.9	260.3	8.3

Table 6.15: Planets where a 3-σ detection can be accomplished under 100-h

is the required S/N for a 3-σ detection of the planet.

The for all planets in the sample are shown in Figure 4. Table 4 shows the cases where a 3-sigma detection can be accomplished under 100h (in green on Figure 4). Figure 6.13 shows the estimated required exposure times for a 3-σ detection of the planets in Table 6.13 (from Martins et al., 2016). The planets where a 3-σ detection can be accomplished under 100-h are presented in Table 6.15 (green bars in Figure 6.13).

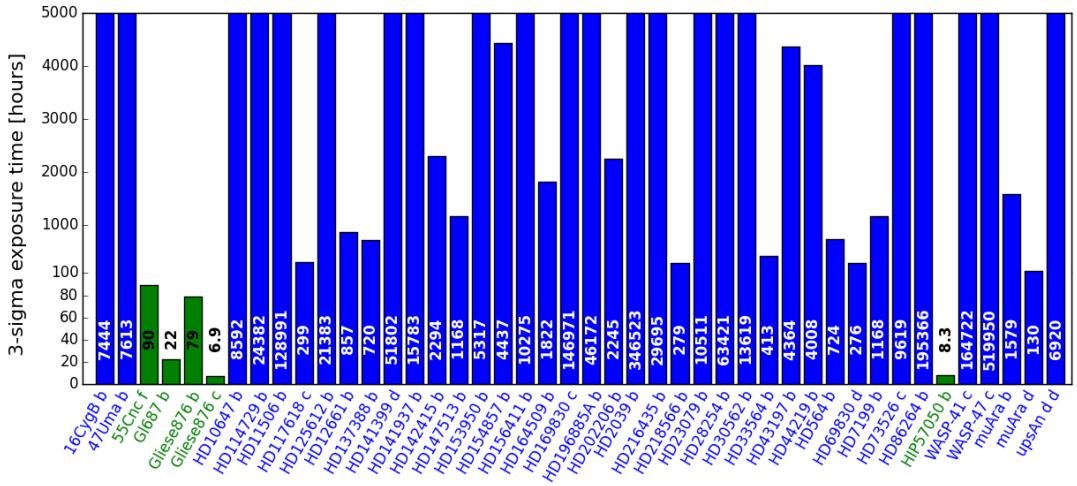

Figure 6.13: Required exposure times for a 3-σ detection of the planets in Table 6.13 (from Martins et al., 2016). The green bars correspond to the planets where a 3-σ detection can be accomplished under 100-h.

DISCUSSION 6.2.3

For all planets in the exoplanet.eu database, we computed the limits of the host's habitable zones using the Kasting et al. (1993) model. Then, we computed the planet-to-star flux ratio for all planets in their hosts Habitable Zones that orbited $V_{mag} \leq 10$ main sequence stars with effective temperatures in the 2000K-8000K range. For these we estimated the time required for a 3-σ detection of their reflected signal with @ELT using the CCF technique. From these targets, only 5 have can be detected with less that 100-h worth of observing time. It is worth noting that these 5 planets are all giant planets, making them unsuitable for life as we know it. However, they might be orbited by satellites with conditions to support life as we know it and be habitable.

From the final sample, all planets orbiting FJK hosts have $V_{mag} \leq 6$. This means that even with 30-m class telescopes, it will be extremely difficult to detect planets in their host's Habitable Zone. However, for M dwarfs, despite the host low intrinsic brightness, the Habitable Zone is close enough to the star to make the planets detectable with the ELT. Of particular interest are the cases of Gliese 876 c and is HIP 57050 b as their required exposure time is under 8-h due to their proximity to their host. Extrapolating to a VLT sized telescope, this means a 3-σ detection under 40-h, implying that even current generation facilities could used to detect these targets.

As a final note, this analysis assumes that the planetary CCF has not been broadened by planetary rotation relatively to the host's (e.g. Kawahara, 2012). A planet with a high rotation rate will have its signal broadened relatively to the host's. Since the area of the CCF is conserved, this implies a reduced CCF amplitude, making it harder to detect.

Chapter 7.
Summary

Atmospheric characterization of exoplanets is a daunting task, at the limit of the capabilities of current generation observing facilities. Nonetheless, in-depth knowledge of an exoplanet's atmosphere is fundamental towards our understanding of the planet's chemistry, physics, origins and ultimately its capability of sustaining life.

In this thesis, we proposed to use the optical high-resolution spectrum of a star reflected on an orbiting exoplanet to recover the planetary albedo and thus characterize the planet's atmosphere. The main problem faced with this approach is the extremely low planet-to-star flux ratio, typically inferior to 10^{-4} for the best case scenario, large planets in close orbits. To surpass this low planet-to-star flux ratio, we proposed a technique that cross-correlates high-resolution spectra with binary masks representing the stellar spectrum. With it, the S/N as measured in the CCF is increased by the square root of the number of spectral lines identified in the mask. This allows the planetary signature to surface above the noise and make it detectable. The application of this technique to HARPS observations of the 51 Pegasi system yielded great results. With it, we were able to recover the reflected optical spectrum of 51 Pegasi b with a 3-σ confidence, and infer that this planet is most likely a highly inflated hot Jupiter planet with a high albedo ($A_g = 0.5$ for $R_p = 1.9 R_{Jup}$). This detection was performed from a total of 2.5-h of exposure time with the HARPS spectrograph. Due to the increased collecting power of the VLT and its higher efficiency, ESPRESSO@VLT should permit us to recover the albedo function from hot Jupiters with just a few hours of observing time (e.g 1-h for 51 Pegasi b and $\sim$ 8-h for HD 209458 b assuming 15 wavelength bins). Similarly, HIRES – and following similar stable high-resolution optical spectrographs to be mounted on 30-m class telescopes (e.g G-CLEF@Giant Magellan Telescope (GMT) Szentgyorgyi et al., 2014) – should permit to recover the albedo function from the same planets but with an increased number of wavelength bins, effectively increasing the level of detail for which this function can be measured. Lowering the number of wavelength bins and/or increasing the total exposure time will permit to probe smaller and/or with larger period planets.

The recovery of the albedo function from exoplanets should permit to place important constrains in the

composition and dynamics of exoplanetary atmospheres. In terms of chemistry, the albedo function will permit to infer the planet's cloud coverage and composition (for example, high reflectances are usually indicative of high-altitude clouds, Garcia-Muñoz et al., 2015). The phase function can be used to infer the atmosphere's back scattering properties, a quantity dependent on the clouds/dust particle size (e.g. Buey et al., 2015). In what regards the physics of the atmosphere, the broadening of the CCF of the planet relatively to the star permits to infer the planet's rotation rate and/or velocity of high-altitude clouds (e.g. Kawahara, 2012). Periodic variations in the reflected flux correlated to the planetary rotation period might hint at the planet's topography. However, the albedo from an exoplanet is not the only factor that modulates the reflected spectrum from an exoplanet. An exciting prospect to further characterize the planet comes from the observation of the phase function of the planet. This function describes the light curve of a planet as a function of orbital phase. It depends not only on the fraction of the planet illuminated by the host star but also on the back scattering properties of the planet's atmosphere.

From the analysis of the UVES observations of the 51 Pegasi system, it is clear that unknown sources of noise are hampering the recovery of the planetary signal (Section 5.2). As such, it is essential to perform an in-depth study of systematic noise sources that might be significant at the signal amplitude level. Some possibilities for the origin of the noise we detected i) the impact of telluric/micro telluric lines; ii) inner reflections in the instrument and/or iii) stitching of the CCD. This genre of study might have important implications in the design and use of future facilities like ESPRESSO@VLT and HIRES@ELT, regardless of the technique used to recover the planetary signal.

The results we present of this work are encouraging, as they exemplify the power of the CCF technique as a powerful tool in the characterization of exoplanetary atmospheres from their optical reflected spectra. To summarize the most important results of this work:

- using the CCF technique, we were able to recover the optical reflected signal from 51 Pegasi b with a 3-σ+ significance, which suggests that 51 Pegasi b is most likely a highly inflated hot Jupiter planet with a high albedo ($A_g = 0.5$ for $R_p = 1.9 R_{Jup}$) (Martins et al., 2015a);

- the CCF technique permits the recovery of the wavelength dependence of reflected spectra of exoplanets, and consequently their albedo function. It allows to distinguish between possible albedo configurations and hint at the planetary atmosphere composition (Martins et al., 2017);

- it will be possible to probe at planetary atmospheres for planets in a vastly accessible orbital parameter range not accessible to other techniques such as transit spectroscopy (Martins et al., 2017);

- even in cases where a low number of wavelength bins is possible, the ratio between the albedo at redder and bluer wavelengths should help constrain possible chemical and physical atmospheric configurations (Martins et al., 2017).

- as close as 2018, ESPRESSO should already be able to recover the albedo function from hot Jupiter class exoplanets with a few hours of exposure time (e.g. 51 Pegasi b with 1-h) (Martins et al., 2017);

- the advent of HIRES will allow to probe smaller planets (e.g. hot Neptunes and super-earths) with just with a few hours of exposure time (e.g. HD 76700 b with around 5-h and 55 Cancri e with about 4-h) (Martins et al., 2017);

- HIRES should also permit to detect the reflected optical signature from exoplanets in their host's Habitable Zones (Martins et al., 2016).

The next-generation of observing facilities will be paramount to build up our understanding of exoplanets as a whole and their atmospheres in particular. Future space-based missions such as PLATO (Rauer et al., 2013) and TESS (Ricker et al., 2014) will be invaluable in the detection of large quantities of exoplanets by performing large-scale photometric transit surveys, with special emphasis given to the search of Earth-like exoplanets in their hosts Habitable Zones. The most promising planets will then be followed closely by both space (e.g., CHEOPS – Fortier et al., 2014; JWST – Gardner et al., 2006) and ground-based (e.g., ESPRESSO@VLT – Pepe et al., 2010; HIRES@ELT – Maiolino et al., 2013) observatories for a detailed characterization. Being free from the influence of Earth's atmosphere, space-based observatories such as the JWST or dedicated space missions such as ARIEL (Tinetti et al., 2016) are expected to provide exquisite photometric measurements and recover low-resolution transmission and reflection/emission profiles from detected transiting planets (e.g. Beichman et al., 2014; Greene et al., 2015). Although their observations are imprinted with the Earth's atmospheric spectral signature, ground-based observatories are able to complement their space counterparts either in terms of the high-resolution spectroscopic measurements they can provide (e.g., ESPRESSO@VLT – Pepe et al., 2010), the sheer collecting power of 30-m class telescopes (e.g., ESO's ELT – Gilmozzi et al., 2007) or by permitting "easy" upgrades to any available instrument (e.g., the SPHERE+ upgrade mentioned in Lovis et al., 2017), a feature unavailable to space observatories. For ground-based facilities, the impact of the atmosphere can be mitigated with advanced Adaptive Optics (AO) systems (e.g, SPHERE@ESO's VLT – Beuzit et al., 2008) and the fact that the Earth's atmospheric spectral lines will appear separated from their exoplanet counterparts on the RV domain. Furthermore, high-resolution spectroscopy data analysis methods – such as the CCF technique we propose – permit to study in detail the atmospheres of non-transiting planets (e.g. Snellen et al., 2015; Martins et al., 2017). At the limit, synergies between the accurate photometric data obtained by space observatories with the precise high-resolution spectroscopic measurements that only ground-based observatories can achieve, researchers expect to accomplish a detailed and complete characterization of the planets most likely to support life as we know it. The search for bio-signature gases will enter a golden age, and most probably signs of life will be found within the next couple of decades. The future of exoplanet research presents itself extremely bright.

References

Adams, E. R.; S. Seager, and L. Elkins-Tanton (2007). "Ocean Planet or Thick Atmosphere: On the Mass-Radius Relationship for Solid Exoplanets with Massive Atmospheres". In: *The Astrophysical Journal, Volume 673, Issue 2, article id. 1160-1164, pp. (2008).* 673. arXiv: 0710.4941.

Agol, E. et al. (2005). "On detecting terrestrial planets with timing of giant planet transits". In: *Monthly Notices of the Royal Astronomical Society* 359.2, pp. 567–579. arXiv: arXiv:1011.1669v3.

Alonso, R. et al. (2009). "The secondary eclipse of the transiting exoplanet CoRoT-2b". In: *Astronomy & Astrophysics* 26, p. 4. arXiv: 0906.2814.

Anderson, D. R. et al. (2011). "Thermal emission at 4.5 and 8 micron of WASP-17b, an extremely large planet in a slightly eccentric orbit". In: *Monthly Notices of the Royal Astronomical Society, Volume 416, Issue 3, pp. 2108-2122.* 416, pp. 2108–2122. arXiv: 1101.5620.

Angerhausen, D.; E. DeLarme, and J. a. Morse (2015). "A comprehensive study of Kepler phase curves and secondary eclipses – temperatures and albedos of confirmed Kepler giant planets". In: *Publications of the Astronomical Society of the Pacific* Submittted, p. 14. arXiv: 1404.4348.

Anglada-Escudé, G. et al. (2016). "A terrestrial planet candidate in a temperate orbit around Proxima Centauri". In: *Nature, Volume 536, Issue 7617, pp. 437-440 (2016).* 536.7617, pp. 437–440. arXiv: 1609.03449.

Arnold, L. et al. (2014). "The Earth as an extrasolar transiting planet - II: HARPS and UVES detection of water vapor, biogenic O$_2$, and O$_3$". In: *Astronomy & Astrophysics, Volume 564, id.A58, 18 pp.* 564. arXiv: 1402.0592.

Baranne, A. et al. (1996). "ELODIE: A spectrograph for accurate radial velocity measurements". In: *Astronomy and Astrophysics Supplement Series* 119.2, pp. 373–390.

Barman, T. S. et al. (2011). "CLOUDS AND CHEMISTRY IN THE ATMOSPHERE OF EXTRASOLAR PLANET HR8799b". In: *The Astrophysical Journal* 733.1, p. 65. arXiv: 1103.3895.

Barnes, J. W. and J. W. (2007). "Effects of Orbital Eccentricity on Extrasolar Planet Transit Detection and Lightcurves". In: *The Publications of the Astronomical Society of the Pacific, Volume 119, Issue 859, pp. 986-993.* 119, pp. 986–993. arXiv: 0708.0243.

Barros, S. C. C. et al. (2016). "Discovery of WASP-113b and WASP-114b, two inflated hot-Jupiters with contrasting densities". In: pp. 1–10. arXiv: 1607.02341.

Batalha, N. M. et al. (2013). "Planetary Candidates Observed by Kepler, III: Analysis of the First 16 Months of Data". In: *The Astrophysical Journal Supplement, Volume 204, Issue 2, article id. 24, 21 pp. (2013).* 204. arXiv: 1202.5852.

Batista, V. et al. (2015). "CONFIRMATION OF THE OGLE-2005-BLG-169 PLANET SIGNATURE AND ITS CHARACTERISTICS WITH LENS–SOURCE PROPER MOTION DETECTION". In: *The Astrophysical Journal* 808.2, p. 170.

Beaulieu, J.-P. et al. (2006). "Discovery of a cool planet of 5.5 Earth masses through gravitational microlensing". In: *Nature* 439.7075, pp. 437–440. arXiv: 0601563 [astro-ph].

Beichman, C. et al. (2014). "Observations of Transiting Exoplanets with the James Webb Space Telescope (JWST)". In: *Publications of the Astronomical Society of the Pacific* 126.946, pp. 1134–1173.

Bennett, D. P. et al. (2010). "MASSES AND ORBITAL CONSTRAINTS FOR THE OGLE-2006-BLG-109Lb,c JUPITER/SATURN ANALOG PLANETARY SYSTEM". In: *The Astrophysical Journal* 713.2, pp. 837–855. arXiv: 0911.2706.

Bennett, D. P. et al. (2015). "CONFIRMATION OF THE PLANETARY MICROLENSING SIGNAL AND STAR AND PLANET MASS DETERMINATIONS FOR EVENT OGLE-2005-BLG-169". In: *The Astrophysical Journal* 808.2, p. 169.

Beuzit, J.-L. et al. (2008). "SPHERE: a 'Planet Finder' instrument for the VLT". In: *Ground-based and Airborne Instrumentation for Astronomy II. Edited by McLean, Ian S.; Casali, Mark M. Proceedings of the SPIE, Volume 7014, article id. 701418, 12 pp. (2008).* Ed. by I. S. McLean and M. M. Casali. Vol. 7014, p. 701418.

Birkby, J. et al. (2017). "Discovery of water at high spectral resolution in the atmosphere of 51 Peg b". In: *The Astronomical Journal* 153.3, pp. 1–18. arXiv: 1701.07257.

Boley, A. C.; A. P. G. Contreras, and B. Gladman (2016). "The In Situ Formation of Giant Planets at Short Orbital Periods". In: arXiv: 1510.04276.

Bolton, S. J. et al. (2017). "Jupiter's interior and deep atmosphere: The initial pole-to-pole passes with the Juno spacecraft". In: *Science* 356.6340, pp. 821–825.

Bonfils, X. et al. (2013). "The HARPS search for southern extra-solar planets XXXI. The M-dwarf sample". In: *Astronomy & Astrophysics, Volume 549, id.A109, 75 pp.* 549. arXiv: 1111.5019.

Borucki, W. J. et al. (2010). "Kepler Planet-Detection Mission: Introduction and First Results". In: *Science* 327.5968, pp. 977–980.

Borucki, W. J. et al. (2012). "Kepler-22b: A 2.4 EARTH-RADIUS PLANET IN THE HABITABLE ZONE OF A SUN-LIKE STAR". In: *The Astrophysical Journal* 745.2, p. 120. arXiv: 1112.1640.

Braun, K. von et al. (2012). "55 Cancri: Stellar Astrophysical Parameters, a Planet in the Habitable Zone, and Implications for the Radius of a Transiting Super-Earth". In: *The Astrophysical Journal, Volume 740, Issue 1, article id. 49, 6 pp. (2011).* 740. arXiv: 1106.1152.

Brogi, M. et al. (2012). "The signature of orbital motion from the dayside of the planet τ Boötis b". In: *Nature* 486.7404, pp. 502–504. arXiv: 1206.6109 [astro-ph.EP].

Brogi, M. et al. (2013). "DETECTION OF MOLECULAR ABSORPTION IN THE DAYSIDE OF EXOPLANET 51 PEGASI b?" In: *The Astrophysical Journal* 767.1, p. 27. arXiv: 1302.6242.

Brogi, M. et al. (2014). "Carbon monoxide and water vapor in the atmosphere of the non-transiting exoplanet HD 179949 b". In: *aa* 565, A124. arXiv: 1404.3769.

Brogi, M. et al. (2015). "Rotation and winds of exoplanet HD 189733 b measured with high-dispersion transmission spectroscopy". In: p. 24. arXiv: 1512.05175.

Brogi, M. et al. (2016). "Rotation and Winds of Exoplanet HD 189733 b Measured with High-dispersion Transmission Spectroscopy". In: *The Astrophysical Journal, Volume 817, Issue 2, article id. 106, 15 pp. (2016).* 817. arXiv: 1512.05175.

Buey, J.-T. et al. (2015). "Tables of phase functions, opacities, albedos, equilibrium temperatures, and radiative accelerations of dust grains in exoplanets". In: *Monthly Notices of the Royal Astronomical Society* 454.1, pp. 2–27. arXiv: 1505.08013.

Buratti, B. J.; J. A. Mosher, and T. V. Johnson (1990). "Albedo and color maps of the Saturnian satellites". In: *Icarus* 87.2, pp. 339–357.

Butler, P. et al. (2004). "A Neptune-Mass Planet Orbiting the Nearby M Dwarf GJ 436". In: *The Astrophysical Journal, Volume 617, Issue 1, pp. 580-588.* 617. arXiv: 0408587 [astro-ph].

Butler, R. P. et al. (1997). "Three New "51 Pegasi–Type" Planets". In: *The Astrophysical Journal* 474.

Butler, R. P. et al. (2006). "Catalog of Nearby Exoplanets". In: *The Astrophysical Journal* 646.1, pp. 505–522. arXiv: 0607493 [astro-ph].

Cameron, A. C. (2012). "Extrasolar planets: Astrophysical false positives". In: *Nature* 492.7427, pp. 48–50.

Cameron, A. C. et al. (1999). "Probable detection of starlight reflected from the giant planet orbiting [tau] Bootis". In: *Nature* 402.6763, pp. 751–755. arXiv: 9911314 [astro-ph].

Charbonneau, D. et al. (1999). "An Upper Limit on the Reflected Light from the Planet Orbiting the Star tau Bootis". In: *The Astrophysical Journal* 522.1997, p. L145. arXiv: 9907195 [astro-ph].

Charbonneau, D. et al. (2000). "Detection of Planetary Transits Across a Sun-like Star". In: *The Astrophysical Journal, Volume 529, Issue 1, pp. L45-L48.* 529, pp. L45–L48. arXiv: 9911436 [astro-ph].

Charbonneau, D. et al. (2002). "Detection of an Extrasolar Planet Atmosphere". In: *Astrophysical Journal* 568.1, pp. 377–384. arXiv: 0111544 [astro-ph].

Chauvin, G. et al. (2004). "A Giant Planet Candidate near a Young Brown Dwarf". In: *Astronomy and Astrophysics, v.425, p.L29-L32 (2004)* 425, pp. L29–L32. arXiv: 0409323 [astro-ph].

Chauvin, G. et al. (2017). "Discovery of a warm, dusty giant planet around HIP65426". In: *eprint arXiv:1707.01413.* arXiv: 1707.01413.

Christiansen, J. L. et al. (2010). "STUDYING THE ATMOSPHERE OF THE EXOPLANET HAT-P-7b VIA SECONDARY ECLIPSE MEASUREMENTS WITH EPOXI , SPITZER , AND KEPLER". In: *The Astrophysical Journal* 710.1, pp. 97–104. arXiv: 0912.2132.

Civeit, T. et al. (2005). "On measuring planetary winds using high-resolution spectroscopy in visible wavelengths". In: *Astronomy and Astrophysics* 431.3, pp. 1157–1166.

Cosentino, R. et al. (2012). "Harps-N: the new planet hunter at TNG". In: *Ground-based and Airborne Instrumentation for Astronomy IV. Proceedings of the SPIE, Volume 8446, article id. 84461V, 20 pp. (2012).* Ed. by I. S. McLean; S. K. Ramsay, and H. Takami. Vol. 8446, p. 84461V.

Coughlin, J. L. et al. (2016). "Planetary Candidates Observed by Kepler. VII. The First Fully Uniform Catalog Based on The Entire 48 Month Dataset (Q1-Q17 DR24)". In: *The Astrophysical Journal Supplement Series, Volume 224, Issue 1, article id. 12, 27 pp. (2016).* 224. arXiv: 1512.06149.

Cowan, N. B. and E. Agol (2011). "the Statistics of Albedo and Heat Recirculation on Hot Exoplanets". In: *The Astrophysical Journal* 729.11pp, p. 54. arXiv: 1001.0012 [astro-ph.EP].

Cunha, D. et al. (2013). "Impact of stellar companions on precise radial velocities". In: *Astronomy & Astrophysics* 550, A75. arXiv: 1212.2848.

Cunha, D. et al. (2014). "Impact of micro-telluric lines on precise radial velocities and its correction". In: *Astronomy & Astrophysics, Volume 568, id.A35, 7 pp.* 568. arXiv: 1407.0181.

David, T. J. et al. (2016). "A Neptune-sized transiting planet closely orbiting a 5-10-million-year-old star." In: *Nature* 534.7609, p. 42. arXiv: 1606.06729.

Dekker, H. et al. (2000). "Design, construction, and performance of UVES, the echelle spectrograph for the UT2 Kueyen Telescope at the ESO Paranal Observatory". In: *Proc. SPIE Vol. 4008, p. 534-545, Optical and IR Telescope Instrumentation and Detectors, Masanori Iye; Alan F. Moorwood; Eds.* Ed. by M. Iye and A. F. M. Moorwood. Vol. 4008, p. 534.

Del Genio, A. D. and J. M. Barbara (2017). "An objective classification of Saturn cloud features from Cassini ISS images". In: *Icarus, Volume 271, p. 222-236.* 271, pp. 222–236. arXiv: 1709.08549.

Delgado-Mena, E. et al. (2010). "Chemical Clues on the Formation of Planetary Systems: C/O vs Mg/Si for HARPS GTO Sample". In: *The Astrophysical Journal, Volume 725, Issue 2, pp. 2349-2358 (2010).* 725, pp. 2349–2358. arXiv: 1009.5224.

Deming, D. et al. (2005). "Infrared radiation from an extrasolar planet". In: *Nature* 434.7034, pp. 740–743. arXiv: 0503554 [astro-ph].

Demory, B.-O. (2014). "The Albedos of Kepler's Close-in super-Earths". In: *The Astrophysical Journal Letters* 789.1. arXiv: 1405.3798.

Demory, B.-O. et al. (2011). "THE HIGH ALBEDO OF THE HOT JUPITER KEPLER-7 b". In: *The Astrophysical Journal* 735.1, p. L12. arXiv: arXiv:1105.5143v1.

Des Marais, D. J. et al. (2002). "Remote Sensing of Planetary Properties and Biosignatures on Extrasolar Terrestrial Planets". In: *Astrobiology* 2.2, pp. 153–181.

Díaz, R. F. et al. (2014). "Pastis: Bayesian extrasolar planet validation-I. General framework, models, and performance". In: *Monthly Notices of the Royal Astronomical Society* 441.2, pp. 983–1004. arXiv: arXiv:1403.6725v1.

Dumusque, X. et al. (2012). "An Earth-mass planet orbiting α Centauri B". In: *Nature* 491.7423, pp. 207–211.

Endl, M. et al. (2011). "KEPLER-15b: A HOT JUPITER ENRICHED IN HEAVY ELEMENTS AND THE FIRST KEPLER MISSION PLANET CONFIRMED WITH THE HOBBY-EBERLY TELESCOPE". In: *The Astrophysical Journal Supplement Series* 197.1, p. 13. arXiv: 1107.2596.

Esteves, L. J.; E. J. W. De Mooij, and R. Jayawardhana (2015). "Changing Phases of Alien Worlds: Probing Atmospheres of Kepler Planets with High-Precision Photometry". In: *The Astrophysical Journal* 804, p. 28. arXiv: 1407.2245.

Esteves, L. J.; E. J. De Mooij, and R. Jayawardhana (2013). "Optical phase curves of kepler exoplanets". In: *Astrophysical Journal* 772.1, p. 51. arXiv: 1305.3271.

Evans, T. M. et al. (2013). "THE DEEP BLUE COLOR OF HD 189733b: ALBEDO MEASUREMENTS WITH HUBBLE SPACE TELESCOPE /SPACE TELESCOPE IMAGING SPECTROGRAPH AT VISIBLE WAVELENGTHS". In: *The Astrophysical Journal* 772.2, p. L16. arXiv: 1307.3239.

Figueira, P. R. L. (2010). "Radial Velocities in the Infra-Red: New Light Shed on Planets". PhD thesis. Université de Genève.

Fischer, D. A. et al. (2008). "Five Planets Orbiting 55 Cancri". In: *The Astrophysical Journal* 675.1, pp. 790–801. arXiv: 0712.3917.

Fortier, A. et al. (2014). "CHEOPS: a space telescope for ultra-high precision photometry of exoplanet transits". In: *Proceedings of the SPIE, Volume 9143, id. 91432J 12 pp. (2014).* Ed. by J. M. Oschmann et al. Vol. 9143, 91432J.

Fortney, J. J.; I. Baraffe, and B. Militzer (2009). "Giant Planet Interior Structure and Thermal Evolution". In: *Exoplanets, edited by S.˜Seager.˜ Tucson, AZ: University of Arizona Press, 2011, 526 pp.˜ ISBN 978-0-8165-2945-2., p.397-418.* Ed. by S. Seager, pp. 397–418. arXiv: 0911.3154.

Fortney, J. J. et al. (2011). "Discovery and Atmospheric Characterization of Giant Planet Kepler-12b: An Inflated Radius Outlier". In: *The Astrophysical Journal Supplement Series* 197.1, p. 9. arXiv: 1109.1611.

Fressin, F. et al. (2013). "The false positive rate of Kepler and the occurrence of planets". In: *The Astrophysical Journal, Volume 766, Issue 2, article id. 81, 20 pp. (2013).* 766. arXiv: 1301.0842.

Freudling, W. et al. (2013). "Automated data reduction workflows for astronomy". In: *aa* 559, A96. arXiv: arXiv:1311.5411v1.

Fukui, A. et al. (2015). "OGLE-2012-BLG-0563Lb: A SATURN-MASS PLANET AROUND AN M DWARF WITH THE MASS CONSTRAINED BY SUBARU AO IMAGING". In: *The Astrophysical Journal* 809.1, p. 74.

Garcia-Muñoz, A. and K. G. Isaak (2015). "Probing exoplanet clouds with optical phase curves". In: *Proceedings of the National Academy of Sciences* 112.44, pp. 13461–13466. arXiv: 1511.01424.

Garcia-Muñoz, A. et al. (2012). "Glancing Views of the Earth: From a Lunar Eclipse To an Exoplanetary Transit". In: *The Astrophysical Journal* 755.2, p. 103. arXiv: 1206.4344.

Gardner, J. P. et al. (2006). "The James Webb Space Telescope". In: *Space Science Reviews, Volume 123, Issue 4, pp.485-606* 123, pp. 485–606. arXiv: 0606175 [astro-ph].

Gilmozzi, R. and J. Spyromilio (2007). "The European Extremely Large Telescope (E-ELT)". In: *The Messenger, volume 127, page 11* 127.

Goldreich, P. and S. Soter (1966). "Q in the solar system". In: *Icarus* 5.1-6, pp. 375–389.

Goodman, J. (2009). "Thermodynamics of Atmospheric Circulation on Hot Jupiters". In: *The Astrophysical Journal* 693.2, pp. 1645–1649. arXiv: 0810.1282.

Gould, A. and Andrew (2000). "A Natural Formalism for Microlensing". In: *The Astrophysical Journal, Volume 542, Issue 2, pp. 785-788.* 542, pp. 785–788. arXiv: 0001421 [astro-ph].

Gould, A. et al. (2010). "Frequency of Solar-Like Systems and of Ice and Gas Giants Beyond the Snow Line From High-Magnification Microlensing Events in 2005-2008". In: *The Astrophysical Journal* 720.2, pp. 1073–1089. arXiv: 1001.0572 [astro-ph.EP].

Gray, D. F. and D. F. (1992). "The observation and analysis of stellar photospheres." In: *Camb. Astrophys. Ser., Vol. 20,* 20.

Greco, J. P. and A. S. Burrows (2015). "the Direct Detectability of Giant Exoplanets in the Optical". In: *The Astrophysical Journal* 808.2, p. 172. arXiv: 1505.07832.

Greene, T. P. et al. (2015). "Characterizing transiting exoplanet atmospheres with JWST". In: *The Astrophysical Journal, Volume 817, Issue 1, article id. 17, 22 pp. (2016).* 817. arXiv: 1511.05528.

Grunblatt, S. K.; A. W. Howard, and R. D. Haywood (2015). "Determining the Mass of Kepler-78b With Nonparametric Gaussian Process Estimation". In: *The Astrophysical Journal, Volume 808, Issue 2, article id. 127, 10 pp. (2015).* 808. arXiv: 1501.00369.

Guillot, T. and A. P. Showman (2002). "Evolution of "51Peg b-like" Planets". In: *Astronomy and Astrophysics, v.385, p.156-165 (2002)* 385, pp. 156–165. arXiv: 0202234 [astro-ph].

Guillot, T. et al. (2006). "A correlation between the heavy element content of transiting extrasolar planets and the metallicity of their parent stars". In: *Astronomy and Astrophysics, Volume 453, Issue 2, July II 2006, pp.L21-L24* 453.2, pp. L21–L24. arXiv: 0605751 [astro-ph].

Hatzes, A. P. and H. Rauer (2015). "a Definition for Giant Planets Based on the Mass–Density Relationship". In: *The Astrophysical Journal* 810.2, p. L25. arXiv: 1506.05097.

Hedges, C. and N. Madhusudhan (2016). "Effect of Pressure Broadening on Molecular Absorption Cross Sections in Exoplanetary Atmospheres". In: *Monthly Notices of the Royal Astronomical Society* 458.2, pp. 1427–1449. arXiv: 1602.00751.

Henry, G. W. et al. (1997). "Properties of Sun-like Stars with Planets: 51 Pegasi, 47 Ursae Majoris, 70 Virginis, and HD 114762". In: *The Astrophysical Journal* 474.1, pp. 503–510.

Hermes, J. J. and J. J. (2017). "Timing by Stellar Pulsations as an Exoplanet Discovery Method". In: *eprint arXiv:1708.00896.* arXiv: 1708.00896.

Holman, M. J. et al. (2010). "Kepler-9: A System of Multiple Planets Transiting a Sun-Like Star, Confirmed by Timing Variations". In: *Science* 330.6000, pp. 51–54.

Holman, M. J. and N. W. Murray (2004). "The Use of Transit Timing to Detect Extrasolar Planets with Masses as Small as Earth". In: *Science, Volume 307, Issue 5713, pp. 1288-1291 (2005).* 307.2005, pp. 1288–1291. arXiv: 0412028 [astro-ph].

Horak, H. G. (1950). "Diffuse Reflection by Planetary Atmospheres." In: *The Astrophysical Journal* 112, p. 445.

Howard, A. W. et al. (2010). "The Occurrence and Mass Distribution of Close-in Super-Earths, Neptunes, and Jupiters". In: *Science* 330.6004, pp. 653–655. arXiv: 1011.0143 [astro-ph.EP].

Howell, S. B. and S. B. (2000). "Handbook of CCD Astronomy". In: *Handbook of CCD astronomy / Steve B. Howell. Cambridge, U.K. ; New York : Cambridge University Press, c2000. (Cambridge observing handbooks for research astronomers ; 2).*

Howell, S. B. et al. (2014). "The K2 Mission: Characterization and Early results". In: *Publications of the Astronomical Society of Pacific, Volume 126, Issue 938, pp. 398 (2014).* 126.938, p. 398. arXiv: 1402.5163.

Hu, R. et al. (2015). "A Semi-Analytical Model of Visible-Wavelength Phase Curves of Exoplanets and Applications to Kepler-7 b and Kepler-10 b". In: *The Astrophysical Journal* 802.1, p. 51. arXiv: 1501.03876.

Huang, S.-S. (1959). "Occurrence of Life in the Universe". In: *American Scientist, Vol. 47, No. 3, p. 397-402* 47, pp. 397–402.

Iribarne, J. V. (V. and W. L. Godson (1981). *Atmospheric thermodynamics*. D. Reidel, p. 259.

Iro, N.; B. Bézard, and T. Guillot (2005). "A time-dependent radiative model of HD 209458b". In: *Astronomy & Astrophysics* 436, pp. 719–727. arXiv: 0409468 [astro-ph].

Jones, H. R. A. et al. (2010). "A long-period planet orbiting a nearby Sun-like star". In: *Monthly Notices of the Royal Astronomical Society* 403.4, pp. 1703–1713.

Jorissen, A.; M. Mayor, and S. Udry (2001). "The distribution of exoplanet masses". In: *Astronomy and Astrophysics, v.379, p.992-998 (2001)* 379.3, pp. 992–998. arXiv: 0105301 [astro-ph].

Kalas, P. et al. (2008). "Optical Images of an Exosolar Planet 25 Light Years from Earth". In: arXiv: 0811.1994.

Kasting, J. F.; D. P. Whitmire, and R. T. Reynolds (1993). "Habitable Zones around Main Sequence Stars". In: *Icarus* 101.1, pp. 108–128.

Kawahara, H. (2012). "The Spin Effect on Planetary Radial Velocimetry of Exoplanets". In: *The Astrophysical Journal Letters*. arXiv: 1209.0101.

Kempton, E. M.-R.; R. Perna, and K. Heng (2014). "High Resolution Transmission Spectroscopy As a Diagnostic for Jovian Exoplanet Atmospheres: Constraints From Theoretical Models". In: *The Astrophysical Journal* 795.1, p. 24. arXiv: 1409.1250.

Kervella, P. et al. (2016). "The close circumstellar environment of Betelgeuse - III. SPHERE/ZIMPOL visible polarimetry of the inner envelope and photosphere". In: *Astronomy & Astrophysics, Volume 585, id.A28, 5 pp.* 585. arXiv: 1511.04451.

Khalafinejad, S. et al. (2017). "Exoplanetary atmospheric sodium revealed by orbital motion". In: *Astronomy & Astrophysics* 598, A131. arXiv: 1610.01610.

Kitchin, C. R. and C. R. (2003). "Astrophysical techniques". In: *Astrophysical techniques, by C.R. Kitchin. 4th ed. Bristol; Philadelphia: Institute of Physics Publishing, 2003.*

Kley, W. and R. P. Nelson (2012). "Planet-Disk Interaction and Orbital Evolution". In: *Annual Review of Astronomy and Astrophysics, vol. 50, p.211-249* 50, pp. 211–249. arXiv: 1203.1184.

Knutson, H. A. (2013). "Exoplanet atmospheres". In: *Physics Today* 66.7, pp. 64–65. arXiv: 1005.4037.

Knutson, H. A. et al. (2009). "THE 8 μm PHASE VARIATION OF THE HOT SATURN HD 149026b". In: *The Astrophysical Journal* 703.1, pp. 769–784. arXiv: arXiv:0908.1977v1.

Knutson, H. A. et al. (2012). "3.6 AND 4.5 μm PHASE CURVES AND EVIDENCE FOR NON-EQUILIBRIUM CHEMISTRY IN THE ATMOSPHERE OF EXTRASOLAR PLANET HD 189733b". In: *The Astrophysical Journal* 754.1, p. 22. arXiv: 1206.6887.

Kok, R. J. de et al. (2013). "Detection of carbon monoxide in the high-resolution day-side spectrum of the exoplanet HD 189733b". In: *Astronomy & Astrophysics* 554.2011, A82. arXiv: arXiv:1304.4014v1.

Koll, D. D. B. and D. S. Abbot (2016). "Temperature Structure and Atmospheric Circulation of Dry, Tidally Locked Rocky Exoplanets". In: *The Astrophysical Journal, Volume 825, Issue 2, article id. 99, 22 pp. (2016).* 825. arXiv: 1605.01066.

Komacek, T. D.; A. P. Showman, and X. Tan (2016). "Atmospheric Circulation of Hot Jupiters: Dayside-Nightside Temperature Differences. II. Comparison with Observations". In: *The Astrophysical Journal, Volume 835, Issue 2, article id. 198, 14 pp. (2017).* 835. arXiv: 1610.03893.

Konopacky, Q. M. et al. (2013). "Detection of Carbon Monoxide and Water Absorption Lines in an Exoplanet Atmosphere". In: *Science* 339.6126, pp. 1398–1401. arXiv: 1303.3280.

Kraus, A. L. and M. J. Ireland (2012). "LkCa 15: A Young Exoplanet Caught at Formation?" In: *The Astrophysical Journal, Volume 745, Issue 1, article id. 5, 12 pp. (2012).* 745. arXiv: 1110.3808.

Kubas, D. et al. (2012). "A frozen super-Earth orbiting a star at the bottom of the main sequence". In: *Astronomy & Astrophysics* 540, A78.

Kurucz, R. L. (2006). "High Resolution Irradiance Spectrum from 300 to 1000 nm". In: *I Can* June, p. 3. arXiv: 0605029v1 [arXiv:astro-ph].

Kuzuhara, M. et al. (2013). "Direct Imaging of a Cold Jovian Exoplanet in Orbit Around the Sun-Like Star Gj 504". In: *The Astrophysical Journal* 774.1, p. 11. arXiv: 1307.2886.

Langford, S. V. et al. (2010). "A comparison of spectroscopic methods for detecting the starlight scattered by transiting hot Jupiters, with an application to Subaru data for HD 209458b and HD 189733b". In: *Monthly Notices of the Royal Astronomical Society* 415.1, pp. 673–686. arXiv: 1006.5492.

Langlois, M. et al. (2010). "High contrast imaging with IRDIS near infrared polarimeter". In: *Proceedings of the SPIE, Volume 7735, id. 77352U (2010).* Ed. by I. S. McLean; S. K. Ramsay, and H. Takami. Vol. 7735, 77352U.

Lavvas, P.; T. Koskinen, and R. V. Yelle (2014). "Electron Densities and Alkali Atoms in Exoplanet Atmospheres". In: *The Astrophysical Journal* 796.1, p. 15.

Lee, Y. J. et al. (2017). "Scattering Properties of the Venusian Clouds Observed by the UV Imager on board Akatsuki". In: *The Astronomical Journal* 154.2, p. 44.

Léger, A. et al. (2009). "Transiting exoplanets from the CoRoT space mission". In: *Astronomy & Astrophysics* 506.1, pp. 287–302.

Leigh, C. et al. (2003). "A search for starlight reflected from HD 75289 b". In: *Monthly Notices of the Royal Astronomical Society, Volume 346, Issue 2, pp. L16-L20.* 346, pp. L16–L20. arXiv: 0310489 [astro-ph].

Line, M. R. and V. Parmentier (2016). "the Influence of Nonuniform Cloud Cover on Transit Transmission Spectra". In: *The Astrophysical Journal* 820.1, p. 78. arXiv: 1511.09443.

Lissauer, J. J. et al. (2012). "Almost All of Kepler's Multiple Planet Candidates are Planets". In: *The Astrophysical Journal, Volume 750, Issue 2, article id. 112, 15 pp. (2012).* 750. arXiv: 1201.5424.

Lissauer, J. J. et al. (2014). "Validation of Kepler's Multiple Planet Candidates. II: Refined Statistical Framework and Descriptions of Systems of Special Interest". In: *The Astrophysical Journal, Volume 784, Issue 1, article id. 44, 21 pp. (2014).* 784.1, p. 44. arXiv: 1402.6352.

Lo Curto, G. et al. (2012). "Astronomical Spectrograph Calibration at the Exo-Earth Detection Limit". In: *The Messenger, vol. 149, p. 2-6* 149, pp. 2–6.

Lodders, K. (2010). "Exoplanet Chemistry". In: *Formation and Evolution of Exoplanets*, pp. 157–186. arXiv: 0910.0811.

Lopez, E. D. and J. J. Fortney (2014). "Understanding the Mass-Radius Relation for Sub-Neptunes: Radius As a Proxy for Composition". In: *The Astrophysical Journal* 792.1, p. 1. arXiv: 1311.0329.

Louden, T. and P. J. Wheatley (2015). "SPATIALLY RESOLVED EASTWARD WINDS AND ROTATION OF HD 189733b". In: *The Astrophysical Journal* 814.2, p. L24. arXiv: 1511.03689.

Lovis, C. and D. A. Fischer (2010). "Radial Velocity Techniques for Exoplanets". In: *Exoplanets*. Ed. by S. Seager, p. 30.

Lovis, C. et al. (2006). "The exoplanet hunter HARPS: unequalled accuracy and perspectives toward 1 cm s -1 precision". In: *Proceedings of SPIE*. Ed. by I. S. McLean and M. Iye. Vol. 6269, 62690P.

Lovis, C. et al. (2011). "The HARPS search for southern extra-solar planets. XXXI. Magnetic activity cycles in solar-type stars: statistics and impact on precise radial velocities". In: *ArXiv e-prints* 58, p. 25. arXiv: 1107.5325.

Lovis, C. et al. (2017). "Atmospheric characterization of Proxima b by coupling the SPHERE high-contrast imager to the ESPRESSO spectrograph". In: *Astronomy & Astrophysics* 599, A16. arXiv: 1609.03082.

Luhman, K. L. and R. Jayawardhana (2002). "An Adaptive Optics Search for Companions to Stars with Planets". In: *The Astrophysical Journal, Volume 566, Issue 2, pp. 1132-1146.* 566, pp. 1132–1146. arXiv: 0110550 [astro-ph].

MacDonald, R. J. and N. Madhusudhan (2017). "HD 209458b in New Light: Evidence of Nitrogen Chemistry, Patchy Clouds and Sub-Solar Water". In: *Monthly Notices of the Royal Astronomical Society, Volume 469, Issue 2, p.1979-1996* 469, pp. 1979–1996. arXiv: 1701.01113.

Macintosh, B. A. et al. (2008). "The Gemini Planet Imager: from science to design to construction". In: *Adaptive Optics Systems. Edited by Hubin, Norbert; Max, Claire E.; Wizinowich, Peter L. Proceedings of the SPIE, Volume 7015, article id. 701518, 13 pp. (2008).* Ed. by N. Hubin; C. E. Max, and P. L. Wizinowich. Vol. 7015, p. 701518.

Madhusudhan, N. and A. S. Burrows (2012). "Analytic Models for Albedos, Phase Curves, and Polarization of Reflected Light From Exoplanets". In: *The Astrophysical Journal* 747.1, p. 25. arXiv: 1112.4476.

Maiolino, R. et al. (2013). "A Community Science Case for E-ELT HIRES". In: *eprint arXiv:1310.3163*. arXiv: 1310.3163.

Marley, M. S. et al. (1999). "Reflected Spectra and Albedos of Extrasolar Giant Planets. I. Clear and Cloudy Atmospheres". In: *The Astrophysical Journal* 513.2, pp. 879–893. arXiv: 9810073 [astro-ph].

Marois, C. et al. (2010). "Images of a fourth planet orbiting HR 8799". In: *Nature* 468.7327, pp. 1080–1083. arXiv: 1011.4918.

Marois, C. et al. (2005). "Angular Differential Imaging: a Powerful High-Contrast Imaging Technique". In: *The Astrophysical Journal, Volume 641, Issue 1, pp. 556-564.* 641, pp. 556–564. arXiv: 0512335 [astro-ph].

Martins, J. H. C. et al. (2013). "Spectroscopic direct detection of reflected light from extrasolar planets". en. In: *Monthly Notices of the Royal Astronomical Society* 436.2, pp. 1215–1224. arXiv: 1308.6516 [astro-ph.EP].

Martins, J. H. C. et al. (2015a). "Evidence for a spectroscopic direct detection of reflected light from 51 Pegasi b". In: *Astronomy & Astrophysics* 576.51, A134. arXiv: 1504.0596.

Martins, J. H. C. et al. (2015b). "Exoplanet Reflections: the light from 51 Peg b". In: *Proceedings of colloquium 'Twenty years of giant exoplanets' held at Observatoire de Haute Provence, France, October 5-9, 2015. Edited by I. Boisse, O. Demangeon, F. Bouchy {\amp} L. Arnold, p. 66-74. Published by the Observatoire de Haute-Provence, Insti*. Ed. by I. Boisse et al., pp. 66–74.

Martins, J. H. C. et al. (2016). "Reflected Light from Giant Planets in Habitable Zones: Tapping into the Power of the Cross-Correlation Function". In: *Origins of Life and Evolution of Biospheres* 46.4, pp. 487–498. arXiv: 1604.01086.

Martins, J. H. C. et al. (2017). "Recovering the color-dependent albedo of exoplanets with high-resolution spectroscopy: from ESPRESSO to the ELT. (submitted)". In: *Monthly Notices of the Royal Astronomical Society*.

Mawet, D. et al. (2005). "Annular Groove Phase Mask Coronagraph". In: *The Astrophysical Journal* 633.2, pp. 1191–1200.

Mayor, M. and D. Queloz (1995). "A Jupiter-mass companion to a solar-type star". In: *Nature* 378.6555, pp. 355–359.

Mayor, M. et al. (2003). "Setting New Standards with HARPS". In: *The Messenger (ISSN0722-6691)* 114, pp. 20–24.

Mayor, M. et al. (2011). "The HARPS search for southern extra-solar planets XXXIV. Occurrence, mass distribution and orbital properties of super-Earths and Neptune-mass planets". In: *ArXiv e-prints*. arXiv: 1109.2497.

Miller-Ricci Kempton, E. and E. Rauscher (2012). "Constraining High-Speed Winds in Exoplanet Atmospheres Through Observations of Anomalous Doppler Shifts During Transit". In: *The Astrophysical Journal* 751.2, p. 117. arXiv: 1109.2270.

Montalto, M. et al. (2015). "Further constraints on the optical transmission spectrum of HAT-P-1b". In: *The Astrophysical Journal, Volume 811, Issue 1, article id. 55, 12 pp. (2015).* 811. arXiv: 1508.06696.

Mordasini, C. et al. (2012). "Extrasolar planet population synthesis IV. Correlations with disk metallicity, mass and lifetime". In: *Astronomy & Astrophysics* 541, A97. arXiv: 1201.1036.

Morton, T. D. and J. A. Johnson (2011). "On the Low False Positive Probabilities of Kepler Planet Candidates". In: *The Astrophysical Journal, Volume 738, Issue 2, article id. 170, 12 pp. (2011).* 738. arXiv: 1101.5630.

Motalebi, F. et al. (2015). "The HARPS-N Rocky Planet Search". In: *Astronomy & Astrophysics* 584, A72.

Muterspaugh, M. W. et al. (2010). "the Phases Differential Astrometry Data Archive. V. Candidate Substellar Companions To Binary Systems". In: *The Astronomical Journal* 140.6, pp. 1657–1671. arXiv: 1010.4048.

Naef, D. et al. (2004). "The ELODIE survey for northern extra-solar planets III. Three planetary candidates detected with ELODIE". In: *Astronomy and Astrophysics, v.414, p.351-359 (2004)* 414, p. 351. arXiv: 0310261 [astro-ph].

N'Diaye, M. et al. (2016). "Apodized pupil Lyot coronagraphs for arbitrary apertures. V. Hybrid Shaped Pupil designs for imaging Earth-like planets with future space observatories". In: arXiv: 1601.02614.

Nelson, B. E. et al. (2014). "The 55 Cancri Planetary System: Fully Self-Consistent N-body Constraints and a Dynamical Analysis". In: *Monthly Notices of the Royal Astronomical Society, Volume 441, Issue 1, p.442-451* 441, pp. 442–451. arXiv: 1402.6343.

Nidever, D. L. et al. (2002). "Radial Velocities for 889 Late-type Stars". In: *The Astrophysical Journal Supplement Series, Volume 141, Issue 2, pp. 503-522.* 141, pp. 503–522. arXiv: 0112477 [astro-ph].

Nielsen, L. et al. (2016). "The JWST/NIRSpec exoplanet exposure time calculator". In: *Proceedings of the SPIE, Volume 9904, id. 99043O 12 pp. (2016).* Ed. by H. A. MacEwen et al. Vol. 9904, 99043O.

Oreshenko, M.; K. Heng, and B.-O. Demory (2016). "Optical phase curves as diagnostics for aerosol composition in exoplanetary atmospheres". In: *Monthly Notices of the Royal Astronomical Society* 457.4, pp. 3420–3429. arXiv: 1601.03050.

Paddock, G. F. and G. F. (1913). "The Derivation of the Radial Velocity Equation". In: *Publications of the Astronomical Society of the Pacific* 25, p. 208.

Pater, I. de et al. (2010). "A multi-wavelength study of the 2009 impact on Jupiter: Comparison of high resolution images from Gemini, Keck and HST". In: *Icarus* 210.2, pp. 722–741.

Pätzold, M. et al. (2012). "Transiting exoplanets from the CoRoT space mission". In: *Astronomy & Astrophysics* 545, A6. arXiv: 1504.01532.

Pepe, F. A. et al. (2000). "HARPS: a new high-resolution spectrograph for the search of extrasolar planets". In: *Proc. SPIE*. Ed. by M. Iye and A. F. M. Moorwood. Vol. 4008, p. 582.

Pepe, F. A. et al. (2002). "The CORALIE survey for southern extra-solar planets VII. Two short-period Saturnian companions to HD108147 and HD168746". In: *Astronomy and Astrophysics, v.388, p.632-638 (2002)* 388, pp. 632–638. arXiv: 0202457 [astro-ph].

Pepe, F. A. et al. (2010). "ESPRESSO: the Echelle spectrograph for rocky exoplanets and stable spectroscopic observations". In: *Ground-based and Airborne Instrumentation for Astronomy III. Edited by McLean*. Ed. by I. S. McLean; S. K. Ramsay, and H. Takami. Vol. 7735. Society of Photo-Optical Instrumentation Engineers (SPIE) Conference Series, p. 14.

Pepe, F. A. et al. (2011). "The HARPS search for Earth-like planets in the habitable zone: I – Very low-mass planets around HD20794, HD85512 and HD192310". In: *Astronomy & Astrophysics, Volume 534, id.A58, 16 pp.* 534. arXiv: 1108.3447.

Perryman, M. A. C. (2000). "Extra-solar planets". In: *Reports on Progress in Physics* 63.8, pp. 1209–1272. arXiv: 0005602 [astro-ph].

Perryman, M. A. C. (2011). *The exoplanet handbook*. Cambridge University Press, p. 410.

Perryman, M. et al. (2014). "Astrometric exoplanet detection with Gaia". In: *The Astrophysical Journal, Volume 797, Issue 1, article id. 14, 22 pp. (2014).* 797. arXiv: 1411.1173.

Phillips, J. A. and S. E. Thorsett (1994). "Planets around pulsars: A review". In: *Astrophysics and Space Science* 212.1-2, pp. 91–106.

Pollack, J. B. et al. (1996). "Formation of the Giant Planets by Concurrent Accretion of Solids and Gas". In: *Icarus* 124.1, pp. 62–85.

Queloz, D. et al. (2001). "No planet for HD 166435". In: *Astronomy & Astrophysics* 379.1, pp. 279–287. arXiv: 0109491 [astro-ph].

Quirrenbach, A. (2010). "Astrometric Detection and Characterization of Exoplanets". In: *Exoplanets, edited by S. Seager*. Ed. by S. Seager. University of Arizona Press, p. 526.

Rajpaul, V. et al. (2015). "A Gaussian process framework for modelling stellar activity signals in radial velocity data". In: *Monthly Notices of the Royal Astronomical Society* 452.3, pp. 2269–2291.

Rauer, H. et al. (2013). "The PLATO 2.0˜{m}ission". In: *European Planetary Science Congress 2013, held 8-13 September in London, UK.˜Online at: http://meetings.copernicus.org/epsc2013, id.EPSC2013-707* 8, p. 707. arXiv: 1310.0696 [astro-ph.EP].

Redfield, S. et al. (2008). "Sodium Absorption From the Exoplanetary Atmosphere of HD189733b Detected in the Optical Transmission Spectrum". In: *The Astrophysical Journal* 673.1, p. 12. arXiv: 0712.0761.

Ricker, G. R. et al. (2014). "The Transiting Exoplanet Survey Satellite". In: *Proceedings of the SPIE, Volume 9143, id. 914320 15 pp. (2014).* 1.1, p. 014003. arXiv: 1406.0151.

Robin, A. C. et al. (2003). "A synthetic view on structure and evolution of the Milky Way". In: *Astronomy & Astrophysics* 409.2, pp. 523–540.

Rodler, F.; M. Kürster, and T. Henning (2010). "τ Boötis b: Hunting for reflected starlight". In: *Astronomy and Astrophysics* 514, A23. arXiv: 1002.1638 [astro-ph.SR].

Rothman, L. S. et al. (2010). "HITEMP, the high-temperature molecular spectroscopic database". In: *Journal of Quantitative Spectroscopy and Radiative Transfer* 111.15, pp. 2139–2150. arXiv: arXiv:1102.0063.

Rowe, J. F. et al. (2008). "The Very Low Albedo of an Extrasolar Planet: MOST Space-based Photometry of HD 209458". In: *The Astrophysical Journal* 689, p. 1345. arXiv: 0711.4111.

Rowe, J. F. et al. (2014). "VALIDATION OF KEPLER 'S MULTIPLE PLANET CANDIDATES. III. LIGHT CURVE ANALYSIS AND ANNOUNCEMENT OF HUNDREDS OF NEW MULTI-PLANET SYSTEMS". In: *The Astrophysical Journal* 784.1, p. 45. arXiv: 1402.6534.

Sallum, S. et al. (2015). "New Spatially Resolved Observations of the T Cha Transition Disk and Constraints on the Previously Claimed Substellar Companion". In: *The Astrophysical Journal, Volume 801, Issue 2, article id. 85, 23 pp. (2015).* 801. arXiv: 1501.01964.

Santerne, A. et al. (2011). "Radial velocity follow-up of CoRoT transiting exoplanets". In: *EPJ Web of Conferences* 11, p. 02001.

Santerne, A. et al. (2012). "SOPHIE velocimetry of Kepler transit candidates". In: *Astronomy & Astrophysics* 545, A76.

Santerne, A. et al. (2016). "Spectroscopic characterisation of microlensing events Towards a new interpretation of OGLE-2011-BLG-0417". In: *Astronomy & Astrophysics, Volume 595, id.L11, 8 pp.* 595. arXiv: 1610.04446.

Santos, N. C.; G. Israelian, and M. Mayor (2001). "The metal-rich nature of stars with planets". In: *Astronomy & Astrophysics* 373.3, pp. 1019–1031.

Santos, N. C. et al. (2014). "The HARPS search for southern extra-solar planets XXXV. The interesting case of HD41248: stellar activity, no planets?" In: *Astronomy & Astrophysics, Volume 566, id.A35, 14 pp.* 566. arXiv: 1404.6135.

Santos, N. C. et al. (2017). "Constraining planet structure and composition from stellar chemistry: trends in different stellar populations". In: *eprint arXiv:1711.00777*. arXiv: 1711.00777.

Santos, N. C.; G. Israelian, and M. Mayor (2004a). "Spectroscopic [Fe/H] for 98 extra-solar planet-host stars". In: *Astronomy & Astrophysics* 415.3, pp. 1153–1166.

Santos, N. C. et al. (2004b). "The CORALIE survey for southern extra-solar planets". In: *Astronomy & Astrophysics* 379.1, pp. 391–402. arXiv: 0310316v2 [arXiv:astro-ph].

Santos, N. C. et al. (2013). "SWEET-Cat: A catalogue of parameters for Stars With ExoplanETs. I. New atmospheric parameters and masses for 48 stars with planets". In: *Astronomy & Astrophysics* 556, p. 150. arXiv: 1307.0354 [astro-ph.SR].

Santos, N. C. et al. (2015). "Detecting ring systems around exoplanets using high resolution spectroscopy: the case of 51 Pegasi b". In: *Astronomy & Astrophysics* 583.1, A50. arXiv: 1509.00723.

Schmid, H. M. et al. (2005). "Search and investigation of extra-solar planets with polarimetry". In: *Proceedings of the International Astronomical Union* 1.C200, pp. 165–170.

Schneider, G. et al. (1999). "NICMOS Imaging of the HR 4796A Circumstellar Disk". In: *The Astrophysical Journal, Volume 513, Issue 2, pp. L127-L130.* 513, pp. L127–L130. arXiv: 9901218 [astro-ph].

Schneider, J. et al. (2011). "Defining and cataloging exoplanets: the exoplanet.eu database". In: *Astronomy & Astrophysics* 532, A79. arXiv: 1106.0586.

Schwartz, J. C. and N. B. Cowan (2015). "Balancing the energy budget of short-period giant planets: Evidence for reflective clouds and optical absorbers". In: *Monthly Notices of the Royal Astronomical Society* 449.4, pp. 4192–4203. arXiv: 1502.06970.

Schwartz, J. C. et al. (2017). "Phase Offsets and the Energy Budgets of Hot Jupiters". In: arXiv: 1707.05790.

Seager, S. (2011). *Exoplanets*.

Seager, S.; W. Bains, and R. Hu (2013). "Biosignature Gases in H2-Dominated Atmospheres on Rocky Exoplanets". In: *The Astrophysical Journal, Volume 777, Issue 2, article id. 95, 19 pp. (2013).* 777. arXiv: 1309.6016.

Seager, S.; R. Dotson, and Lunar and Planetary Institute. (2010). *Exoplanets*. University of Arizona Press, p. 526.

Seager, S. and D. D. Sasselov (1998). "Extrasolar Giant Planets under Strong Stellar Irradiation". In: *The Astrophysical Journal* 502.2, pp. L157–L161. arXiv: 9805335v1 [arXiv:astro-ph].

Seager, S. et al. (2007). "Mass-Radius Relationships for Solid Exoplanets". en. In: *The Astrophysical Journal* 669.2, pp. 1279–1297. arXiv: 0707.2895.

Ségransan, D. et al. (2011). "The HARPS search for southern extrasolar planets. XXV. Four new planets in orbit around the moderatly active dwarfs HD 63765, HD 104067, HD 125595, and HIP 70849". In: 54, p. 8. arXiv: 1107.0339.

Selsis, F. et al. (2007). "Habitable planets around the star Gl 581?" In: *Astronomy and Astrophysics* 476.3, pp. 1373–1387. arXiv: 0710.5294.

Showman, A. P. and T. Guillot (2002). "Atmospheric circulation and tides of/?51?Pegasus?b-like? planets". In: *Astron. Astrophys.* 385.1, pp. 166–180. arXiv: astro-ph/0202236v1 [astro-ph].

Shvartzvald, Y. et al. (2015). "The frequency of snowline-region planets from four-years of OGLE-MOA-Wise second-generation microlensing". In: *Monthly Notices of the Royal Astronomical Society, Volume 457, Issue 4, p.4089-4113* 457, pp. 4089–4113. arXiv: 1510.04297.

Simpson, E. K. et al. (2010). "Rotation periods of exoplanet host stars". In: *Monthly Notices of the Royal Astronomical Society* 408.3, pp. 1666–1679. arXiv: 1006.4121.

Sing, D. K. et al. (2016). "A continuum from clear to cloudy hot-Jupiter exoplanets without primordial water depletion". In: *Nature* 529.7584, pp. 59–62. arXiv: 1512.04341.

Sirbu, D. et al. (2017). "Prospects for exoplanet imaging in multi-star systems with starshades". In: *eprint arXiv:1709.00041*. arXiv: 1709.00041.

Smette, A. et al. (2015). "Molecfit: A general tool for telluric absorption correction". In: *Astronomy & Astrophysics* 576, A77. arXiv: 1501.07239 [astro-ph.IM].

Snellen, I. A. G.; E. J. W. de Mooij, and S. Albrecht (2009). "The changing phases of extrasolar planet CoRoT-1b". In: *Nature* 459.7246, pp. 543–545. arXiv: 0904.1208.

Snellen, I. A. G. et al. (2010). "The orbital motion, absolute mass and high-altitude winds of exoplanet HD 209458b". In: *Nature* 465.7301, pp. 1049–1051. arXiv: 1006.4364.

Snellen, I. A. G. et al. (2014). "Fast spin of the young extrasolar planet β Pictoris b". In: *Nature* 509.7498, pp. 63–65. arXiv: 1404.7506.

Snellen, I. A. G. et al. (2015). "Combining high-dispersion spectroscopy (HDS) with high contrast imaging (HCI): Probing rocky planets around our nearest neighbors". In: *Astronomy & Astrophysics* 576.3, A59. arXiv: 1503.01136.

Sobolev, B. and V. V. W. M. Irvine (1975). "Light Scattering in Planetary Atmospheres (International Series of Monographs in Natural Philosophy , V . 76)". In: pp. 2–5.

Spiegel, D. S. and A. Burrows (2011). "Spectral and Photometric Diagnostics of Giant Planet Formation Scenarios". In: arXiv: 1108.5172.

Squyres, S. W. et al. (2004). "In Situ Evidence for an Ancient Aqueous Environment at Meridiani Planum, Mars". In: *Science* 306.5702, pp. 1709–1714.

Stamnes, K. et al. (1988). "Numerically stable algorithm for discrete-ordinate-method radiative transfer in multiple scattering and emitting layered media." In: *Applied optics* 27.12, pp. 2502–2509.

Steffen, J. H. et al. (2007). "Detecting and Characterizing Planetary Systems with Transit Timing". In: *eprint arXiv:0704.0632*. arXiv: 0704.0632.

Steffen, J. H. et al. (2010). "Five Kepler target stars that show multiple transiting exoplanet candidates". In: *The Astrophysical Journal, Volume 725, Issue 1, pp. 1226-1241 (2010).* 725, pp. 1226–1241. arXiv: 1006.2763.

Stern, S. A. and H. F. Levison (2002). "Regarding the criteria for planethood and proposed planetary classification schemes". In: *In: Highlights of Astronomy*. Ed. by A. L. H. Rickman. Vol. 12. IAU, pp. 205–213.

Stevenson, K. B. et al. (2014). "Deciphering the Atmospheric Composition of WASP-12b: A Comprehensive Analysis of its Dayside Emission". In: *The Astrophysical Journal, Volume 791, Issue 1, article id. 36, 8 pp. (2014).* 791.1, p. 36. arXiv: 1406.7567.

Sumi, T. et al. (2010). "A COLD NEPTUNE-MASS PLANET OGLE-2007-BLG-368Lb: Cold neptunes are common". In: *The Astrophysical Journal, Volume 710, Issue 2, pp. 1641-1653 (2010).* 710.2, pp. 1641–1653. arXiv: 0912.1171.

Sumi, T. et al. (2011). "Unbound or Distant Planetary Mass Population Detected by Gravitational Microlensing". In: *Nature, Volume 473, Issue 7347, pp. 349-352 (2011).* 473, pp. 349–352. arXiv: 1105.3544.

Suzuki, D. et al. (2016). "The Exoplanet Mass-Ratio Function from the MOA-II Survey: Discovery of a Break and Likely Peak at a Neptune Mass". In: *The Astrophysical Journal, Volume 833, Issue 2, article id. 145, 26 pp. (2016).* 833. arXiv: 1612.03939.

Swain, M. R.; G. Vasisht, and G. Tinetti (2008). "The presence of methane in the atmosphere of an extrasolar planet". In: *Nature* 452.7185, pp. 329–331.

Swift, D. C. et al. (2012). "Mass-Radius Relationships for Exoplanets". In: *The Astrophysical Journal* 744.1, p. 59. arXiv: 1001.4851.

Szentgyorgyi, A. et al. (2014). "A Preliminary Design for the GMT-Consortium Large Earth Finder". In: *Society of Photo-Optical Instrumentation Engineers (SPIE) Conference Series*. Ed. by S. K. Ramsay; I. S. McLean, and H. Takami. Vol. 9147, pp. 1–16.

Tiatco, S. A. P. (2016). *The possibilities and problems of entanglement in contemporary Manila theater: Pista as model, Rizal X as exemplar*. Vol. 13. 2, pp. 127–162. arXiv: arXiv:1011.1669v3.

Tinetti, G. et al. (2007). "Water vapour in the atmosphere of a transiting extrasolar planet". In: *Nature* 448.7150. arXiv: 0707.3064.

Tinetti, G. et al. (2016). "The science of ARIEL (Atmospheric Remote-sensing Infrared Exoplanet Large-survey)". In: *Proceedings of the SPIE, Volume 9904, id. 99041X 10 pp. (2016).* Ed. by H. A. MacEwen et al. Vol. 9904, p. 99041X.

Trauger, J. T. and W. A. Traub (2007). "A laboratory demonstration of the capability to image an Earth-like extrasolar planet". In: *Nature* 446.7137, pp. 771–773.

Underwood, D.; B. Jones, and P. Sleep (2003). "The evolution of habitable zones during stellar lifetimes and its implications on the search for extraterrestrial life". In: *International Journal of Astrobiology* 2.4, pp. 289–299. arXiv: 0312522 [astro-ph].

Vazan, A. et al. (2016). "The Evolution and Internal Structure of Jupiter and Saturn with Compositional Gradients". In: *The Astrophysical Journal, Volume 829, Issue 2, article id. 118, 11 pp. (2016).* 829. arXiv: 1606.01558.

Wahl, S. M. et al. (2017). "Comparing Jupiter interior structure models to Juno gravity measurements and the role of a dilute core". In: *Geophysical Research Letters, Volume 44, Issue 10, pp. 4649-4659* 44, pp. 4649–4659. arXiv: 1707.01997.

Wall, J. V. and C. R. Jenkins (2003). *Practical Statistics for Astronomers*.

Wang, J. et al. (2015). "INFLUENCE OF STELLAR MULTIPLICITY ON PLANET FORMATION. IV. ADAPTIVE OPTICS IMAGING OF KEPLER STARS WITH MULTIPLE TRANSITING PLANET CANDIDATES". In: *The Astrophysical Journal* 813.2, p. 130. arXiv: 1510.01964.

Wang, J. et al. (2017). "Observing Exoplanets with High Dispersion Coronagraphy. I. The scientific potential of current and next-generation large ground and space telescopes". In: *The Astronomical Journal, Volume 153, Issue 4, article id. 183, 23 pp. (2017).* 153. arXiv: 1703.00582.

Weiss, L. M. and G. W. Marcy (2014). "The Mass-Radius Relation for 65 Exoplanets Smaller than 4 Earth Radii". In: *The Astrophysical Journal Letters, Volume 783, Issue 1, article id. L6, 7 pp. (2014).* 783.1, p. L6. arXiv: 1312.0936.

Weiss, L. M. et al. (2013). "THE MASS OF KOI-94d AND A RELATION FOR PLANET RADIUS, MASS, AND INCIDENT FLUX". In: *The Astrophysical Journal* 768.1, p. 14. arXiv: 1303.2150.

Whitmore, J. B.; M. T. Murphy, and K. Griest (2010). "Wavelength Calibration of the VLT-UVES Spectrograph". In: *The Astrophysical Journal, Volume 723, Issue 1, pp. 89-99 (2010).* 723, pp. 89–99. arXiv: 1004.3325.

Winn, J. (2011). "Exoplanet Transits and Occultations". In: *Exoplanets, edited by S.˜Seager.˜ Tucson, AZ: University of Arizona Press, 2011, 526 pp.˜ ISBN 978-0-8165-2945-2., p.55-77*. Ed. by S. Seager, pp. 55–77.

Wolszczan, A. and D. A. Frail (1992). "A planetary system around the millisecond pulsar PSR1257 + 12". In: *Nature* 355.6356, pp. 145–147. arXiv: arXiv:0901.0974v2.

Wright, J. T. et al. (2012). "The Frequency of Hot Jupiters Orbiting Nearby Solar-Type Stars". In: *The Astrophysical Journal, Volume 753, Issue 2, article id. 160, 5 pp. (2012).* 753. arXiv: 1205.2273.

Wyttenbach, A. et al. (2015). "Spectrally resolved detection of sodium in the atmosphere of HD 189733b with the HARPS spectrograph". In: *Astronomy & Astrophysics* 577, A62. arXiv: 1503.05581.

Zhou, G. et al. (2017). "HAT-P-67b: An Extremely Low Density Saturn Transiting an F-Subgiant Confirmed via Doppler Tomography". In: *The Astronomical Journal, Volume 153, Issue 5, article id. 211, 13 pp. (2017).* 153. arXiv: 1702.00106.

Zhu, W.; J. Wang, and C. Huang (2016). "Dependence of Small Planet Frequency on Stellar Metallicity Hidden by Their Prevalence". In: *The Astrophysical Journal, Volume 832, Issue 2, article id. 196, 8 pp. (2016).* 832. arXiv: 1605.04310.

Zinn, R. and M. J. West (1984). "The globular cluster system of the galaxy. III - Measurements of radial velocity and metallicity for 60 clusters and a compilation of metallicities for 121 clusters". In: *The Astrophysical Journal Supplement Series* 55, p. 45.

Zurlo, A. et al. (2015). "First light of the VLT planet finder SPHERE. III. New spectrophotometry and astrometry of the HR8799 exoplanetary system". In: *Astronomy & Astrophysics, Volume 587, id.A57, 13 pp.* 587. arXiv: 1511.04083.

Appendix A.
PhD output

This section lists the activities in which I have been involved over the duration of my doctoral training, from scientific output (e.g. articles, talks) to outreach or other topics I deemed relevant.

In summary, over the duration of my doctoral training:

- I authored 3 first author articles – of which two got accepted (Martins et al., 2015a; Martins et al., 2016) and another is currently undergoing the reviewing process (Martins et al., 2017) – and one article in conference proceedings (Martins et al., 2015b).
- I also got involved as a co-author in 4 more articles (Santos et al., 2014; Santos et al., 2015; Montalto et al., 2015; Lovis et al., 2017).
- I also had the opportunity to attend 4 international conferences and 2 workshop, on which I presented 4 oral communications and 2 posters. Additionally, I presented 3 seminars.
- I tutored at the 10^{th} edition of the Physics Summer School from the Faculty of Science of the University of Porto.
- In parallel to my scientific work, I participated in several outreach events, both as a organizer and presenter.
- I also gained experience as an observer, with 3 observing runs and 1 accepted proposal.

I now proceed to list all the above in detail.

PUBLICATIONS A.1

A&A 576, A134 (2015)
DOI: 10.1051/0004-6361/201425298

Astronomy & Astrophysics

Evidence for a spectroscopic direct detection of reflected light from 51 Pegasi b⋆,⋆⋆

J. H. C. Martins[1,2,3,6], N. C. Santos[1,2,3], P. Figueira[1,2], J. P. Faria[1,2,3], M. Montalto[1,2], I. Boisse[4], D. Ehrenreich[5], C. Lovis[5], M. Mayor[5], C. Melo[6], F. Pepe[5], S. G. Sousa[1,2], S. Udry[5], and D. Cunha[1,2,3]

[1] Instituto de Astrofísica e Ciências do Espaço, Universidade do Porto, CAUP, Rua das Estrelas, 4150-762 Porto, Portugal
e-mail: jorge.martins@iastro.pt
[2] Centro de Astrofísica, Universidade do Porto, Rua das Estrelas, 4150-762 Porto, Portugal
[3] Departamento de Física e Astronomia, Faculdade de Ciências, Universidade do Porto, Rua do Campo Alegre, 4169-007 Porto, Portugal
[4] Aix-Marseille Université, CNRS, LAM (Laboratoire d'Astrophysique de Marseille) UMR 7326, 13388 Marseille, France
[5] Observatoire de Genève, Université de Genève, 51 Ch. des Maillettes, 1290 Sauverny, Switzerland
[6] European Southern Observatory, Casilla 19001 Santiago, Chile

Received 7 November 2014 / Accepted 24 March 2015

ABSTRACT

Context. The detection of reflected light from an exoplanet is a difficult technical challenge at optical wavelengths. Even though this signal is expected to replicate the stellar signal, not only is it several orders of magnitude fainter, but it is also hidden among the stellar noise.
Aims. We apply a variant of the cross-correlation technique to HARPS observations of 51 Peg to detect the reflected signal from planet 51 Peg b.
Methods. Our method makes use of the cross-correlation function (CCF) of a binary mask with high-resolution spectra to amplify the minute planetary signal that is present in the spectra by a factor proportional to the number of spectral lines when performing the cross correlation. The resulting cross-correlation functions are then normalized by a stellar template to remove the stellar signal. Carefully selected sections of the resulting normalized CCFs are stacked to increase the planetary signal further. The recovered signal allows probing several of the planetary properties, including its real mass and albedo.
Results. We detect evidence for the reflected signal from planet 51 Peg b at a significance of $3\sigma_{\rm noise}$. The detection of the signal permits us to infer a real mass of $0.46^{+0.06}_{-0.01}$ $M_{\rm Jup}$ (assuming a stellar mass of 1.04 $M_{\rm Sun}$) for the planet and an orbital inclination of 80^{+10}_{-19} degrees. The analysis of the data also allows us to infer a tentative value for the (radius-dependent) geometric albedo of the planet. The results suggest that 51Peg b may be an inflated hot Jupiter with a high albedo (e.g., an albedo of 0.5 yields a radius of 1.9 ± 0.3 $R_{\rm Jup}$ for a signal amplitude of $6.0 \pm 0.4 \times 10^{-5}$).
Conclusions. We confirm that the method we perfected can be used to retrieve an exoplanet's reflected signal, even with current observing facilities. The advent of next generation of instruments (e.g. VLT-ESO/ESPRESSO) and observing facilities (e.g. a new generation of ELT telescopes) will yield new opportunities for this type of technique to probe deeper into exoplanets and their atmospheres.

Key words. planetary systems – planets and satellites: detection – techniques: spectroscopic – techniques: radial velocities

1. Introduction

Since the discovery in 1995 of a planet orbiting 51 Peg (Mayor & Queloz 1995), over 1900 planets in around 1200 planetary systems have been found (Schneider et al. 2011)[1]: this number increases steadily. Furthermore, close to 470 multiple planetary systems have been detected, some of which are highly complex (e.g., Borucki et al. 2013).

The search for exoplanets has been following two different, but complementary, paths: the detection of exoplanets with increasingly lower masses, and the characterization of these exoplanets and their atmospheres. On the detection side, the radial velocity (e.g., Lovis & Fischer 2010; Bonfils et al. 2013) and transit methods (e.g., Borucki et al. 2010; Winn 2010) have been the most prolific. One of the most important results of planet detection surveys is the ubiquity of planets around solar-type stars (e.g., Howard et al. 2010).

On the characterization side, the current frontier of exoplanet characterization has been pushed toward the study of exoplanet atmospheres, both from a composition and from a dynamics point of view. To overcome this difficult challenge, several indirect techniques have been developed. Transmission spectroscopy relies on observing the host star spectrum as it is filtered by a planet atmosphere during a transit (e.g., Charbonneau et al. 2002; Knutson et al. 2014). Occultation photometry and

⋆ Based on observations made with ESO Telescopes at the La Silla Paranal Observatory under programme ID 091.C-0271 (with the HARPS spectrograph at the ESO 3.6 m telescope).
⋆⋆ The radial velocity data for the HARPS observations of 51 Pegasi are only available at the CDS via anonymous ftp to cdsarc.u-strasbg.fr (130.79.128.5) or via http://cdsarc.u-strasbg.fr/viz-bin/qcat?J/A+A/576/A134
[1] http://exoplanet.eu/

Twenty years of giant exoplanets - Proceedings of the Haute Provence Observatory Colloquium, 5-9 October 2015
Edited by I. Boisse, O. Demangeon, F. Bouchy & L. Arnold

Exoplanet Reflections: the light from 51 Peg b

J. H. C. Martins[1,2,3], N. Santos[1,3], P. Figueira[1], C. Melo[2]

Talk given at OHP-2015 Colloquium

[1]Instituto de Astrofísica e Ciências do Espaço, Universidade do Porto, CAUP, Rua das Estrelas, 4150-762 Porto, Portugal
[2]European Southern Observatory, Alonso de Córdova 3107, Santiago, Chile
[3]Departamento de Física e Astronomia, Faculdade de Ciências, Universidade do Porto, Rua do Campo Alegre, 4169-007 Porto, Portugal

Abstract

The direct detection of reflected light from an exoplanet is, even in the most favourable cases, a herculean task, close to the detection limit of current observing facilities. To surpass this problem, we made used of a technique (Martins et al. 2013, MNRAS, 436, 1215) that uses the power of the Cross Correlation Function to recover the minute reflected signal from 51 Pegasi b with a 3-σ+ significance. This allowed us to conclude that this prototypical hot-Jupiter is most likely a highly inflated planet with a high albedo. These results were presented in the *OHP2015: Twenty years of giant exoplanets* conference and published in Martins et al. 2015, A&A, 576, A134.

1 Introduction

Twenty years have passed since the pioneering discovery of the prototypical Hot-Jupiter 51 Peg b (Mayor & Queloz 1995), the first planet to be discovered around a solar-type star other than our Sun. Now over two thousand exoplanets have been confirmed (see `http://exoplanet.eu` , Schneider et al. 2011), some of them in systems with a level of complexity that challenges our own (e.g. HD10180 with 7 planets, Lovis et al. 2011). An interesting result in this line of research is the correlation between stellar metallicity and the presence of giant planets: stars hosting the giant planets are systematically more metallic than a normal sample of stars (Bond et al. 2008; Sousa et al. 2011). Curiously, this correlation was found not to hold for low-mass rocky planets (Sousa et al. 2011), which are now believed to be abundant and outnumber the higher-mass population characterized up to now (Mayor et al. 2011).

A rarity at first, exoplanets have been found to be ubiquitous around solar-type stars (Howard et al. 2010) and extremely diverse in terms of characteristics (Schneider et al. 2011). Their characterization is one of the greatest challenges in exoplanet science, to the point that it is now possible to determine the bulk composition and planetary structure of several planets, some of which seem to be mostly rocky/iron in nature (e.g. Batalha et al. 2011; Léger et al. 2009). The boundaries of this line of research are being pushed towards the characterization of planetary atmospheres, for which several techniques have been developed.

Transmission spectroscopy (e.g. Charbonneau et al. 2002; Knutson et al. 2014) measures the wavelength dependence of the radius of a planet during transits to infer the atmosphere's composition. Occultation photometry and spectroscopy techniques measure the wavelength dependency of the depth of the occultation of a transiting planet to infer the planetary thermal (e.g. Snellen et al. 2010) and reflected (e.g. Rodler et al. 2013) signals. The measurement of the flux variation of a planet along its orbit allows to reconstruct the planetary phase variation along its orbit and recover its reflected signal (e.g. Knutson et al. 2009).

Another approach in the study of planetary atmospheres is the measurement of their albedo as it permits to constrain current atmosphere models (Cowan & Agol 2011; Demory 2014) and infer their composition (e.g. the presence of clouds in HD 189733 b, see Barstow et al. 2014). Unfortunately, the measurement of the optical spectroscopic reflected signal from exoplanets has been elusive for many years. The main challenge to this is the low planet-to-star flux ratio in the optical, which is in the most favourable scenarios of the order of 10^{-4}, at the detection limit of current observing facilities. Consequently, the initial attempts at capturing the reflected signal of

Orig Life Evol Biosph (2016) 46:487–498
DOI 10.1007/s11084-016-9493-2

ASTROBIOLOGY

Reflected Light from Giant Planets in Habitable Zones: Tapping into the Power of the Cross-Correlation Function

J. H. C. Martins[1,2,3] · **N. C. Santos**[2,3] · **P. Figueira**[2,3] · **C. Melo**[1]

Received: 30 August 2015 / Accepted: 13 January 2016 /
Published online: 31 March 2016

Abstract The direct detection of reflected light from exoplanets is an excellent probe for the characterization of their atmospheres. The greatest challenge for this task is the low planet-to-star flux ratio, which even in the most favourable case is of the order of 10^{-4} in the optical. This ratio decreases even more for planets in their host's habitable zone, typically lower than 10^{-7}. To reach the signal-to-noise level required for such detections, we propose to unleash the power of the Cross Correlation Function in combination with the collecting power of next generation observing facilities. The technique we propose has already yielded positive results by detecting the reflected spectral signature of 51 Pegasi b (see Martins et al. 2015). In this work, we attempted to infer the number of hours required for the detection of several planets in their host's habitable zone using the aforementioned technique from theoretical EELT observations. Our results show that for 5 of the selected planets it should be possible to directly recover their reflected spectral signature.

Keywords Planetary systems · Habitability zone · High resolution spectroscopy

Paper presented at the conference: Habitability in the Universe: From the Early Earth to Exoplanets 22–27 March 2015, Porto, Portugal

✉ J. H. C. Martins
Jorge.Martins@astro.up.pt

[1] European Southern Observatory, Casilla 19001 Santiago, Chile

[2] Instituto de Astrofísica e Ciências do Espaço, Universidade do Porto, CAUP, Rua das Estrelas, 4150-762 Porto, Portugal

[3] Departamento de Física e Astronomia, Faculdade de Ciências, Universidade do Porto, Rua do Campo Alegre, 4169-007 Porto, Portugal

MNRAS **000**, 1–24 (2017) Preprint 12 October 2017 Compiled using MNRAS LATEX style file v3.0

Recovering the color-dependent albedo of exoplanets with high-resolution spectroscopy: from ESPRESSO to the ELT.

J. H. C. Martins[1,2,3,⋆], P. Figueira[1], N. C. Santos[1,3], C. Melo[2], A. Garcia Muñoz[4], J. Faria[1,3], F. Pepe[5], and C. Lovis[5]
[1] *Instituto de Astrofísica e Ciências do Espaço, Universidade do Porto, CAUP, Rua das Estrelas, 4150-762 Porto, Portugal*
[2] *European Southern Observatory, Alonso de Córdova 3107, Vitacura, Región Metropolitana, Chile*
[3] *Departamento de Física e Astronomia, Faculdade de Ciências, Universidade do Porto, Rua do Campo Alegre, 4169-007 Porto, Portugal*
[4] *Zentrum fÃijr Astronomie und Astrophysik, Technische UniversitÃd't Berlin, D-10623 Berlin, Germany*
[5] *Observatoire de Genève, Université de Genève, 51 ch. des Maillettes, CH-1290 Sauverny, Switzerland*

Accepted XXX. Received YYY; in original form ZZZ

ABSTRACT
The characterization of planetary atmospheres is a daunting task, at the limit of current observing facilities. The next generation of high-resolution spectrographs mounted on large telescopes – such as ESPRESSO@VLT and HIRES@ELT – will allow to probe exoplanetary atmospheres and characterize them. We present a method that permits the recovery of the color-dependent reflectivity of exoplanets from high-resolution spectroscopic observations. This wavelength-dependent albedo is highly controlled by the planetary atmosphere chemical properties and weather dynamics.

For this work, we simulated ESPRESSO@VLT and HIRES@ELT high-resolution observations of known planetary systems with several albedo configurations. Furthermore, we demonstrate how the cross correlation function of theses simulated observations can be used to successfully recover the geometric albedo function from exoplanets. In all cases, we were able to recover the wavelength dependent albedo of the simulated exoplanets and distinguish between several distinct atmospheric models representing different atmospheric chemistry.

In brief, we demonstrate that the cross correlation technique allows for the recovery of exoplanetary albedo functions from optical observations with the next generation of high-resolution spectrographs that will be mounted on large telescopes with reasonable exposure times. Its recovery should permit the characterization of exoplanetary atmospheres in terms of composition and dynamics and makes the cross correlation technique a powerful tool for exoplanet characterization.

Key words: Stars: Planetary systems, Planets and satellites: atmospheres, techniques: spectroscopy, techniques: radial velocities

1 INTRODUCTION

The detection of what turned out to be the prototypical hot Jupiter planet around the solar twin 51 Pegasi (Mayor & Queloz 1995) paved the way for one of the most prolific fields in Astronomy. Currently over 3600 planets in around 2700 planetary systems have been discovered[1], with more than 2600 additional candidates from the Kepler (Borucki et al. 2010) and K2 (Howell et al. 2014) missions still awaiting confirmation.

Nowadays, one of the main research paths of exoplanetology is the study and characterization of exoplanetary atmospheres. Atmospheric characterization of exoplanets is a formidable task, at the limit of the capabilities of current generation observing facilities. However, in-depth knowledge of exoplanetary atmospheres is fundamental towards our understanding of the planet's chemistry, physics, origin and ultimately its capability of sustaining life (e.g. see Seager et al. 2010).

The main challenge for the study of exoplanetary atmospheres is the extreme contrast ratio required to detect even a hot Jupiter class planet. At infrared wavelengths, the planet-to-star flux ratio at opposition can reach 10^{-3}, mainly due to the thermal emission of the planet peaking at these wavelengths. At optical wavelengths, the planet-to-star flux

⋆ E-mail: Jorge.Martins@astro.up.pt
[1] From the `http://exoplanet.eu/` database (Schneider et al. 2011)

A&A 566, A35 (2014)
DOI: 10.1051/0004-6361/201423808

Astronomy & Astrophysics

The HARPS search for southern extra-solar planets⋆,⋆⋆,⋆⋆⋆

XXXV. The interesting case of HD 41248: stellar activity, no planets?

N. C. Santos[1,2], A. Mortier[1], J. P. Faria[1,2], X. Dumusque[3,4], V. Zh. Adibekyan[1], E. Delgado-Mena[1], P. Figueira[1], L. Benamati[1,2], I. Boisse[8], D. Cunha[1,2], J. Gomes da Silva[1,2], G. Lo Curto[5], C. Lovis[3], J. H. C. Martins[1,2], M. Mayor[3], C. Melo[5], M. Oshagh[1,2], F. Pepe[3], D. Queloz[3,9], A. Santerne[1], D. Ségransan[3], A. Sozzetti[7], S. G. Sousa[1,2,6], and S. Udry[3]

[1] Centro de Astrofísica, Universidade do Porto, Rua das Estrelas, 4150-762 Porto, Portugal
e-mail: nuno@astro.up.pt
[2] Departamento de Física e Astronomia, Faculdade de Ciências, Universidade do Porto, Rua do Campo Alegre, 4169-007 Porto, Portugal
[3] Observatoire de Genève, Université de Genève, 51 Ch. des Maillettes, 1290 Sauverny, Switzerland
[4] Harvard-Smithsonian Center for Astrophysics, 60 Garden Street, Cambridge, MA 02138, USA
[5] European Southern Observatory, Casilla 19001 Santiago, Chile
[6] Instituto de Astrofísica de Canarias, 38200 La Laguna, Tenerife, Spain
[7] INAF – Osservatorio Astrofisico di Torino, via Osservatorio 20, 10025 Pino Torinese, Italy
[8] Aix-Marseille Université, CNRS, LAM (Laboratoire d'Astrophysique de Marseille) UMR 7326, 13388 Marseille, France
[9] Institute of Astronomy, University of Cambridge, Madingley Road, Cambridge, CB3 0HA, UK

Received 14 March 2014 / Accepted 22 April 2014

ABSTRACT

Context. The search for planets orbiting metal-poor stars is of utmost importance for our understanding of planet formation models. However, no dedicated searches have been conducted so far for very low mass planets orbiting such objects. Only a few cases of low-mass planets orbiting metal-poor stars are thus known. Amongst these, HD 41248 is a metal-poor, solar-type star on the orbit of which a resonant pair of super-Earth-like planets has been announced. This detection was based on 62 radial velocity measurements obtained with the HARPS spectrograph (public data).
Aims. We present a new planet search program that is using the HARPS spectrograph to search for Neptunes and super-Earths that orbit a sample of metal-poor FGK dwarfs. We then present a detailed analysis of 162 additional radial velocity measurements of HD 41248, obtained within this program, with the goal of confirming the existence of the proposed planetary system.
Methods. We analysed the precise radial velocities, obtained with the HARPS spectrograph, together with several stellar activity diagnostics and line profile indicators.
Results. A careful analysis shows no evidence for the planetary system. One of the signals, with a period of ∼25 days, is shown to be related to the rotational period of the star, and is clearly seen in some of the activity proxies. We were unable to convincingly retrieve the remaining signal ($P \sim 18$ days) in the new dataset.
Conclusions. We discuss possible causes for the complex (evolving) signals observed in the data of HD 41248, proposing that they might be explained by the appearance and disappearance of active regions on the surface of a star with strong differential rotation, or by a combination of the sparse data sampling and active region evolution.

Key words. planetary systems – stars: individual: HD 41248 – stars: solar-type – stars: activity – stars: abundances – surveys

1. Introduction

Precise spectroscopic studies of stars with giant planets show that their frequency is a strong function of the stellar metallicity. It is easier to find such a planet around a metal-rich star than around a metal-poor object (Gonzalez 1998; Santos et al. 2001, 2004b; Reid 2002; Fischer & Valenti 2005; Sousa et al. 2011b). Several studies on solar neighbourhood stars have shown that at least 25% of stars with [Fe/H] above +0.3 dex (twice the solar value) have an orbiting giant planet. This frequency decreases to about 5% for solar metallicity stars. This observational result is usually interpreted to be due to a higher probability of forming a giant-planet core before the dissipation of the proto-planetary disk in a metal-rich environment (e.g. Mordasini et al. 2009).

A number of questions are still open, however, whose answer may have strong implications for planet formation models, especially in the metal-poor regime. In the context of one of the HARPS surveys, a search for giant planets around a sample of ∼100 metal-poor stars was conducted. Three new giant-planet candidates were discovered, and a fourth interesting candidate was announced (Santos et al. 2007, 2011). As expected, the results seem to confirm that metal-poor stars have a lower

⋆ Based on observations collected at ESO facilities under programs 082.C-0212, 085.C-0063, 086.C-0284, and 190.C-0027 (with the HARPS spectrograph at the ESO 3.6-m telescope, La Silla-Paranal Observatory).
⋆⋆ Table 1 is available in electronic form at http://www.aanda.org
⋆⋆⋆ Radial velocity data are only available at the CDS via anonymous ftp to cdsarc.u-strasbg.fr (130.79.128.5) or via http://cdsarc.u-strasbg.fr/viz-bin/qcat?J/A+A/566/A35

A&A 583, A50 (2015)
DOI: 10.1051/0004-6361/201526673

Astronomy & Astrophysics

Detecting ring systems around exoplanets using high resolution spectroscopy: the case of 51 Pegasi b⋆,⋆⋆

N. C. Santos[1,2], J. H. C. Martins[1,2,5], G. Boué[3], A. C. M. Correia[3,4], M. Oshagh[1], P. Figueira[1], A. Santerne[1], S. G. Sousa[1], C. Melo[5], M. Montalto[1], I. Boisse[6], D. Ehrenreich[7], C. Lovis[7], F. Pepe[7], S. Udry[7], and A. Garcia Munoz[8]

[1] Instituto de Astrofísica e Ciências do Espaço, Universidade do Porto, CAUP, Rua das Estrelas, 4150-762 Porto, Portugal
e-mail: nuno@astro.up.pt
[2] Departamento de Física e Astronomia, Faculdade de Ciências, Universidade do Porto, Rua do Campo Alegre, 4169-007 Porto, Portugal
[3] ASD, IMCCE-CNRS UMR8028, Observatoire de Paris, UPMC, 77 Av. Denfert-Rochereau, 75014 Paris, France
[4] CIDMA, Departamento de Física, Universidade de Aveiro, Campus de Santiago, 3810-193 Aveiro, Portugal
[5] European Southern Observatory, Casilla 19001, Santiago, Chile
[6] Aix Marseille Université, CNRS, LAM (Laboratoire d'Astrophysique de Marseille) UMR 7326, 13388 Marseille, France
[7] Observatoire de Genève, Université de Genève, 51 ch. des Maillettes, 1290 Sauverny, Switzerland
[8] Scientific Support Office, Directorate of Science and Robotic Exploration, ESA/ESTEC, Keplerlaan 1, 2201 AZ, Noordwijk, The Netherlands

Received 4 June 2015 / Accepted 4 August 2015

ABSTRACT

Aims. In this paper we explore the possibility that the recently detected reflected light signal of 51 Peg b could be caused by a ring system around the planet.
Methods. We use a simple model to compare the observed signal with the expected signal from a short-period giant planet with rings. We also use simple dynamical arguments to understand the possible geometry of such a system.
Results. We provide evidence that, to a good approximation, the observations are compatible with the signal expected from a ringed planet, assuming that the rings are non-coplanar with the orbital plane. However, based on dynamical arguments, we also show that this configuration is unlikely. In the case of coplanar rings we then demonstrate that the incident flux on the ring surface is about 2% the value received by the planet, a value that renders the ring explanation unlikely.
Conclusions. The results suggest that the signal observed cannot in principle be explained by a planet+ring system. We discuss, however, the possibility of using reflected light spectra to detect and characterize the presence of rings around short-period planets. Finally, we show that ring systems could have already been detected by photometric transit campaigns, but their signal could have been easily misinterpreted by the expected light curve of an eclipsing binary.

Key words. techniques: spectroscopic – planets and satellites: dynamical evolution and stability – planets and satellites: rings – planetary systems

1. Introduction

The detection of the atmospheres of extrasolar planets is becoming one of the major research topics in the exoplanet field (for a recent review see Burrows 2014). Current technology and a detailed data analysis have already allowed the signature of the atmospheres of other worlds to be detected using different methods, such as transmission spectroscopy (e.g., Charbonneau et al. 2002; Vidal-Madjar et al. 2003; Madhusudhan et al. 2014), occultations (e.g., Deming et al. 2005; Demory et al. 2012), and phase curve variations (e.g., Angerhausen et al. 2014). These studies allowed several detailed analyses of exoplanet atmospheres, including tracing of thermal or albedo maps of the planets (e.g., Knutson et al. 2007; Stevenson et al. 2014; Demory et al. 2013).

Although a large majority of the exoplanet atmosphere studies involved space-based data, the use of ground-based instrumentation to detect exoplanet atmospheres is providing a growing amount of information. This is particularly true concerning the use of high-resolution spectroscopic techniques. Using both optical and the near-infrared (near-IR) wavelengths, these methods allowed the spectrum to be probed in detail for several exoplanets (for some examples see Snellen et al. 2010; Birkby et al. 2013; Wyttenbach et al. 2015).

In a recent paper, Martins et al. (2015) have explored a new technique for detecting the signature of a high-resolution (optical) reflected light spectrum from an exoplanet. This detection allowed estimation of the radius and albedo of the historical 51 Peg b planet (Mayor & Queloz 1995), suggesting that this planet may be a high-albedo, inflated hot-Jupiter such as Kepler-7 b (with $A_g = 0.35$ Demory et al. 2013).

The predicted star-to-planet flux ratio for a star+planet system be estimated from (e.g., Seager 2010):

$$\frac{F_{\rm planet}}{F_*} = A_g\, g(\alpha) \left(\frac{R_p}{a}\right)^2 \quad (1)$$

where A_g is the geometric albedo of the planet, a the semi-major axis of the orbit, $g(\alpha)$ the phase function, and R_p the

⋆ Based on observations collected at ESO facilities under program 091.C-0271 (with the HARPS spectrograph at the ESO 3.6-m telescope, La Silla-Paranal Observatory).
⋆⋆ Appendices are available in electronic form at http://www.aanda.org

The Astrophysical Journal, 811:55 (12pp), 2015 September 20 doi:10.1088/0004-637X/811/1/55

FURTHER CONSTRAINTS ON THE OPTICAL TRANSMISSION SPECTRUM OF HAT-P-1b

M. Montalto[1], N. Iro[2], N. C. Santos[1,3], S. Desidera[4], J. H. C. Martins[1,3,5], P. Figueira[1,3], and R. Alonso[1,6]
[1] Instituto de Astrofísica e Ciências do Espaço, Universidade do Porto, CAUP, Rua das Estrelas, PT4150-762 Porto, Portugal; Marco.Montalto@astro.up.pt
[2] Theoretical Meteorology Group Klimacampus, University of Hamburg Grindelberg 5, D-20144, Hamburg, Germany
[3] Departamento de Física e Astronomia, Faculdade de Ciências, Universidade do Porto, Rua do Campo Alegre 687, PT4169-007 Porto, Portugal
[4] INAF—Osservatorio Astronomico di Padova, Vicolo dellOsservatorio 5, Padova, I-35122, Italy
[5] European Southern Observatory, Alonso de Cordova 3107, Vitacura Casilla 19001, Santiago 19, Chile
[6] Departamento de Astrofísica, Universidad de La Laguna, E-38206 La Laguna, Tenerife, Spain
Received 2015 May 27; accepted 2015 August 15; published 2015 September 18

ABSTRACT

We report on novel observations of HAT-P-1 aimed at constraining the optical transmission spectrum of the atmosphere of its transiting hot-Jupiter exoplanet. Ground-based differential spectrophotometry was performed over two transit windows using the DOLORES spectrograph at the Telescopio Nazionale Galileo. Our measurements imply an average planet to star radius ratio equal to $R_p/R_* = (0.1159 \pm 0.0005)$. This result is consistent with the value obtained from recent near-infrared measurements of this object, but differs from previously reported optical measurements, being lower by around 4.4 exoplanet scale heights. Analyzing the data over five different spectral bins of ∼600 Å wide, we observed a single peaked spectrum ($3.7\,\sigma$ level) with a blue cutoff corresponding to the blue edge of the broad absorption wing of sodium and an increased absorption in the region in-between 6180 and 7400 Å. We also infer that the width of the broad absorption wings due to alkali metals is likely narrower than the one implied by solar abundance clear atmospheric models. We interpret the result as evidence that HAT-P-1b has a partially clear atmosphere at optical wavelengths with a more modest contribution from an optical absorber than previously reported.

Key words: planets and satellites: atmospheres – planets and satellites: individual (HAT-P-1b) – techniques: spectroscopic

1. INTRODUCTION

The possibility to characterize transiting exoplanet atmospheres by means of high precision spectrophotometric measurements acquired during transits was theorized in a few works earlier in this century (Seager & Sasselov 2000; Brown 2001). The light of the hosting star, filtered by the planeary atmosphere in the terminator region is absorbed and scattered by chemical compounds so that, once observed at different wavelenghts, the atmosphere may appear more or less opaque to the observer. Hence, transit depth determinations obtained in different spectral domains can be used to reconstruct a low-resolution spectrum of the planetary atmosphere.

Models predict that atmospheres of cloud free hot-Jupiter planets should be dominated in the optical by broad absorption features of the alkali metals Na and K. Studies so far have revealed a certain diversity of atmospheric features. Sodium was first detected by Charbonneau et al. (2002) in the atmosphere of HD 209458b using the STIS spectrograph on board the *Hubble Space Telescope* (*HST*) and also confirmed later on by ground-based observations (Snellen et al. 2008). Subsequent studies have also revealed the presence of alkali metals in the atmospheres of other planets, for example sodium was detected in WASP-17b (e.g., Wood et al. 2011; Zhou & Bayliss 2012) and HAT-P-1b (Nikolov et al. 2014) while potassium has been detected in XO-2b (Sing et al. 2011), WASP-31b (Sing et al. 2015), and HAT-P-1b (Wilson et al. 2015). The atmospheres of other planets seem to be obscured by clouds or hazes, as in the case of WASP-12b (Sing et al. 2013) and HD 189733 (Pont et al. 2013), albeit for this planet narrow line cores of sodium were also found (Redfield et al. 2008; Huitson et al. 2012; Jensen et al. 2011).

Near infrared studies have soon complemented analysis conducted in the optical domain, particularly exploiting the *Spitzer Space Telescope* and lead to the conclusion that close-in extrasolar planets could be broadly subdivided into two big categories according to the structure of their temperature–pressure profiles (Hubeny et al. 2003; Fortney et al. 2006, 2008; Burrows et al. 2007, 2008). The pM class planets show a high altitude temperature inversion in their atmospheres whereas the pL class planets do not, resulting in different emergent spectral energy distributions in the near-infrared domain and different spectral signatures (like the flipping of water bands from absorption to emission passing from non-inverted to inverted atmospheres). The origin of such inversion is identified with the absorption of strong stellar irradiation in the optical domain by a variety of possible absorbers (Burrows et al 2007; Zahnle et al. 2009; Fortney et al. 2010).

The present study is focussed on HAT-P-1b, one interesting member of the family of hot-Jupiter planets. HAT-P-1b is a low mean density ($\rho_p \sim 0.35$ g cm^{-3}) giant exoplanet ($R_p \sim 1.2\,R_J$) discovered by the HATNet transit survey (Bákos et al. 2007). The host star ($V = 10.4$) is a member of a visual binary system with the two components separated by around 11″ on the sky (∼1500 AU). Both are G0V stars and the companion star is around half a magnitude brighter than the target in the V filter. The low density of the exoplanet, the brightness of the host star, and the presence of a close-by stellar companion make HAT-P-1b an ideal target for follow-up studies aiming at characterizing its atmosphere using transmission spectroscopy. In particular, the close stellar companion can be used to correct for systematic effects performing simultaneous differential spectrophotometric measurements of the two stars.

Astronomy & Astrophysics manuscript no. proxima
January 5, 2017

Atmospheric characterization of Proxima b by coupling the SPHERE high-contrast imager to the ESPRESSO spectrograph

C. Lovis[1], I. Snellen[2], D. Mouillet[3,4], F. Pepe[1], F. Wildi[1], N. Astudillo-Defru[1], J.-L. Beuzit[3,4], X. Bonfils[3,4], A. Cheetham[1], U. Conod[1], X. Delfosse[3,4], D. Ehrenreich[1], P. Figueira[5], T. Forveille[3,4], J. H. C. Martins[5,6], S. P. Quanz[7], N. C. Santos[5,8], H.-M. Schmid[7], D. Ségransan[1], and S. Udry[1]

[1] Observatoire astronomique de l'Université de Genève, 51 ch. des Maillettes, 1290 Versoix, Switzerland
[2] Leiden Observatory, Leiden University, Postbus 9513, 2300 RA Leiden, The Netherlands
[3] Univ. Grenoble Alpes, IPAG, F-38000 Grenoble, France
[4] CNRS, IPAG, F-38000 Grenoble, France
[5] Instituto de Astrofísica e Ciências do Espaço, Universidade do Porto, CAUP, Rua das Estrelas, 4150-762 Porto, Portugal
[6] European Southern Observatory, Casilla 19001, Santiago, Chile
[7] Institute for Astronomy, ETH Zurich, Wolfgang-Pauli-Strasse 27, 8093 Zurich, Switzerland
[8] Departamento de Física e Astronomia, Faculdade de Ciências, Universidade do Porto, Rua do Campo Alegre, 4169-007 Porto, Portugal

Received 10 September 2016 / Accepted

ABSTRACT

Context. The temperate Earth-mass planet Proxima b is the closest exoplanet to Earth and represents what may be our best ever opportunity to search for life outside the Solar System.
Aims. We aim at directly detecting Proxima b and characterizing its atmosphere by spatially resolving the planet and obtaining high-resolution reflected-light spectra.
Methods. We propose to develop a coupling interface between the SPHERE high-contrast imager and the new ESPRESSO spectrograph, both installed at ESO VLT. The angular separation of 37 mas between Proxima b and its host star requires the use of visible wavelengths to spatially resolve the planet on a 8.2-m telescope. At an estimated planet-to-star contrast of $\sim 10^{-7}$ in reflected light, Proxima b is extremely challenging to detect with SPHERE alone. However, the combination of a $\sim 10^3$-10^4 contrast enhancement from SPHERE to the high spectral resolution of ESPRESSO can reveal the planetary spectral features and disentangle them from the stellar ones.
Results. We find that significant but realistic upgrades to SPHERE and ESPRESSO would enable a 5-σ detection of the planet and yield a measurement of its true mass and albedo in 20-40 nights of telescope time, assuming an Earth-like atmospheric composition. Moreover, it will be possible to probe the O_2 bands at 627, 686 and 760 nm, the water vapour band at 717 nm, and the methane band at 715 nm. In particular, a 3.6-σ detection of O_2 could be made in about 60 nights of telescope time. Those would need to be spread over 3 years considering optimal observability conditions for the planet.
Conclusions. The very existence of Proxima b and the SPHERE-ESPRESSO synergy represent a unique opportunity to detect biosignatures on an exoplanet in the near future. It is also a crucial pathfinder experiment for the development of Extremely Large Telescopes and their instruments, in particular the E-ELT and its high-resolution visible/near-IR spectrograph.

Key words. Planets and satellites: individual: Proxima b – Planets and satellites: atmospheres – Techniques: high angular resolution – Techniques: spectroscopic

1. Introduction

1.1. Observing exoplanet atmospheres

The field of exoplanets has seen tremendous progress over the past two decades, evolving from a niche research field with marginal reputation to mainstream astrophysics. The number of exoplanet properties that have become accessible to observations has been continuously growing. The radial velocity and transit techniques have been the two pillars over which exoplanet studies have developed, providing the two most fundamental physical properties of an exoplanet: mass and radius. Simultaneously, spatially-resolved imaging has been studying the properties of young and massive exoplanets on wide orbits. More recently, the field has been moving towards a more detailed characterization of planets and planetary systems, from their orbital architecture to their internal structure to the composition of their atmospheres. The study of exoplanet atmospheres, in particular, is widely seen as the new frontier in the field, a necessary step to elucidate the nature of the mysterious and ubiquitous super-Earths and mini-Neptunes. It is also the only means of directly addressing the fundamental question: has life evolved on other worlds?

Atmospheric characterization heavily relies on the availability of favourable targets, given the extremely low-amplitude signals to be detected and the present instrumental limitations. That is why a major effort is being made to systematically search for the nearest exoplanets with the largest possible atmospheric signatures. One of the most successful techniques so far has been transit spectroscopy, where an exoplanet atmosphere is il-

Send offprint requests to: C. Lovis, e-mail: christophe.lovis@unige.ch

TALKS AND SEMINARS A.2

SEMINAR

Exoplanet Reflections in the era of Giant Telescopes

Location: ESO Thirty Minute Talk, ESO - Chile **Date:** 2016-11-30
File: N/A

Abstract:

The detection of reflected light from exoplanets is a daunting task, pushing current observing facilities to their limits. The advent of 30m class telescopes will get us past these boundaries, enabling us not only to detect reflected light from exoplanets, but recover the color dependence of those planets albedo function. This quantity is paramount towards the understanding of exoplanet atmospheres as it is highly dependent on the constituents of a planet's atmosphere and is a direct measure on how these reflect the incident light under a given conditions of temperature and pressure.

In this talk I will show how the Cross Correlation Technique presented in Martins et al 2015 can be used to recover recover the color dependence of the albedo function from exoplanets with next generation observing facilities. I will present some results on the recovery of the color dependence of the albedo function from selected known planets from simulated observations with ESPRESSO@VLT and HIRES@ELT.

TALK

Exoplanet Reflections in the era of Giant Telescopes

Location: E^{3}LT: Exoplanets in the Era of Extremely Large Telescopes, Asilomar Conference Grounds, Pacific Grove, CA, USA **Date:** 2016-09-28

File: N/A

Abstract:

The detection of reflected light from exoplanets is a daunting task, pushing current observing facilities to their limits. The advent of 30m class telescopes will get us past these boundaries, enabling us not only to detect reflected light from exoplanets, but recover the color dependence of those planets albedo function. This quantity is paramount towards the understanding of exoplanet atmospheres as it is highly dependent on the constituents of a planet's atmosphere and is a direct measure on how these reflect the incident light under a given conditions of temperature and pressure.

In this talk I will the present our latest results using the current instrumentation available in the 4-m to 8-m class telescopes. In a second part, I will explore the future perspectives brought by the next generation of 30m class telescopes such as the GMT and ESO's ELT in the recovery of the color dependence of the albedo function from exoplanets. I will focus on how to recover this color dependence using the Cross Correlation Technique presented in Martins et al. (2015a). I will also present the results of recent simulations in which we were able to recover the color dependence of the albedo function for several prototypical exoplanet classes.

TALK

Exoplanet Reflections: the light from 51 Peg b

Location: *OHP2015 : 20 Years of Giant Exoplanets*, Observatoire Haute Provence, France **Date:** 2015-10-07

File: http://interferometer.osupytheas.fr/colloques/OHP2015/slides/OHP2015_JorgeMartins.pdf

Abstract:

This talk was presented at the *OHP2015 : 20 Years of Giant Exoplanets* conference at the Observatoire Haute Provence (France). This conference was intended to celebrate the 20 years of discovery of the first exoplanet confirmed around a solar-type star by discussing key questions regarding giant planets and how to solve them in the coming years.

In this conference talk, I presented a technique based on the Cross Correlation Function to detect the reflected spectroscopic optical signature from exoplanets (Martins et al., 2013) and how it was applied the first time to recover the signal from 51 Pegasi b (Martins et al., 2015a)

TALK

Reflected light from exoplanets via high resolution spectroscopy

Location: *Astrobiology and Planetary Atmospheres*, ESO - Chile **Date:** 2015-10-01
File: `http://www.eso.org/sci/meetings/2015/AstroBio2015/Talks/Thursday/MartinsJ.pdf`

Abstract:

The direct detection of reflected light from exoplanets is an excellent probe for the characterization of an exoplanet's atmosphere. In this talk we will introduce a technique that makes use of high resolution spectra to surpass the difficult technical challenge this genre of detection represents. We will also present its application to real observations of the prototypical planet 51 Pegasi b and show the potential of this technique when applied to future observing facilities.

TALK

Detecting the optical reflected spectrum of 51 Peg b

Location: *Exoplanet Focus Meeting for the Chilean Scientific Community*, ESO - Chile **Date:** 2015-06-04
File: `www.eso.org/sci/meetings/2015/Exoplanet2015/Talks/Jorge_martins.pdf`

Abstract:

The direct detection of reflected light from an exoplanet is, even in the most favourable cases, a herculean task, close to the detection limit of current observing facilities. In this talk, we will show how the Cross Correlation Function can be used to recover the minute reflected signal from an exoplanet in the optical (see Martins et al., 2015a). We will also present the evidences for the first direct detection of the optical reflected spectrum of 51 Peg on its orbiting planet, as well as how this result can be used to tentatively infer some of the planet's characteristics as detaily described in Martins et al. (2015a)

SEMINAR

Reflected light from exoplanets: The case of 51 Peg b

Location: ESO Thirty Minute Talk, ESO - Chile **Date:** 2015-04-24
File: N/A

Abstract:

The direct detection of reflected light from an exoplanet is, even in the most favourable cases, a herculean task, close to the detection limit of current observing facilities. In this talk, we will show how the Cross Correlation Function can be used to recover the minute reflected signal from an exoplanet in the optical (Martins et al., 2013). We will also present the evidences for the first direct detection of the optical reflected spectrum of 51 Peg on its orbiting planet, as well as how this result can be used to tentatively infer some of the planet's characteristics as detaily described in Martins et al. (2015a).

SEMINAR

Complementarity Between Detection Methods

Location: Cookie Seminar, CAUP, Portugal **Date:** 2014-04-30
File: N/A

Abstract:

Planet detection methods have evolved greatly over the last few years, allowing for the detection of over 1700 planets in over one thousand planetary systems. Nonetheless,individually detection methods are extremely limited and in most cases they do not allow to fully characterize the planetary systems. To access the unavailable parameter spaces we need combine several detection methods, usually spending more time on follow up observations. In this talk, I will make a brief introduction on current planet detection methods. Next, I intend to present a few examples where the combination of planet detection methods allows for a full characterization of the detected systems, not only in terms of directly detectable parameters, but also to infer and constrain information otherwise inaccessible (e.g. composition).

POSTERS A.3

POSTER

A method to detect reflected light from giant planets in habitable zones

Location: *K2 meeting*, IA - Porto, Portugal **Date:** 2016-05-10
File: `http://www.iastro.pt/research/conferences/k2meeting/index.html?opt=posters`

Abstract:
In this poster we describe how the Cross Correlation Function can be used to make the planetary signal surface above the noise level of our observations and how it can be used to detect giant planets in their host's habitable zone. These restults were published in Martins et al., 2016

POSTER

Spectroscopic direct detection of reflected light from an exoplanet

Location: *Towards Other Earths II: The star-planet connection*, Porto, Portugal **Date:** 2014, Sep 15-19
File: `http://www.astro.up.pt/investigacao/conferencias/toe2014/index.php?opt=posters`

Abstract:
In this poster I presented the preliminary results on the detection of the reflected optical spectrum from an unamed exoplanet. This work led to the puclication of the aforementioned article on the detection of reflected light from the prototypical Hot-Jupiter 51 Pegasi b (see Martins et al., 2015a)

ATTENDED CONFERENCES AND WORKSHOPS A.4

CONFERENCE

E^3LT: Exoplanets in the Era of Extremely Large Telescopes

Location: Asilomar Conference Grounds, Pacific Grove, CA, USA **Date:** 2016, Sep 26-28
Website http://www.gmtconference.org/welcome-reception/

Description:

From September 25-28 more than a hundred astronomers gathered at the Asilomar Conference Grounds in Pacific Grove, CA to participate in the Fourth Annual GMT Community Science Meeting, *Exoplanets in the Era of Extremely Large Telescopes*. GMTO's policy of supporting young astronomers to attend these meetings ensured there were many students and postdocs presenting their cutting-edge research.

The conference highlighted how the next generation of Extremely Large Telescopes (ELTs), and in particular the GMT and its suite of instruments, are needed to make progress in the field of exoplanet science.

CONFERENCE

OHP2015 : 20 Years of Giant Exoplanets

Location: Observatoire Haute Provence, France **Date:** 2015, Oct 5-9
Website http://ohp2015.sciencesconf.org/

Description:

The *OHP2015 : 20 Years of Giant Exoplanets* conference at the Observatoire Haute Provence (France) was intended to celebrate the 20 years of discovery of the first exoplanet confirmed around a solar-type star by discussing key questions regarding giant planets and how to solve them in the coming years.

CONFERENCE

Astrobiology and Planetary Atmospheres

Location: ESO - Chile **Date:** 2015, Sep 28 to Oct 2
Website http://www.eso.org/sci/meetings/2015/AstroBio2015.html

Description:

The discovery of an imensity of exoplanets over the past 20 years brought forward an ages question old question: *Are we alone in the Universe?* To answer this question, the organization fo this conference brought together researchers from the major astrobiology groups from the World and their South American counterparts to share knowledge and foster colaborations among the major subjects in the field of astrobiology.

WORKSHOP

Exoplanet Focus Meeting for the Chilean Scientific Community

Location: ESO - Chile **Date:** 2015-06-04
Website http://www.eso.org/sci/meetings/2015/Exoplanets2015.html

Description:

Chile hosts some of the most advanced observing facilities in the world and thus is of paramount importance for exoplanetary research. The purpose of this workshop was to bring together exoplanets researchers from the Chilean Scientific Community and give a better understanding of the status of exoplanetary research in Chile.

WORKSHOP

K2 meeting

Location: IA - Porto, Portugal **Date:** 2016-05-10
Website http://www.iastro.pt/research/conferences/k2meeting/

Description:

The K2 mission is finding very interesting planetary candidates that can be characterised with ground-based facilities. Several groups are participating independently to the follow-up efforts. While competition is a good source of motivation, duplication of the work is also a waste of time (both human and facility resources). With a better communication, coordination or even collaboration between the groups, it would be possible to improve the exploitation of the K2 data and the use of available resources. Organising the various K2 efforts will also be a good practice for the upcoming follow-up of the TESS and PLATO candidates.

CONFERENCE

Towards Other Earths II: The star-planet connection

Location: Porto, Portugal **Date:** 2014, Sep 15-19
Website http://www.astro.up.pt/investigacao/conferencias/toe2014/

Description:

The study of extrasolar planets is one of the most active areas of research of modern astronomy. The number of discoveries attests for the importance of a topic that reaches out and captivates the imagination of scientists and public alike. This conference aims at reviewing the state of the art of star-planet connection, with some focus on the detection and characterization of Earth like planets orbiting other stars. We propose to debate how the field of extrasolar planets will evolve in respect to this and how it will face the challenges of the upcoming years.

OUTREACH A.5

TALK

From here to Infinity

Location: Astronomy on Tap, The Shamrock, Santiago, Chile **Date:** 2015-06-24
File: `https://www.facebook.com/AstronomyonTapChile/`

Abstract:

Astronomy on Tap ([link]) is a international outreach programme that consists of a monthly series of outreach talks given by Astronomers at a local pub the intent to reduce the gap between Astronomers and the general Public. I presented a talk of the series in June 2015 regarding distances and dimensions in Astronomy from the smallest to the largest objects/distances.

OUTREACH

Organization and hosting of Astronomy on Tap - Chile

Location: The Shamrock, Santiago, Chile **Date:** 2015 May-Aug
Website `N/A`

Description:

Astronomy on Tap ([link]) is a international outreach programme that consists of a monthly series of outreach talks given by Astronomers at a local pub the intent to reduce the gap between Astronomers and the general Public. ESO-Chile got involved in this programme through Dr. Amy Tyndal (while she was a PhD student at ESO-Chile), for which she would be responsible to prepare and host the events. Between March and August 2015, I took over the hosting of Astronomy on Tap - Chile and was responsible for the preparation of each individual event in colaboration with several Pos-Docs/Fellows at ESO Chile.

OUTREACH

ESO/ALMA Open House Day, Chile

Location: ESO - Chile **Date:** 2015-03-20
Website N/A

Description:

On March 20th, Chile celebrated the second edition of *Día de la Astronomía* organised by *Planetario de la Universidad de Santiago* (http://www.planetariochile.cl/) and *Conicyt* (http://www.conicyt.cl/). This year, ESO joined the celebrations with an Open House Day at Vitacura premises. During this day, over 140 children from local public schools visited the ESO/Atacama Large Millimeter Array (ALMA) premises, where several activities expected them. These activities were supported by ESO/ALMA volunteers which gave the visitors a walking tour around the ESO/ALMA facilities, showed them the Sun on solar telescopes and the southern sky in an inflatable planetarium. My participation in these activities included showing them the premises, explaining some astronomical images spread across the ESO/ALMA fences and solar observations.

TALK

Four Elements - Earth

Location: Municipal Library of Porto, Portugal **Date:** 2017-10-28
File: N/A

Abstract:

Informal talk between myself, an astro-philosopher and the curator responsible for the Earth element of an art exhibit at the Municipal Library of Porto, Portugal. This talk was part of the art exhibit and the subject was the Earth element. My approach was the scientific perspective of the detection of New Earths around other stars.

OTHER A.6

ACCEPTED PROPOSALS

ESO P93 Proposal: 093.C-0929(D)

Detecting the optical reflected light from exoplanets

Location: ESO's La Silla-Paranal Observatory, Chile **Date:** 2014 Apr-Sep
Website https://www.eso.org/sci/observing/teles-alloc/All_proposals/P93_All_Scheduled_Runs.pdf

Description:

We submitted a proposal to ESO call P93 regarding the detection of reflected light from exoplanets. Of the 4 runs we proposed (once per planet), one was accepted and we acquired UVES observations of 51 Peg totalling around 9h of total exposure time (17h with overheads). I propose 20 points for this task.

TEACHING

Monitor at the 10thPhysics Summer School

Location: Faculty of Science, University of Porto, Portugal **Date:** 2014 Sep
Website http://e-fisica.fc.up.pt/edicoes/10a-edicao

Description:

Na sua 10a Edição a Escola desafia os participantes com o programa mais radical de sempre com projectos envolvendo lasers, supercondutores, nanotecnologias, física espacial, fibras ópticas, biosensores e astrofísica. Projectos que abrangem as três grandes áreas de investigação do DFA, Física, Astronomia e Engenharia Física. Assim, se tens apetência pelo conhecimento e pelo processo de investigação que permite inquirir a Natureza e testar hipóteses acerca das causas das coisas, então deixa-te arrastar pelo encantamento da experimentação e do entendimento das ideias mais profundas e abrangentes. O DFA garante uma viagem através do Universo, do microcosmo ao macrocosmo, inserindo-te num projecto que te dilatará a imaginação. Tens coragem? Aparece!

OBSERVING RUNS

HARPS@3.6m observing run

Location: ESO's La Silla-Paranal Observatory, Chile **Date:** 2014-2016
Website N/A

Description:

Observing runs are an essential part of the training of any astronomer. During my PhD I realized the following runs:

- ⋆ 2014, February 9-16
- ⋆ 2015, February 6-13
- ⋆ 2016, May 6-10

In all of them I went observing for mixed programs from IA-Porto researchers and collaborators.

Appendix B.
Observations of 51 Pegasi b

The tables presented in this appendix present the values for the most relevant parameters for each individual HARPS observation of the 51 Pegasi system with HARPS (Table B.1) and UVES (Table B.2). The presented parameters are:

BJD	barycentric Julian date at the start of each observation minus 2 400 000 days;
RV	RV of the stellar CCF;
$\sigma(RV)$	error on the RV of the stellar CCF;
FWHM	FWHM of the stellar CCF;
$\sigma(FWHM)$	error on the FWHM of the stellar CCF (only for UVES);
Contrast	depth of the stellar CCF of the stellar CCF, with the continuum defined as one;
t_{exp}	individual exposure time for each observation;
S/N	S/N at the center of order XXX ($\lambda = YYYnm$) for HARPS and order XXX ($\lambda = YYYnm$) for UVES;

HARPS B.1

BJD	RV	$\sigma(RV)$	FWHM	Contrast	t_{exp}	S/N
56506.318050	-33.147	0.438	7.422	0.482	600	17
56565.084257	-33.181	0.230	7.427	0.484	450	35
56565.229447	-33.170	0.199	7.427	0.484	450	40
56508.344226	-33.154	0.217	7.432	0.484	500	36
56565.056347	-33.183	0.252	7.428	0.484	450	30

Description of the available data on a per night basis. (continued ...)

BJD	RV	$\sigma(RV)$	FWHM	Contrast	t_{exp}	S/N
56544.085928	-33.168	0.361	7.425	0.482	600	19
56468.299933	-33.155	0.301	7.426	0.483	550	23
56565.026221	-33.185	0.326	7.426	0.483	300	21
56565.145630	-33.178	0.187	7.430	0.484	450	42
56565.022382	-33.185	0.337	7.425	0.483	300	20
56508.282646	-33.149	0.294	7.429	0.483	500	27
56565.140051	-33.178	0.202	7.429	0.484	450	39
56565.095415	-33.181	0.212	7.428	0.484	450	38
56451.341380	-33.158	0.277	7.427	0.483	420	25
56565.089832	-33.182	0.200	7.429	0.484	450	40
56565.179101	-33.175	0.184	7.429	0.484	450	43
56565.117741	-33.181	0.199	7.428	0.484	450	40
56544.144477	-33.164	0.385	7.425	0.482	600	19
56508.338069	-33.152	0.228	7.434	0.484	500	35
56565.106578	-33.181	0.210	7.427	0.484	450	38
56544.107891	-33.168	0.256	7.430	0.484	600	30
56565.128893	-33.180	0.196	7.428	0.484	450	41
56544.166448	-33.163	0.422	7.427	0.482	600	17
56565.223747	-33.171	0.183	7.430	0.485	450	42
56544.173775	-33.163	0.361	7.425	0.483	600	21
56540.178824	-33.143	0.302	7.428	0.483	600	26
56565.167949	-33.176	0.193	7.429	0.484	450	41
56565.134472	-33.179	0.198	7.429	0.484	450	40
56565.100994	-33.180	0.218	7.429	0.484	450	37
56565.173523	-33.175	0.203	7.430	0.484	450	40
56540.164174	-33.145	0.270	7.428	0.484	600	29
56508.288809	-33.149	0.267	7.431	0.484	500	30
56565.033910	-33.185	0.329	7.425	0.483	450	22
56565.151211	-33.178	0.198	7.428	0.484	450	40
56468.417741	-33.144	0.202	7.429	0.484	500	36
56565.061925	-33.184	0.232	7.428	0.484	450	33
56508.368854	-33.156	0.261	7.432	0.484	500	30
56565.030068	-33.186	0.381	7.427	0.482	300	18

Description of the available data on a per night basis. (continued ...)

BJD	RV	$\sigma(RV)$	FWHM	Contrast	t_{exp}	S/N
56565.156791	-33.177	0.205	7.430	0.484	450	39
56468.284909	-33.156	0.260	7.426	0.484	450	29
56565.207014	-33.173	0.188	7.432	0.484	450	42
56508.387322	-33.156	0.245	7.433	0.484	500	30
56508.301124	-33.151	0.239	7.430	0.484	500	33
56540.186127	-33.143	0.342	7.427	0.483	600	23
56544.159118	-33.162	0.539	7.420	0.481	600	12
56508.270334	-33.148	0.289	7.431	0.483	500	27
56508.325748	-33.153	0.224	7.432	0.484	500	35
56508.381170	-33.156	0.263	7.432	0.484	500	29
56468.411151	-33.145	0.220	7.428	0.484	500	33
56565.162370	-33.176	0.212	7.430	0.484	450	37
56565.078679	-33.183	0.225	7.426	0.484	450	35
56508.350383	-33.154	0.234	7.434	0.484	500	33
56508.319590	-33.151	0.227	7.431	0.484	500	35
56508.294967	-33.151	0.250	7.428	0.484	500	32
56565.190264	-33.174	0.176	7.430	0.484	450	44
56451.336146	-33.157	0.281	7.429	0.483	420	25
56540.171503	-33.144	0.271	7.429	0.483	600	29
56508.313433	-33.152	0.219	7.433	0.484	500	36
56565.039607	-33.185	0.283	7.425	0.483	450	26
56451.346607	-33.158	0.233	7.431	0.484	520	31
56544.137157	-33.165	0.345	7.425	0.483	600	21
56565.050768	-33.184	0.285	7.426	0.483	450	26
56544.093251	-33.169	0.311	7.426	0.483	600	23
56508.331905	-33.152	0.236	7.432	0.484	500	33
56544.115219	-33.168	0.264	7.427	0.484	600	29
56565.123319	-33.180	0.204	7.428	0.484	450	39
56508.356540	-33.155	0.216	7.434	0.484	500	36
56565.184682	-33.175	0.185	7.431	0.484	450	43
56565.212591	-33.171	0.184	7.431	0.484	450	43
56468.307488	-33.155	0.392	7.423	0.482	600	17
56544.151803	-33.164	0.430	7.423	0.482	600	17

Description of the available data on a per night basis. (continued ...)

BJD	RV	$\sigma(RV)$	FWHM	Contrast	t_{exp}	S/N
56544.129842	-33.166	0.291	7.429	0.483	600	26
56468.436622	-33.145	0.198	7.428	0.484	500	36
56506.325361	-33.148	0.457	7.424	0.482	493	16
56544.122533	-33.166	0.291	7.426	0.483	600	26
56508.375012	-33.156	0.246	7.432	0.484	500	31
56468.443203	-33.145	0.204	7.429	0.484	500	35
56565.073089	-33.182	0.227	7.427	0.484	450	35
56565.067510	-33.183	0.234	7.427	0.484	450	33
56468.430464	-33.144	0.201	7.428	0.484	500	36
56508.276493	-33.147	0.309	7.432	0.483	500	25
56565.045194	-33.185	0.257	7.425	0.484	450	29
56565.195849	-33.174	0.178	7.431	0.484	450	44
56468.291639	-33.157	0.207	7.428	0.484	600	38
56544.100565	-33.169	0.262	7.428	0.483	600	29
56468.424306	-33.144	0.200	7.431	0.484	500	36
56565.201434	-33.174	0.179	7.431	0.484	450	44
56508.307280	-33.151	0.232	7.432	0.484	500	34
56565.218169	-33.171	0.176	7.430	0.485	450	44
56565.112157	-33.181	0.212	7.428	0.484	450	38
56508.362692	-33.155	0.233	7.433	0.484	500	33

Table B.1: Description of the available data on a per night basis.

UVES B.2

BJD	RV $[km/s]$	$\sigma(RV)$ $[km/s]$	FWHM $[km/s]$	$\sigma(FWHM)$ $[km/s]$	Contrast	t_{exp} $[s]$	S/N
56869.388921	-32.477	0.015	7.916	0.037	0.361	23	181
56958.063755	-32.652	0.007	7.958	0.018	0.358	105	219
56958.085150	-32.727	0.007	7.961	0.018	0.357	150	281
56958.069122	-32.677	0.007	7.950	0.018	0.359	105	207
56958.106642	-32.752	0.007	7.955	0.018	0.358	77	224
56958.065543	-32.661	0.007	7.963	0.018	0.358	105	221

Description of each individual UVES observation. (continued ...)

BJD	RV $[km/s]$	$\sigma(RV)$ $[km/s]$	FWHM $[km/s]$	$\sigma(FWHM)$ $[km/s]$	Contrast	t_{exp} $[s]$	S/N
56958.075922	-32.660	0.007	7.964	0.018	0.358	150	256
56958.103720	-32.753	0.007	7.954	0.018	0.358	77	217
56958.044102	-32.587	0.007	7.953	0.018	0.358	105	215
56958.051244	-32.600	0.007	7.954	0.018	0.358	105	215
56958.078230	-32.662	0.007	7.960	0.018	0.358	150	262
56958.109568	-32.770	0.007	7.962	0.018	0.358	77	227
56958.098994	-32.777	0.007	7.966	0.018	0.356	150	312
56958.087456	-32.741	0.007	7.956	0.018	0.357	150	291
56958.040528	-32.594	0.007	7.952	0.018	0.359	105	211
56958.054819	-32.619	0.007	7.957	0.018	0.358	105	226
56958.067330	-32.661	0.007	7.957	0.018	0.358	105	229
56958.082847	-32.700	0.007	7.955	0.018	0.358	150	272
56958.061964	-32.635	0.007	7.957	0.018	0.358	105	233
56958.118330	-32.762	0.007	7.964	0.018	0.358	77	217
56958.092068	-32.742	0.007	7.963	0.018	0.357	150	283
56958.094375	-32.742	0.007	7.969	0.018	0.357	150	283
56958.115411	-32.722	0.007	7.963	0.018	0.358	77	208
56958.108106	-32.736	0.007	7.953	0.018	0.358	77	222
56958.038745	-32.585	0.007	7.955	0.017	0.358	105	215
56958.116872	-32.737	0.007	7.955	0.018	0.358	77	199
56958.111027	-32.800	0.007	7.959	0.018	0.358	77	224
56958.080542	-32.679	0.007	7.956	0.018	0.358	150	275
56958.053032	-32.616	0.007	7.957	0.018	0.358	105	216
56958.112490	-32.780	0.007	7.962	0.018	0.358	77	232
56958.056606	-32.612	0.007	7.954	0.018	0.358	105	221
56958.036958	-32.585	0.007	7.950	0.018	0.359	105	201
56958.042317	-32.576	0.007	7.947	0.018	0.359	105	213
56958.096685	-32.755	0.007	7.966	0.018	0.356	150	306
56958.113950	-32.755	0.007	7.962	0.018	0.358	77	222
56958.058388	-32.635	0.007	7.945	0.018	0.359	105	226
56958.089763	-32.728	0.007	7.964	0.018	0.357	150	291
56958.072690	-32.660	0.007	7.957	0.018	0.358	105	214

Description of each individual UVES observation. (continued . . .)

BJD	RV $[km/s]$	$\sigma(RV)$ $[km/s]$	FWHM $[km/s]$	$\sigma(FWHM)$ $[km/s]$	Contrast	t_{exp} $[s]$	S/N
56958.049461	-32.602	0.007	7.956	0.018	0.358	105	217
56958.105180	-32.745	0.007	7.963	0.018	0.358	77	222
56958.102259	-32.786	0.007	7.956	0.018	0.358	77	224
56958.060172	-32.640	0.007	7.956	0.018	0.358	105	224
56958.047675	-32.609	0.007	7.959	0.018	0.358	105	212
56958.045888	-32.588	0.007	7.951	0.018	0.359	105	215
56958.070905	-32.659	0.007	7.952	0.018	0.358	105	227
56928.216316	-33.111	0.007	7.946	0.018	0.361	34	159
56928.117549	-32.706	0.007	7.882	0.018	0.363	34	183
56928.097690	-32.887	0.007	7.915	0.019	0.361	49	207
56928.151249	-32.642	0.007	7.891	0.018	0.362	34	161
56928.127180	-32.623	0.007	7.879	0.018	0.363	34	178
56928.204742	-33.028	0.007	7.906	0.019	0.362	34	171
56928.199932	-33.106	0.007	7.914	0.018	0.361	34	164
56928.081779	-33.018	0.011	8.184	0.028	0.359	49	205
56928.038738	-32.770	0.007	7.967	0.019	0.359	34	142
56928.062836	-32.892	0.008	7.949	0.019	0.360	34	155
56928.162652	-32.725	0.019	8.309	0.049	0.360	34	152
56928.168437	-32.590	0.007	7.888	0.018	0.363	34	138
56928.163616	-32.502	0.007	7.863	0.019	0.364	34	153
56928.182889	-32.992	0.007	7.942	0.018	0.360	34	154
56928.188665	-33.005	0.008	7.893	0.019	0.362	34	155
56928.206673	-33.032	0.008	7.928	0.019	0.361	34	161
56928.034877	-32.802	0.007	7.980	0.019	0.359	34	140
56928.094282	-32.861	0.007	7.939	0.018	0.360	49	200
56928.211494	-32.930	0.007	7.927	0.019	0.361	34	155
56928.201858	-33.041	0.008	7.926	0.019	0.361	34	164
56928.152209	-32.689	0.007	7.905	0.018	0.362	34	158
56928.070545	-32.844	0.007	7.944	0.018	0.360	34	160
56928.147398	-32.688	0.007	7.899	0.018	0.362	34	163
56928.121402	-32.678	0.007	7.875	0.019	0.363	34	181
56928.190589	-33.001	0.008	7.895	0.019	0.362	34	172

Description of each individual UVES observation. (continued . . .)

BJD	RV $[km/s]$	$\sigma(RV)$ $[km/s]$	FWHM $[km/s]$	$\sigma(FWHM)$ $[km/s]$	Contrast	t_{exp} $[s]$	S/N
56928.222085	-33.107	0.008	7.956	0.021	0.360	34	149
56928.064762	-32.836	0.008	7.964	0.019	0.359	34	164
56928.044520	-32.827	0.008	7.969	0.019	0.359	34	149
56928.063800	-32.870	0.008	7.947	0.019	0.360	34	157
56928.126216	-32.648	0.007	7.888	0.019	0.362	34	177
56928.082918	-32.880	0.008	7.951	0.019	0.360	49	191
56928.105654	-32.843	0.007	7.916	0.019	0.361	49	207
56928.210530	-32.919	0.008	7.911	0.019	0.361	34	155
56928.224974	-33.055	0.009	7.971	0.022	0.360	34	140
56928.145471	-32.692	0.007	7.880	0.019	0.363	34	171
56928.200891	-33.044	0.007	7.922	0.019	0.361	34	162
56928.221123	-33.150	0.009	7.964	0.022	0.361	34	157
56928.074961	-32.890	0.007	7.951	0.019	0.359	49	194
56928.035841	-32.774	0.007	7.977	0.018	0.358	34	143
56928.112480	-32.797	0.008	7.887	0.019	0.362	49	213
56928.054152	-32.766	0.007	7.974	0.019	0.359	34	142
56928.132952	-32.524	0.007	7.836	0.018	0.365	34	172
56928.217281	-33.014	0.008	7.947	0.021	0.361	34	153
56928.058008	-32.778	0.007	7.963	0.019	0.359	34	142
56928.089734	-32.860	0.007	7.962	0.019	0.359	49	201
56928.212461	-32.914	0.008	7.921	0.019	0.361	34	153
56928.150286	-32.652	0.007	7.894	0.018	0.362	34	158
56928.115629	-32.711	0.007	7.871	0.019	0.363	34	186
56928.109069	-32.832	0.007	7.910	0.019	0.361	49	208
56928.169402	-32.513	0.007	7.870	0.018	0.363	34	143
56928.137767	-32.702	0.007	7.868	0.018	0.363	34	183
56928.043555	-32.813	0.007	7.979	0.019	0.359	34	146
56928.042591	-32.826	0.007	7.968	0.019	0.359	34	150
56928.122362	-32.678	0.008	7.891	0.019	0.362	34	178
56928.203780	-33.012	0.008	7.938	0.019	0.360	34	173
56928.224010	-33.110	0.008	7.965	0.020	0.360	34	142
56928.125251	-32.671	0.008	7.900	0.019	0.362	34	177

Description of each individual UVES observation. (continued . . .)

BJD	RV $[km/s]$	$\sigma(RV)$ $[km/s]$	FWHM $[km/s]$	$\sigma(FWHM)$ $[km/s]$	Contrast	t_{exp} $[s]$	S/N
56928.031985	-32.783	0.008	7.977	0.019	0.358	34	143
56928.061874	-32.918	0.007	7.953	0.019	0.360	34	161
56928.156875	-32.624	0.007	7.896	0.018	0.362	34	156
56928.088600	-32.923	0.007	7.935	0.019	0.360	49	204
56928.234593	-33.262	0.009	7.972	0.022	0.360	34	132
56928.036812	-32.787	0.008	7.980	0.019	0.358	34	142
56928.041628	-32.770	0.007	7.982	0.019	0.359	34	145
56928.090871	-32.926	0.008	7.944	0.019	0.359	49	214
56928.186739	-33.068	0.007	7.912	0.019	0.361	34	156
56928.060909	-32.847	0.008	7.963	0.019	0.359	34	161
56928.079508	-32.946	0.008	7.932	0.019	0.360	49	201
56928.191551	-32.978	0.007	7.910	0.019	0.361	34	176
56928.159762	-32.644	0.007	7.894	0.018	0.362	34	147
56928.161688	-32.613	0.007	7.882	0.019	0.363	34	149
56928.184813	-32.991	0.007	7.915	0.019	0.361	34	153
56928.129104	-32.594	0.007	7.869	0.018	0.363	34	170
56928.148363	-32.682	0.008	7.898	0.019	0.362	34	162
56928.138729	-32.735	0.008	7.881	0.019	0.363	34	182
56928.235560	-33.269	0.007	7.962	0.019	0.360	34	134
56928.096554	-32.884	0.007	7.931	0.019	0.360	49	204
56928.111345	-32.781	0.007	7.897	0.019	0.361	49	213
56928.215353	-33.042	0.009	7.948	0.022	0.361	34	163
56928.173254	-32.697	0.007	7.907	0.018	0.362	34	147
56928.095421	-32.893	0.007	7.937	0.018	0.360	49	199
56928.149323	-32.691	0.007	7.891	0.018	0.363	34	156
56928.197043	-32.912	0.007	7.903	0.018	0.362	34	177
56928.170364	-32.603	0.007	7.887	0.018	0.363	34	140
56928.055117	-32.782	0.007	7.966	0.018	0.359	34	141
56928.205706	-32.997	0.007	7.941	0.019	0.360	34	162
56928.180007	-32.798	0.007	7.919	0.018	0.361	34	158
56928.039699	-32.781	0.007	7.979	0.018	0.359	34	139
56928.051258	-32.756	0.008	7.971	0.019	0.359	34	137

Description of each individual UVES observation. (continued . . .)

BJD	RV $[km/s]$	$\sigma(RV)$ $[km/s]$	FWHM $[km/s]$	$\sigma(FWHM)$ $[km/s]$	Contrast	t_{exp} $[s]$	S/N
56928.059945	-32.826	0.007	7.960	0.019	0.359	34	159
56928.154135	-32.636	0.007	7.886	0.018	0.363	34	163
56928.130067	-32.601	0.007	7.866	0.018	0.363	34	173
56928.037776	-32.785	0.007	7.974	0.019	0.359	34	140
56928.067657	-32.813	0.008	7.949	0.019	0.360	34	161
56928.143546	-32.680	0.007	7.889	0.018	0.363	34	165
56928.194435	-32.974	0.008	7.908	0.019	0.362	34	169
56928.053189	-32.779	0.007	7.990	0.019	0.358	34	143
56928.068621	-32.823	0.008	7.957	0.019	0.360	34	159
56928.098828	-32.863	0.007	7.928	0.019	0.360	49	207
56928.198009	-32.914	0.007	7.890	0.018	0.362	34	164
56928.057044	-32.769	0.007	7.963	0.019	0.359	34	138
56928.230746	-33.190	0.007	7.975	0.018	0.360	34	134
56928.202820	-33.056	0.008	7.928	0.019	0.361	34	158
56928.192511	-32.927	0.007	7.908	0.019	0.361	34	176
56928.144510	-32.690	0.007	7.874	0.018	0.363	34	174
56928.226898	-33.164	0.009	7.963	0.022	0.361	34	139
56928.076099	-32.920	0.007	7.941	0.019	0.360	49	197
56928.093144	-32.903	0.013	8.020	0.031	0.361	49	205
56928.106792	-32.836	0.007	7.914	0.019	0.361	49	205
56928.118509	-32.694	0.007	7.877	0.019	0.363	34	179
56928.193476	-32.946	0.008	7.912	0.019	0.361	34	176
56928.180969	-32.947	0.007	7.945	0.019	0.360	34	156
56928.233634	-33.263	0.007	7.969	0.018	0.360	34	135
56928.214388	-33.071	0.008	7.957	0.020	0.361	34	155
56928.110207	-32.804	0.007	7.924	0.019	0.360	49	205
56928.131989	-32.542	0.007	7.849	0.019	0.364	34	175
56928.080642	-32.959	0.007	7.959	0.019	0.359	49	209
56928.128141	-32.636	0.007	7.879	0.018	0.363	34	170
56928.116587	-32.717	0.007	7.865	0.019	0.363	34	185
56928.136803	-32.713	0.007	7.876	0.019	0.363	34	185
56928.181929	-32.961	0.008	7.940	0.019	0.360	34	156

Description of each individual UVES observation. (continued . . .)

BJD	RV $[km/s]$	$\sigma(RV)$ $[km/s]$	FWHM $[km/s]$	$\sigma(FWHM)$ $[km/s]$	Contrast	t_{exp} $[s]$	S/N
56928.078372	-32.949	0.008	7.934	0.020	0.360	49	198
56928.208605	-32.979	0.008	7.902	0.019	0.362	34	160
56928.179043	-32.753	0.007	7.899	0.019	0.362	34	156
56928.139694	-32.719	0.007	7.883	0.018	0.363	34	181
56928.135841	-32.724	0.007	7.868	0.018	0.363	34	185
56928.131027	-32.554	0.007	7.861	0.018	0.364	34	171
56928.167468	-32.582	0.007	7.891	0.018	0.363	34	144
56928.052224	-32.760	0.008	7.977	0.019	0.359	34	132
56928.140659	-32.732	0.008	7.893	0.019	0.362	34	176
56928.225934	-33.104	0.007	7.956	0.018	0.360	34	133
56928.032951	-32.773	0.008	7.978	0.019	0.358	34	138
56928.229787	-33.083	0.008	7.973	0.020	0.360	34	139
56928.033915	-32.792	0.007	7.986	0.019	0.358	34	136
56928.120436	-32.669	0.008	7.866	0.019	0.363	34	183
56928.172293	-32.495	0.007	7.856	0.018	0.364	34	141
56928.231710	-33.263	0.007	7.973	0.017	0.360	34	134
56928.077235	-32.928	0.008	7.939	0.019	0.360	49	202
56928.207643	-32.990	0.008	7.921	0.019	0.361	34	165
56928.209567	-33.026	0.008	7.903	0.019	0.362	34	167
56928.219203	-33.164	0.008	7.936	0.020	0.362	34	154
56928.101104	-32.856	0.008	7.942	0.019	0.360	49	206
56928.048368	-32.819	0.008	7.974	0.019	0.359	34	145
56928.171329	-32.505	0.007	7.869	0.018	0.364	34	139
56928.119473	-32.702	0.007	7.876	0.019	0.363	34	176
56928.157838	-32.656	0.007	7.905	0.018	0.362	34	152
56928.040662	-32.774	0.007	7.978	0.019	0.359	34	147
56928.123327	-32.656	0.007	7.871	0.018	0.363	34	176
56928.107930	-32.803	0.008	7.910	0.019	0.361	49	197
56928.142587	-32.664	0.007	7.884	0.019	0.363	34	175
56928.218244	-33.109	0.008	7.929	0.021	0.361	34	154
56928.058970	-32.794	0.008	7.976	0.019	0.359	34	151
56928.134878	-32.731	0.007	7.878	0.019	0.363	34	181

Description of each individual UVES observation. (continued . . .)

BJD	RV $[km/s]$	$\sigma(RV)$ $[km/s]$	FWHM $[km/s]$	$\sigma(FWHM)$ $[km/s]$	Contrast	t_{exp} $[s]$	S/N
56928.133916	-32.747	0.007	7.874	0.019	0.363	34	178
56928.198970	-32.993	0.007	7.895	0.019	0.362	34	168
56928.099966	-32.876	0.007	7.924	0.019	0.360	49	203
56928.213424	-32.893	0.008	7.917	0.019	0.361	34	155
56928.153174	-32.642	0.007	7.887	0.018	0.363	34	164
56928.046442	-32.857	0.007	7.975	0.018	0.359	34	152
56928.185777	-33.034	0.008	7.910	0.019	0.362	34	159
56928.087461	-32.920	0.008	7.934	0.019	0.360	49	200
56928.141623	-32.670	0.007	7.883	0.018	0.363	34	176
56928.227860	-33.163	0.007	7.956	0.018	0.360	34	136
56928.050296	-32.748	0.007	7.958	0.018	0.359	34	137
56928.165543	-32.555	0.007	7.876	0.018	0.363	34	149
56928.056082	-32.803	0.007	7.967	0.018	0.359	34	146
56928.189626	-33.004	0.007	7.889	0.019	0.362	34	159
56928.085192	-32.867	0.007	7.945	0.018	0.360	49	191
56928.146435	-32.689	0.007	7.906	0.018	0.362	34	161
56928.164577	-32.554	0.007	7.890	0.019	0.363	34	149
56928.049333	-32.769	0.007	7.971	0.019	0.359	34	143
56928.103378	-32.833	0.007	7.933	0.019	0.360	49	209
56928.158801	-32.700	0.007	7.906	0.018	0.362	34	150
56928.183851	-33.047	0.007	7.929	0.019	0.361	34	156
56928.045482	-32.861	0.008	7.965	0.019	0.359	34	149
56928.175179	-32.885	0.007	7.923	0.018	0.361	34	159
56928.086327	-32.899	0.008	7.934	0.019	0.360	49	198
56928.228823	-33.155	0.008	7.968	0.019	0.360	34	126
56928.160723	-32.575	0.007	7.876	0.019	0.363	34	155
56928.069585	-32.793	0.007	7.949	0.019	0.360	34	152
56928.232670	-33.243	0.010	7.988	0.024	0.360	34	136
56928.174219	-32.849	0.007	7.924	0.019	0.361	34	163
56928.047406	-32.785	0.007	7.975	0.019	0.359	34	140
56928.124286	-32.682	0.007	7.907	0.018	0.362	34	178
56928.102243	-32.854	0.008	7.948	0.019	0.359	49	202

Description of each individual UVES observation. (continued . . .)

BJD	RV $[km/s]$	$\sigma(RV)$ $[km/s]$	FWHM $[km/s]$	$\sigma(FWHM)$ $[km/s]$	Contrast	t_{exp} $[s]$	S/N
56928.092008	-32.918	0.007	7.940	0.019	0.359	49	212
56928.220163	-33.163	0.008	7.946	0.020	0.361	34	150
56928.176146	-32.848	0.007	7.903	0.019	0.362	34	147
56928.065730	-32.813	0.008	7.964	0.019	0.359	34	163
56928.066697	-32.828	0.007	7.958	0.018	0.359	34	161
56928.177110	-32.817	0.007	7.884	0.019	0.363	34	165
56928.178078	-32.781	0.007	7.890	0.019	0.363	34	157
56928.104518	-32.853	0.007	7.917	0.019	0.361	49	209
56928.195399	-32.962	0.007	7.899	0.019	0.362	34	172
56928.084055	-32.878	0.007	7.946	0.019	0.360	49	191
56928.166509	-32.549	0.007	7.878	0.018	0.363	34	143
56928.223045	-33.176	0.009	7.965	0.022	0.361	34	144
56928.187701	-33.004	0.008	7.909	0.019	0.362	34	155
56894.307248	-32.706	0.015	7.927	0.037	0.358	49	198
56894.271282	-32.728	0.008	7.997	0.021	0.357	49	195
56894.244608	-32.808	0.011	7.939	0.028	0.358	49	215
56894.163099	-32.730	0.008	7.988	0.021	0.358	49	146
56894.152854	-32.748	0.007	7.990	0.018	0.358	49	166
56894.172201	-32.732	0.009	7.985	0.024	0.357	49	157
56894.236645	-32.784	0.010	7.939	0.025	0.357	49	209
56894.158545	-32.742	0.007	7.994	0.019	0.357	49	153
56894.220697	-32.775	0.009	7.986	0.024	0.358	34	136
56894.200452	-32.757	0.009	8.026	0.022	0.357	34	113
56894.341368	-32.587	0.007	7.903	0.018	0.359	49	218
56894.310660	-32.711	0.016	7.974	0.039	0.358	49	209
56894.196611	-32.747	0.010	7.999	0.025	0.358	34	126
56894.250294	-32.814	0.013	7.999	0.033	0.358	49	206
56894.161963	-32.741	0.008	7.998	0.019	0.357	49	155
56894.279239	-32.716	0.009	7.986	0.024	0.357	49	185
56894.273555	-32.724	0.010	7.991	0.025	0.358	49	179
56894.166512	-32.735	0.009	7.984	0.022	0.357	49	157
56894.209123	-32.733	0.010	7.999	0.026	0.357	34	124

Description of each individual UVES observation. (continued . . .)

BJD	RV $[km/s]$	$\sigma(RV)$ $[km/s]$	FWHM $[km/s]$	$\sigma(FWHM)$ $[km/s]$	Contrast	t_{exp} $[s]$	S/N
56894.344784	-32.591	0.009	7.977	0.023	0.357	49	193
56894.243474	-32.804	0.010	7.944	0.026	0.357	49	211
56894.149441	-32.722	0.008	8.004	0.021	0.358	49	129
56894.286068	-32.686	0.007	7.979	0.019	0.358	49	175
56894.280375	-32.732	0.012	7.959	0.031	0.357	49	177
56894.315198	-32.704	0.011	7.999	0.027	0.358	49	210
56894.221661	-32.808	0.007	7.981	0.018	0.358	34	144
56894.259391	-32.767	0.008	7.998	0.020	0.357	49	184
56894.234375	-32.765	0.010	7.973	0.026	0.358	49	212
56894.335681	-32.637	0.008	7.960	0.020	0.359	49	191
56894.194682	-32.795	0.007	7.981	0.017	0.358	34	135
56894.249156	-32.812	0.009	7.963	0.023	0.357	49	212
56894.180164	-32.757	0.008	7.984	0.021	0.358	49	160
56894.171062	-32.735	0.008	7.991	0.019	0.358	49	157
56894.228696	-32.741	0.010	7.961	0.024	0.357	49	197
56894.238923	-32.770	0.008	7.965	0.020	0.357	49	214
56894.169928	-32.724	0.009	7.985	0.023	0.358	49	157
56894.304266	-32.727	0.080	8.294	0.203	0.362	49	187
56894.151719	-32.767	0.008	7.974	0.020	0.358	49	162
56894.212013	-32.763	0.010	7.974	0.026	0.357	34	140
56894.297445	-32.709	0.015	7.978	0.039	0.357	49	186
56894.253709	-32.857	0.009	8.009	0.023	0.357	49	214
56894.222625	-32.855	0.011	7.982	0.028	0.358	34	155
56894.290618	-32.767	0.014	8.012	0.035	0.358	49	208
56894.150580	-32.733	0.007	7.984	0.018	0.358	49	148
56894.235512	-32.759	0.009	7.971	0.022	0.358	49	203
56894.298581	-32.694	0.008	7.987	0.021	0.358	49	185
56894.164238	-32.708	0.008	7.991	0.021	0.357	49	147
56894.241202	-32.742	0.008	7.971	0.020	0.358	49	202
56894.204312	-32.761	0.009	7.998	0.023	0.358	34	120
56894.229834	-32.727	0.009	7.970	0.024	0.357	49	188
56894.308388	-32.763	0.008	7.963	0.021	0.358	49	207

Description of each individual UVES observation. (continued . . .)

BJD	RV $[km/s]$	$\sigma(RV)$ $[km/s]$	FWHM $[km/s]$	$\sigma(FWHM)$ $[km/s]$	Contrast	t_{exp} $[s]$	S/N
56894.274694	-32.768	0.010	7.969	0.025	0.358	49	199
56894.201418	-32.773	0.009	7.994	0.023	0.357	34	136
56894.146033	-32.762	0.011	7.945	0.028	0.358	49	161
56894.257119	-32.791	0.009	7.974	0.022	0.357	49	195
56894.328855	-32.660	0.009	7.980	0.024	0.359	49	183
56894.295169	-32.777	0.009	7.969	0.023	0.358	49	198
56894.187937	-32.779	0.012	7.964	0.030	0.357	34	143
56894.258255	-32.780	0.012	7.988	0.030	0.358	49	183
56894.311797	-32.684	0.019	7.965	0.047	0.361	49	189
56894.199491	-32.769	0.008	7.992	0.020	0.358	34	126
56894.289481	-32.721	0.010	7.995	0.024	0.358	49	204
56894.218763	-32.847	0.009	7.993	0.023	0.358	34	153
56894.226425	-32.727	0.010	7.999	0.025	0.358	49	190
56894.267861	-32.766	0.008	7.967	0.020	0.358	49	199
56894.342512	-32.610	0.007	7.931	0.018	0.358	49	220
56894.312932	-32.714	0.041	7.833	0.103	0.357	49	200
56894.207202	-32.756	0.009	7.993	0.021	0.357	34	134
56894.208160	-32.738	0.009	8.005	0.023	0.358	34	126
56894.301993	-32.733	0.011	7.951	0.027	0.358	49	194
56894.242339	-32.765	0.010	7.964	0.024	0.358	49	203
56894.195647	-32.750	0.009	7.988	0.022	0.358	34	119
56894.276967	-32.766	0.014	8.033	0.034	0.359	49	202
56894.251433	-32.832	0.010	7.952	0.026	0.357	49	207
56894.288341	-32.689	0.009	7.980	0.022	0.357	49	184
56894.160825	-32.738	0.008	7.989	0.020	0.357	49	151
56894.334544	-32.641	0.010	7.940	0.024	0.358	49	193
56894.190831	-32.752	0.008	7.975	0.021	0.357	34	126
56894.193719	-32.774	0.008	7.992	0.021	0.358	34	127
56894.203347	-32.784	0.008	7.991	0.019	0.357	34	134
56894.212973	-32.757	0.008	7.992	0.019	0.358	34	125
56894.320888	-32.693	0.010	7.970	0.024	0.358	49	208
56894.240063	-32.753	0.009	7.965	0.023	0.358	49	195

Description of each individual UVES observation. (continued . . .)

BJD	RV $[km/s]$	$\sigma(RV)$ $[km/s]$	FWHM $[km/s]$	$\sigma(FWHM)$ $[km/s]$	Contrast	t_{exp} $[s]$	S/N
56894.326579	-32.690	0.008	7.964	0.020	0.358	49	188
56894.168787	-32.699	0.008	7.987	0.021	0.358	49	149
56894.189864	-32.777	0.017	7.974	0.043	0.356	34	145
56894.216828	-32.762	0.010	7.974	0.025	0.358	34	135
56894.319751	-32.724	0.008	7.971	0.020	0.358	49	208
56894.270141	-32.694	0.010	7.972	0.026	0.358	49	183
56894.292898	-32.815	0.014	8.010	0.036	0.359	49	201
56894.314064	-32.695	0.011	7.953	0.027	0.357	49	187
56894.167652	-32.739	0.008	7.990	0.020	0.358	49	150
56894.275830	-32.741	0.013	7.971	0.033	0.358	49	200
56894.197572	-32.727	0.010	8.000	0.025	0.358	34	133
56894.327717	-32.625	0.008	7.987	0.019	0.358	49	182
56894.144895	-32.754	0.015	7.935	0.038	0.358	49	162
56894.213936	-32.761	0.014	8.026	0.036	0.357	34	133
56894.148304	-32.741	0.008	7.985	0.020	0.358	49	145
56894.157409	-32.727	0.009	7.996	0.022	0.358	49	151
56894.176755	-32.777	0.008	7.995	0.021	0.358	49	156
56894.337956	-32.604	0.009	7.964	0.022	0.358	49	213
56894.300855	-32.813	0.014	7.982	0.035	0.358	49	207
56894.340231	-32.601	0.014	7.922	0.035	0.359	49	202
56894.331133	-32.626	0.016	7.939	0.041	0.357	49	190
56894.333405	-32.704	0.007	7.970	0.018	0.358	49	195
56894.303133	-32.765	0.009	7.945	0.023	0.358	49	198
56894.227558	-32.726	0.012	7.982	0.029	0.358	49	192
56894.159687	-32.747	0.008	8.007	0.019	0.357	49	151
56894.323163	-32.689	0.007	7.973	0.019	0.358	49	203
56894.217796	-32.828	0.008	7.997	0.020	0.358	34	153
56894.210086	-32.761	0.009	8.012	0.023	0.358	34	128
56894.232107	-32.732	0.008	7.981	0.019	0.358	49	190
56894.186970	-32.754	0.007	7.987	0.019	0.358	34	144
56894.316338	-32.706	0.014	7.932	0.035	0.357	49	216
56894.262800	-32.909	0.011	8.016	0.028	0.358	49	203

Description of each individual UVES observation. (continued . . .)

BJD	RV $[km/s]$	$\sigma(RV)$ $[km/s]$	FWHM $[km/s]$	$\sigma(FWHM)$ $[km/s]$	Contrast	t_{exp} $[s]$	S/N
56894.215864	-32.732	0.008	8.003	0.021	0.358	34	138
56894.322028	-32.669	0.008	7.969	0.020	0.358	49	202
56894.177892	-32.739	0.008	7.992	0.019	0.358	49	158
56894.294033	-32.788	0.020	7.912	0.051	0.357	49	212
56894.317475	-32.743	0.011	7.997	0.028	0.357	49	223
56894.268999	-32.723	0.014	7.946	0.035	0.357	49	195
56894.223589	-32.908	0.011	7.975	0.027	0.357	34	158
56894.173340	-38.529	2.807	41.182	19.122	0.551	49	154
56894.254847	-32.831	0.015	7.979	0.037	0.357	49	209
56894.299720	-32.747	0.008	7.967	0.021	0.359	49	202
56894.246883	-32.843	0.011	7.967	0.029	0.357	49	214
56894.324304	-32.636	0.010	7.972	0.025	0.358	49	202
56894.318612	-32.723	0.021	7.949	0.053	0.358	49	211
56894.181302	-32.760	0.007	7.994	0.019	0.358	49	157
56894.230970	-32.706	0.008	8.001	0.021	0.357	49	180
56894.185040	-32.817	0.009	7.988	0.023	0.358	34	142
56894.296307	-32.742	0.046	7.812	0.117	0.356	49	201
56894.191792	-32.791	0.009	7.981	0.023	0.358	34	136
56894.272418	-32.749	0.012	7.991	0.031	0.358	49	189
56894.165377	-32.730	0.007	7.994	0.019	0.357	49	157
56894.260528	-32.796	0.011	7.995	0.028	0.357	49	187
56894.147167	-32.761	0.011	7.965	0.027	0.357	49	156
56894.278105	-32.749	0.008	7.994	0.021	0.358	49	191
56894.182442	-32.747	0.009	7.970	0.023	0.358	49	166
56894.248021	-32.836	0.014	7.932	0.035	0.357	49	217
56894.219730	-32.834	0.011	7.952	0.028	0.358	34	157
56894.339093	-32.608	0.007	7.935	0.019	0.359	49	202
56894.206241	-32.752	0.008	8.001	0.021	0.358	34	137
56894.336819	-32.659	0.007	7.972	0.018	0.357	49	191
56894.282655	-32.732	0.008	7.983	0.020	0.357	49	188
56894.174477	-32.734	0.010	7.978	0.024	0.358	49	160
56894.153990	-32.757	0.008	7.991	0.019	0.357	49	163

Description of each individual UVES observation. (continued . . .)

BJD	RV $[km/s]$	$\sigma(RV)$ $[km/s]$	FWHM $[km/s]$	$\sigma(FWHM)$ $[km/s]$	Contrast	t_{exp} $[s]$	S/N
56894.198532	-32.789	0.010	7.984	0.025	0.357	34	134
56894.325440	-32.680	0.012	7.963	0.030	0.357	49	199
56894.261664	-32.869	0.008	7.987	0.021	0.357	49	195
56894.156270	-32.741	0.008	7.997	0.020	0.357	49	153
56894.233239	-32.741	0.009	7.952	0.022	0.357	49	199
56894.205278	-32.768	0.012	8.005	0.029	0.358	34	132
56894.281517	-32.722	0.007	7.974	0.018	0.358	49	182
56894.284928	-32.686	0.010	7.980	0.025	0.358	49	170
56894.263938	-32.880	0.013	7.973	0.032	0.358	49	202
56894.309521	-32.717	0.010	7.922	0.026	0.358	49	209
56894.202383	-32.810	0.009	7.994	0.022	0.358	34	139
56894.155128	-32.747	0.008	7.991	0.020	0.357	49	158
56894.255981	-32.813	0.008	8.018	0.020	0.357	49	200
56894.188899	-32.766	0.008	8.000	0.020	0.358	34	141
56894.237784	-32.759	0.028	8.065	0.072	0.359	49	211
56894.332272	-32.653	0.018	7.936	0.044	0.357	49	202
56894.192754	-32.748	0.007	7.987	0.017	0.358	34	124
56894.266721	-32.715	0.010	7.993	0.026	0.358	49	188
56894.283792	-32.690	0.009	7.974	0.022	0.358	49	171
56894.175614	-32.756	0.007	7.996	0.018	0.358	49	165
56894.245744	-32.855	0.011	7.984	0.028	0.358	49	220
56894.252570	-32.809	0.011	7.975	0.027	0.358	49	201
56894.329996	-32.639	0.008	7.984	0.020	0.358	49	196
56894.179025	-32.739	0.008	7.983	0.019	0.357	49	154
56894.211047	-32.794	0.009	7.983	0.021	0.357	34	143
56894.343645	-32.586	0.008	7.960	0.021	0.358	49	205
56894.287205	-32.692	0.007	7.996	0.018	0.357	49	174
56894.186004	-32.809	0.009	7.980	0.022	0.358	34	140
56894.291761	-32.726	0.009	7.987	0.023	0.357	49	191
56894.214900	-32.726	0.012	7.980	0.031	0.357	34	113
56886.290168	-32.824	0.007	8.015	0.019	0.357	77	175
56886.213311	-32.896	0.007	8.012	0.018	0.357	49	141

Description of each individual UVES observation. (continued . . .)

BJD	RV $[km/s]$	$\sigma(RV)$ $[km/s]$	FWHM $[km/s]$	$\sigma(FWHM)$ $[km/s]$	Contrast	t_{exp} $[s]$	S/N
56886.269736	-32.824	0.008	8.012	0.019	0.357	77	181
56886.200792	-32.899	0.008	8.005	0.019	0.357	49	164
56886.342610	-32.744	0.007	8.032	0.019	0.356	105	214
56886.243455	-32.814	0.007	8.020	0.019	0.356	77	180
56886.297485	-32.795	0.008	8.019	0.019	0.356	77	159
56886.216715	-32.891	0.008	8.021	0.019	0.356	49	147
56886.229244	-32.895	0.007	8.034	0.018	0.356	49	138
56886.218994	-32.909	0.007	8.010	0.018	0.357	49	153
56886.222413	-32.891	0.008	8.008	0.019	0.357	49	157
56886.208756	-32.861	0.008	8.007	0.019	0.357	49	142
56886.211038	-32.924	0.007	8.014	0.019	0.356	49	154
56886.326540	-32.744	0.008	8.028	0.019	0.356	105	207
56886.335469	-32.781	0.007	8.022	0.019	0.356	105	213
56886.266819	-32.797	0.007	8.004	0.019	0.357	77	188
56886.288701	-32.839	0.007	8.024	0.019	0.356	77	163
56886.234685	-32.887	0.007	8.032	0.019	0.356	77	171
56886.203063	-32.899	0.007	8.003	0.018	0.357	49	153
56886.252218	-32.837	0.007	8.019	0.018	0.356	77	186
56886.258058	-32.806	0.007	8.005	0.019	0.357	77	187
56886.293088	-32.820	0.007	8.019	0.019	0.357	77	170
56886.265361	-32.805	0.007	8.005	0.019	0.357	77	180
56886.347962	-32.729	0.008	8.023	0.019	0.356	105	199
56886.328323	-32.761	0.008	8.012	0.019	0.356	105	208
56886.294559	-32.837	0.007	8.022	0.019	0.356	77	172
56886.274085	-32.845	0.007	8.007	0.019	0.357	77	175
56886.304796	-32.796	0.007	8.025	0.019	0.356	77	154
56886.349754	-32.714	0.008	8.022	0.019	0.356	105	193
56886.300412	-32.813	0.007	8.020	0.019	0.357	77	142
56886.322962	-32.783	0.008	8.036	0.019	0.356	105	194
56886.315830	-32.760	0.008	8.017	0.019	0.356	105	210
56886.212173	-32.883	0.007	8.000	0.018	0.357	49	148
56886.199654	-32.910	0.007	7.997	0.019	0.357	49	163

Description of each individual UVES observation. (continued . . .)

BJD	RV $[km/s]$	$\sigma(RV)$ $[km/s]$	FWHM $[km/s]$	$\sigma(FWHM)$ $[km/s]$	Contrast	t_{exp} $[s]$	S/N
56886.324751	-32.749	0.008	8.022	0.019	0.356	105	207
56886.314044	-32.775	0.008	8.028	0.019	0.356	105	206
56886.277016	-32.823	0.007	8.007	0.019	0.357	77	175
56886.330108	-32.755	0.008	8.034	0.019	0.356	105	208
56886.224696	-32.902	0.007	8.002	0.019	0.357	49	156
56886.281395	-32.851	0.007	8.015	0.019	0.357	77	173
56886.247834	-32.830	0.007	8.023	0.018	0.356	77	173
56886.217854	-32.879	0.007	7.995	0.018	0.357	49	142
56886.346177	-32.733	0.007	8.026	0.019	0.356	105	211
56886.279932	-32.848	0.008	8.010	0.019	0.357	77	177
56886.307715	-32.816	0.007	8.034	0.019	0.356	77	156
56886.193964	-32.903	0.007	7.985	0.018	0.358	49	148
56886.226969	-32.922	0.007	8.023	0.019	0.356	49	148
56886.195101	-32.905	0.007	8.023	0.018	0.356	49	144
56886.207616	-32.915	0.008	8.008	0.019	0.357	49	129
56886.249296	-32.834	0.007	8.021	0.018	0.356	77	180
56886.223550	-32.908	0.008	8.001	0.019	0.357	49	155
56886.244914	-32.843	0.007	8.023	0.018	0.356	77	170
56886.225831	-32.923	0.008	8.013	0.019	0.357	49	158
56886.236143	-32.858	0.007	8.022	0.018	0.356	77	155
56886.298949	-32.797	0.007	8.018	0.018	0.356	77	145
56886.201927	-32.890	0.007	7.999	0.019	0.357	49	165
56886.306255	-32.805	0.007	8.014	0.019	0.356	77	154
56886.337254	-32.762	0.007	8.028	0.019	0.356	105	211
56886.255134	-32.814	0.007	8.014	0.019	0.356	77	192
56886.198516	-32.926	0.008	8.032	0.019	0.356	49	160
56886.241991	-32.834	0.007	8.022	0.019	0.356	77	167
56886.333680	-32.756	0.008	8.027	0.019	0.356	105	220
56886.221271	-32.902	0.007	8.012	0.018	0.357	49	152
56886.296022	-32.816	0.007	8.019	0.019	0.356	77	168
56886.317616	-32.781	0.008	8.017	0.019	0.356	105	213
56886.197376	-32.917	0.007	7.999	0.019	0.357	49	151

Description of each individual UVES observation. (continued . . .)

BJD	RV $[km/s]$	$\sigma(RV)$ $[km/s]$	FWHM $[km/s]$	$\sigma(FWHM)$ $[km/s]$	Contrast	t_{exp} $[s]$	S/N
56886.291628	-32.814	0.008	8.019	0.019	0.357	77	169
56886.284318	-32.850	0.007	8.016	0.018	0.356	77	174
56886.209895	-32.909	0.007	8.003	0.019	0.357	49	144
56886.260985	-32.792	0.008	8.007	0.019	0.357	77	187
56886.268278	-32.793	0.008	8.011	0.019	0.357	77	179
56886.206478	-32.893	0.008	8.002	0.019	0.357	49	133
56886.196238	-32.905	0.007	7.997	0.018	0.358	49	150
56886.278474	-32.833	0.007	8.025	0.019	0.356	77	182
56886.240530	-32.847	0.007	8.038	0.019	0.356	77	173
56886.262442	-32.795	0.007	8.011	0.019	0.357	77	175
56886.287238	-32.847	0.008	8.022	0.019	0.356	77	173
56886.246372	-32.826	0.007	8.017	0.018	0.356	77	165
56886.303335	-32.807	0.007	8.031	0.019	0.356	77	145
56886.214445	-32.873	0.008	8.004	0.019	0.357	49	147
56886.340823	-32.727	0.007	8.021	0.019	0.356	105	206
56886.285778	-32.872	0.008	8.011	0.019	0.357	77	174
56886.239063	-32.814	0.007	8.019	0.019	0.356	77	177
56886.282855	-32.860	0.007	8.017	0.019	0.357	77	174
56886.205341	-32.874	0.007	7.994	0.018	0.358	49	144
56886.344393	-32.734	0.008	8.010	0.019	0.356	105	208
56886.256596	-32.804	0.007	8.009	0.019	0.357	77	190
56886.253676	-32.831	0.008	8.020	0.019	0.356	77	184
56886.230379	-32.899	0.008	8.006	0.019	0.357	49	148
56886.321180	-32.771	0.008	8.026	0.019	0.356	105	208
56886.309181	-32.813	0.007	8.039	0.018	0.356	77	159
56886.310640	-32.784	0.007	8.013	0.018	0.356	77	161
56886.319398	-32.779	0.007	8.020	0.019	0.356	105	214
56886.233226	-32.900	0.007	8.016	0.019	0.357	77	173
56886.259523	-32.821	0.007	8.019	0.019	0.356	77	187
56886.228109	-32.888	0.007	8.018	0.019	0.356	49	139
56886.215576	-32.885	0.007	8.023	0.019	0.356	49	147
56886.192827	-32.890	0.008	7.973	0.020	0.358	49	163

Description of each individual UVES observation. (continued . . .)

BJD	RV $[km/s]$	$\sigma(RV)$ $[km/s]$	FWHM $[km/s]$	$\sigma(FWHM)$ $[km/s]$	Contrast	t_{exp} $[s]$	S/N
56886.263901	-32.792	0.007	8.014	0.019	0.357	77	171
56886.275552	-32.814	0.007	8.014	0.019	0.357	77	174
56886.301872	-32.812	0.007	8.017	0.019	0.357	77	154
56886.331896	-32.768	0.007	8.035	0.019	0.355	105	223
56886.220133	-32.908	0.008	8.004	0.019	0.357	49	149
56886.339039	-32.727	0.008	8.023	0.019	0.356	105	206
56886.204200	-32.941	0.008	8.001	0.019	0.357	49	149
56886.237602	-32.866	0.007	8.031	0.018	0.356	77	164
56886.250760	-32.829	0.007	8.027	0.019	0.356	77	182
56869.376347	-32.529	0.007	7.932	0.017	0.359	23	138
56869.377186	-32.567	0.007	7.926	0.017	0.359	23	139
56869.387248	-32.494	0.007	7.906	0.017	0.360	23	142
56869.392273	-32.474	0.007	7.881	0.017	0.361	23	147
56869.369655	-32.607	0.007	7.922	0.017	0.360	23	149
56869.373000	-32.563	0.007	7.931	0.017	0.359	23	133
56869.395621	-32.440	0.007	7.852	0.017	0.363	23	126
56869.394784	-32.433	0.007	7.892	0.017	0.361	23	135
56869.381369	-32.500	0.007	7.908	0.017	0.360	23	134
56869.380531	-32.527	0.007	7.928	0.016	0.359	23	142
56869.383887	-32.488	0.007	7.909	0.016	0.360	23	132
56869.372158	-32.595	0.007	7.934	0.017	0.359	23	143
56869.383053	-32.518	0.006	7.912	0.016	0.360	23	131
56869.378025	-32.504	0.006	7.924	0.016	0.359	23	144
56869.382207	-32.468	0.007	7.886	0.017	0.361	23	134
56869.359607	-32.780	0.007	7.926	0.017	0.359	23	155
56869.362127	-32.731	0.007	7.924	0.017	0.360	23	150
56869.388081	-32.485	0.007	7.912	0.017	0.360	23	144
56869.361290	-32.772	0.007	7.924	0.016	0.360	23	155
56869.364642	-32.696	0.007	7.916	0.017	0.360	23	143
56869.374677	-32.534	0.007	7.905	0.017	0.360	23	138
56869.365476	-32.697	0.007	7.904	0.017	0.361	23	150
56869.386411	-32.484	0.007	7.887	0.017	0.361	23	144

Description of each individual UVES observation. (continued . . .)

BJD	RV $[km/s]$	$\sigma(RV)$ $[km/s]$	FWHM $[km/s]$	$\sigma(FWHM)$ $[km/s]$	Contrast	t_{exp} $[s]$	S/N
56869.375510	-32.569	0.007	7.929	0.017	0.359	23	141
56869.360451	-32.794	0.007	7.919	0.017	0.360	23	155
56869.379694	-32.503	0.006	7.924	0.016	0.360	23	142
56869.371325	-32.581	0.007	7.936	0.016	0.359	23	131
56869.391439	-32.446	0.007	7.891	0.017	0.361	23	141
56869.390595	-32.499	0.007	7.914	0.017	0.360	23	133
56869.367143	-32.713	0.007	7.940	0.017	0.359	23	156
56869.357933	-32.761	0.007	7.938	0.017	0.359	23	149
56869.393946	-32.447	0.007	7.880	0.017	0.361	23	145
56869.393112	-32.478	0.007	7.890	0.017	0.361	23	147
56869.368817	-32.624	0.007	7.919	0.017	0.360	23	155
56869.384726	-32.501	0.006	7.913	0.016	0.360	23	135
56869.370492	-32.598	0.007	7.930	0.017	0.360	23	143
56869.396455	-32.390	0.007	7.857	0.017	0.362	23	136
56869.363802	-32.694	0.007	7.938	0.017	0.359	23	152
56869.366310	-32.685	0.007	7.909	0.017	0.360	23	157
56869.388921	-32.505	0.007	7.878	0.017	0.361	23	147
56869.378861	-32.506	0.007	7.931	0.016	0.359	23	142
56869.362965	-32.719	0.007	7.932	0.017	0.359	23	146
56869.357097	-32.783	0.007	7.919	0.017	0.360	23	147
56869.358773	-32.728	0.007	7.928	0.017	0.360	23	151
56869.389759	-32.437	0.007	7.873	0.017	0.362	23	146
56869.385566	-32.467	0.007	7.883	0.017	0.361	23	144
56869.367978	-32.694	0.006	7.934	0.016	0.359	23	153
56869.373837	-32.565	0.006	7.901	0.016	0.361	23	129

Table B.2: Description of each individual UVES observation.

Appendix C.
Reflected light from 55 Cnc b

Although not initially part of this PhD project, we acquired through our collaborators observations from the 55 Cnc system obtained with HARPS and HARPS-N which we analyzed in parallel to this PhD project. The original purpose of this data was the observation of the transit of Super-Earth type planet 55 Cancri e. Since these observations were taken during (and close to) transit, the phase function is close to zero and as such it is extremely unlikely to detect reflected light from this planet. Nonetheless, these observations could (in theory) be applied to recover the reflected signal from one of its planetary companions, hot Jupiter type 55 Cancri b. However, the noise level on the results is much higher than the expected signal for 55 Cancri b. The observations consist in 179 HARPS spectra (ESO ID: 288.C-5010, PI: TRIAUD) and 261 HARPS-N spectra (ID: CAT13B_33) observed in $4+7$ different nights adding up to around $8+22.3$ h of observing time. The properties of these data are summarized in C.1.

Due to their orbital characteristics (See Table C.2), the reflected signal at opposition of both 55 Cancri b and 55 Cancri e are of similar amplitude, assuming a similar albedo for both planets. The S/N of the data permitted to infer a detection limit of $\sim 7.2 \times 10^{-6}$ for the HARPS-North data and a detection limit of $\sim 6.2 \times 10^{-5}$ for the HARPS-South data. Combining both data sets we should be able to reach a noise level $\sim 6.2 \times 10^{-6}$. This should permit to infer down to a $3-\sigma$ limit for $A_g = 0.5$, or a $1-\sigma$ limit for $A_g = 0.18$ (assuming the planet has the radius of Jupiter). Although the radius of 55 Cancri b is unknown, we expected to be able to put an upper limit for $A_g \times R_p^2$.

The HARPS DRS pipeline was used to reduced the data and compute the CCFs. For the CCF parameters we used: spectral mask - $K0$; initial RV - $27.58\ km/s$; CCF width - 320; CCF step - $100\ m/s$;

We applied the CCF technique to retrieve the reflected light spectrum from planet 55 Cancri b as done with *51 pegasi b* in Martins et al., 2015a. To compute the RV of both the planet and the star, we used the orbital parameters in Table C.2.

As can be seen on Figure C.1a the noise level on the results ($\sim 2.6 \times 10^{-4}$ for both data sets) is much higher

Night	Number of spectra	Total exposure [hours]	S/N range
HARPS			
2012-01-28	47	2.32	105-172
2012-02-14	55	1.83	112-133
2012-02-28	36	1.80	136-183
2012-03-16	41	2.05	40-135
HARPS-N			
2012-12-26	27	2.70	182-296
2013-11-15	53	3.53	140-290
2013-11-29	61	4.07	119-225
2014-01-01	33	3.30	279-381
2014-01-27	30	3.00	97-182
2014-02-26	30	3.00	77-146
2014-03-29	27	2.70	248-400

Table C.1: Description of the available data on a per night basis.

than the expected signal for 55 Cancri b ($\frac{F_p}{F_*} \simeq 1.7 \times 10^{-5}$ for $A_g = 0.5$). Please note that the spectra we were analyzing contain not only the spectroscopic signature of planet 55 Cancri b and its host star, but also the signature of 55 Cancri e, only at a different radial velocity on each spectra.

To confirm that the issue was not with the quality of the data, we attempted to perform an analysis for planet 55 Cancri e from the same data. Albeit no signal was expected– all data was taken during (or close to) transit of 55 Cancri e – we would be able to place a lower limit on the detection limit possible with our data as at the end

Parameter	Unit	55 Cnc b	55 Cnc e
RV_{system}	$[km/s]$	$27.58^{(1)}$	
$period$	$[days]$	14.65314	0.7365478
e		0.0023	0.028
a	$[AU]$	0.11339	0.015439
k_*	$[m/s]$	71.47	6.12
$m_p\ sin(i)$	$[M_{Jup}]$	0.84	0.02547
m_p	$[M_{Jup}]$	0.84	0.02547
i	$[degrees]$	89.73	90.36
m_*	$[M_\odot]$	$0.905^{(2)}$	
ω	$[degrees]$	110	170.0
t_0	$[BJD - 2400000]$	53035.0	49999.83643

Table C.2: Orbital parameters for the 55 Cnc e/b planets (from Nelson et al., 2014). (1) Nidever et al. (2002) (2) Braun et al. (2012)

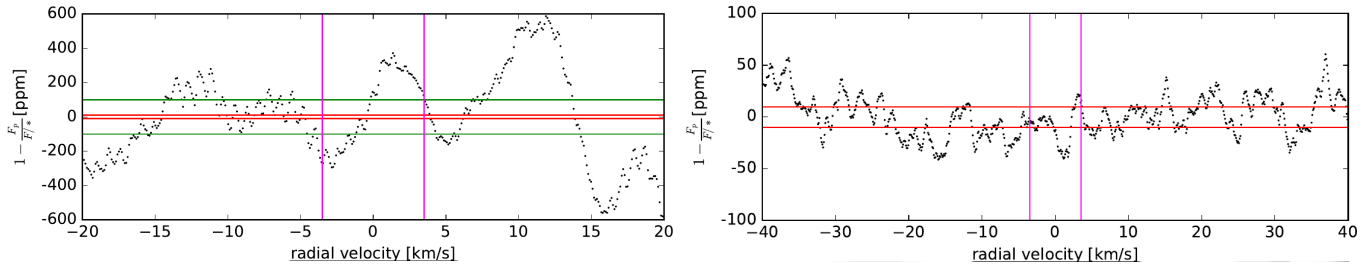

(a) CCF for 55 Cnc b **(b)** CCF for 55 Cnc e

Figure C.1: Results for the analysis of reflected light from *55 Cnc b/e*. The green horizontal lines correspond to the $\pm 10^{-4}$ noise levels, the red ones to $\pm 10^{-5}$. The pink lines correspond to $\pm FWHM_* \simeq 3.5 km/s$ on each side of the expected radial velocity of the planet.

of the analysis only noise should remain. With this, we were able to place a limit of $\sim 2.0 \times 10^{-5}$ (predicted limit $\sim 7.2 \times 10^{-6}$) to the HARPS-North data and $\sim 4.6 \times 10^{-5}$ (predicted limit$\sim 1.3 \times 10^{-5}$) to the HARPS-South data. Combining both data sets we should be able to reach a noise level $\sim 1.8 \times 10^{-5}$, allowing a $1-\sigma$ detection of 55 Cancri b for $A_g = 0.5$.

What could explain the disparity in SN from the CCF of both planets, if the data is the same? The answer appears to be related with the radial velocity variation of each planet over a night. On Figure C.2, it can be seen that the radial velocity of planet 55 Cancri e (green stars) varies very rapidly, and the vertical noise structures get diluted amidst the noise as we stack the normalized CCFs corrected for the planet radial velocity. On the contrary 55 Cancri b (red stars) varies very little and thus the noise structures are amplified and create the peaks/dips that can be seen in figure C.1a. Albeit no detection is expected in this case, this study is of great use toward similar future reflected light studies. These results have shown us the importance of a careful sampling in time of the observations, namely to make sure that they span over a sufficiently large radial velocity range to avoid boosting static noise structures. Furthermore, it is important to identify the source of the these structures that can be seen in Figure C.1a and if they can be removed.

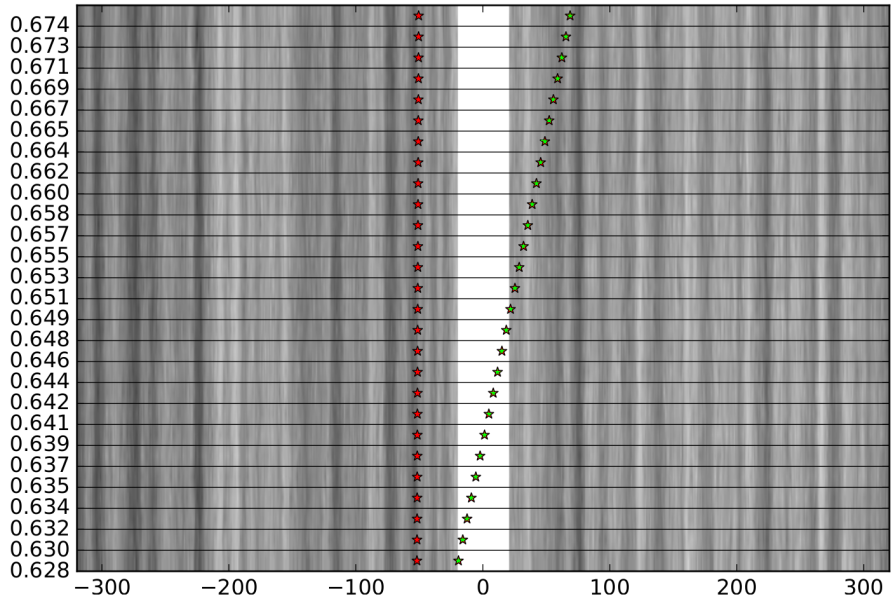

Figure C.2: CCF for HARPS-S observations on night 2012-02-14. Each row corresponds to a different observation. The y-axis correspond to the fraction of the corresponding Julian day. The x-axis corresponds to the radial velocity of each point ($RV_{Star} = 0$). The red stars correspond to the expected radial velocity of planet 55 Cancri e and the green stars to the position of 55 Cancri b.

Appendix A.
Target lists for Chapter 6

The following tables present the list of possible targets that can be detected byt both ESPRESSO and HIRES with $t_{total} < 30$ hours and assuming $A_g = 0.2$.

Planet	M_p $[M_{Jup}]$	R_p $[R_{Jup}]$	P $[AU]$	I [deg]	mag_v	Host type	N_{bins}	F_p/F_* $[ppm]$	t_{total} $[hours]$
HD 75289 b	0.470	1.030	3.509	90.0	6.3	G0 V	15	20.90	4.00
HD 179949 b	0.920	1.050	3.092	90.0	6.2	F8 V	15	25.70	3.00
HD 63454 b	0.390	1.060	2.817	90.0	9.4	K4 V	15	29.66	30.00
WASP-76 b	0.920	1.830	1.810	88.0	9.5	F7	15	159.41	2.00
KELT-3 b	1.418	1.333	2.703	84.6	9.8	F	15	49.38	16.00
HD 189733 b	1.142	1.138	2.219	85.5	7.7	K1-K2	15	46.90	3.00
WASP-72 b	1.461	1.270	2.217	90.0	9.6	F7	15	58.62	10.00
KELT-2 A b	1.486	1.306	4.114	90.0	8.7	F7V	15	27.18	18.00
HD 149143 b	1.330	1.050	4.072	90.0	7.9	G0 IV	15	17.81	22.00
WASP-74 b	0.970	1.560	2.138	79.8	9.7	F9	15	91.63	5.00
51 Peg b	0.470	1.900	4.231	80.0	5.5	G2 IV	15	54.73	1.00
HD 86081 b	1.500	1.080	1.998	90.0	8.7	F8V	15	48.68	6.00
HD 83443 b	0.400	1.040	2.986	90.0	8.2	K0 V	15	26.43	13.00
HD 209458 b	0.690	1.380	3.525	86.6	7.7	G0 V	15	37.24	4.00
HD 212301 b	0.400	1.070	2.246	90.0	7.8	F8 V	15	40.89	4.00

Table A.1: Hot Jupiters type planets detectable by ESPRESSO with $t_{total} < 30$ hours for $N_{bins} = 15$ and assuming $A_g = 0.2$.

Planet	M_p $[M_{Jup}]$	R_p $[R_{Jup}]$	P $[AU]$	I [deg]	mag_v	Host type	N_{bins}	F_p/F_* $[ppm]$	t_{total} $[hours]$
HD 75289 b	0.470	1.030	3.509	90.0	6.3	G0 V	70	20.90	4.00
HD 179949 b	0.920	1.050	3.092	90.0	6.2	F8 V	70	25.70	3.00
HD 63454 b	0.390	1.060	2.817	90.0	9.4	K4 V	70	29.66	30.00
WASP-76 b	0.920	1.830	1.810	88.0	9.5	F7	70	159.41	2.00
KELT-3 b	1.418	1.333	2.703	84.6	9.8	F	70	49.38	16.00
HD 189733 b	1.142	1.138	2.219	85.5	7.7	K1-K2	70	46.90	3.00
WASP-72 b	1.461	1.270	2.217	90.0	9.6	F7	70	58.62	10.00
KELT-2 A b	1.486	1.306	4.114	90.0	8.7	F7V	70	27.18	18.00
HD 149143 b	1.330	1.050	4.072	90.0	7.9	G0 IV	70	17.81	22.00
WASP-74 b	0.970	1.560	2.138	79.8	9.7	F9	70	91.63	5.00
51 Peg b	0.470	1.900	4.231	80.0	5.5	G2 IV	70	54.73	1.00
HD 86081 b	1.500	1.080	1.998	90.0	8.7	F8V	70	48.68	6.00
HD 83443 b	0.400	1.040	2.986	90.0	8.2	K0 V	70	26.43	13.00
HD 209458 b	0.690	1.380	3.525	86.6	7.7	G0 V	70	37.24	4.00
HD 212301 b	0.400	1.070	2.246	90.0	7.8	F8 V	70	40.89	4.00

Table A.2: Hot Jupiters type planets detectable by HIRES with $t_{total} < 30$ hours for $N_{bins} = 70$ and assuming $A_g = 0.2$.

Planet	M_p $[M_{Jup}]$	R_p $[R_{Jup}]$	P $[AU]$	I [deg]	mag_v	Host type	N_{bins}	F_p/F_* $[ppm]$	t_{total} $[hours]$
HD 49674 b	0.100	0.980	4.947	90.0	8.1	G5 V	5	11.97	5.00
WASP-69 b	0.260	1.057	3.868	86.7	9.9	K5	5	19.30	10.00
HD 46375 b	0.230	1.020	3.024	90.0	7.9	K1 IV	5	25.00	1.00
HD 76700 b	0.230	0.990	3.971	90.0	8.1	G6 V	5	16.37	3.00
KELT-11 b	0.195	1.370	4.737	85.8	8.0	G8	5	24.73	1.00
HD 88133 b	0.300	1.000	3.416	90.0	8.0	G5 IV	5	20.42	2.00
HD 109749 b	0.280	0.990	5.239	90.0	8.1	G3 IV	5	11.31	6.00

Table A.3: Hot Neptune type planets detectable by ESPRESSO with $t_{total} < 30$ hours for $N_{bins} = 5$ and assuming $A_g = 0.2$.

Planet	M_p $[M_{Jup}]$	R_p $[R_{Jup}]$	P $[AU]$	I [deg]	mag_v	Host type	N_{bins}	F_p/F_* $[ppm]$	t_{total} $[hours]$
HD 49674 b	0.100	0.980	4.947	90.0	8.1	G5 V	6	11.97	5.00
WASP-69 b	0.260	1.057	3.868	86.7	9.9	K5	6	19.30	10.00
HD 46375 b	0.230	1.020	3.024	90.0	7.9	K1 IV	6	25.00	1.00
HD 76700 b	0.230	0.990	3.971	90.0	8.1	G6 V	6	16.37	3.00
KELT-11 b	0.195	1.370	4.737	85.8	8.0	G8	6	24.73	1.00
HD 88133 b	0.300	1.000	3.416	90.0	8.0	G5 IV	6	20.42	2.00
HD 109749 b	0.280	0.990	5.239	90.0	8.1	G3 IV	6	11.31	6.00

Table A.4: Hot Neptune type planets detectable by HIRES with $t_{total} < 30$ hours for $N_{bins} = 6$ and assuming $A_g = 0.2$.

Planet	M_p $[M_{Jup}]$	R_p $[R_{Jup}]$	P $[AU]$	I [deg]	mag_v	Host type	N_{bins}	F_p/F_* $[ppm]$	t_{total} $[hours]$
55 Cnc e	0.025	0.178	0.737	90.4	6.0	K0IV-V	5	4.98	4.00

Table A.5: Super-Earth type planets detectable by HIRES with $t_{total} < 30$ hours for $N_{bins} = 5$ and assuming $A_g = 0.2$.

Appendix B.
Atmospheric models used in Chapter 6

In Chapter 6, we tested the recovery of albedo functions from modeled exoplanet atmospheres that include real physics. These models were generated by our collaborator Antonio Garcia-Muñoz, lecturer and researcher at the *Zentrum für Astronomie und Astrophysik* of the *Technische Universität Berlin*, Germany.

For both simulated hot Jupiter and hot Neptune class planets, the albedo functions were created by solving the problem of multiple scattering of starlight in the atmosphere. The integration over the planetary disk was computed with the algorithm described in Horak, 1950. Partial solutions at the integration points were obtained with a discrete-ordinate method (Stamnes et al., 1988). The line lists for molecular absorption were taken from HITEMP (Rothman et al., 2010). The absorption by the alkalis was estimated from the parameterization presented in Iro et al., 2005. The base albedo function for each simulated atmospheric model was computed for full illumination (i.e., assuming superior conjunction and no orbital inclination) and then projected for each orbital phase assuming a Lambert phase function (see Equation 2.2).

In terms of atmospheric configuration, we assumed hydrostatic balance in the atmosphere, with an equilibrium temperature for the planet equal to $1150K$. Another assumption is that the gas absorption at wavelengths shorter than 1 μm is dominated by water and alkalis (Na and K). The contribution from other gases (e.g. $V\,O$, $Ti\,O$) was ignored.

In terms of composition, we choose two different configurations (*Model A* and *Model B*) for the altitude-independent Volume Mixing Ratio (VMR) of water and the alkalis.

The *Model A* configuration assumes VMRs for both the water and alkali content of about half the one in the solar atmosphere. The *Model B* configuration assumes the same VMR for water content, while for the alkalis the VMR are 0.5% the VMR in the solar atmosphere. By reducing the alkali content relatively to water, will enhance the impact of water bands on the simulated atmosphere and create a more structured spectrum. Note that we are assuming that both water and alkali behave as well-mixed gases, which is probably more realistic for water than for the alkalis. According to the photo-chemical models of hot Jupiters (e.g. Lavvas et al., 2014), Na and K should

	$Model\ A$	$Model\ B$
Volume Mixing Ratios		
H_2O	5×10^{-4}	
Na	1.5×10^{-6}	1.5×10^{-8}
K	1.2×10^{-7}	1.2×10^{-9}
Configurations		
Aerosols	$\times 1,\ \times 100$	$\times 1,\ \times 100$

Table B.1: Atmospheric models composition (from Martins et al., 2017).

ionize lower in the atmosphere, which will result in the removal of their neutral forms at pressures less than 10^4 bars. Both these models also include Rayleigh scattering by the H_2/He component of the atmosphere. Aerosol scattering is also included in the models by adding extra scattering opacity and assuming that aerosols scatter without absorbing. Each *A* and *B* configuration was simulated for two different scattering scenarios ($\times 1$, $\times 100$), where the baseline $\times 1$ scenario corresponds to the gas opacity and the $\times 100$ scenario corresponds to 100 times the baseline opacity. Table B.1 summarizes the parameters for these configurations and Figure B.1 exemplifies the different albedo functions obtained for each configuration.

It can be seen that in wavelength ranges far from the water and alkali bands, the geometric albedo is around 0.75, as expected for a semi-infinite, conservative Rayleigh atmosphere. However, in wavelength ranges where water and alkali absorption is significant (e.g., around the 589-nm neutral sodium line), the albedo depends strongly on the adopted aerosol and gas content.

For more details on the simulated atmospheric and albedo models we refer the reader to Garcia-Muñoz et al. (2012) and Nielsen et al. (2016).

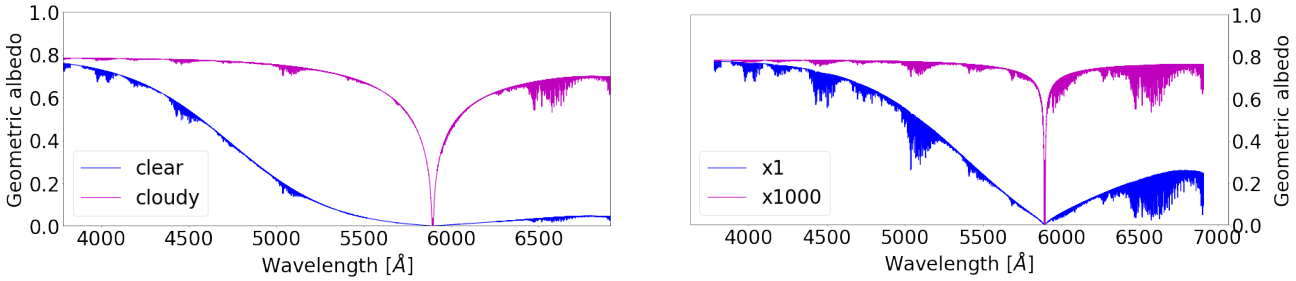

Figure B.1: Albedo function for the different configurations of the atmospheric models in Table B.1. *Top Panel:* Model A ($\times 1, \times 100$ configurations); *Bottom Panel:* Model B ($\times 1, \times 100$ configurations). The $\times 1, \times 100$ scenarios correspond respectively to different scattering configurations, where the opacity in the $\times 100$ configuration is 100 times larger that on the $\times 1$ baseline configuration (from Martins et al., 2017).

Appendix C.

Relevant spectroscopy statistics

In this Appendix we will summarize some statistical properties of spectral white noise that are relevant for this work. For a more detailed analysis, we refer you to (e.g. Wall et al., 2003).

SPECTRAL NOISE AS A POISSON DISTRIBUTION C.1

Stellar spectral noise is of thermal origin and thus follows Bose-Einstein statistics

$$\sigma_n = \sqrt{n}\left(1 + \frac{1}{e^{\frac{h\nu}{K_b T}} - 1}\right)^{-1} \tag{C.1}$$

where n and σ_n are respectively the number of photons and the photon noise, h the Planck constant, K_B the Boltzmann constant, and T surface temperature of the star.

In the optical, where $h\nu \gg KT$, the photons collected by a detector follow a Poisson distribution (e.g. Kitchin et al., 2003) as

$$\sigma_n = \sqrt{n} \tag{C.2}$$

and thus Poisson Statistics can be used to describe the behavior of stellar spectra.

The Poisson distribution is a statistical distribution defined by:

$$prob(n) = \frac{\mu^n}{n!} e^{-\mu} \tag{C.3}$$

where $\mu = \sqrt{n}$ is the expected value of the random variable n – in this context the number of photos – with standard deviation $\sigma_n = \sqrt{n} = \mu$.

The Poisson distribution is linear, i.e., the sum of Poisson distributions is still a Poisson distribution. Therefore, the sum of several spectra will still be a spectrum and its noise will still follow a Poisson distribution. Since the signal will be constant in in all summed spectra, it will add to itself. However, white noise, being of random nature, will average out. As such, the S/N of the sum of multiple spectra is given by

$$S/N^2_{sum} = \sum_i S/N^2_i \tag{C.4}$$

where S/N_i and S/N_{sum} are respectively the S/N of each individual spectrum and of their sum. In the particular case where all spectra have similar S/N:

$$S/N_{sum} \approx \sqrt{N}\ \ \langle S/N_i \rangle \tag{C.5}$$

where N is the number of spectra we are summing and $\langle S/N_i \rangle$ is the average of the S/N of all spectra. Note that red noise does not follow a Poisson statistic and needs to be treated as a signal by itself.

NOISE AS A GAUSSIAN DISTRIBUTION C.2

As $N \rightarrowtail \infty$, the Central Limit Theorem dictates that Poisson distributions can be approximated by a Gaussian (or normal) distribution with $mean = \sigma = \lambda$. Therefore, for large values of N, this discrete variable can be approximated by a continuous variale and Equation C.3 becomes

$$P(x) = \frac{1}{\sigma\sqrt{2\pi}}\, e^{\frac{(x-\mu)^2}{2\,\sigma^2}} \tag{C.6}$$

This means that for a large number of photons, spectral noise will follow a Gaussian (or normal) distribution. This is applicable to the high S/N domain we worked through this project and as such CCF noise has a Gaussian distribution.

This property is particularly useful in our work when removing the stellar signal by normalizing the CCF of each individual observations by the stellar template CCF. Let's define Defining $Z = \frac{X}{Y}$, where X and Y are two arbitrary normal random variables whose distributions have parameters μ_X, σ_X, μ_Y and σ_Y. By definition, for each variables X, Y and Z, the S/N is given by

$$S/N_{X,Y,Z} = \mu_{X,Y,Z}/\sigma_{X,Y,Z} = \sqrt{\mu_{X,Y,Z}} \tag{C.7}$$

The error propagation formula for measured quantities states that:

$$\frac{\sigma_Z}{\mu_Z} = \sqrt{\left(\frac{\sigma_X}{\mu_X}\right)^2 + \left(\frac{\sigma_Y}{\mu_Y}\right)^2} \tag{C.8}$$

which applied to the ratio of an individual spectrum k by the stellar template, gives that the S/N of that ratio is

$$\begin{aligned} S/N_{k,Normalized} \approx & \left(\sqrt{S/N_k^{-2} + S/N_{Template}^{-2}}\right)^{-1} \\ \approx & \; S/N_k \left(\sqrt{1 + \tfrac{1}{N}}\right)^{-1} \end{aligned} \tag{C.9}$$

where S/N_k and $S/N_{Template}$ are respectively the S/N of spectrum k and of the star template and $S/N_{k,Normalized}$ is the S/N of their ratio. Therefore, for a template constructed from a high number of spectra ($N > 100$)

$$S/N_{k,Normalized} \approx S/N_k \tag{C.10}$$

and thus the removal of the stellar CCF from our observations by normalization does not impact significantly the S/N the resulting obsevations